Characterization of individual Bi_2Te_3 nanowires electrodeposited in etched ion-track membranes for nano-ARPES and electrical transport studies

Charakterisierung von elektrochemisch in ionspurgeätzen Membranen abgeschiedenen, einzelnen Bi_2Te_3 Nanodrähten für nano-ARPES- und elektrische Transportuntersuchungen

Zur Erlangung des Grades eines Doktors der Naturwissenschaften (Dr. rer. nat.)
genehmigte Dissertation von M.Sc. Janina Maria Krieg aus Simmern
Tag der Einreichung: 24. April 2017, Tag der Prüfung: 19. Juli 2017
Darmstadt 2017 — D 17

1. Gutachten: Prof. Dr. Christina Trautmann
2. Gutachten: Prof. Dr. Ralph Krupke

TECHNISCHE UNIVERSITÄT DARMSTADT

Fachbereich
Material- und Geowissenschaften
Ionenstrahlmodifizierte Materialien

Characterization of individual Bi_2Te_3 nanowires electrodeposited in etched ion-track membranes for nano-ARPES and electrical transport studies
Charakterisierung von elektrochemisch in ionspurgeätzen Membranen abgeschiedenen, einzelnen Bi_2Te_3 Nanodrähten für nano-ARPES- und elektrische Transportuntersuchungen

Genehmigte Dissertation von M.Sc. Janina Maria Krieg aus Simmern

1. Gutachten: Prof. Dr. Christina Trautmann
2. Gutachten: Prof. Dr. Ralph Krupke

Tag der Einreichung: 24. April 2017
Tag der Prüfung: 19. Juli 2017

Darmstadt 2017— D 17

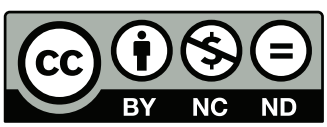

Erklärung zur Dissertation

Hiermit versichere ich, die vorliegende Dissertation ohne Hilfe Dritter nur mit den angegebenen Quellen und Hilfsmitteln angefertigt zu haben. Alle Stellen, die aus Quellen entnommen wurden, sind als solche kenntlich gemacht. Diese Arbeit hat in gleicher oder ähnlicher Form noch keiner Prüfungsbehörde vorgelegen.

Darmstadt, den 24. April 2017

(J. Krieg)

Zusammenfassung

Vielversprechende Forschungsfelder aus dem Bereich der Festkörperphysik, wie zum Beispiel Thermoelektrik und Spintronik, werden durch die einzigartigen Eigenschaften von Bismut-basierten Materialien geprägt. Bismuttellurid (Bi_2Te_3) ist beispielsweise ein Halbleiter mit kleiner Bandlücke und exzellenten thermoelektrischen Eigenschaften, die für die Umwandlung von thermischer in elektrische Energie bei Raumtemperatur eine der höchsten Effizienzen aufweist. Außerdem wird Bismuttellurid einer neuen Klasse von Quantenmaterialen, den **T**opologischen **I**solatoren (TI) zugeordnet, die Spin-Bahn-gekoppelte Oberflächenleitfähigkeit bei gleichzeitig isolierendem Verhalten im Volumen besitzen. Beide Eigenschaften verheißen Anwendungen in der Elektronik und Spintronik, die durch Energieeffizienz und hohe Rechenleistung bestechen.

Die experimentelle Bestimmung der speziellen Charakteristika des TIs stellt jedoch eine besondere Herausforderung dar, weil die Leitfähigkeit des Volumens das elektrische Signal dominiert und die Oberflächenzustände nur schwer zugänglich sind. Um diese Hürde zu überwinden beschäftigt sich diese Dissertation zunächst mit der Herstellung von Bi_2Te_3 Nanodrähten, deren Oberflächen-zu-Volumen Verhältnis extrem groß ist und deren geometrische, kristallographische und morphologische Eigenschaften unabhängig von einander kontrolliert eingestellt werden können. Dadurch können die Anteile der Oberflächenzustände aufgelöst werden.

Bi_2Te_3 Nanodrähte wurden durch elektrochemische Abscheidung in ionenstrahlgeätzten Polymermembranen synthetisiert. Hierfür wurden zuerst 30 µm dicke Polycarbonatfolien mit hochenergetischen Schwerionen bestrahlt. Jedes einzelne Ion erzeugt eine Ionenspur, die durch einen selektiven chemischen Ätzprozess in zylindrische Nanoporen umgewandelt wird. In diesen Poren wurden anschließend Nanodrähte mit Durchmessern zwischen 25 und 100 nm abgeschieden. Röntgendiffraktometrie und Transmissionselektronenmikroskopie zeigen texturierte Nanodrähte, die aus mehreren einkristallinen und bis zu mehreren hundert Nanometern langen Segmenten bestehen. Die chemische Zusammensetzung wurde durch energiedispersive Röntgenspektroskopie und Röntgenphotoemissionsspektroskopie, sowohl für das Volumen als auch für die Oberfläche, bestimmt. Erstere zeigt dabei eine homogene, beinahe stöchiometrische Zusammensetzung, während letztere das Vorhandensein von Sauerstoff- und Kohlenstoffkontaminationen bestätigt. Diese Kontamination wird Polymerresten zugeschrieben, die von der Auflösung des Polymertemplates herrühren.

Untersuchungen der elektronischen Eigenschaften einzelner Bi_2Te_3 Nanodrähte wurde mit Hilfe von nano-winkelaufgelöster Photoemissionsspektroskopie (nano-ARPES) am französischen Synchrotron SOLEIL durchgeführt. In einem speziellen Aufbau, der für das Detektieren von Photoemissionssignalen von Nanoobjekten entwickelt wurde, wurden einzelne Abschnitte der Nanodrähte analysiert. Winkelintegrierte Messungen von Rumpfelektronenniveaus entlang der Drahtoberfläche bestätigen die homogene chemische Zusammensetzung. Mit winkelaufgelösten Messungen wurde die Valenzbandstruktur einzelner Drahtabschnitte erfolgreich aufgenommen. First-Prinzipal Rechnungen für die bevorzugt abgeschiedenen Kristallorientierungen stimmen gut mit den experimentellen nano-ARPES Ergebnissen überein.

Um elektrische Transportmessungen durchzuführen, wurden einzelne Nanodrähte mittels Laser- und

Elektronenstrahllithographie kontaktiert. Der spezifische Widerstand weist die für Metalle typische Temperaturabhängigkeit auf und steigt mit abnehmendem Drahtdurchmesser an. Des Weiteren wurden Magnetotranportmessungen in gepulsten (bis 60 T) und statischen (bis 12 T) Magnetfeldern mit paralleler und senkrechter Orientierung bezüglich der Drahtachse, durchgeführt. Im Allgemeinen ist der Magnetwiderstand positiv und steigt mit größer werdendem Magnetfeld linear oder quadratisch an ohne zu saturieren. Schwache Antilokalisierungseffekte, die bei kleinen Temperaturen und in schwachen Magnetfeldern auftreten, weisen auf das Vorhandensein von Quanteninterferenzphänomenen aufgrund der hohen Spin-Bahn-Wechselwirkung hin. Die erhaltenen Ergebnisse sind erste Hinweise auf Quantenphänomene an elektrochemisch in Polymermembranen abgeschiedenen, zylindrischen Bi_2Te_3 Nanodrähten.

Die in dieser Arbeit dargelegte erfolgreiche Vermessung von elektrochemisch abgeschiedenen, einzelnen Bi_2Te_3 Nanodrähten mittels Nano-ARPES und Magnetotransportmessungen eröffnen neue Möglichkeiten, die für weiterreichende Untersuchungen von topologischen Isolator-Nanostrukturen von großer Bedeutung sind. Die entwickelten experimentellen Methoden legen den Grundstein für künftige Untersuchungen in Abhängigkeit des Drahtdurchmessers, der Kristallorientierung und der Korngröße. Dieses Wissen, in Kombination mit der hier gebrauchten einfachen und kontrollierbaren Bi_2Te_3 Nanodrahtherstellung, verspricht ein großes Anwendungsportfolio als innovative Elektronik- und Spintronikbauteile.

Abstract

Promising research fields associated to solid state physics, such as thermoelectrics and spintronics, have been influenced by the unique properties of bismuth-based materials. Bismuth telluride (Bi_2Te_3), for example, is a semiconductor with a very small band gap and excellent thermoelectric properties which show one of the highest thermal to electrical energy conversion efficiency at room temperature. Moreover, bismuth telluride belongs to a new class of materials called **T**opological **I**nsulators (TI), which exhibit surface conductivity with spin-momentum-locked electronic surface states while being bulk insulators. Both properties promise many application possibilities in electronic and spintronic devices with regards to energy efficiency and faster computing.

The experimental investigation of the special topological insulator characteristics is very challenging, because the bulk conductivity dominates the electrical signal resulting in hardly accessible surface states. In order to overcome this challenge, the present dissertation initially presents the fabrication of Bi_2Te_3 nanowires with extremely large surface-to-volume ratio and independently controllable geometric, crystallographic and morphologic properties that enable a resolution of the surface states.

The Bi_2Te_3 nanowires were synthesized by electrodeposition in ion-track etched polymer templates. For this purpose, 30-µm thick polycarbonate foils were irradiated by highly energetic heavy ions. Each ion creates an ion track, which can be converted into cylindrical nanopores by selective chemical etching. Subsequent electrochemical deposition within these nanopores resulted in nanowires with diameters between 25 and 100 nm. X-ray diffraction and transmission electron microscopy reveals highly textured nanowires consisting of single crystalline sections that are several hundreds of nanometers long. For both, bulk and surface, the chemical composition was analyzed by energy-dispersive x-ray spectroscopy and x-ray photoemission spectroscopy. The former shows a chemically homogeneous composition close to stoichiometry, while the latter revealed oxide and carbon contaminations, which is attributed to polymer residues from the template.

Investigations of the electronic properties of individual Bi_2Te_3 nanowires were performed using nano-angle-resolved photoemission spectroscopy (nano-ARPES) at the French synchrotron SOLEIL. Sections of single nanowires were analyzed by employing a setup that was especially developed to obtain photoemission signals from individual nanoobjects. Angle-integrated measurements along the length of the nanowire recording the core levels, confirmed the homogeneous chemical composition. Employing the angle-resolved mode, the valence band structure of single nanowires sections was successfully revealed. First principles calculations of the preferably deposited crystallographic orientation are in good agreement with the experimental nano-ARPES results.

In order to conduct electrical transport measurements, individual nanowires were contacted by laser and electron beam lithography. The resistivity recorded as a function of temperature exhibits typical metallic behavior and increases with decreasing wire diameter. Magnetotransport investigations for different nanowire diameters were successfully performed by applying pulsed (up to 60 T) or static (up to 12 T) magnetic fields perpendicular and parallel to the wire axis. Generally, the magnetoresistance was found to be positive, increasing either linearly or quadratically with the magnetic field and shows no saturation.

At low temperatures and within the zero-magnetic-field regime, the appearance of weak antilocalization effects indicates the presence of quantum interference caused by large spin-orbit coupling. The obtained results provide first signs of quantum phenomena in electrochemically deposited Bi_2Te_3 nanowires.

The presented successful investigation of electrodeposited Bi_2Te_3 nanowires by nano-ARPES and magnetotransport measurements opens new possibilities that are of great importance for future investigations of the electrical transport characteristics of topological insulators nanostructures. The developed experimental methods lay the groundwork to pursue these studies as a function of various nanowire properties such as diameter, crystallographic structure and grain boundaries. This knowledge combined with the easy and controlled fabrication of the unique nanowire samples employed here, promises many applications as innovative electronic and spintronic devices.

Publications

Parts of this thesis have been published in

- **Peer-reviewed publication**
  J. Krieg, C. Chen, J. Avila, Z. Zhang, W. Sigle, H. Zhang, C. Trautmann, M. C. Asensio, M. E. Toimil-Molares *Exploring the electronic structure and chemical homogeneity of individual Bi_2Te_3 nanowires by nano-angle-resolved photoemission spectroscopy*
  Nano Lett. **16** (7), 4001 (2016)

- **Book publication**
  O. Picht, J. Krieg and M. E. Toimil-Molares
  Bi_2Te_3 nanowires by electrodeposition in polymeric etched ion track membranes: Synthesis and characterization
  "Thermoelectric Bi_2Te_3 Nanomaterials" edited by O. Eibl, K. Nielsch, N. Peranio and F. Völklein, ISBN: 978-3-527-33489-6, Wiley-VCH publishers (2015)

- **Further publication**
  J. Krieg, C. Chen, J. Avila, C. Trautmann, M. C. Asensio, M. E. Toimil-Molares
  XPS measurements on single Bi_2Te_3 nanowires fabricated by electrodeposition in etched ion-track membranes
  GSI Scientific Report (2014)

Difficulties are just things to overcome, after all.

- Ernest Shackleton -

Contents

Motivation

The accelerating technological advances continue to impact on various fields of human life revolutionizing our social and working environment [1].
Initially, interaction via networks was limited to people communicating via personal computers. As a result of the invention of smartphones and tablets, more and more electric devices offered similar applications and access to wireless interconnection enabling data sharing and synchronization between different devices. The next area of innovation and growth is the so called *Internet of Things*, a term defined by K. Ashton in [2], where physical devices intelligently communicate with each other without the permanent control of a human operator. One famous and already commercially available system is the smart home, where light sensors, window blinds, thermostats, entertainment devices and even home appliances are interconnected, sharing data and operating independently according to weather data, time schedules and personal preferences of the resident. Further areas of human life in which the *Internet of Things* develop a great impact are mobility and transportation, worksites and factories as well as consumerism and health care.
On the one hand, technical advances such as the ongoing miniaturization and decreasing costs of microelectronics, the expansion of wireless connectivity, the increasing data storage and processing capacities as well as innovative software solutions triggered a rapid expansion of the *Internet of Things* [3]. On the other hand, global challenges such as efficient energy usage, fast computing performance and data security are faced when developing electronic devices for implementation in everyday items. Especially mobile devices and wearables require energy efficient operation as one way to increase battery lifetime [4].
These challenges have inspired multiple strategies to develop innovative materials. One example for enhanced energy efficiency is the ongoing optimization of thermoelectric materials, such as Bi_2Te_3 and $Bi_{1-x}Sb_x$, to be used as thermal to electric energy converters [5, 6]. A promising idea to increase the data processing speed, while lowering the power consumption, is to not only use the charge, but also the spin of electrons for information processing. In contrast to semiconductor field-effect transistors using the on- and off-state for information transport, a device based on both, charge and spin state, can provide more efficient information transport as well as storage [7, 8]. For this reason, materials allowing for a manipulation of the spin states opened up a progressing field of research [7].
Topological insulators, for example, posses unique properties, because their spin is locked to the momentum of the electrons. They belong to a new class of quantum materials opening an exciting branch in solid state physics by exhibiting an insulating bulk and a conductive surface [9, 10]. The surface, or edge states in the case of 2D objects, are unique due to their spin-momentum locking properties giving rise to electrons in helical spin states. Furthermore, the surface states are protected by time-reversal symmetry preventing their destruction by non-magnetic impurities resulting in dissipationless transport. Both of these exotic characteristics lead to many application possibilities, especially in electronics, spintronics and optoelectronics [5]. Additionally, many proposed **T**opological **I**nsulators (TIs), such as Bi_2Te_3, $Bi_{1-x}Sb_x$ are good thermoelectric materials extending their range of application even further [5, 6]. Apart

from new devices for applications, TIs are predicted to be excellent model systems for testing fundamental theories of solid state physics such as the prediction of new particles like the Majorana fermions [11]. Furthermore, the new concept of classifying matter topologically gives rise to many new material classes, such as topological crystalline insulators [12] and Weyl semimetals [13, 14].

Surface sensitive techniques including **A**ngle-**R**esolved **P**hoto**E**mission **S**pectroscopy (ARPES) and scanning tunneling microscopy [15, 16] provide an easy way of probing the surface states without overlapping their signal by the background bulk charge carriers. Transport measurements are challenging due to the dominance of the bulk charge carriers compared to their surface counterparts and intrinsic doping of the material. Ways to overcome this challenge are TI nanomaterials. They provide a large surface-to-volume ratio, reducing the bulk contributions geometrically [17, 18]. Furthermore, the Fermi level can be adjusted to the surface states inside the bulk band gap, by making use of field-effect gating especially efficient for nanostructure-based devices [19, 20]. Another advantage of TI nanomaterials are the possibility to manipulate the 2D surface states by geometry and morphology [21] as well as by fabricating TI nano-heterostructures [22].

So far, the search for topological surface states in Bi_2Te_3 nano-objects such as nanowires has been lad by electrical transport measurements providing an indirect investigation of these unique surface states [23–28]. However, it is well-known that a heterogeneous stoichiometry drives important electronic modifications such as changing the doping, carrier density, gaps as well as massless properties and thus influences the thermoelectric [29, 30] and electrical transport properties [31]. Consequently, the direct investigation of the electronic band structure of TI nanowires and their surface states requires a full study using ARPES. This is extremely challenging, but possible by ARPES measurements with enough spatial resolution and sufficient signal intensity that had to be specifically developed to characterize nano-objects [32–36].

On that basis, the present dissertation aims for the investigation of the electronic properties of bismuth telluride nanowires electrochemically deposited in etched ion-track polymer membranes. For this purpose, nano-ARPES and magnetotransport experiments were developed and conducted on cylindrical nanowires of different diameters. In general, Bi_2Te_3 is one of the first discovered TI materials, but exhibits a small bulk band gap leading to a significant bulk state contribution to an electrical transport signal. The high surface-to-volume ratio of the nanowires investigated in this work is expected to reduce the bulk contribution and thus providing access to measure the surface states.

Chapter 1 introduces bismuth telluride in context of the discovery of TI materials and as a well-known thermoelectric material. Chapter 2 describes the synthesis method to obtain nanowires with controlled properties and parameters. The wires are characterized in terms of their geometry, morphology, chemical composition, crystallographic orientation and annealing behavior using various methods. The results presented in chapter 3 provide important knowledge for the optimal sample preparation for nano-ARPES and magnetotransport measurements. Chapter 4 presents the nano-ARPES investigations by introducing the unique setup, the sample preparation and the measurement results. These experimental results were compared to those obtained by first principles calculations of similar samples. Finally, the magnetotransport experiments conducted in pulsed and static magnetic fields for various wire diameters are described in chapter 5.

1 Introduction to bismuth telluride (Bi_2Te_3)

In the last decades bismuth telluride (Bi_2Te_3) based materials have attracted great interest due to their potential application for thermoelectric cooling and power generation. Besides being the most efficient room-temperature bulk thermoelectric material [37] for 60 years, in 2009, Bi_2Te_3 was predicted to be a three-dimensional **T**opological **I**nsulator (TI) [38].

Bismuth telluride is a compound between the post-transition metal bismuth (^{83}Bi) and the metalloid tellurium (^{52}Te). Besides Bi_2Te_3, other compositions of bismuth and tellurium have been reported, including BiTe, Bi_4Te_5, Bi_4Te_3, Bi_6Te_7 and Bi_7Te_3 [30]. Naturally, Bi_2Te_3 occurs in minerals in combination with elements such as Se, S, Pb, Au, etc. Recently two of them, Kawazulite ($Bi_2(Te,Se)_2(Se,S)$) [39] and Aleksite ($PbBi_2Te_2S_2$) [40] were found to be natural topological insulators. In pure combination of Bi and Te, the commonly known minerals are tellurobismuthite (Bi_2Te_3), pilsenite (Bi_4Te_3) [41], tsumoite (BiTe) [42] and hedleyite (Bi_7Te_3) [43]. Bi_2Te_3 is commercially produced as gray powder and exhibits a bulk melting point of 573°C [44].

Bismuth telluride has a trigonal crystal structure with space group R-3m and is described in the rhombohedral or hexagonal lattice system as schematically depicted in figure 1.0.1. Within the hexagonal description a quintuple with an alternating -$Te^{(1)}$-Bi-$Te^{(2)}$-Bi-$Te^{(1)}$- structure is formed [45]. The index on the Te layer denotes a different arrangement of the Te atoms in reference to the surrounding Bi and Te layers. Three quintuples form the hexagonal unit cell. While the intra-atomic layers are covalently and ionically bond, the $Te^{(1)}$-$Te^{(1)}$ bondings exhibit van der Waals interaction resulting in easy cleavage along these planes [46] oriented perpendicular to the c-axis. Due to their crystal structure, Bi_2Te_3 single crystals feature a high degree of anisotropy of their (thermo-)electric transport properties [47]. The lattice parameters for rhombohedral [48] and hexagonal [45] systems are indicated in figure 1.0.1.

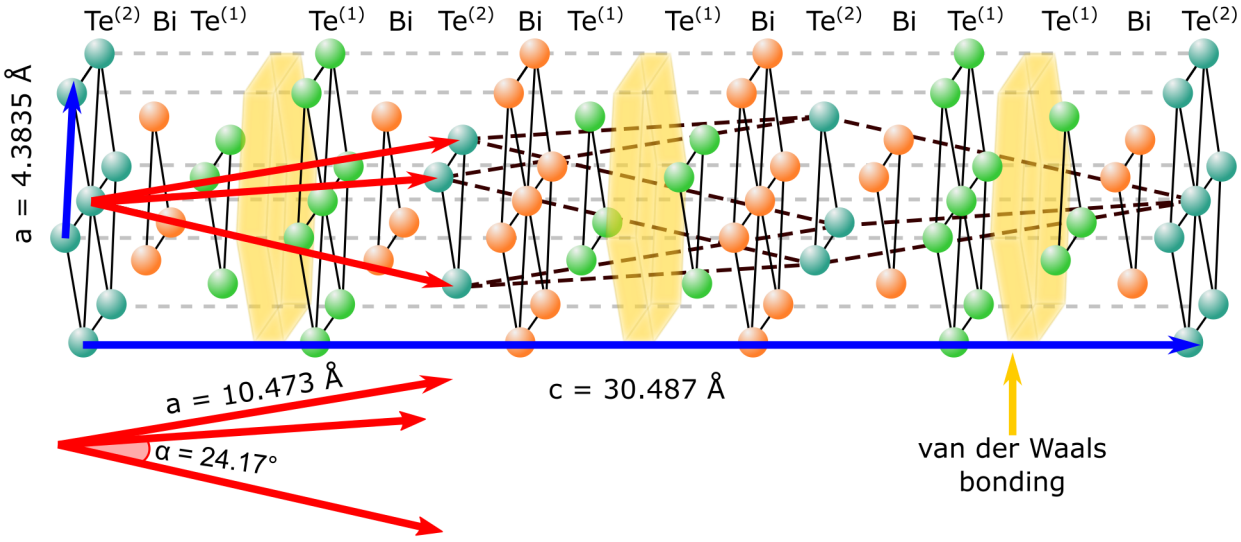

Figure 1.0.1: Schematic representation of the Bi_2Te_3 crystal: hexagonal (blue; a = 4.3835 Å, c = 30.487Å [45]) and rhombohedral (red; a = 10.473 Å, $\alpha = 24.17°$ [48]) unit cell.

In this chapter the concept of topological insulators as well as thermoelectric materials is introduced. Besides the basics and most important experimental breakthroughs, special attention is given to the relevance of bismuth telluride as a thermoelectric and topological insulator material. In this work the term bismuth telluride refers to the chemical composition of Bi_2Te_3.

1.1 Topological insulators

Throughout the evolution of the different disciplines in physics, materials have been classified employing various criteria. Figure 1.1.1 provides a schematic summary of different selected material classes dependent on the (mathematical) space on which they are defined.

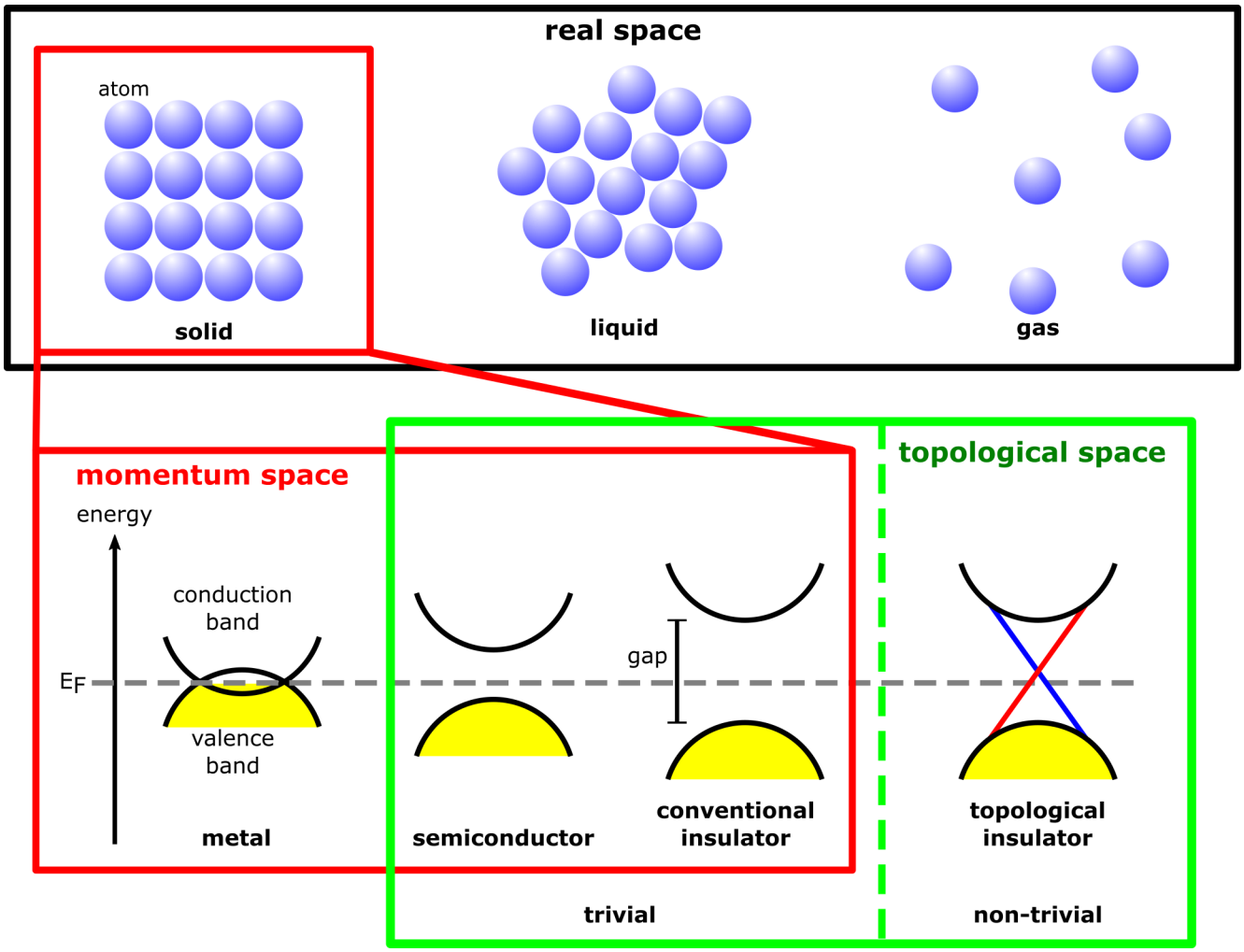

Figure 1.1.1: Concepts for the classification of states of matter using selected examples: solid, liquid and gas phase are distinguished in real space (black box). Solids are characterized as metals, semiconductors and insulators by their energy gap in momentum space (red box). Applying topology distinguishes trivial and non-trivial topology (green box). Semiconductors and conventional insulators are topologically equivalent, while a topological insulator is an example for non-trivial topology.

The most commonly known approach is to distinguish states of matter in real space by considering the geometrical arrangement of their atoms (blue spheres) resulting in solid, liquid and gas phases (black box). Following this concept for condensed matter, various crystal symmetry classes are defined in real space such as cubic and hexagonal.
Considering different electronic properties, condensed matter is classified depending on its band structure and density of states requiring a transition of the translation symmetry of the crystal into momentum space (red box). Consequently, metals and insulators are distinguished according to their energy band structure. In metals, overlapping or partially filled bands allow for easy excitation of electrons into unoccupied states, while the completely occupied (yellow) lower (valence) band in insulators is separated from the upper (conduction) band by an energy gap. This energy gap, though much smaller than for conventional insulators, is also a characteristic of semiconductors allowing thermal excitation across the small energy gap into the conduction band. Tuning the band structure, i.e. the Hamiltonian, in a way that the finite size of the energy gap changes but does not reach zero, a conventional insulator can be transformed into a semiconductor and vice versa. In a certain sense, the two different states are related and this relation is ascribed to the topology of the states of matter rather than their geometry.
In a topological understanding (green box), conventional insulators and semiconductors are equivalent. On the other hand, not all insulators are topologically equivalent giving rise to a new class of quantum matter: the topological insulator. The most simple picture of a topological insulator is a bulk insulator exhibiting metallic states on its surface (more precise: on its interface to e.g. vacuum). In terms of band theory, the energy gap is closed by the so called surface states (red and blue lines). The closing of the gap is an indicator of the topological change, while the bulk band gap defines the insulating nature of the material.
In the following sections, the concept of applying topology to classify quantum states (section 1.1.1), the chronological development (section 1.1.2) and the key "ingredients" to obtain a TI (section 1.1.3) are summarized. The hype about TIs becomes obvious by the fact that they were experimentally discovered only two years after their prediction. The two breakthrough experiments are shortly introduced in section 1.1.4, marking the starting point of an extremely fast developing and fascinating field of research. Lastly, the topological non-trivial properties of Bi_2Te_3 are introduced in section 1.1.5.

1.1.1 Applying topology to classify quantum states

Topology is a fundamental branch of mathematics developed on the basis of geometrical problems. The key studies are properties of mathematical spaces that are preserved under continuous deformations. The most figurative illustration of topology is again linked to geometry, namely classifying objects into topological classes according to their number of holes. A schematic illustration is provided in figure 1.1.2. By definition a sphere belongs to the same topological class as a disc, because squishing a sphere deforms it into a disc[1]. Similarly, a cup and a donut are topologically equivalent, being transformable into each other and possessing one hole. On the contrary, a sphere is not convertible into a donut, because it requires the creation of a hole, which corresponds to a non-continuous deformation. In this way geometrical objects are described by only one parameter called genus g ($g = 0$ for a sphere and $g = 1$ for a donut)

[1] In more mathematical terms, one says that the sphere is homeomorphic to the disc. A homeomorphism is a continuous map between two topological spaces that also has a continuous inverse [49].

and are classified regardless of their actual geometrical shape [50]. Gauss and Bonnet independently described the link between the geometry and the topology of an object (without boundaries) by

$$\int_S K dA = 2\pi\chi(S), \tag{1.1}$$

where S is the surface, dA any area element, K the Gaussian curvature and $\chi(S) = 2(1-g)$ the Euler characteristic. It follows that the total Gaussian curvature is given by an integer only dependent on the genus and thus the topology of an object, while its exact local shape is irrelevant [49].
In physics, smooth transformations are considered adiabatic. Analogous to the geometrical objects, the electronic band structure of materials is deformable by adiabatic transformation. Changing the Hamiltonian smoothly, gapped band structures are transformed into each other, making both insulator and semiconductor topologically equivalent (like a sphere and a disc).

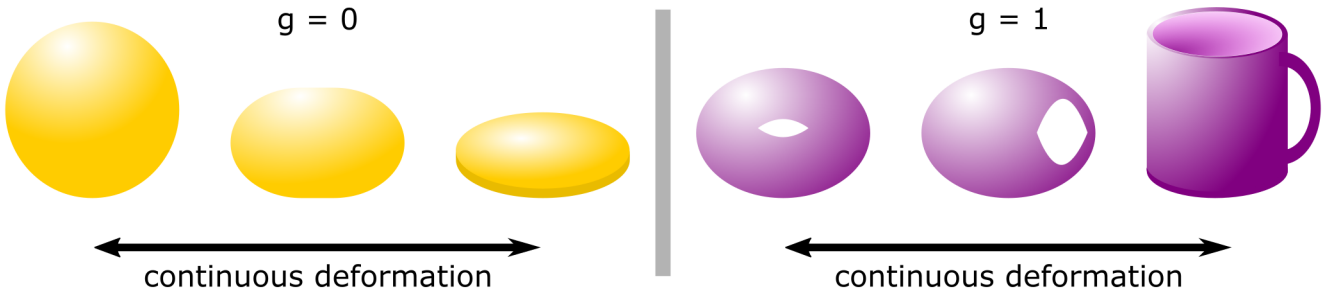

Figure 1.1.2: Geometric examples of different topologies: Under continuous deformation a sphere is formed into a disc (left) and a donut into a cup (right). The topological class is determined by the number of holes in the object, called genus g.

If a system undergoes adiabatic changes, its wavefunction picks up a so called Berry phase while traveling on a closed loop in its parameter space [51]. A simple picture of a Berry phase is the angle by which an arrow or a compass needle pointing in one direction is rotated as it is moved on a closed loop along the surface of a sphere. Once it returns to its starting point, the compass needle has been rotated by a certain angle. The Berry phase is defined as

$$\gamma_n = \oint_C \mathbf{A}_n(\mathbf{R}) \overset{\text{Stokes}}{=} \int_S dA(\nabla_{\mathbf{R}} \times \mathbf{A}_n(\mathbf{R})) = \int_S dA\Omega_n(\mathbf{R}), \tag{1.2}$$

with $\mathbf{R} = (R_1, R_2, ...)$ denoting a vector with varying parameters, $\mathbf{A}_n = i\langle n(\mathbf{R})|\nabla_{\mathbf{R}}|n(\mathbf{R})\rangle$ being the Berry vector potential with the Nabla operator $\nabla_{\mathbf{R}}$ defined with respect to the parameters and Ω_n denoting the Berry flux.
The equivalence classes differ by a topological invariant called the Chern invariant $n \in \mathbb{Z}$. The physical correspondence to the Gauss-Bonnet Theorem (equation 1.1) writes as

$$n = \sum_i^N \frac{1}{2\pi} \int_{BZ} d^2\mathbf{k}\Omega_n(\mathbf{k}) \tag{1.3}$$

with **B**rillouin **Z**one (BZ). It follows that for quantum mechanical systems, the total Chern invariant n over all occupied bands N corresponds to the total Berry flux in the BZ.
The first time topology was considered to describe a special state of matter was the explanation of the **Q**uantum **H**all **S**tate (QHS). This state occurs, when a **Two**-**D**imensional **E**lectron **G**as (2DEG), in which electrons are confined in two dimensions, is exposed to a strong magnetic field at very low temperatures of a few Kelvin [52]. The electrons are then forced on circular orbits resulting in their localization within the 2D plane. Furthermore, their energy is quantized into so called **L**andau **L**evel (LL) whose energy $\epsilon_{LL} = \hbar\omega_c(LL + 1/2)$ is defined by the cyclotron frequency ω_c. Viewing the LL splitting as a kind of band structure manifests the similarity to the insulating state, since the filled and empty Landau levels are separated by an energy gap of $\hbar\omega_c$. Nevertheless unlike for an insulator, a quantized Hall conductance

$$\sigma_{xy} = \nu\frac{e^2}{h}, \tag{1.4}$$

is measured across (xy-direction) the 2DEG with ν being an integer, e being the elementary charge and h denoting Planck's constant. **T**houless **K**ohmoto **N**ightingale and den **N**ijs (TKNN) realized that the difference between a QHS and a conventional insulator derives from their differing topology. They showed that ν is identical to n in equation 1.3 [53]. In the following, $\nu = \nu_{TKNN}$ was also referred to as TKNN invariant which does not change under adiabatic transformations of the Hamiltonian. For his work on the topological characterization of new quantum states, Thouless was one of the physics Nobel laureates in 2016. In the QHS, $\nu_{TKNN} > 0$ (or 1) while in the conventional insulator $\nu_{TKNN} = 0$ manifesting two different topological classes.
The occurrence of the quantum Hall conductivity can now be explained in two different ways that are sketched in figure 1.1.3 (a). In a geometrical picture, the electrons (red) close to the edge of the 2DEG (blue) are not able to complete a full circular motion due to its boundary or interface. Instead, half circles are described resulting in chiral propagation along the edges of the 2DEG. The motion is chiral in the sense that its direction (red arrow) is predetermined by the orientation of the magnetic field (green) and by the lack of energy states available for backscattering. Thus, the electronic transport at the edges is robust against disorder (e.g. kinks) and can be considered dissipationless. In the topological picture, the edge states arise at the interface between two materials of different topological classes namely the QHS with $\nu_{TKNN} > 0$ and, in the simplest case, vacuum of $\nu_{TKNN} = 0$. Considering that the topology is invariant under continuous transformation, the band gap has to vanish and reopen again at the interface. Consequently, metallic edge states are formed for which the energy gap amounts to zero.
Two possible band structures for the QHS are sketched in figure 1.1.3 (b). The most straightforward possibility is a single edge state (red) exhibiting a positive group velocity $v_g = \partial E/\hbar\partial k$ (corresponding to a right moving mode), connecting the valence and conduction bands directly. Imagining transformations of the Hamiltonian close to the edge, that change the energy landscape in a way that kinks are arbitrarily introduced (green). Consequently, also negative group velocities (or left moving modes) are created. Due to the requirement of gapless edge states, the difference between the number of right N_R and left N_L moving modes remains constant

$$N_R - N_L = \triangle\nu_{TKNN}. \tag{1.5}$$

This relation is called the bulk-boundary correspondence, because the edge state dispersion is uniquely determined by the topology of the bulk material.

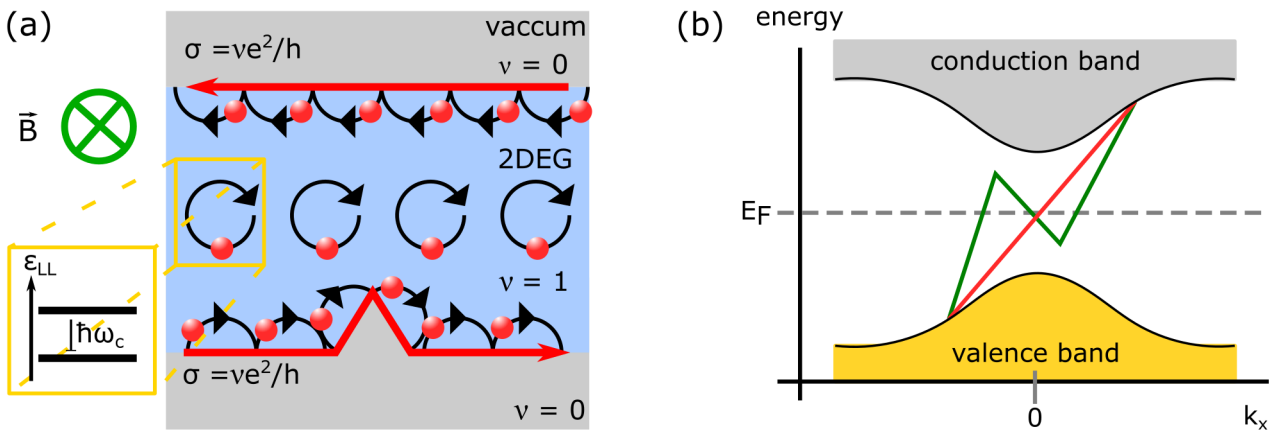

Figure 1.1.3: Schematic representation of the quantum Hall state (a) and its band structure (b). Electrons (red) confined in a 2DEG (blue) exposed to a magnetic field (green) move on circular orbitals. Inside the 2DEG, the splitting of the energy bands into Landau levels leads to a localization of the electrons creating a gapped band structure (yellow box). On the edges, the incomplete circular motion leads to a conductance σ that is not destroyed by disorder (kink). The topological invariants change from $\nu_{TKNN} = 0$ to $\nu_{TKNN} = 1$ crossing the interface between the 2DEG and vacuum. (b) Possible surface states connect the valence and the conduction band crossing the Fermi level by an odd number of times (red and green).

In order to explain the quantum Hall state, the mathematical branch of topology was applied leading to a new classification of quantum states of matter. While a semiconductor and a conventional insulator are topologically equivalent, the quantum Hall state presents a different state distinguishable by the topological TKNN invariant. The beaming question is, if this topologically non-trivial QHS can be realized elsewhere.

1.1.2 The search for exotic quantum states

The realization of the QHS requires strong magnetic fields of about 15 T and very low temperatures of approximately 4 K [52]. Searching for quantum Hall-like systems without such extreme condition requirements, Haldane investigated a model system of a graphene-like crystal structure which exhibits Dirac points where the valence and conduction bands touch each other following a linear dispersion relation [54]. Since all atoms are considered to be identical, such a system fulfills inversion and time-reversal symmetry, protecting the existence of the Dirac points. If one of these symmetries is broken, the degeneracy at the Dirac points is lifted. In the case of broken inversion symmetry (different kinds of atoms), a mass term is added to the Dirac Hamiltonian resulting in an energy gap in the dispersion relation and thus the system becomes a conventional insulator. Haldane achieved the broken time-reversal symmetry by adding a magnetic flux following the crystal periodicity and that amounts to zero over the complete unit cell. In that case, he found that each Dirac point adds $\pm e^2/2h$ to σ_{xy}, resulting in a quantum Hall state. For his work on this model, amongst others, Haldane was another laureate of the physics Nobel prize in 2016. The importance of his research was to show that the QHS is possible in other systems, but yet, it still required the breaking of time-reversal symmetry (i.e. a magnetic flux).

Almost 20 years later, Kane and Mele studied the effect of spin-orbit coupling on the basis of Haldane's model for graphene [55] in order to replace the magnetic flux. In this system the time-reversal symmetry is unbroken and a new topological state of gapped band structures was found, the **Q**uantum **S**pin **H**all **S**tate (QSHS). Although the TKNN invariant amounts to zero, it exhibits a Chern number which is a Z_2 invariant [56]. Later on, Moore proposed the term "topological insulator" for the QSHS [57].

1.1.3 Key requirements for Z_2 topological insulators

According to Kane and Mele, the key requirements for a QSHS are spin-orbit coupling and time-reversal symmetry. The former describes the interaction between the electron orbital angular momentum **L** generating a magnetic field **B** and the electron spin **S** resulting in an energy increase for parallel orientation and a decrease in the anti-parallel case. In solids, the spin-orbit coupling results in the splitting of energy bands according to their spin direction that are otherwise degenerate. The heavier the atoms in the solid, the higher is the electric field of their nucleii and the more pronounced is the spin-orbit splitting [58].
In a time-reversal invariant system, its state remains unchanged under time-reversal transformations $t \rightarrow -t$. The time-reversal operator Θ effectuates the change of the direction of time [59]. The position operator remains unchanged, while momentum and spin operators switch signs. Within a classical picture, applying Θ twice, i.e. reversing the time twice, should reestablish the original state. A half-integer spin system yields $\Theta^2 = -1$, leading to a constraint called the Kramers theorem [60]. It can be easily understood by assuming that the states $|\psi\rangle$ and $\Theta|\psi\rangle$ are the same quantum state only differing by a certain constant c, $\Theta|\psi\rangle = c|\psi\rangle$, then applying Θ results in

$$\Theta^2|\psi\rangle = |c|^2|\psi\rangle\,. \tag{1.6}$$

With $\Theta^2 = -1$ and $|c|^2 \neq -1$, it follows that $|\psi\rangle$ and its time-reversed state $\Theta|\psi\rangle$ are not equal. Hence, Kramers concluded that the energy states of a time-reversal invariant half-integer spin system have to be at least twofold degenerate [59, 60]. In the trivial case without spin-orbit interaction, this degeneracy is provided by the two different spin states $(\uparrow, \downarrow)$ satisfying

$$E_\uparrow(\mathbf{k}) = E_\downarrow(\mathbf{k}). \tag{1.7}$$

However, the situation in a spin-orbit coupled system is more complicated provided that the spin degeneracy is lifted by definition. A time-reversal invariant Hamiltonian satisfies the condition

$$\Theta H(\mathbf{k})\Theta^{-1} = H(-\mathbf{k}). \tag{1.8}$$

Consequently, for every energy state with momentum $\mathbf{k}$ and a certain spin direction, there must by a state available at the same energy with opposite spin at momentum $-\mathbf{k}$. Any two states satisfying

$$E\uparrow(\mathbf{k}) = E_\downarrow(-\mathbf{k}), \tag{1.9}$$

are thus called Kramers pairs. From equation 1.9 it directly follows that the Kramers pairs are degenerate at the **T**ime-**R**eversal Invariant **M**omenta (TRIM), $\mathbf{k} = 0$ and $\mathbf{k} = \pm\pi/a$ of the BZ with a denoting the interatomic distance. Figure 1.1.4 displays two possibilities of how edge states can occur for time-reversal invariant insulators exhibiting spin-orbit coupling. In both cases the bands are spin-split for momenta between $-\pi/a < \mathbf{k} < 0$ and $0 < \mathbf{k} < \pi/a$ (red and blue lines).

In a conventional insulator, the bands connect pairwise at the TRIM (pink circle) crossing the Fermi energy an even number of times (green circles) between $0 < \mathbf{k} < \pi/a$ as depicted in figure 1.1.4 (a). By changing the Hamiltonian, these edge states can be pushed out of the energy gap. This means that they are not robust against adiabatic transformations. On the contrary, figure 1.1.4 (b) shows how Kramers degeneracy is fulfilled by the crossing of the spin-split bands (pink circles) at $\mathbf{k} = 0$ and $\mathbf{k} = \pm\pi/a$. Consequently, they intersect the Fermi energy an odd number of times (green circles) between $0 < \mathbf{k} < \pi/a$. The bands cannot be eliminated by pushing them out of the bulk band gap under continuous transformations. This is the topological insulator case in which the metallic edge states are protected by time-reversal symmetry.

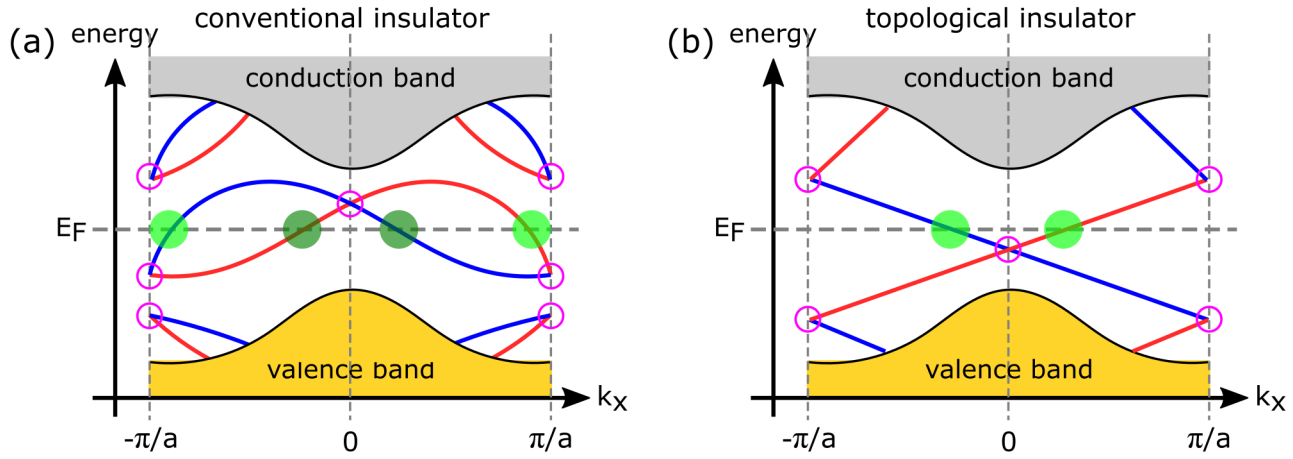

Figure 1.1.4: Examples of band structures of time-reversal invariant systems exhibiting strong spin-orbit coupling (schematics inspired by [9, 61]). In the conventional insulator (a) the spin-split edge states (red and blue) degenerate pairwise at the TRIM (pink circles). An even number of Kramers points cross the Fermi level E_F between $0 < \mathbf{k} < \pi/a$ (green circles). In the topological insulator (b) the surface states intersect at the TRIM and an odd number of Kramers pairs cross E_F. These edge states are robust against adiabatic deformations.

Compared to the QHS in figure 1.1.3 (b), the edge states of a topological insulator exhibit a spin-momentum locking. As a consequence of the time-reversal invariance, there are two edge states with opposite group velocities. Furthermore, they belong to the same Kramers pair resulting in electrons with opposite spin direction moving in different transport channels in the opposite direction. Similar to the QHS, elastic back scattering at non-magnetic impurities is forbidden[2].

The new $\mathbb{Z}_2$ invariant $\nu_{\mathbb{Z}_2}$ defines a new bulk boundary correspondence analogous to the one of the QHS in equation 1.5 as

$$\triangle\nu_{\mathbb{Z}_2} = N_{KP} \bmod 2, \tag{1.10}$$

[2] Scattering at magnetic impurities can change the spin direction and thus allows for backscattering.

with N_{KP} being the number of Kramers pairs and $\triangle\nu_{\mathbb{Z}_2}$ the difference of the $\nu_{\mathbb{Z}_2}$ across the interface. In other words, if the topology changes across the interface, the number of Kramers pairs is odd.
Until now only two-dimensional systems were considered, but the above concepts are also applicable to three dimensions. Instead of crossing edge states, the surface states form Dirac cones at the TRIM. A 3D TI is then characterized by four $\mathbb{Z}_2$ invariants, namely $(\nu_0;\nu_1\nu_2\nu_3)$ with $\nu_i = 0,1$ for $i = 0,1,2,3$. The invariant ν_0 describes if the system is a weak ($\nu_0 = 0$) or a strong ($\nu_0 = 1$) topological insulator determined by the number of Dirac cones encircled by the Fermi surface: an even number for a weak TI and an odd number for a strong TI. The invariants $(\nu_1\nu_2\nu_3)$ can be related to the direction of the encircled Dirac cones and viewed as Miller indices [62].

1.1.4 The discovery of topological insulators - experimental breakthroughs

Soon after their theoretical prediction, experimentalists started to verify the existence of topological edge and surface states. Since graphene exhibits a rather weak spin-orbit interaction, **B**ernevig, **H**ughes and **Z**hang (BHZ) theoretically predicted that a topological insulator can be realized in a mercury-cadmium telluride semiconductor quantum well (CdTe-HgTe-CdTe) [63]. By increasing the thickness of the quantum well above a certain value $d_c = 6.3$ nm, its band structure is changed from a normal to a band-inverted type. Figure 1.1.5 (a) depicts the sample dimensions (green) and the corresponding band structures (black and yellow) schematically.

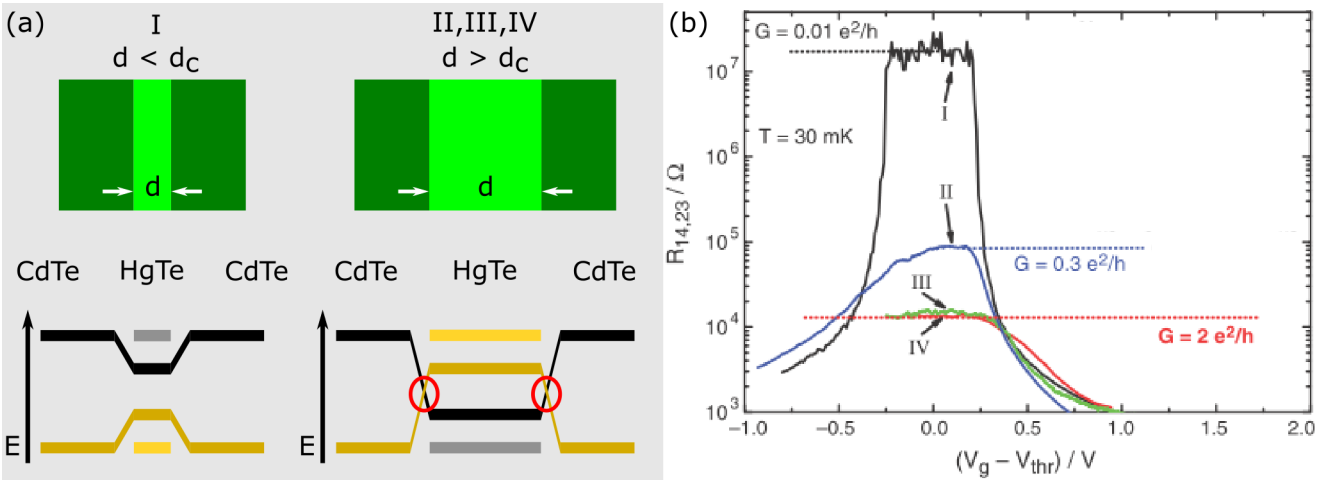

Figure 1.1.5: Topological edge states in CdTe-HgTe-CdTe quantum wells (green): (a) The band structure (black, yellow) changes from a normal ($d < d_c$) to an inverted type ($d > d_c$), resultin in edge states (red circles). (b) The resistance versus gate voltage for increasing d (I, II, III, IV) saturates at a constant value corresponding to a conductance value of $G = 2e^2/h$. This behavior marks the transition between a trivial insulating state and a QSHS. From [64]. Reprinted with permission from AAAS.

HgTe is a semiconductor with inverted bands with respect to CdTe (light grey and light yellow). Bringing both materials in contact results in the lifting of the band inversion for $d < d_c$ (black and yellow) and the occurrence of surface states (red circles) for $d > d_c$. BHZ proposed purely electrical measurements of the conductance across the system in a two-terminal configuration under application of a gate voltage sweeping the Fermi level across the bulk band gap. About one year later, in 2007, König et al. realized

the experiment and their originally obtained results are presented in figure 1.1.5 (b). They discovered a large (or infinite) resistance for $d < d_c$ (I) and a small (or finite) resistance for $d > d_c$ (II, III, IV) at gate voltages corresponding to a Fermi level inside the energy gap [64]. Additionally, the conductance measured for III and IV remains constant exhibiting an integer QHS. Obviously, a transition between the trivial insulating and the QSHS is substantiated. This experiment is commonly known as the first proof of the existence of topological edge states.

Simultaneously to the predictions of BHZ, $Bi_{1-x}Sb_x$ was calculated to be the first strong 3D TI [61]. The evolution of the topological insulator phase with Sb doping is schematically depicted in figure 1.1.6 (a) identifying the topological insulating phase (orange) for $0.07 < x < 0.22$ [65]. Both elements exhibit a finite negative indirect gap with the electron pockets located around the L points. The hole pocket for Bi is found at the T point, while in Sb the holes are at the H point. The L_S and L_A symmetric bands denote the bottom of the conduction band for Bi and Sb, respectively. As the Sb content is increased, a band inversion of L_S and L_A is created exhibiting the inversion point at $x = 0.04$. Additionally, the T and H valence bands for Bi and Sb, respectively, drop below the corresponding conduction bands for $0.07 < x < 0.22$ inverting the otherwise negative band gaps and creating the semiconductor phase of $Bi_{1-x}Sb_x$ [65]. Together with the L-band inversion enforced by Sb, the topological phase occurs within this range and exhibits conducting surface states. The maximum positive energy gap amounts to 30 meV (green) at about $x = 0.18$ [61].

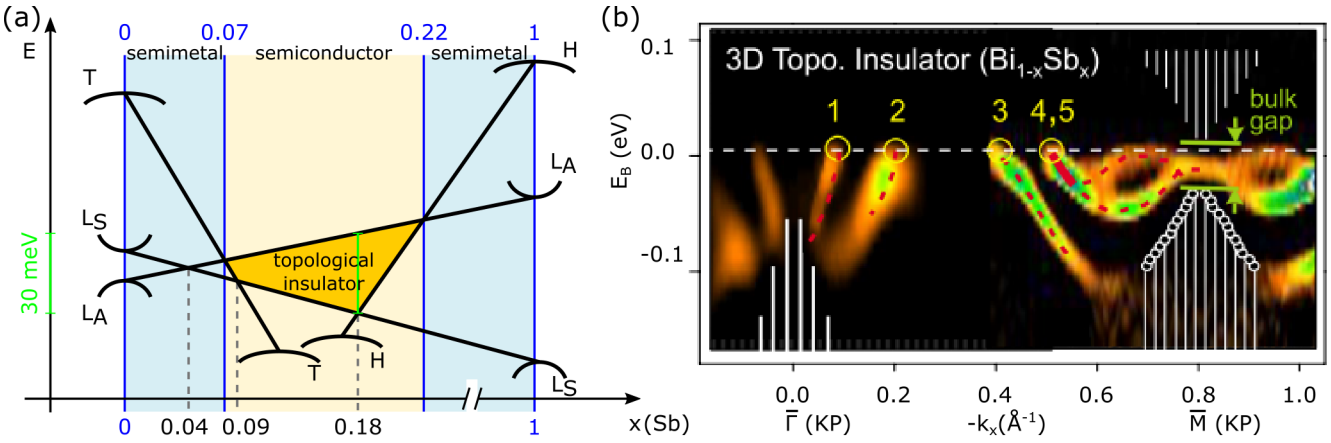

Figure 1.1.6: $Bi_{1-x}Sb_x$ being the first strong 3D TI: (a) The evolution of energy bands with increasing Sb content leads to a transition between the semimetallic (blue) and -conducting (yellow) phase as the valence bands T and H for Bi and Sb, respectively, drop below the conduction bands between $0.07 < x < 0.22$. A topological insulator phase (orange) is arising due to the band inversion of the L_S and L_A bands enforced by the Sb content. The maximum direct energy gap amounts to 30 meV (green) at about $x = 0.18$ (schematic inspired by [9, 61, 65]). (b) The ARPES results visualize the electronic band structure close to the Fermi level ($E_B = 0$) which is crossed an odd number of times (yellow circles) between the Kramers points $\bar{\Gamma}$ and $\bar{M}$. The bulk energy bands are shaded white. Reprinted by permission from Macmillan Publishers Ltd: Nature Physics (reference [66]), copyright (2009).

In order to confirm the topological surface states, **A**ngle-**R**esolved **P**hoto**E**mission **S**pectroscopy (ARPES) was the experiment of choice due to its surface sensitivity [9]. Using this method, Hsieh et al. directly mapped the electronic band structure by detecting the kinetic energy and emission angle of pho-

toelectrons emitted from the sample surface under photon irradiation [66]. Their result is presented in figure 1.1.6 (b) showing the surface band dispersion between the Kramers points $\bar{\Gamma}$ and $\bar{M}$. The energy bands cross the Fermi level ($E_B = 0$) an odd number of times (yellow circles) confirming $Bi_{1-x}Sb_x$ being a 3D TI belonging to the (1;111) class.

In 2009, Zhang et al. predicted the three binary chalcogenides, Bi_2Se_3, Sb_2Te_3 and Bi_2Te_3 to be 3D topological insulators with a single Dirac cone on the surface[38]. This triggered enhanced interest in this field by experimentalists discovering the existence of the TI surface states by ARPES on thin films of Bi_2Se_3 [67], Sb_2Te_3 [68] and Bi_2Te_3 [68–70] shortly after.

To date, many more materials were predicted and identified experimentally as topological insulators [71]. In most cases their TI nature is confirmed by angle-resolved photoemission spectroscopy on thin films or bulk single crystals. Although (magneto-) electrical transport measurements seem to be a very straightforward method in order to investigate the unique non-trivial topological edge or surface states, they are until now very scarce. This is due to the fact that the known 3D topological insulators exhibit bulk energy gaps of only few hundred meV resulting in a signal dominated by the bulk states hindering the detection of surface states. One-dimensional nanostructures offer a possible solution to overcome this problem. Their large surface-to-volume ratio reduces the otherwise dominating contributions from the bulk, thus improving the access to surface contributions. To date such measurements are still very challenging, but essential on the route to develop future spintronics devices based on topological insulators [7, 21, 72–75].

1.1.5 Bi_2Te_3 as 3D topological insulator

Bismuth telluride belongs to the so called second generation of TIs predicted by first principles calculations [38]. Figure 1.1.7 (a) displays the calculation by Zhang et al. revealing a bulk band gap of about 100 meV.

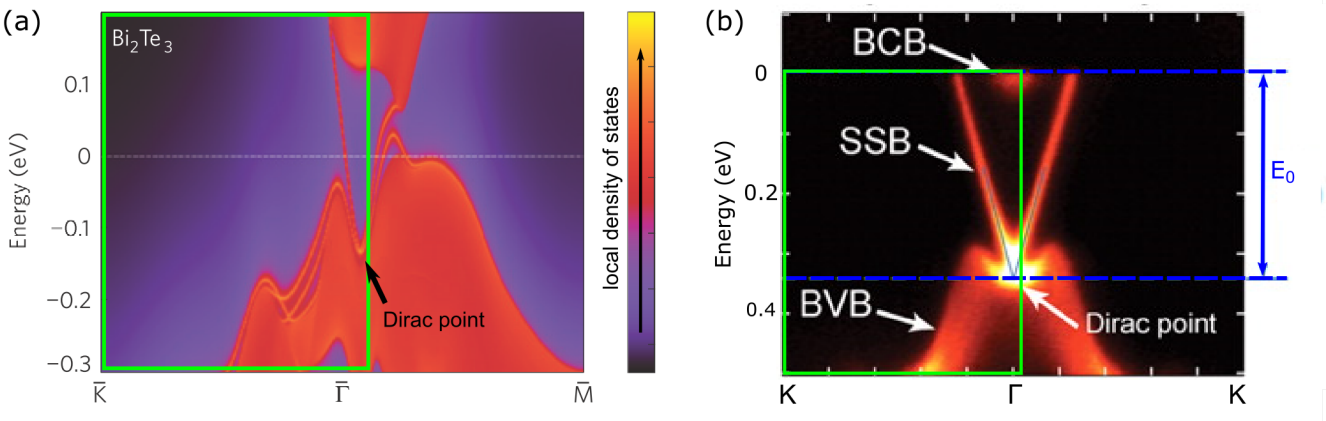

Figure 1.1.7: Topological non-trivial surface states in Bi_2Te_3: (a) first principles calculations revealing a single Dirac cone in the bulk energy gap with the Dirac point inside the valence band. Reprinted by permission from Macmillan Publishers Ltd: Nat. Phys. [38], copyright (2009). (b) ARPES investigation on single Bi_2Te_3 crystals showing the bulk conduction and valence band (BCB and BVB) connected by the surface state band (SSB) confirming the calculated band structure (green frame in (a)). From [69]. Reprinted by permission from AAAS.

Within this gap, Bi_2Te_3 exhibits a rather simple structure with only one Dirac cone located in the middle of the BZ. The Dirac point of Bi_2Te_3 lies within the valence band about 130 meV below its maximum [69]. Contrarily, in other bismuth-based TIs, such as Bi_2Se_3, the Dirac point is found within the bulk energy gap [38].
In the case of Bi_2Te_3, first ARPES studies were performed on high-quality thin films and single crystals [68–70] revealing the important role of strong spin-orbit coupling and the existence of surface states [70], as well as showing their Dirac-like nature and visualizing the band gap [68, 69]. Figure 1.1.7 (b) presents results of the ARPES studies of Chen et al. performed on Bi_2Te_3 single crystals confirming the existence of a single Dirac cone at the Γ-point of the BZ. The Dirac point is located 340 meV below the bulk conduction band (BCB) minimum. The green frames in (a) and (b) indicate the calculated and corresponding measured regions of the band structure, respectively.
Additionally, Bi_2Te_3 nanowires were used to address the surface states employing magnetoresistance measurements [17, 22, 24, 25, 27].

1.2 Thermoelectrics

The term **T**hermo**E**lectric (TE) describes the conversion of thermal into electrical energy or vice versa. TE materials exhibit three effects based on this ability, namely the Seebeck, the Peltier and the Thomson effect which are all named after their discoverer [76].
The Seebeck effect describes the occurrence of a potential difference dU between two ends of a thermoelectric material when a temperature gradient dT is applied. The reason for that is the thermodiffusion generated by the different kinetic energies of the charge carriers at the hot and cold end of the material. In order to maintain the equilibrium state, an electric field is created in reverse direction to the thermodiffusion. The Seebeck coefficient $S = dU/dT$ quantifying the phenomenon is a material property.
The opposite situation is known as the Peltier effect, describing the emergence of a temperature gradient based on the application of a current. The Peltier $\Pi = Q/I$ coefficient determines the ratio between the obtained heat exchange Q and the applied electric current I.
The third effect, named after Thompson (later Lord Kelvin) is always present once the material experiences a temperature gradient. In that case, heat is absorbed and emitted proportionally to the applied current I and the temperature gradient dT. The Thomson coefficient τ is thus defined as $\tau = Q/(IdT)$. All three effects are related through the so called Thomson relations

$$\Pi = S \cdot T \text{ and } \tau = T\frac{dS}{dT}. \tag{1.11}$$

Making use of these effects, thermoelectric generators and refrigerators are constructed by connecting a p- and n-type TE materials electrically in series and thermally in parallel. Consequently, a current is generated by applying a temperature gradient as schematically shown in figure 1.2.1 (a). In the contrary situation depicted in (b), the different ends of the device are heated and cooled by applying a current [76]. Thermoelectric devices are especially of interest, because they exhibit a long lifetime while at the same time requiring less maintenance due to the absence of moving parts. They can be fabricated on very small length scales, making them attractive for use as small coolers for, e.g. laser diodes.

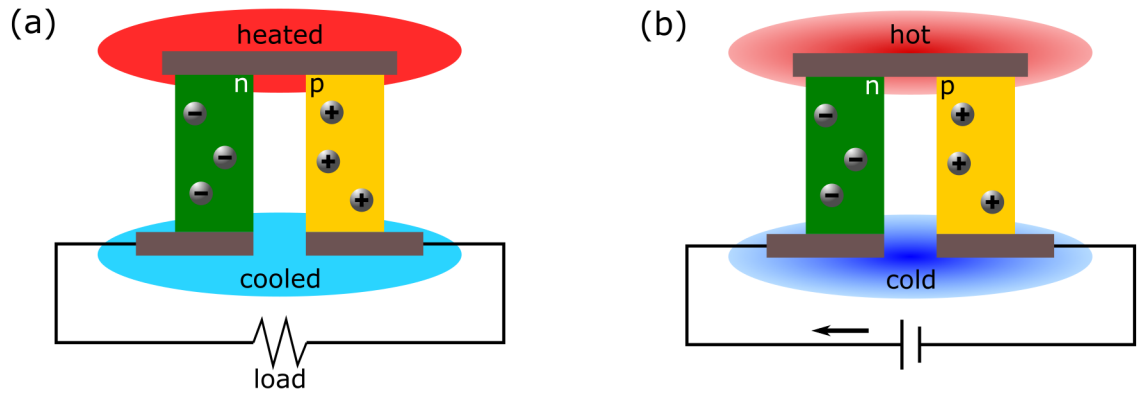

Figure 1.2.1: Schematic representation of a thermoelectric generator (a) and refrigerator (b) consisting of a n- (green) and p-type (yellow) TE material arranged electrically in series and thermally in parallel.

Furthermore, TE refrigerators are environmentally-friendly, by not employing e.g. chlorofluorocarbons [77, 78].
For the purpose of quantifying and comparing the thermoelectric conversion efficiency of different TE materials, the dimensionless figure of merit ZT is defined as

$$ZT = \frac{S^2\sigma}{\kappa} \cdot T, \tag{1.12}$$

with σ denoting the electrical conductivity and $\kappa = \kappa_e + \kappa_{phonon}$ being the sum of the electron and the phonon (lattice) thermal conductivity contributions. During the past 60 years, many efforts have been undertaken to obtain a highly efficient thermoelectric material maximizing ZT. The aim is to increase the power facter $S^2\sigma$ while, at the same time, decreasing the thermal conductivity κ. Unfortunately, in bulk materials these parameters are not independent. In metals, for example, the electrical and thermal conductivities are related by the empirical Wiedeman-Franz law given by

$$\frac{\kappa_e}{\sigma} = L \cdot T, \tag{1.13}$$

with $L = 2.44 \cdot 10^{-8}\ W\Omega K^{-2}$ being the Lorenz number [58, 79]. In general, S, σ and κ_e change as a function of the charge carrier density and temperature. With more charge carriers available, σ and κ_e increase naturally, while S favors a gapped band structure. The highest ZT materials are thus expected to be semiconductors or semimetals such as bismuth. Additionally, due to the temperature dependence of S, σ and κ, the thermoelectric efficiency is maximized in a certain temperature range specific for the material. Bi_2Te_3 exhibits the largest ZT of approximately 1 at room temperature [37] making it a promising candidate for thermoelectric devices.
Until the 1990s, after receiving little attention so far, the TE field of research experienced a boost provoked by the prediction of several approaches for increasing ZT beyond 1, of which one is to reduce the dimensions of the material. Hicks and Dresselhaus suggested quantum-well superlattices [80] and 1D nanowire structures [6] in order to decouple S, σ and κ and manipulate them independently. As

the dimension of a system is lowered and charge carriers are confined, the density of states $\rho(E)$ of a material as a function of energy changes from a square root (3D), to a stepwise (2D) over an inverse square root (1D) to a delta distribution (0D) [81]. Consequently, the derivative $d\rho(E)/dE$ and with that the differential density of carriers $dn(E)/dE$ increases as the dimension is lowered. According to Drude, the electrical conductivity σ

$$\sigma(E) = n(E)e\mu(E), \tag{1.14}$$

directly depends on the density of carriers $n(E)$, their charge e and their mobility $\mu(E)$. The Mott relation connects the differential electric conductivity to the Seebeck coefficient

$$S = \frac{\pi^2}{3}\frac{k_B^2 T}{e}\left(\frac{d\left[\ln(\sigma(E))\right]}{dE}\right), \tag{1.15}$$

where k_B is the Boltzmann constant. By implementing equation 1.14 in 1.15 the proportionality between S and the derivative density of carrier becomes clear

$$S \propto \left(\frac{dn(E)}{ndE} + \frac{d\mu(E)}{\mu dE}\right). \tag{1.16}$$

The Seebeck coefficient is maximized for low numbers of charge carrier densities changing largely with energy. At this point is becomes clear that S and therefor ZT change as a function of the Fermi energy. For example, $\rho(E)$ of a 1D structure consists of spikes and, hence, maximizing $d\rho(E)/dE$ accounts for a Fermi energy adjustment. Alternatively, $d\mu(E)/dE$ can be increased in order to enhance the Seebeck coefficient. This can be realized by increasing the energy dependence of the scattering time so that the electrons are scattered depending on their energy. This approach is referred to as energy filtering and is technically accessible by counter doping the TE material [82]. Furthermore, introducing more sample interfaces enhances the phonon scattering while reducing the thermal conductivity without affecting the electrical conductivity much. Recently, a molecular dynamics study compared Bi_2Te_3 nanowires with smooth and rough surfaces within a diameter range of 3-30 nm. It was confirmed that the reduction of κ by 30-40% for smooth and 55% for rough nanowires below 10 nm thickness compared to bulk at room temperature [83].

Both effects, the improvement of the power factor $S^2\sigma$ and the reduction of the thermal conductivity, promise an enhancement of ZT. First calculations for Bi_2Te_3 predict a ZT up to 6.9 for a single layer, 3.8 Å thick quantum well [80] and a ZT up to 14 for a 1D nanowire with a diameter of 5 Å [6]. Experimentally, the highest ZT measured for nanostructured Bi_2Te_3-based materials are ~2.4 for p-type Bi_2Te_3/Sb_2Te_3 superlattices [84] and 1.35 for Bi_2Te_3 bulk exhibiting a layered nanostructure [85]. Furthermore, $ZT > 2.5$ has been achieved in SnSe single crystals [86] and lamella-structured $Cu_{1.94}Al_{0.02}Se$ [87] at elevated temperatures above 700 K.

Complete measurements of all thermoelectrically relevant parameters (S, σ and κ) in order to determine ZT for nanowires are up to now scarce. This is due to the complex challenge of downscaling the experimental setup to measure the TE properties of an individual nanowire. The design of special measurement microchips, such as the Z-chip [88], promise to overcome this challenge. Additionally, only few synthe-

sis methods allow for a controlled downscaling of the TE sample. Here, especially the development of template-assisted fabrication of nanowires, as employed in this work, provides property control and is of important interest. For Bi_2Te_3 nanowires with a diameter of about 55 nm electrochemically deposited in alumina membranes, a ZT of 0.1 at 400 K [89] was realized. Furthermore, a study investigating the influence of crystal defects obtained a maximum ZT of 0.31 for twin-boundary containing Bi_2Te_3 nanowires with 50 nm diameter [90]. In contrast to the predictions made by Hicks and Dresselhaus, the experimental values are still much lower than those obtained for their bulk counterpart.

1.2.1 Coexistence of thermoelectric and topological insulator properties

In the first decade after nanostructuring excellent bulk thermoelectric materials became a popular approach to enhance ZT, topological insulators had not been discovered. That is why the influence of the non-trivial topological surface (edge) states are only very recently taken into account when predicting ZT for TE nanostructures [91–97]. In a recent approach, the comparatively low ZT values measured for nanowires until today were explained by the topological surface state contributions.
Both, TE and TI materials feature heavy atoms and small bulk energy gaps[3] in the order of a few hundred meV (~0.1 meV for Bi_2Te_3). For TE materials the heavy elements account for low thermal conductivity, while they generate the necessary spin-orbit coupling to create the topological insulating phase. In combination with the small energy gap, a band inversion is favored and, regarding thermoelectric properties, the power factor $S^2\sigma$ is increased. For this reason almost all so far known TIs experience good TE properties. When searching for TIs, good TE materials are thus preferably considered. The most commonly known examples are the chalcogenide 3D TIs (Bi_2Te_3, Sb_2Te_3, Bi_2Se_3, $Bi_{1-x}Sb_x$). However, exceptions of this relation exist, for example, PbTe is a good TE material, but has an even number of Kramers pairs intersecting the Fermi level and is, hence, no topological insulator [98].
Consequently, the question arose how the TE and TI properties influence each other. Generally, the bulk and surface (edge) contributions to ZT coexist in TE materials. As the surface-to-volume ratio of a material increases, the role of the surface (edge) states becomes much more pronounced to the point where the TE bulk properties converge to those of the surface (edge) [96]. The two most important differences are: firstly, backscattering at nonmagnetic impurities is forbidden for surface (edge) states while in the bulk scattering occurs at any disorder. Secondly, the bulk states possess an energy gap, while those at the surface (edge) are gapless, which leads to a lower S. In both cases, ZT is a function of the Fermi level and, generally their maximum values do not coincide at the same energy, reducing the overall ZT as the surface contributions become more important [97]. First calculations separately observing bulk and surface (edge) states were performed for 3D TI thin films assuming an overall ZT determined as

$$ZT = \frac{(S_s\sigma_s + S_b\sigma_b d)^2\, T}{(\sigma_s + \sigma_b d)\,(\kappa_s + \kappa_b d)}, \tag{1.17}$$

with the indices s and b denoting the surface and bulk contribution, respectively and d being the film thickness [91].

[3] For electrical transport in TIs a large bulk energy gap is favored in order to suppress the bulk conductivity signal by placing the Fermi level within the band gap.

For very thin films ($d < 10$ nm) the surface states are known to hybridize opening an additional gap of a few meV at the Dirac point [91]. Consequently, ZT is enhanced above the known bulk value of 1 due to a maximum S value close to the surface state gap. Here, the narrow gap imitates the difference between a metallic and a semiconducting phase for surface states. In the latter, the Seebeck coefficient is larger, because electronic states below and above the Fermi level do not compensate each other as for the metallic case. Additionally, ZT increases with decreasing temperature [92]. For this reason an improved TE efficiency exceeding $ZT \sim 1$ is predicted for TIs with gapped surface states, when the Fermi level position dependent on temperature and doping is optimized [91]. Very recent calculations without Fermi level optimization comparing Bi_2Te_3, Sb_2Te_3 and Bi_2Se_3 thin films with $1\,nm \leqslant d \leqslant 20\,nm$ indicate no ZT beyond 2, although the ZT value of the surface (ZT_s) tends to be much larger. Especially in the calculations for Bi_2Te_3, the total ZT of the film exceeds that of the bulk for film thicknesses smaller than 2 nm [96].

In more experimentally accessible regimes of nanowires with diameters greater than 10 nm, calculations revealed an increase of the electrical and thermal conductivity with decreasing wire diameter, while the Seebeck coefficient changes depending on the position of the Fermi level and thus dominates the total ZT. The thermoelectric efficiency is thus predicted to be enhanced for materials with $ZT_b > ZT_s$ and limited for $ZT_b < ZT_s$. In the case of Bi_2Te_3 for both thin films ($ZT_s \approx 0.5$) and nanowires ($ZT_s \approx 0.9$) of 10 nm diameter, the surface TE efficiency does not exceed that of the bulk counterpart. In order to increase ZT, the suppression of the surface states by magnetic impurities is proposed [97].

On the other hand, predictions made for the 2D TI fluorinated stanene expect a ZT value larger than bulk as the dimensions are changed. In this approach, ZT is not considered to be an intrinsic material property but rather size-dependent due to the different dimensions of the transport channels [95].

In summary, the TI nature of materials is clearly affecting their thermoelectric performance due to their unique band structure [94]. For all theoretical calculations, the additional conducting surface states seem to hinder the TE efficiency as the material is downscaled. Only if the surface states hybridize and a band gap appears at the Dirac point an increase of ZT above the bulk value might be possible. Since this effect occurs only below dimensions of 10 nm, experimental confirmation has yet to be provided.

2 Fundamentals of Bi_2Te_3 nanowire synthesis

The ongoing miniaturization and the demand for nanoscale opto-, thermo- and electrical devices as well as sensors have triggered many advances and innovations in the field of nanowire fabrication [99]. Commonly, bottom-up and top-down methods are distinguished for nanowire synthesis.

Amongst many bottom-up approaches the **V**apor-**L**iquid-**S**olid (VLS) growth is an established method since the 1960s. As the name suggests, the nanowires grow from vapor sources using nanoparticles, mostly made of gold, as catalysts [100]. The VLS method enabled the mass fabrication of large amounts of single-crystalline nanowires. Their shape, size and morphology are determined by the crystal structure of the desired material. On the other hand, this technique suffers from contamination caused by the incorporation of the metallic catalyst influencing, for example, the crystalline quality [101, 102] of the wires. Different variations of the VLS growth were developed and an exhaustive review on the existing techniques is given in [103]. For synthesizing Bi_2Te_3 nanowires, the VLS growth is commonly used [104, 105] and is even performed catalyst-free [106].

The second widely used bottom-up method for Bi_2Te_3 nanowire fabrication is the template-assisted solution-based growth developed in the 1970s [107]. Using this approach, a template serves as a scaffold or form in which the nanowire is growing. Various templates have been tested differentiating between "soft templates" such as surfactants [108] and "hard templates". For instance, the step edges in highly oriented pyrolytic graphite [109] and nanochannels in porous alumina [110–114] as well as in polymer membranes [115–117] are considered to be "hard templates". Employing the latter, the nanowires are generally synthesized from solution by electrochemical deposition in a layout that forces them to grow within the template. Compared to the VLS techniques, the nanowires fabricated by template-assisted electrodeposition in nanochannel membranes replicate the shape, size and morphology of the template providing the flexibility to tune these properties. Furthermore, the process of electrodeposition enables the control of the crystallographic properties and chemical composition within a broad spectrum [116, 118]. Another very important advantage of template-assisted methods is the ability to handle the samples very easily. Still embedded in their template, various investigations on arrays of nanowires, such as x-ray diffraction and (thermo-)electrical transport measurements are possible. Especially for thermoelectrical investigations on nanowire arrays, the polymer templates are to be preferred over the porous alumina due to their comparatively low thermal conductivity [119, 120]. Furthermore, polymer matrices offer many different pore geometries (cylindrical, conical, etc.) due to their unique etching properties. Additionally, they are fairly easy to dissolve in organic solvents, such as dichloromethane.

At the GSI Helmholtzzentrum für Schwerionenforschung GmbH[1], the research exploring the formation and properties of tracks in ion-irradiated polymers triggered their application as polymer templates for metallic micro- and nanostructure fabrication [121, 122]. Until today the expertise of the Materials Research group in preparing nanowires [123] ranges from metallic [122, 124, 125] over semiconducting [126, 127] and thermoelectric [116, 128–131] to metal-alloyed [132, 133] nanowires.

[1] In the following, it is mostly referred to as GSI.

Figure 2.0.1 summarizes the template-assisted method as employed at GSI schematically. First, the irradiation of polymer foils with swift heavy ions creates tracks of damaged template material along the path of each individual projectile (1, 2). Using an appropriate reactant, tracks are selectively etched and converted into open pores (3) [134, 135]. In the following step, a conductive back layer is sputtered on one side of the template (4) to serve as working electrode for the subsequent electrochemical growth of the nanowires inside the pores (5). Arrays of nanowires with controlled lengths are realized by stopping the deposition process before the nanowires reach the upper side of the template. If the process continues, the material overgrows the polymer forming so called caps on the top of the nanowires (6). For further characterization or nanowire transfer to different substrates, the polymer can be dissolved in an organic solvent (7), releasing the nanowires.

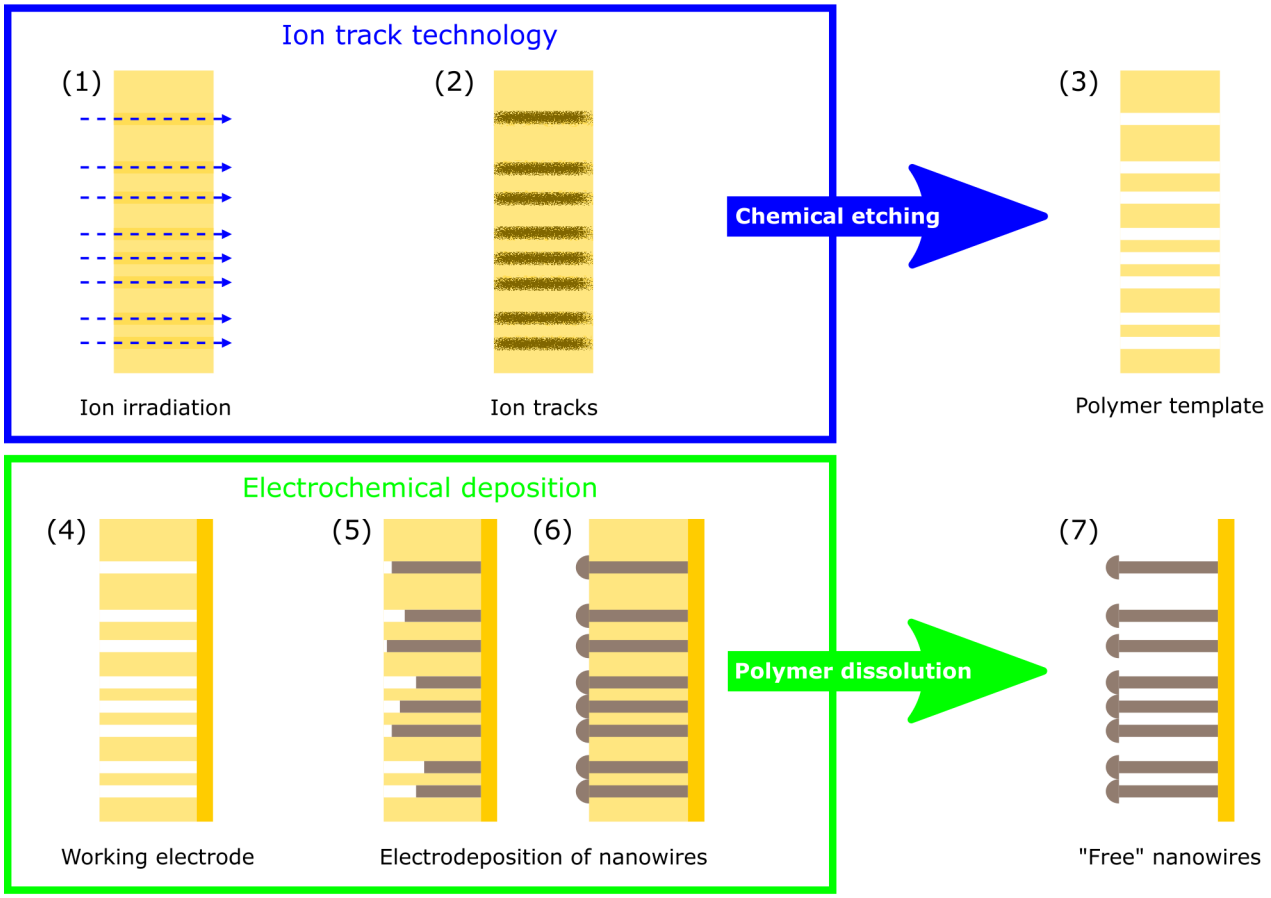

Figure 2.0.1: Schematic representation of the separate steps of the ion-track technology providing nanoporous polymer templates (blue box) and of the electrochemical deposition resulting in the fabrication of nanowires (green box). The detailed explanation for each process step (1-7) is given in the text.

Until now, research on Bi_2Te_3 nanowires elucidating their topological insulator properties has been conducted on wires synthesized by VLS [24], from solution [136] and by electrodeposition in porous alumina templates [25, 26]. Systematic studies are not only scarce due to the complexity of the measurements, but also because these techniques limit the control of crucial nanowire parameters. On the other hand, Bi_2Te_3 nanowires electrodeposited in polymer membranes account for independent control over various wire parameters, such as geometry, morphology, crystallographic orientation and chemical

composition. For this reason, they promise to be excellent model systems to explore their electronic characteristics as a function of these properties which has not been conducted in a systematic manner so far. Furthermore, these nanowires can be fast and easily synthesized in a large quantity.
The present chapter examines the particular synthesis steps of Bi_2Te_3 nanowires and their transfer to different substrates in detail.

2.1 Heavy-ion irradiation and track formation

While penetrating through matter, heavy ions loose their energy by various interaction processes such as Cherenkov radiation, Bremsstrahlung, electronic energy loss and nuclear energy loss. This so called energy loss is defined as the deposited energy per unit path length dE/dx. At specific energies of several MeV/nucleon as employed here, Bremsstrahlung and Cherenkov radiation are negligible due to the large mass of the ions and their comparatively low velocity. This leaves the Coulomb interaction to be the dominant process. Coulomb interaction occurs between the projectile ion and the target nucleii specified as nuclear energy loss, $(dE/dx)_n$, as well as between the ion and the target electrons called electronic energy loss $(dE/dx)_e$ [137]. The sum of both gives the total energy loss

$$\left(\frac{dE}{dx}\right) = \left(\frac{dE}{dx}\right)_n + \left(\frac{dE}{dx}\right)_e . \tag{2.1}$$

The cross sections of these processes are dependent on the velocity of the projectile. For lower ion velocities ($\leqslant$ 0.01 MeV/nucleon) elastic collisions with the target nucleii are dominant, while at higher velocities electronic excitation and ionization play a more important role. This results in the stripping of the orbital electrons of the ions as they pass through the target creating an effective charge state Z_{eff} given as

$$Z_{eff} = Z\left[1 - \exp\left[\frac{-130\beta}{Z^{\frac{2}{3}}}\right]\right], \tag{2.2}$$

with Z being the atomic number of the ions and $\beta = v/c$, the ratio of the speed of the projectile to the speed of light. Considering relativistic velocities $v \approx c$, equation 2.2 is reduced to $Z_{eff} \approx Z$ meaning all electrons are stripped off the projectile. At high energies, the electronic energy loss is described by the Bethe-Bloch formula

$$\left(\frac{dE}{dx}\right)_e = \frac{4\pi \cdot e^4 \cdot N \cdot Z \cdot Z_{eff}^2}{m_e v^2}\left[\ln\left(\frac{2m_e v^2}{I}\right) - \beta^2 - \delta - U\right], \tag{2.3}$$

with e and m_e being the electron charge and mass, respectively. The ion velocity is denoted by v, while N is the density and I the ionization energy of the target atoms. Additionally, two correction factors δ and U are added for relativistic cases and low velocity conditions, respectively. Being proportional to Z_{eff}^2, maximum electronic energy loss values are achieved by using high energetic heavy ions. Interacting with the free or outer electrons of the target atoms, the projectile ions induce excitation and ionization processes of the target atoms. In the latter case, the electrons emitted interact themselves with the

surrounding target ions. If their energy is high enough they effect further ionization, creating an electron cascade in the vicinity of the projectile trajectory. Along the penetration path of the incident ion a so called ion track of modified material is created [138]. Two different phenomenological models are in well-recognized competition to explain the formation of ion tracks: The thermal spike and the Coulomb explosion model. The former assumes a strong rise of temperature confined to the ion trajectory, melting the target material and forming the track due to rapid cooling [139]. The latter originates from strong repulsive electrostatic forces due to the target ionization along the ion track [140].
Polymers such as **P**oly**C**arbonate (PC) and **P**oly**E**thylene **T**erephthalate (PET), exhibit a high sensitivity to ion irradiation causing severe damage to the polymer structure within the ion track [141, 142]. Such an ion track typically consists of a cylindrical track core, that is about 10 nm in diameter surrounded by a track halo created by the electron cascade extending up to several 100 nm [134, 143–145].
In this work, amorphous Makrofol N polycarbonate foils (Bayer AG) of 30 µm thickness were chosen as suitable templates for the Bi_2Te_3 nanowire fabrication. The foils were irradiated at the X0 beamline of the **Uni**versal **L**inear **Ac**celerator (UNILAC) at GSI. Schematic representations of the irradiation facility and setup are shown in figure 2.1.1 (a) and (b). In a typical irradiation experiment, stacks of three foils adding up to 90 µm of PC were bombarded by Au ions with a fluence of 10^9 ions/cm^2. Prior to the next step, the foils were exposed to UV light (λ = 280...400 nm) for 1 h per side under ambient conditions. The UV sensitization mainly affects the ion track and not the surrounding bulk material and results in a more uniform pore size distribution [146–149].

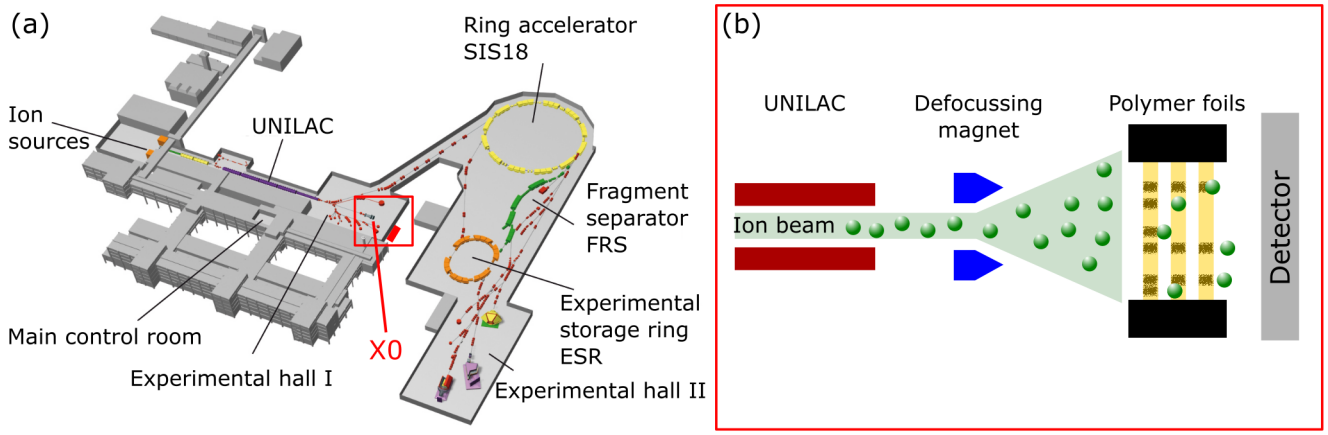

Figure 2.1.1: Schematic representation of the accelerator facilities at the GSI Helmholtzzentrum für Schwerionenforschung (a) with the X0 beamline marked (red) at the end of the UNILAC. The setup of the ion irradiation of three stacked polymer foils at the X0 is schematically shown in (b).

2.2 Selective chemical etching of ion tracks

Immersing the irradiated polymer foils into a suitable chemical agent converts each individual ion track into an empty channel resulting into a porous membrane. The mechanism is based on the fact that the damaged zones in the ion tacks are preferentially dissolved, i.e. chemically more active compared to the unirradiated surrounding bulk material. The process is described by two different etching rates: the bulk etching rate $\vec{v}_b$ and the track etching rate $\vec{v}_t$ [140]. The former is mainly influenced by the

material properties, the etchant concentration and temperature. In addition to those parameters, the latter is obviously defined by the irradiation process (e.g. the energy loss of the ions) as well as post-irradiation treatments and storage conditions [149, 150]. By carefully controlling the entire parameter space, the geometry of the pores is mainly determined by the ratio of the two etching rates defining the cone half-angle α as

$$\sin(\alpha) = \frac{v_b}{v_t}, \tag{2.4}$$

and demonstrated in figure 2.2.1 (a). To create cylindrical channels, v_b/v_t has to be minimized resulting in an etching rate ratio which is as small as possible and thus $\alpha \approx 0°$ [151]. At higher etching rate ratios conical (figure 2.2.1 (b)) or biconical (figure 2.2.1 (c)) channels can be created. The former is achieved by etching the foil asymmetrically only from one side [152, 153]. Combining the symmetric and asymmetric etching configurations results in funnel-shaped pores as depicted in figure 2.2.1 (d) [154].

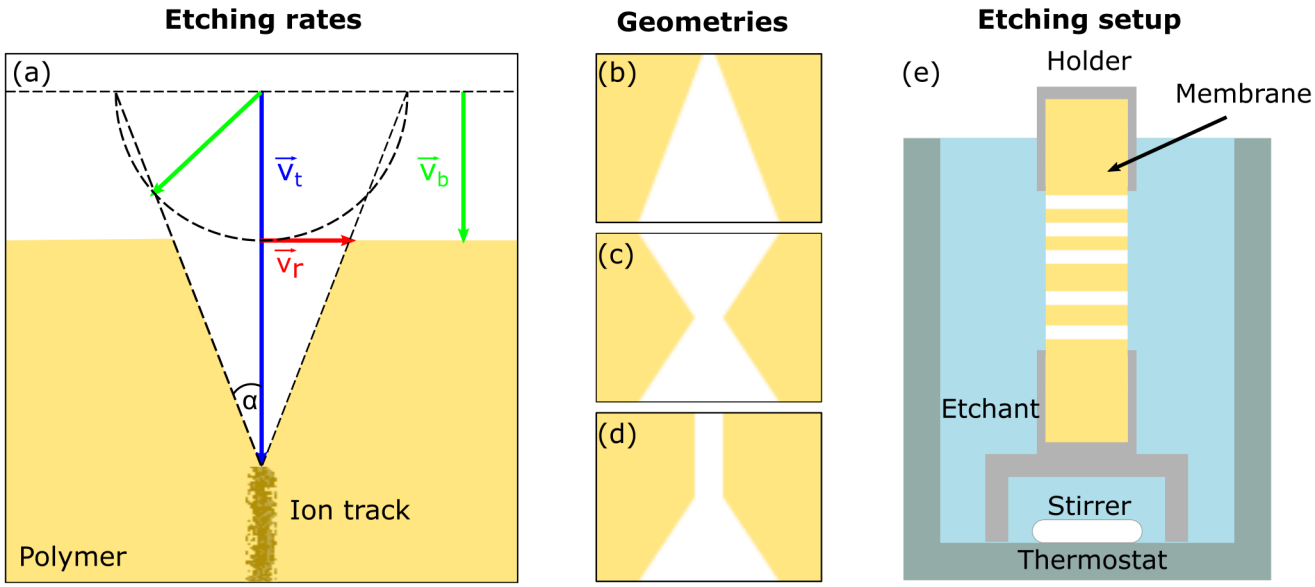

Figure 2.2.1: Schematics of the selective chemical etching of ion tracks in polymers: (a) The interplay of bulk v_b, track v_t and radial v_r etching rates defining the cone half angle α; Different template cross-sections with (b) conical, (c) biconical and (d) funnel-shaped nanopores; (e) Setup for symmetrical etching of cylindrical nanopores in a thermostat.

Experimentally, the ratio v_b/v_t is mainly controlled by the etching conditions such as composition, concentration and temperature of the etchant as well as the etching setup. The pore dimensions on the other hand are configured solely by the etchant concentration, the etching time and the temperature [138, 146, 155]. Taking the pore diameter as a measure, the dimensions of individual pores can be directly investigated using microscopy techniques such as **S**canning **E**lectron **M**icroscopy (SEM) [138] or an average diameter can be measured taking advantage of [148, 151, 156]. Comparing both methods, similar results are found [157, 158].

From the many investigations performed on the detailed etching process, three findings are of crucial importance for this work:

- UV exposure as post-irradiation treatment sensitizes the ion track's chemical reactivity and results in small pore size distributions [148, 149] of 3% [157].

- Using an appropriate etchant, the etching rate ratio can be adjusted to obtain uniform quasi-cylindrical pores [151].

- The pore diameter increases steadily as a function of etching time [151, 159].

In this work, the etching of 30-µm thick irradiated PC foils was performed symmetrically inside a water-circulating thermostat with magnetic stirring. A schematic illustration of the setup is shown in figure 2.2.1 (e). An aqueous sodium hydroxide solution of 6 mol/L concentration at 50°C was chosen as a suitable etchant. Samples were typically etched for 1, 2, 3, 4 and 6 min resulting in pore diameters of about 25, 50, 75, 100 and 150 nm, respectively. The pore diameter was investigated by SEM and measured from pore-replicating nanowires. The etching rate in this work was estimated to (25 $\pm$ 5) nm/min comparable to literature values yielding (23.9 $\pm$ 0.5) nm/min [158] found by **S**mall-**A**ngle **X**-ray **S**cattering (SAXS) investigations and (22 $\pm$ 5) nm/min [160] using SEM analysis.

2.3 Electrochemical deposition of Bi_2Te_3 nanowires

Electrochemical deposition is a process in which an electrolyte is exposed to a potential gradient resulting in the reduction of ions at a cathode. Consequently, the charge transfer at the interface between the electronic (electrodes) and the ionic (electrolyte) conductors is the crucial point of interest. The overall reaction at the electrode is written as

$$M^{n+} + n \cdot e^- \rightleftharpoons M \tag{2.5}$$

with M denoting the ion species and n the number of charges e^-. The reaction from left to right, called reduction, gains electrons while the reaction from right to left liberates them and is called oxidation.
When a metal electrode is immersed into an electrolyte containing ions, oxidation and reduction do not proceed equally fast. This provokes a charging of the electrode forming an electrical or Helmholtz double layer. Assuming more positive ions leave the electrode's crystal lattice and enter the solution than vice versa, effectuating a negatively charged electrode and an excess of positively charged ions in the solution, the oxidation rate will be slowed down because of the repulsion of the equal charges on the interface. On the other hand, the reduction rate will be accelerated until a dynamic equilibrium stabilizes at which the same amount of ions enter than leave the electrode's lattice. The equilibrium potential E_{eq} at the electrode is described by the Nernst equation

$$E_{eq} = E^0 + \frac{RT}{nF} \ln a\left(M^{n+}\right), \tag{2.6}$$

where E^0 is the standard potential, R the gas constant, T the absolute temperature, n the number of transferred electrons, $a\left(M^{n+}\right)$ the activity of the ion M^{n+} and F the Faraday's constant. In an electrochemical cell, at least two electrodes are immersed into the electrolyte creating two half reactions

of the form as in equation 2.5. Applying an external potential leads to a current flow through the electrodes. In this case, the potential E_{cell} of the cell is defined as

$$E_{cell} = E_c - E_a + I_{ext.} \cdot R_{elect.}, \tag{2.7}$$

with E_c and E_a being the cathodic and anodic potentials, $I_{ext.}$ the external current and $R_{elect.}$ the resistance of the electrolyte. The difference between the equilibrium state of the cell while no current is flowing and the potential of the cell as a part of an electric circuit is called overpotential η:

$$\eta = E_{cell} - E_{eq}. \tag{2.8}$$

The algebraic sign of the overpotential indicates whether the reaction taking place in the cell is cathodic ($\eta < 0$) or anodic ($\eta > 0$). In the cathodic process, diluted ions reaching the cathode by diffusion, migration or convection, are adsorbed onto preferred spots (kink sites) of the cathode surface and reduced [161–163]. This process is divided into four separate steps: (a) mass transfer to the electrode surface, (b) charge transfer, (c) chemical reaction and (d) adsorption and crystallization. The slowest of these processes determines the overall cell reaction rate. Whichever process is dominant depends on the value of the overpotential. For small η the charge transfer is the limiting factor, while at large η the mass transfer restricts the process [162].
In general, the initial reduction is dependent on the atomic structure and surface character of the cathode. Consequently, physical and chemical properties related to the growth mechanism such as crystallographic orientation or chemical composition (for alloys) are strongly influenced by the initial electrochemical deposition process [164]. Faraday's law (equation 2.9) describes the relation between the mass of the deposited material and the electric charge Q passing through the electrochemical cell.

$$m_{dep} = \frac{M}{n \cdot F} \cdot Q = \frac{M}{n \cdot F} \int I dt, \tag{2.9}$$

with m_{dep} being the deposited mass, M the molar mass of the deposited material, n the number of valence electrons, $F = 96484$ C the Faraday constant and I the current.
For the nanowire synthesis by electrodeposition of material into nanopores, an appropriate cathode is required. For this reason, the prepared PC templates were sputtered with a thin gold layer in order to prepare the so called working electrode referred to as cathode before. Subsequently, electrodeposition was employed to close the nanopores and reinforce this working electrode by depositing a gold layer. In this case, a commercial electrolyte (AuSF, Metakem) in a two-electrode setup applying a constant potential of -1 V for approximately 10 min was used. For the deposition of Bi_2Te_3 nanowires inside the channels, the electrolyte employed consists of 5 mmol/L bismuth nitrate pentahydrate and 7.5 mmol/L tellurium dioxide in 1 mol/L nitric acid [165]. The overall chemical reaction can be viewed as

$$2Bi^{3+} + 3HTeO_2^+ + 9H^+ + 18e^- \rightharpoonup Bi_2Te_3 + 6H_2O \tag{2.10}$$

The deposition conditions applied here are based on the work of Dr. Oliver Picht providing a detailed characterization of electrodeposited Bi_2Te_3 nanowires in PC templates [166]. By tuning the growth parameters, an influence on morphology, chemical composition and crystallographic texture was found and systematically investigated [116]. Following his findings, those electrodeposition parameters were selected that provide nanowires with a smooth morphology, stoichiometric composition and highly textured crystal orientation. For this reason, the depositions were carried out potentiostatically in a three-electrode configuration applying 0 V in reference to a saturated calomel electrode (SCE) using a Gamry REF600 potentiostat. During the deposition the temperature was kept constant at 30 °C. A schematic cross section of the electrochemical cell is presented in figure 2.3.1 (a).

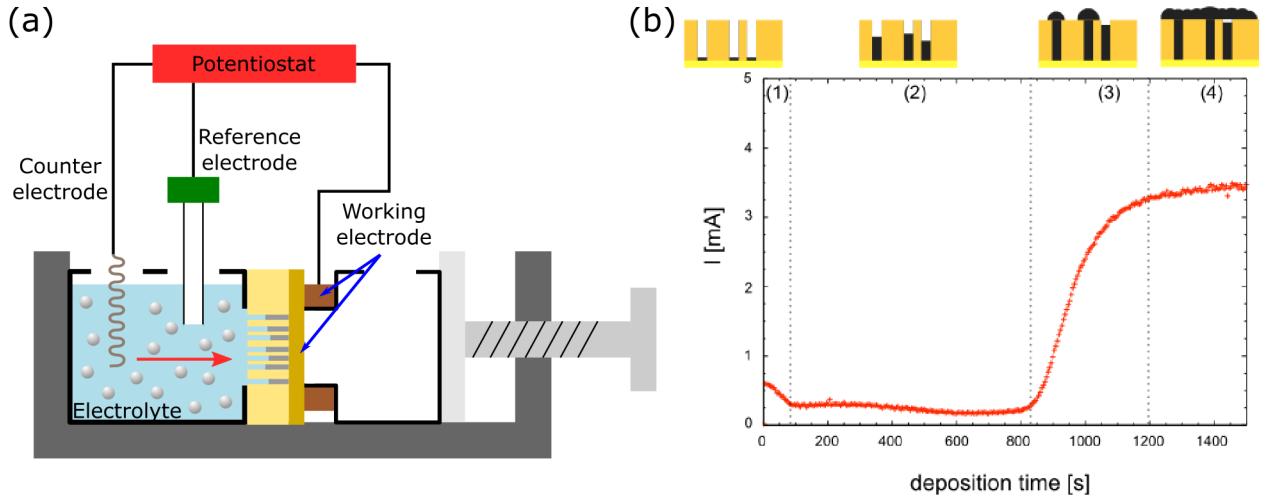

Figure 2.3.1: Electrodeposition of Bi_2Te_3 nanowires: (a) schematic of an electrochemical cell. The three-electrode setup consists of a gold layer on one side of the membrane serving as working electrode, a Pt spiral used as the counter electrode and a saturated calomel reference electrode. (b) Current-time curve recorded during electrodeposition exhibiting four distinct regions: (1) Charging of the Helmholtz double layer, (2) nanowire growth, (3) cap growth and (4) layer formation. Reprinted from [123] (open access)

The ion track-etched PC template was fixed between two teflon compartments in a way that the prepared gold working electrode was pressed against a copper ring serving as contact. The compartment facing the open nanopores of the template was filled with the corresponding electrolyte containing Bi and Te ions. A platinum spiral wire serving as counter electrode and the SCE reference were immersed into the electrolyte. The deposition was started by applying an external potential of 0 V vs. SCE and the process was monitored by recording the deposition current over time.

A typical current-time curve for cylindrical nanowire growth is shown in figure 2.3.1 (b) exhibiting four pronounced regions: (1) The current steeply decreases due to the formation of the Helmholtz double layer. The charge transfer is started and a diffusion layer is formed. (2) A rather constant current value represents the growth of the nanowires within the nanochannels. Since the current density is kept constant and the area of deposition does not change due to the cylindrical channel geometry, the measured current is expected to be constant. (3) A significant increase of the current is ascribed to the complete filling of the nanochannels. As the wires outgrow the nanochannels they form so called caps enlarging the deposition area and hence the current. (4) The second region of constant current is attributed to

the formation of a planar layer due to overlapping caps, resulting an a constant deposition area which is much larger than that in (2). In order to control the length of the nanowires, the I-t-curve is carefully monitored and the electrodeposition is stopped, for example, just before the cap growth starts [123].

2.4 Template dissolution - release of single nanowires

For the characterization of the nanowires employing various analysis techniques as well as for the fabrication of electronic devices based on nanowires, it is crucial to extract single wires from the polymer template. In order to do so, the template has to be removed by a suitable dissolution technique such as wet chemical etching. The released nanowires are, depending on their mechanical stability, either free-standing or collapsed on the gold working electrode also referred to as back electrode. It is also possible to transfer the wires onto a different substrate by releasing them from the gold back electrode, keeping them in solution and depositing them onto the appropriate substrate.
In this work two different approaches were applied using dichloromethane (CH_2Cl_2, Carl Roth, 99.5% purity) as organic solvent to dissolve the polycarbonate membrane. The first method starts with placing a wire-containing membrane on a Si wafer and drop-casting dichloromethane on it. This removes the template and the released nanowires break off the back electrode and flow together with the solvent onto the Si substrate as schematically suggested in figure 2.4.1 (a). In this way, some of the nanowires deposit on the Si substrate within the flow direction of the solvent. To remove possible polymer residues, the nanowire-covered substrates were immersed consecutively in two fresh baths of dichloromethane for several minutes to attain clean wires that are suitable for further characterization. Experience showed, that the nanowires are quite strongly attached to the substrate and after the cleaning process enough nanowires are deposited on the Si substrate. For the preparation of the nanowires on **T**ransmission **E**lectron **M**icroscopy (TEM) sample grids this drop-casting method was modified by replacing the silicon substrate by the desired TEM grid.

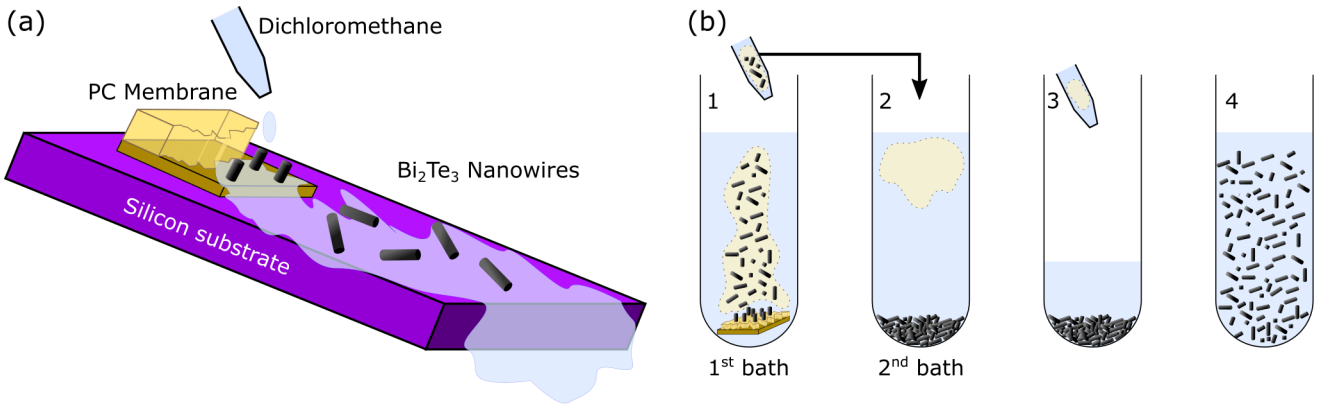

Figure 2.4.1: Two alternative methods for the preparation of released nanowires: (a) as the polymer template is dissolved by an organic solvent, the nanowires deposit on a suitable substrate. (b) Multi-step process to obtain nanowires suspended in a solution: (1) dissolution of the polymer template and transfer to second bath, (2) centrifugation to separate the nanowires and the polymer, (3) discarding of the dissolved polymer, (4) refilling with fresh dichloromethane. Steps (2)-(4) were repeated three times.

In the second method, the polymer matrix filled with nanowires is completely immersed into a bath of dichloromethane (~ 5 mL) inside a test tube. As the PC is dissolved, the nanowires ascend towards the surface of the bath. Short ultrasonication (~ 2 sec) is used to force the nanowires to break away from the supporting back electrode. In this way the back electrode and attached polymer residues remain in the first bath, while the wires are pipetted into a second test tube (1). Fresh dichloromethane is added to the second bath (filling up to ~ 5 mL) for further cleaning of the nanowires. Then the nanowires were centrifuged at 4000 rpm for 45 min up to 1 h at room temperature (Biofuge primo R, Heareus) (2). Subsequently, the upper half of the bath's volume was discarded (3) and replaced by fresh dichloromethane (4). The solution was shaken and centrifuged again. This routine is repeated for three runs to obtain clean nanowires in solution. This solution was then drop-casted onto the desired substrate such as a silicon wafer or TEM grid.

This second method was specifically developed to obtaining controlled wire concentrations as required for the characterization of polymer free individual nanowires. Particularly devices based on single nanowires require a low wire density and a very clean surface provided by the second method as will be shown in chapter 5.

3 Characterization of Bi_2Te_3 nanowires

For Bi_2Te_3 nanowires that are electrochemically deposited in etched ion-track membranes, properties such as geometry, morphology, crystallographic orientation and chemical composition are independently controllable by tuning various parameters during the fabrication process. In order to develop good thermoelectric materials, this has been extensively studied before [166]. Nevertheless, with respect to the new challenge of conducting nano-**A**ngle-**R**esolved **P**hoto**E**mission **S**pectroscopy (ARPES) and electrical transport measurements on individual Bi_2Te_3 nanowires, it is crucial to characterize not only the above mentioned properties, but focusing on the wire surface. A contamination-free surface is absolutely necessary to access the electronic band structure of the nanowire as will be shown in chapter 4 and to contact individual nanowires by lithographical methods as demonstrated in chapter 5. Especially surface-contaminating polymer residues, that are unique to the nanowire synthesis employed here, had not been thoroughly considered to interfere with measurement performed on Bi_2Te_3 nanowires, mainly because the wire surface has not been of primary interest. An extensive **X**-ray **P**hotomission **S**pectroscopy (XPS) study of the contamination degree of the nanowire surface and possible cleaning strategies are an important part of this work, enabling nano-ARPES and electrical transport studies that would not have been possible otherwise.

The following sections present the characterization of Bi_2Te_3 nanowires by means of different analysis methods. Their shape, geometrical size and morphology were explored by microscopy methods including **H**igh **R**esolution **S**canning **E**lectron **M**icroscopy (HRSEM) and **T**ransmission **E**lectron **M**icroscopy (TEM) shown in section 3.1. High resolution images, diffraction patterns and darkfield images in TEM provided information on the crystal structure, grain sizes and boundaries. Additionally, **X**-**R**ay **D**iffraction (XRD) performed on arrays of nanowires embedded in the polymer matrix revealed the average crystal orientation perpendicular to the nanowire axis. The results of the crystallographic structure analysis is presented in section 3.2. The chemical structure of the Bi_2Te_3 nanowires was studied in section 3.3 by **E**nergy **D**ispersive **X**-ray spectroscopy (EDX) and **X**-ray **P**hotomission **S**pectroscopy (XPS) comparing both, the bulk and surface chemical compositions. Finally, the thermal stability of the nanowires was explored in section 3.4, in order to estimate their suitability for device fabrication involving elevated temperatures.

3.1 Geometry and morphology

The geometry and morphology of the synthesized Bi_2Te_3 nanowires were explored by means of HRSEM (JSM-7401F, JEOL) and TEM (ARM200CF, JEOL). The process of releasing the nanowires from the polymer membrane and transferring them onto a suitable substrate (e.g. silicon wafer or TEM grid) is described in the previous section 2.4.

Figures 3.1.1 (a, b) show representative SEM images of cylindrical Bi_2Te_3 nanowires of different diameters. The wires with diameters of (100 $\pm$ 5) nm (a) and (50 $\pm$ 5) nm (b) were grown in 2 min and 4 min etched PC templates, respectively. Nanowires deposited in 30 µm-thick membranes are maximum

27-29 µm long, because the uniform etching rate of the unirradiated polymer results in a thinning of the template. Owing to the breaking away of the wires from their substrate during their release from the polymer matrix, nanowires of lengths of up to 20 µm were observed. In some cases, the Au back electrode was etched away in potassium iodide (KI/I_2 acc. to Lugol, Carl Roth) prior to the template dissolution in order to reduce the amount of broken wires. Nanowires of up to 29 µm were obtained. Figure 3.1.1 (c) displays an SEM image of such a maximally long nanowire which fully outgrew the template as indicated by the cap (inset).

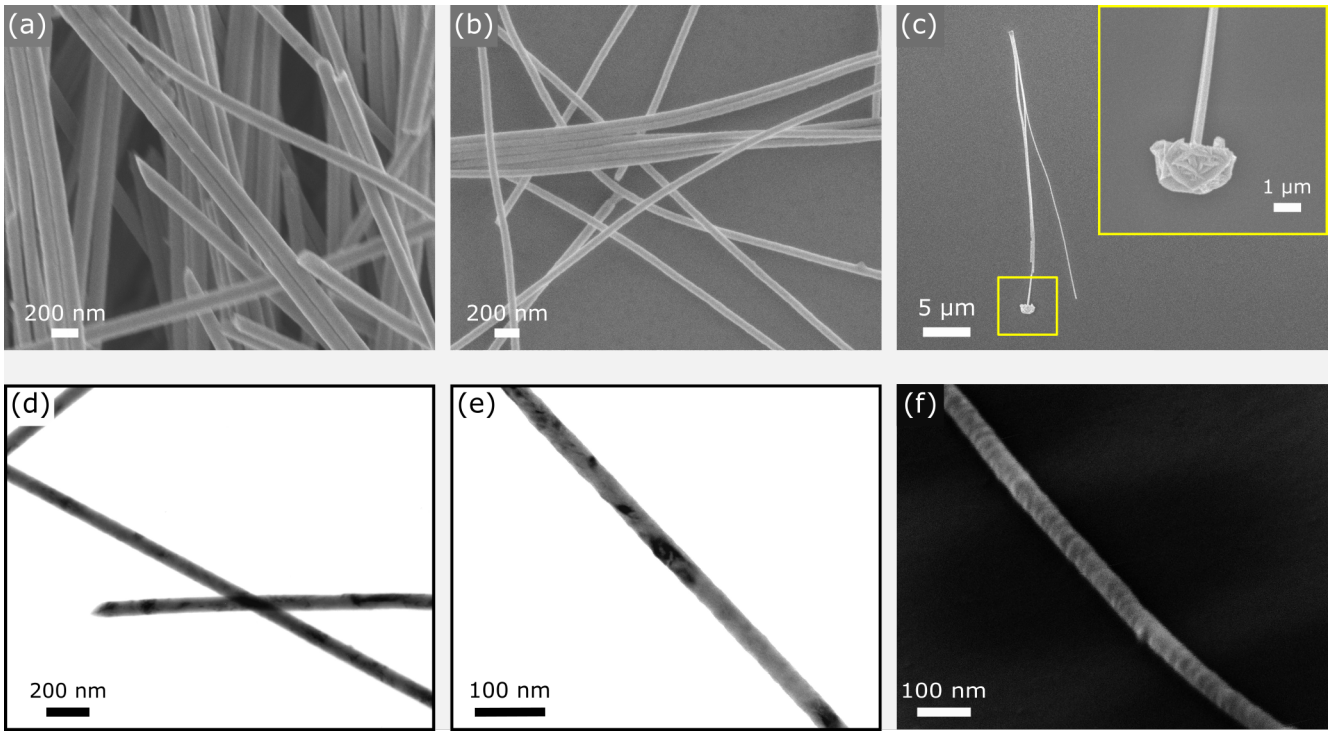

Figure 3.1.1: SEM (a-c, f) and TEM (d, e) images of Bi_2Te_3 nanowires transferred onto a silicon substrate and a Si_3N_4 TEM grid, respectively: The nanopores were etched for (a) 4 min and (b) 2 min revealing nanowires with diameters of (100 $\pm$ 5) nm and (50 $\pm$ 5) nm, respectively. (c) Nanowires of about 30 µm length exhibit cap growth (inset). TEM images reveal the surface contour of nanowires with (100 $\pm$ 5) nm (d) and (50 $\pm$ 5) nm (e). The surface roughness becomes also visible in SEM by a 60° tilt of the wire (f).

Independent of their dimensions, the nanowires exhibit a fairly smooth contour without obvious surface defects like kinks as observed before for nanowires electrodeposited applying 0 V vs. SCE at 30°C in PC [116]. Compared to the previous work, slightly elevated temperatures and a different layout of the electrochemical cell was used here. Figure 3.1.1 presents TEM images of these nanowires with diameters of (100 $\pm$ 5) nm (d) and (50 $\pm$ 5) nm (e). A slight surface roughness is observed in the TEM images, which is best visible in image (e). For SEM, the contrast due to the surface roughness is only well observable by tilting the nanowire by 60° as shown in image (f). The slight deviation from the smooth surface is attributed to the roughness of the PC wall of the nanopores. Their morphology is directly replicated on the nanowire surface. Compared to other polymer templates such as PET, this roughness is relatively small. The contour of the nanopore obviously defines the nanowire shape suppressing crystal orientation dominated growth as it is the case for the VLS method. Generally, the surface roughness can by

adjusted by either selecting the template material (polycarbonate, polyethylene terephthalate) [128] or by increasing the deposition potential [166]. Electrical transport measurements on topological insulator nanowires are not expected to be influenced by the roughness of the surface due to the time-reversal protection of the surface states.

3.2 Crystallographic structure

The investigation of the crystallographic orientation is crucial for the interpretation of data obtained from (thermo-)electrical transport measurements, since the anisotropy of Bi_2Te_3 induces anisotropic transport characteristics [47, 167]. To gather information on the crystallographic orientation and the grain characteristics, such as size and boundary type, XRD diffractograms (section 3.2.1) and **H**igh **R**esolution **T**ransmission **E**lectron **M**icroscopy (HRTEM) images (section 3.2.2) were analyzed. While TEM is a perfectly suitable method to investigate nanoobjects, XRD measurements[1] require a minimum of sample volume to generate meaningful results.

3.2.1 Nanowire arrays - X-ray diffraction

Previous studies revealed that the crystallographic orientation of Bi_2Te_3 nanowires synthesized by electrochemical deposition is controllable by variation of the growth parameters such as the deposition potential and temperature [116, 131, 166]. Because the Bi_2Te_3 nanowires used in this work were fabricated in different electrochemical cell and at slightly higher deposition temperature (30°C) as in [116, 166], the crystallographic orientation was re-assessed.
Four-circle X-ray diffractometry using a HZG 4 diffractometer with a copper anode ($\lambda_{K\alpha 1}$=1.54060 Å) was carried out at GSI. Making use of the perfect parallel alignment of the nanowires within the PC membrane, the nanowires are investigated still embedded in the membrane. In this way an "average" crystallographic information about the planes perpendicular to the nanowire axes are obtained. The term average refers to either many single crystalline nanowires of different orientation or polycrystalline nanowires with subgrain orientations. It is worth pointing out that both scenarios cannot be distinguished employing this sample alignment and further investigations using TEM are necessary to complete the picture. A schematic explaining the sample alignment for XRD measurements is depicted in figure 3.2.1 (a). As mentioned before, a certain minimum sample volume has to be provided for accurate measurements. Samples prepared in 30 µm thick PC membranes irradiated with a fluence of 10^9 ions/cm^2, fulfilled this criterion even for very short etching times of 1 min resulting in a nanowire diameter of approximately 25 nm. Figures 3.2.1 (b, c) present the photographs of two Bi_2Te_3 nanowire array samples prepared for XRD. Due to the dark color of Bi_2Te_3, the area of nanowire deposition is clearly visible (top view of the wires). With thinner diameters or shorter length, the color change of the nanowire array compared to the surrounding polymer matrix is less pronounced as shown in figure 3.2.1 (c). Samples showing a lighter color than that turned out not to be suitable for XRD measurements.
Figure 3.2.1 (d) displays representative ω-2θ-scans for two different Bi_2Te_3 nanowire arrays. The upper pair of diffractograms (blue and red) was recorded from nanowires with a diameter of ~75 nm, while

[1] In this work synchrotron XRD, suitable to investigate individual nanoobjects, was not available.

the lower pair was obtained from ~150 nm thick wires. The reflections were measured within a 2θ angle range of 20-68° with a step size of 0.02° and 15 sec measurement duration per step. Additionally, the known diffraction values of Bi_2Te_3 (black) and Au (green) powder references are added at the bottom of the graph (JCPDS files no. 08-0027 and no. 04-0784, respectively).

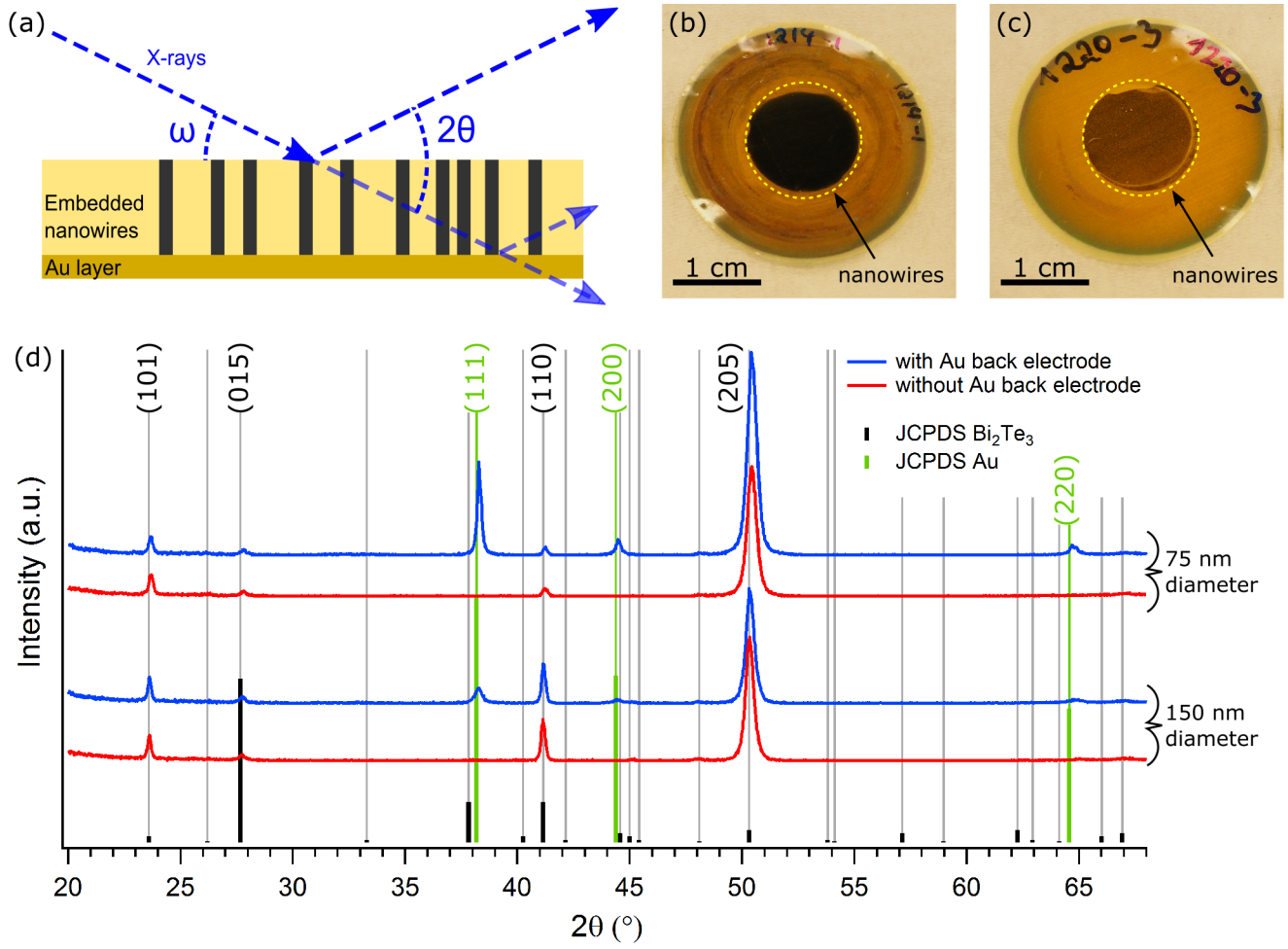

Figure 3.2.1: XRD measurements of the average crystallographic orientation perpendicular to the Bi_2Te_3 nanowire axes: schematic sample alignment of polymer-embedded nanowires (a); photos of 10^9 nanowires/cm^2 embedded in track-etched PC membrane (central dark area, top view) with wire diameters of (b) ~ 150 nm and (c) ~ 25 nm; ω-2θ-scans for two different wire diameters measured before (blue) and after (red) the Au back electrode removal. JCPDS powder standards are given for Bi_2Te_3 (black) and Au (green).

Generally, four main reflections are visible at approximately 23.8°, 27.8°, 41.3° and 50.4°. According to the powder reference, those reflections are assigned to the (101), (015), (110), and (205) planes of Bi_2Te_3, respectively. For some samples, the Au layer was removed in a Lugol's iodine solution (KI/I_2) for a better distinction between the Au and Bi_2Te_3 reflections at around 38.4° and 44.5°. For each pair of diffractograms the blue curve was recorded before and the red curve after the removal of the Au back electrode. The comparison of both clearly shows that the reflections at around 38.4° and 44.5° are solely attributed to the Au back electrode, because they vanish after its removal, while the reflections identified as originating from Bi_2Te_3 remain unchanged. This results was previously obtained in other works [128, 166] and is explained by the long penetration depth of the X-ray beam and its subsequent

reflection at the Au back electrode, as schematically indicated in figure 3.2.1 (a). In all following diffractograms the Au layer was not dissolved.

X-ray diffractograms of six Bi_2Te_3 nanowire arrays, deposited at 30°C and 0 V vs. SCE deposition potential in PC membranes with nanochannel diameter of ~ 50 nm are presented in figure 3.2.2. For a better visualization all diffractograms are normalized to the (101)-peak at 23.6°. They are randomly numbered and either colored red or blue depending on certain characteristics which are explained in the following.

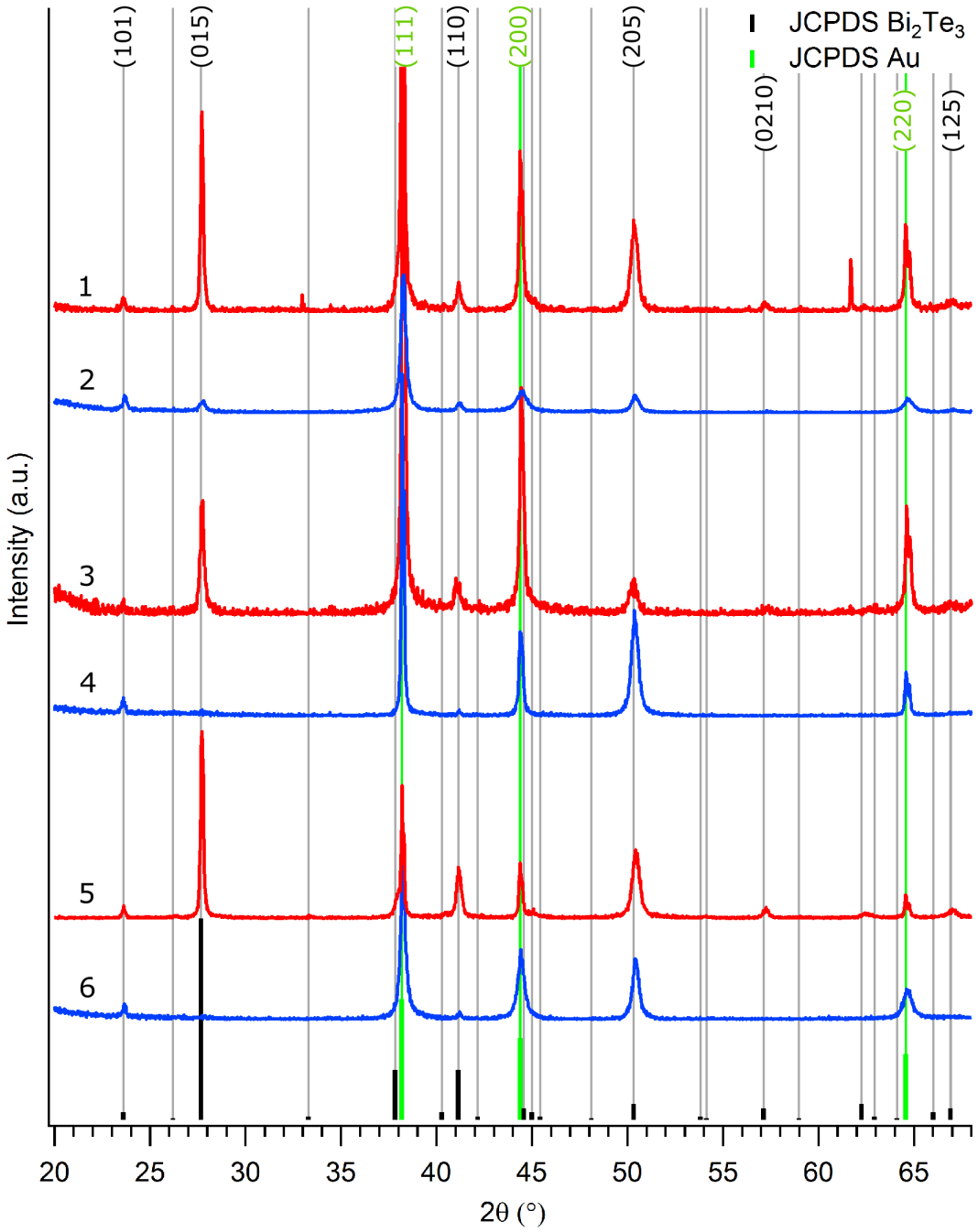

Figure 3.2.2: Six x-ray diffractograms for nanowire arrays yielding a wire diameter of about 50 nm. The diffractograms are normalized to the (101)-peak at 23.6° and numbered randomly. Red and blue distinguishes two different characteristic diffractograms (see text). The powder reference for Bi_2Te_3 (black) and Au (green) are added at the bottom.

In all six diffractograms, the Bi_2Te_3 reflections at about 23.6°, 41.4° and 50.4° corresponding to the respective planes (101), (110) and (205) are present. Reflections at 38.4°, 44.5° and 64.5° are identified to belong to the Au back electrode. For all diffractograms, the (205) reflection is more intense than expected from the powder reference (black bars). Compared to that, the (110) reflection peak is in all cases less pronounced than expected. Furthermore, an intense reflection at 27.7° is observed for diffractograms 1, 3 and 5 (red), corresponding to the (015) plane oriented perpendicular to the nanowire axes. For a Bi_2Te_3 powder reference this reflection is supposed to show the highest intensity. A second criterion for this group is the appearance of additional reflections at about 57.1° and 66.9° originating from the (02 10) (second order of (015)) and (125) planes, respectively. These reflections are not found in diffractograms 2, 4 and 6 (blue). Instead, they feature strong reflections from the (205) planes to yield the dominant peak intensity. Additionally, the intensity corresponding to the (101) reflection is higher than that of the (110) plane, in contrary to the expected ratio from the powder reference.
Obviously, two different types of texture can be distinguished for samples fabricated under the same conditions. Both types indicate polycrystallinity due to multiple reflections and a certain texture because of the differing peak height ratios compared to the powder reference. For a better quantification, the **T**exture **C**oefficient (TC) for each analyzable Bi_2Te_3 peak was calculated as defined by

$$TC(h_i k_i l_i) = N \left[\frac{I(h_i k_i l_i)}{I_0(h_i k_i l_i)} \right] \left[\sum_{n=1}^{N} \left(\frac{I(h_n k_n l_n)}{I_0(h_n k_n l_n)} \right) \right]^{-1}, \tag{3.1}$$

with $h_i k_i l_i$ denoting the specific lattice planes, N the number of reflections considered, I the background subtracted reflection intensity and I_0 the standard peak intensity for the powder reference. To determine the peak intensity and position, a Gaussian was fitted to each signal after the subtraction of a constant background. If $TC \geqslant 1$, a preferential orientation of this particular plane perpendicular to the nanowire axes is observed. For measurements with more than one $TC \geqslant 1$ the hierarchy of the TC values denotes the importance of the particular plane to the texture. Table 3.2.1 presents the TCs calculated for the diffractograms shown in figure 3.2.2. A "-" means that the reflection intensity was too low to obtain an accurate Gaussian fit. In that case the peak was not considered in the TC calculation.

Table 3.2.1: Texture coefficients calculated for reflections shown in figure 3.2.2 sorted by blue and red diffractograms

Planes	Blue			Red		
	2	4	6	1	3	5
(101)	2.38	1.28	0.86	0.81	-	0.84
(110)	0.19	0.36	0.07	0.27	0.54	0.67
(205)	1.37	1.36	2.08	3.04	1.87	2.91
(015)	0.06	-	-	0.57	0.59	0.66
(02 10)	-	-	-	0.32	-	0.51
(125)	-	-	-	-	-	0.41

Overall, only the TCs for the (101) and the (205) are found to reach above 1. For the diffractograms of the red group the preferential texture is clearly the (205) plane. Between those three diffractograms, number 3 exhibits the strongest texture, because for 1 and 5 the $TC_{(205)}$ is not as pronounced relatively

to the number of considered peaks. On the other hand, it is important to remember that small intensities originating from the (02 10) and (125) planes are visible in figure 3.2.2 but could not be accurately fitted. This still justifies the distinction between the red and blue diffractograms. The samples belonging to the blue group exhibit preferential orientation for both the (101) (2) and the (205) (6) planes or no distinct preference between the two (4).

In conclusion, the XRD results of Bi_2Te_3 nanowire arrays deposited in 2 min etched polycarbonate templates (pore diameter of about 50 nm) indicate polycrystallinity. Three pronounced reflections are found in each diffractogram. Although up to three more reflections were measured, the preferred orientation is the (205) plane perpendicular to the nanowire axes followed by the (101) plane. This result is consistent with previous investigations [166].

Figure 3.2.3 displays a series of diffractograms for Bi_2Te_3 nanowire arrays with different wire diameters. In contrast to the samples investigated in figure 3.2.2, the nanowire arrays were synthesized in PC membranes irradiated during the same beamtime. In this way etching rate uncertainties due to ageing effects were avoided. The PC membranes were etched for 6, 4, 3, 2 and 1 min yielding wires with diameters of approximately 150, 100, 75, 50 and 25 nm, respectively. All nanowires were fabricated applying a potential of 0 V vs. SCE at 30°C. As before, reflections at 38.4°, 44.5° and 64.5° are attributed to the gold back electrode. In this case the diffractograms are normalized to the (015) reflection at 27.7°. The diffractogram of the 50 nm nanowire array is the same as displayed in figure 3.2.2 number 2.

Reflections at 23.6°, 27.7°, 41.4° and 50.4° are assigned to the (101), (015), (110) and (205) planes (see fig. 3.2.2). For the smallest diameter of 25 nm only two reflections are visible, namely those of the (015) and the (205) planes. The former is supposed to yield the highest intensity assuming a powder sample. Due to the very low intensity, it is impossible to judge from this measurement if there is a (015) or a (205) texture existent or further peaks are hidden in the background. Obviously, the sample volume generated in nanochannels of about 25 nm is too small for precise measurements. For arrays with nanowire diameters of 75 nm or larger, the (205) reflection at 50.4° is conspicuously dominating the diffractograms, indicating a possible texture.

The TCs of the four identified reflections are summarized in table 3.2.2. In all cases a preferred orientation of the (205) or the (101) plane is observed with a stronger tendency towards the (205) plane.

Table 3.2.2: Texture coefficients calculated for reflections shown in figure 3.2.3 for different nanowire diameters.

Reflection	Etching time					
	150 nm	100 nm	75 nm	75 nm (not shown)	50 nm	25 nm
(101)	1.11	1.73	0.58	1.63	2.38	-
(110)	0.26	0.14	0.04	0.27	0.19	-
(205)	2.62	2.12	3.37	1.76	1.37	1.76
(015)	0.01	0.01	0.01	0.34	0.06	0.24

Outstanding is a TC > 3 by considering four reflections for the nanowires yielding a diameter of approximately 75 nm. This maximum value has also been previously found for nanowires with 50-60 nm deposited at 0 V vs. SCE and room temperature [116, 166]. Contrary to those previous findings a strong texture of the (015) plane was not found for small nanowires diameters, which could be explained by

the trend of decreasing (015)-texture with increasing deposition temperature [166]. It is noteworthy to mention that for nanowires of ~75 nm diameter the XRD results deviate in a similar manner as for the samples presented in figure 3.2.2. This means that the (015) reflection is more intense than expected from powder reference reducing the preferred (205) reflection and emphasizing the contribution of the (101) reflection. The TC of such a case is added to table 3.2.2. For nanowire samples with larger diameter this trend was not observed.

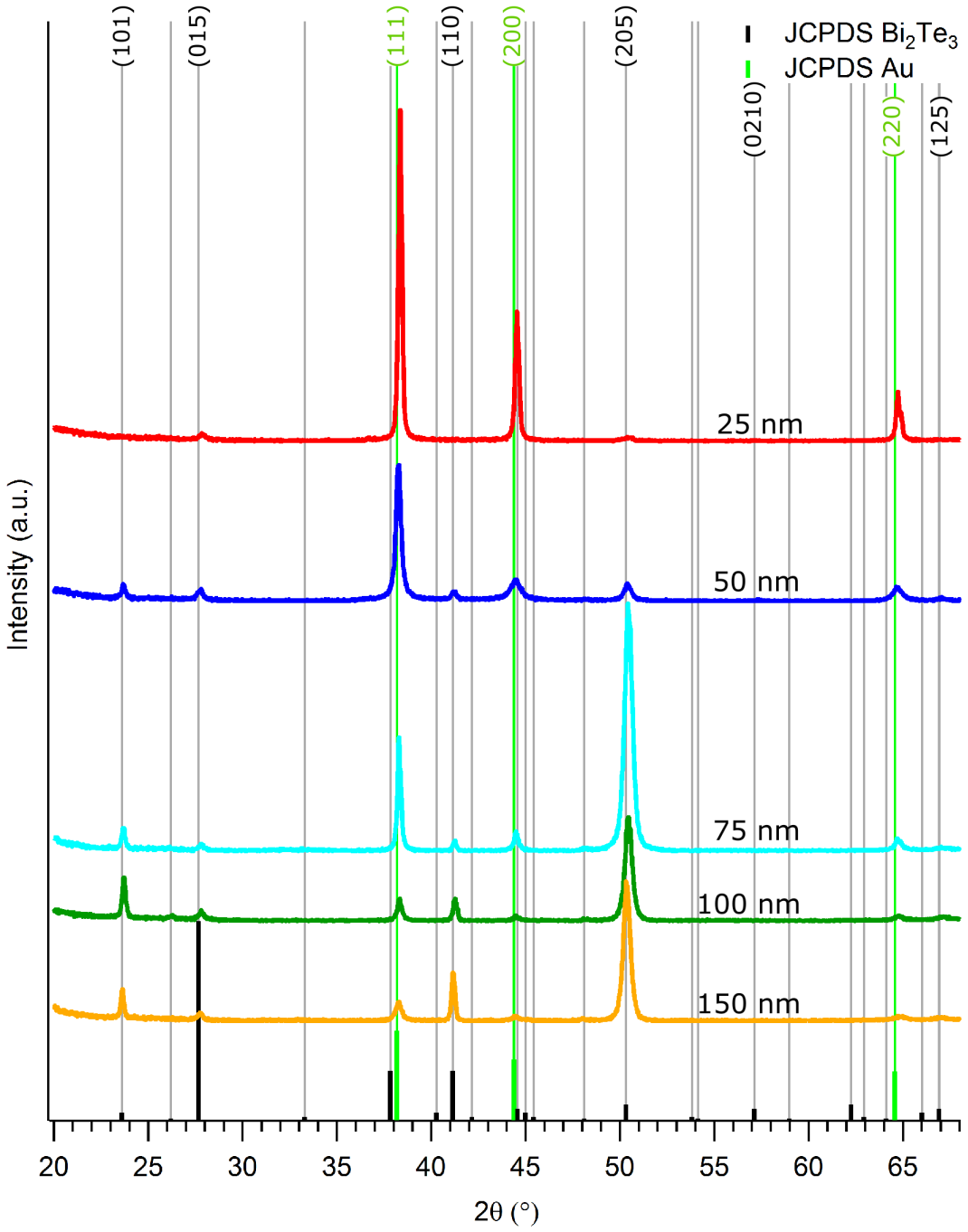

Figure 3.2.3: X-ray diffractograms for nanowires of different diameters. The diffractograms are normalized to the (015)-reflection at 27.7°. The powder reference for Bi_2Te_3 (black) and Au (green) are added at the bottom.

In summary, all Bi_2Te_3 nanowire arrays investigated by XRD feature an overall polycrystalline diffractogram with a high texture. The favored crystallographic orientations are the (205) or the (101) plane oriented perpendicular to the nanowire axes. While nanowire arrays with wire diameters lower than 100 nm show variations in the texture ratio of (205) to the (101) planes, this was not observed for larger nanowire diameters. For the individual nanowires of each array these results either mean that they are polycrystalline themselves, that the wires are single crystalline with different orientations or that they consist of single crystalline segments. In order to elucidate the crystallographic orientations of the individual nanowires, TEM measurements were performed and the results are presented in the following section.

3.2.2 Individual nanowires - transmission electron microscopy

In order to explore the crystallographic orientation of individual Bi_2Te_3 wires, various TEM techniques such as darkfield and high-resolution imaging were performed on several nanowire segments. The goal of these investigations is to find out if an individual nanowire is polycrystalline, single crystalline or segmented and how the crystal grains are aligned. The nanowires were transferred onto TEM grids using one of the two previously described methods. It is important to mention that in this configuration the nanowire is investigated along its axis. Expected plane orientations are those previously found by XRD (see section 3.2.1) and those parallel to the zone axis[2].
By darkfield TEM imaging the nanowires are shown to consist of several hundred nanometer or micrometer long single crystalline sections, separated by grain boundaries. Figure 3.2.4 displays three such single crystalline sections (light areas) and their grain boundaries (white arrows), representatively. The grain in figure 3.2.4 (a), one of the smaller ones found, is about 150 nm long and oriented approximately 20° with respect to the nanowire axis. In this view, the grain is not filling the complete nanowire volume. In contrast, the grains in figures 3.2.4 (b) and (c) extent to a full segment of the nanowire confirming previous observations of grain sizes of up to several hundreds of nanometers [166]. From this point of view the grain boundaries are clearly visible and rotated by about 50° (b) or perpendicular to the wire axis (c).

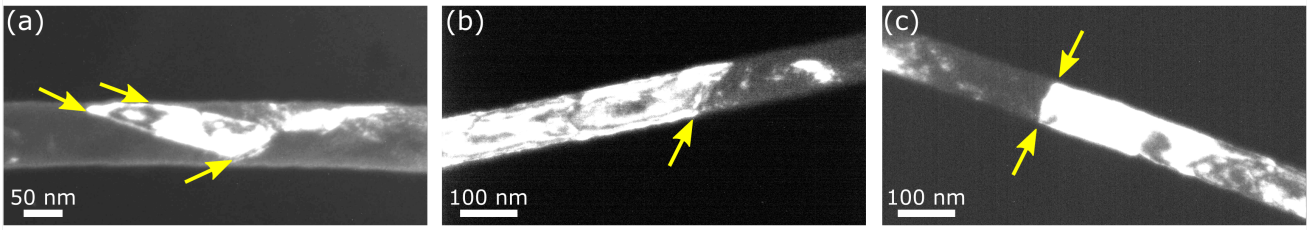

Figure 3.2.4: Darkfield TEM images revealing single crystalline grains of up to several hundreds of nanometers in length. Grain boundaries are found cutting the nanowire along its axis (a) and its cross section (a-c). The grain in (a) is rotated by approximately 20° with respect to the nanowire axis. The grain boundaries in (b) and (c) yield a 50° and 90° orientation to the nanowire axis.

[2] The zone axis is defined as the normal of the TEM projection.

Figure 3.2.5 presents HRTEM images of two sections of a single nanowire from the same sample as in figure 3.2.4 and their corresponding fast Fourier transformation. In both images an ordered atomic structure is visible, which continues up to the nanowire edge as evident from figure 3.2.5 (a). In (a), three different interplanar spacings are identified of which the one amounting to (0.226 ± 0.020) nm is oriented almost parallel to the nanowire axis (indicated in green). The fast Fourier transform of the entire HRTEM image confirms the crystalline nature of the wire segment and three spacings of (0.229 ± 0.020) nm, (0.211 ± 0.020) nm and (0.356 ± 0.020) nm were calculated. Table 3.2.3 gives a selection of literature values for the Bi_2Te_3 interatomic distances and their attributed planes. Considering the measurement uncertainty, the two smaller spacings can be assigned to the (10.11), (10.10) or (110) plane, while the larger spacing can be attributed to the (101) or (104) plane. The planes with this spacing are oriented approximately perpendicular to the nanowire axis, which is consistent with the XRD results showing a preferred (101) plane perpendicular to the axis.

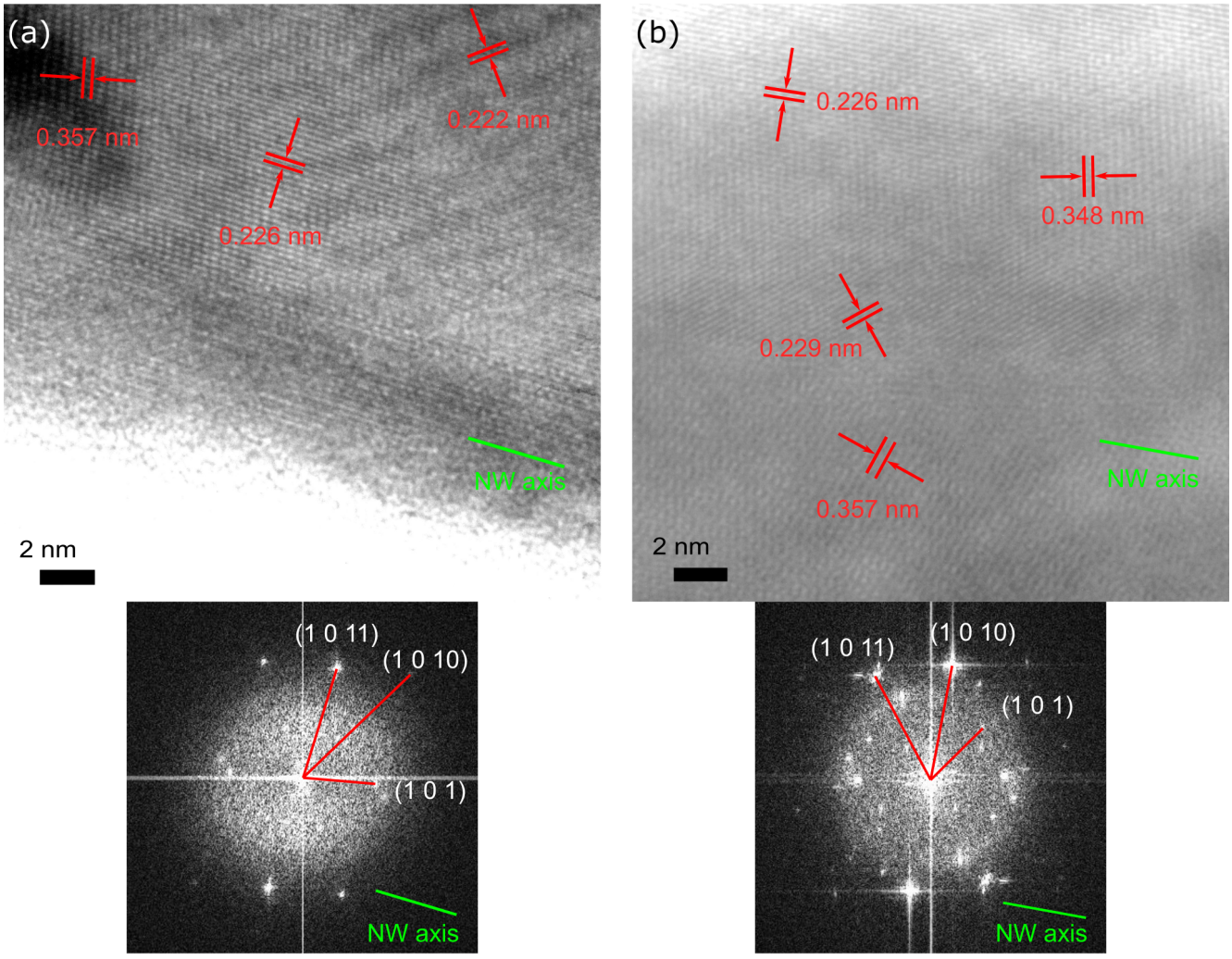

Figure 3.2.5: High-resolution TEM images and the corresponding fast Fourier transformations of two sections of the same Bi_2Te_3 wire. A well-ordered crystal structure through the entire segment is visible. The segment in (a) exhibits an interplanar distance of $d_{(10.11)} = (0.226 \pm 0.020)$ nm perpendicular to the nanowire (NW) axis (green). (b) gives an example of multiple interplanar orientations.

The segment shown in figure 3.2.5 (b) also features an ordered crystal structure. Contrary to (a), various interplanar spacings and orientations are observed. The spacings of (0.226 ± 0.020) nm and (0.229 ± 0.020) nm correspond to the (10.11), (10.10) or (110) planes, while for (0.348 ± 0.020) nm and (0.357 ± 0.020) nm, the (104) or (101) planes are possible. Interestingly, no clear grain boundary is visible hinting a continuous transition between orientations as previously observed [166]. Due to its complexity, the fast Fourier transform of the wire segment confirms the various orientations. The (10.11), (10.10) and (101) were identified.

Table 3.2.3: Literature values from JCPDS file no. 08-0027 for interplanar spacings and the corresponding crystal planes.

Spacing (nm)	0.377	0.340	0.322	0.238	0.224	0.219
Plane (hkl)	(101)	(104)	(105)	(10.10)	(10.11)	(110)

The TEM investigations clearly evidence that the individual nanowires are of polycrystalline nature. A well ordered structure is observed throughout the entire nanowire segments. They exhibit long single crystalline grains, but also experience slight shifts in their plane orientations with no defined boundary outside of the single grains.

3.3 Chemical composition

Depending on their chemical composition the bismuth telluride compounds show various (thermo-)electric properties [30, 168]. Especially the topological insulator character of Bi_2Te_3 makes a thorough investigation of both the bulk and surface chemical composition necessary. Additionally, the degree of surface contamination is crucial to know for the successful contacting of nanowires by lithographical methods and for further conducting of surface sensitive probing techniques such as ARPES. For this reason, the decisive factors for the present investigations of the chemical structure of the wires are:

1. Is the chemical composition stoichiometric along an entire nanowire?
2. Is the nanowire surface free of contamination?

In order to answer the two questions above, EDX and XPS spectroscopy techniques were employed analyzing the chemical composition of the bulk and the surface of the nanowire, respectively. Figure 3.3.1 illustrates the measurement setup and compares both methods schematically. While the EDX in TEM provides information of the bulk of a single nanowire (a), XPS probes the chemical composition of the surface of multiple nanowires (b) as indicated by the yellow areas.

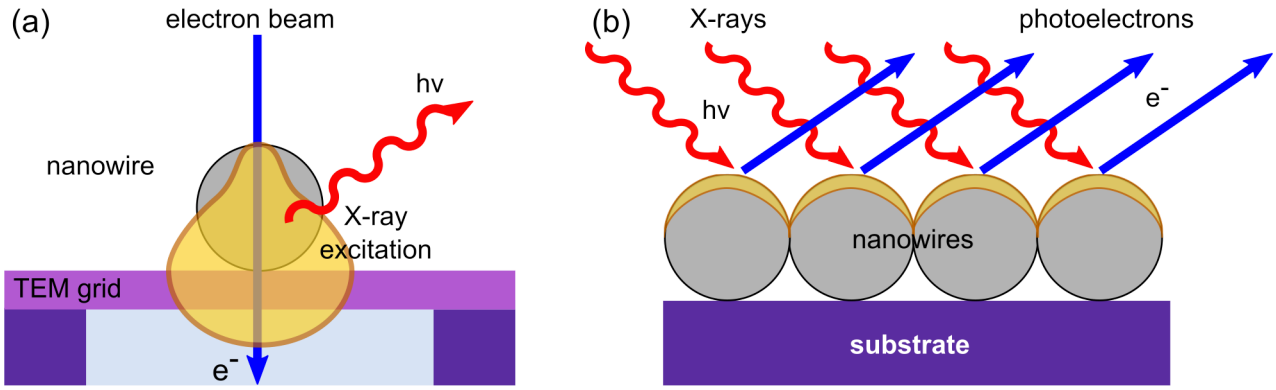

Figure 3.3.1: Principle of measurements for EDX (a) obtaining the chemical composition of the bulk volume and XPS (b) investigating the surface. The yellow area indicates the origin of the signal.

3.3.1 Nanowire bulk - energy dispersive x-ray spectroscopy

The chemical structure analysis by EDX was performed in a JEOL ARM200CF TEM in collaboration with Dr. Wilfried Sigle at the **St**uttgart institute for **E**lectron **M**icroscopy (StEM) of the Max Planck Institute for Solid State Research. Bi_2Te_3 nanowires of ≈100 nm diameter were prepared on a lacey carbon film copper TEM grid. EDX linescans of 50 points with a spatial resolution of approximately 1 nm were recorded along and perpendicular to the nanowire axis.

From the measured energy spectrum the atomic concentration was calculated using the Cliff Lorimeter technique [169] implemented in the Thermo Scientific NSS software (version 3.2) under consideration of the Te L-lines (energy range: 3642 - 3896 eV) and the Bi M-lines (energy range: 2309 - 2535 eV).

The compositional results in atomic percentage for Te and Bi of 100 nm wire diameter samples are presented in figure 3.3.2. The linescans were measured perpendicular to the nanowires axis close to the nanowires edge. Their positions are indicated in the corresponding images obtained by **H**igh-**A**ngle **A**nnular **D**ark-**F**ield imaging (HAADF). As the electron beam is scanned over the wire edge, signals at which the characteristic Te L-line (blue) and the Bi M-line (red) record more than 100 counts were considered to originate from the nanowire. This threshold providing a high signal-to-noise-ratio was chosen randomly. For a better visualization all other points were omitted resulting in shorter linescans than indicated by the arrows. Furthermore, sample drift during the measurement and contrast differences might be responsible for small discrepancies in the distances between the actual EDX linescans and the marker arrows in the HAADF image.

For this sample (A1), six individual nanowires were investigated. Generally, a composition close to stoichiometry is revealed as shown by two representative linescans in figure 3.3.2 (a) recorded from two different wires of the same sample batch. This is consistent with previous observations [116]. For most nanowires the chemical composition is found to be homogeneous within the range of the linescan measurements. However, in two out of six cases the surface of the nanowires exhibits a small local increase of Te, while the core of the nanowire is determined to be constantly close to stoichiometry. A representative EDX spectrum showing this Te-rich layer (marked in grey) is displayed in figure 3.3.2 (b). This observation is especially interesting, because the nanowires originate from the same sample, meaning

they are synthesized under the exact same conditions within the same cell. The Te-rich layers or shells were measured to be up to 2 nm thick. It could not be classified if this Te-richness is a local phenomenon or a kind of core-shell structure of the entire wire.

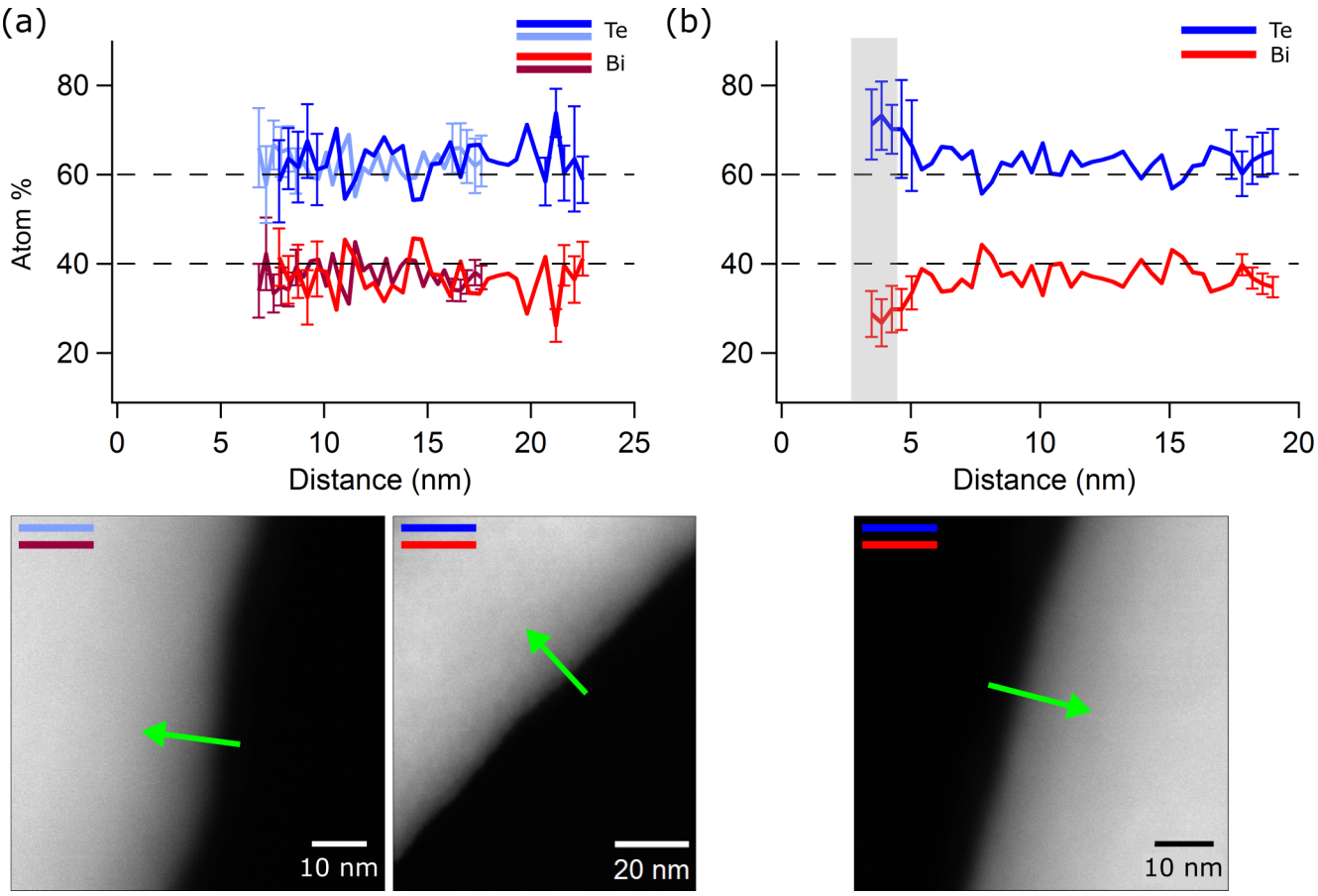

Figure 3.3.2: EDX linescans revealing the chemical composition of Bi_2Te_3 nanowires with about 100 nm diameter close to the nanowire surface (sample A1). In most of the cases a stoichiometric Te/Bi ratio was observed (a); few exceptions reveal a small local Te richness close to the wire surface (b). In the HAADF images the EDX linescan position is indicated by a green arrow.

Figure 3.3.3 presents similar results for Bi_2Te_3 nanowires deposited in 2 min etched templates yielding a diameter of ~50 nm. From this sample, 13 nanowires were investigated. As before, a homogeneous core of close to stoichiometric composition was consistently found, while a Te-rich shell was identified in three of the 13 cases. Additionally, a third compositional structure was observed for two nanowires, namely a Bi-rich intermediate layer between the Te-rich shell and a stoichiometric core (figure 3.3.3 (b)). This layer was measured at approximately 5 nm from the nanowire surface. Further measurements are required in order to describe and explain the slight enrichment of Te or Bi close to the wire surface.
Possible reasons for such local composition fluctuations were already observed in a different context. A local tellurium enrichment in electrodeposited nanowires (with diameters below 100 nm) was observed after annealing the wires at several 100°C for hours. In that case Bi_2Te_3/Te heterostructures with interfaces perpendicular to the wire axis were obtained. This was explained by the higher vapor pressure of tellurium compared to bismuth and the accompanying higher evaporation rate [170–172]. For the present case this explanation is not satisfactory applicable, because the sample was not heated. Mo-

reover, an evaporation of tellurium even at room temperature over about three weeks, would lead to a bismuth-rich shell due to the enhanced evaporation at the surface. In the present case a Bi enrichment was found in two cases and only in combination with a Te-rich surface layer.
Furthermore, cyclic voltametry investigations employing a similar electrolyte, but different Te and Bi concentrations, revealed a preferred deposition of tellurium when a more cathodic potential (about +100 mV) compared to the Bi_2Te_3 reduction potential is applied [117]. In the three-electrode setup used here, the potential is carefully controlled by the SCE reference electrode. Nevertheless, local ion concentration differences due to the different diffusion properties of the nanochannels compared to a planar electrode cannot be excluded. On the other hand, one would expect a more layered than a shell-like structure, if local potential differences influence the growth significantly.

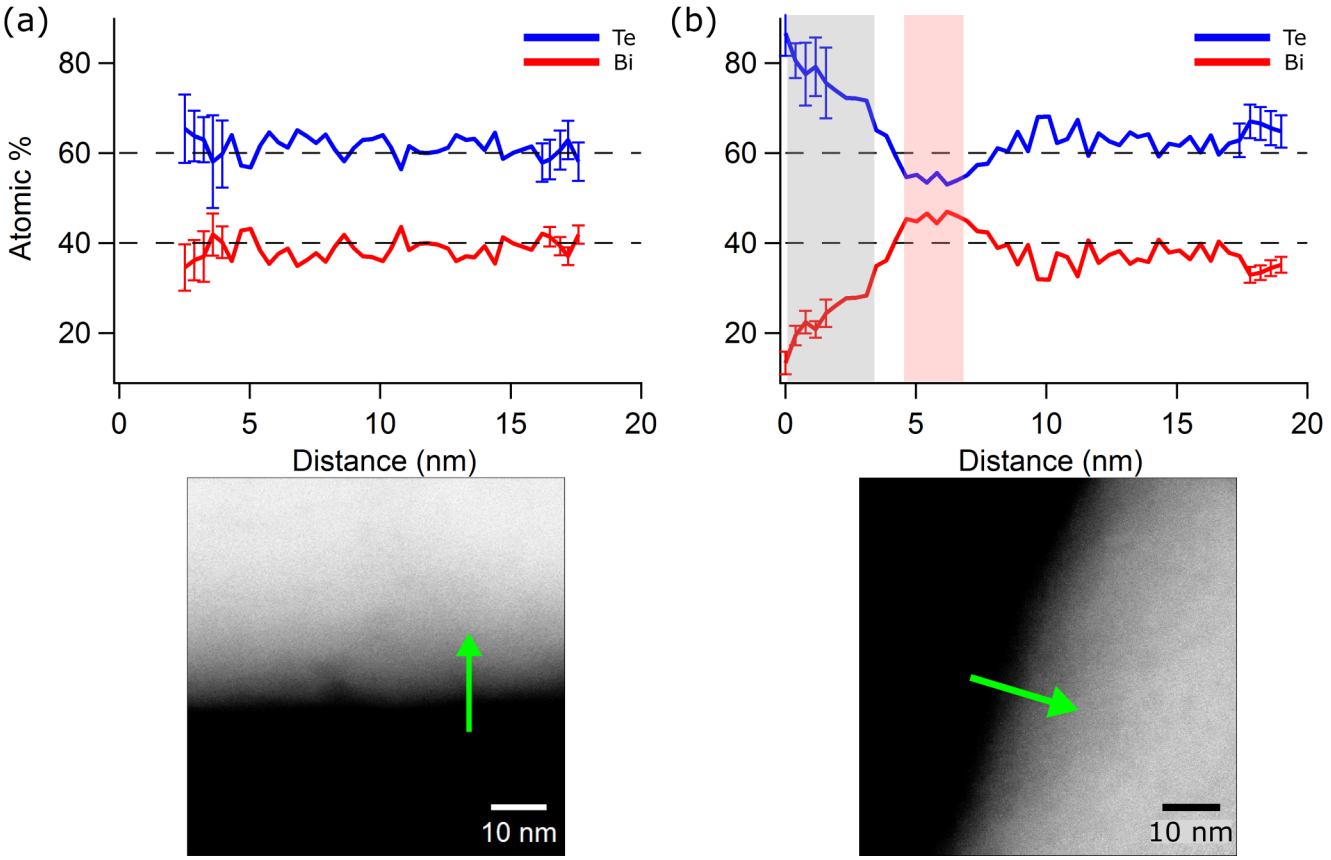

Figure 3.3.3: EDX linescans revealing the chemical composition of Bi_2Te_3 nanowires with about 50 nm diameter close to the nanowire surface (sample A2). Mostly a stoichiometric Te/Bi ratio was observed (a) with few exceptions indicating a local Te enrichment close to the wire surface and an intermediate Bi-rich layer (b). The green arrows in the HAADF images indicate the position at which the EDX linescan was measured.

The chemical compositions of those linescans exhibiting a constant composition along the entire range are summarized in table 3.3.1 revealing a 60:40 Te/Bi ratio within the uncertainty interval.
In conclusion, Bi_2Te_3 nanowires grown in 100 nm and 50 nm diameter polycarbonate nanopores reveal stoichiometric composition. Locally, a Te enrichment of of about 10-20% was found close to the surface. Further systematic measurements are necessary to explore the origin of this anomaly. However, it is

worth mentioning that EDX is not able to provide information on the oxidation states of elements, which are crucial for the evaluation of the surface quality. Amongst others, this information is accessed by XPS experiments and will be described in the following section.

Table 3.3.1: Chemical composition averaged over the complete linescan for four selected spectra from each sample. The error represents the standard deviation.

Sample	Te (atom. %)	Bi (atom. %)
A1	59.5 ± 5.19	40.5 ± 5.19
(fig. 3.3.2)	63.4 ± 4.17	36.6 ± 4.17
	62.5 ± 3.25	37.7 ± 3.25
	63.1 ± 4.62	36.9 ± 4.62
A2	58.6 ± 2.61	41.4 ± 2.61
(fig. 3.3.3)	60.4 ± 2.93	39.6 ± 2.93
	61.4 ± 2.39	38.6 ± 2.39
	60.7 ± 3.25	39.3 ± 3.25

3.3.2 Nanowire surface - X-ray photoelectron spectroscopy

The chemical signature of the nanowire surface was investigated by XPS. This technique is based on the photoelectrical effect [173], where an atom or molecule is excited by a photon resulting in the emittance of a photoelectron. The binding energy E_B of the photoelectron is related to its kinetic energy E_{kin} by

$$E_B = E_{h\nu} - E_{kin} - \phi \tag{3.2}$$

where $E_{h\nu}$ is the energy of the incoming photon and ϕ denotes the work function of the setup. This parameter depends on, for example, the absorbing character of the detector and its material. Measuring the kinetic energy of the emitted photoelectrons while knowing the energy of the exciting photon and the work function results in a characteristic spectrum for each material. A more detailed introduction to spectroscopy based on photoemission is given in chapter 4 where the ARPES results are discussed.
The XPS measurements referred to in this section were conducted in collaboration with Dr. Florent Yang of the surface science group (Prof. Dr. W. Jägermann) at the Technische Universität Darmstadt. The XPS setup used is located in the **DA**rmstädter **I**ntegriertes **SY**stem für **FUN**damentale Untersuchungen (DAISY FUN). The samples were screwed to an aluminum holder and inserted into an **U**ltrahigh **V**acuum (UHV) chamber at 10^{-10} mbar. The measurement principle is schematically sketched in figure 3.3.4 (a) and a photo of the fixed sample is shown in figure 3.3.4 (b).
Three samples were prepared in order to quantify the surface contamination of the nanowires, expected to occur during their synthesis, transfer process and device building as well as during the exposure to different atmospheres (air, UHV). First, Bi_2Te_3 nanowires were grown in a polycarbonate membrane with 10^9 pores/cm^2 of 100 nm diameter and a thick Au back electrode of about 1 µm. One day after the deposition, the sample was cut in four equal pieces. Two quarters were individually immersed in three rounds of fresh dichloromethane baths to remove the polymer membrane. Due to the mechanically stable Au back electrode and the flexibility of the Bi_2Te_3 nanowires, they remain collapsed on the back

electrode in a "spaghetti-like" arrangement. A representative SEM image of such a sample is displayed in figure 3.3.4 (c). The first sample (A) was directly transferred and measured in the XPS UHV chamber after being exposed to ambient air for about one hour. The second sample (B) was kept in a fourth bath of fresh dichloromethane for one complete week. After the measurement, the first sample (A) was stored in ambient air for one week to be remeasured. Unfortunately, the measurements could not be performed after one week due to failure of the XPS. Instead samples (A) and (B) were kept in a storage place in the UHV chamber for about 1 month before being measured. The samples and their measuring order can be summarized as follows:

1. measurement: Sample A was exposed to ambient atmosphere for about 1 hour.
2. measurement: Sample A was kept 1 week exposed to air and 1 month in UHV.
3. measurement: Sample B was kept 1 week in dichloromethane and 1 month in UHV.

The XPS measurements were conducted using an Al K_α photons with an energy of 1486.74 eV. Furthermore, a cleaning protocol was tested to remove possible surface contamination. The samples were cleaned using an Ar ion sputter gun at 500 V and 10 mA for 15 min per cycle. In all cases, two cleaning cycles were applied.

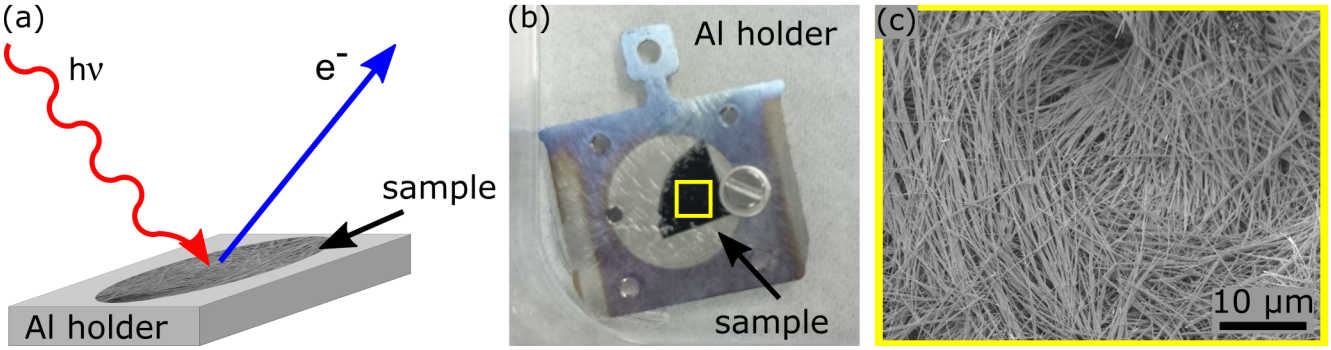

Figure 3.3.4: XPS measurement setup: (a) Schematic of the XPS technique. (b) Photo of a Bi_2Te_3 nanowires sample screwed to an aluminum holder. (c) SEM image of Bi_2Te_3 nanowires collapsed on the Au back electrode.

The results presented are structured as follows: an overview spectrum (E_B = 0...1350 eV) was recorded as well as close-ups of Bi 4f (E_B = 154...168 eV), Te 3d (E_B = 591...568 eV), C 1s (E_B = 297...280 eV) and O 1s (E_B = 540...525 eV) core levels. The corresponding photolines for each identified core level are indicated by dashed lines. Peaks occurring due to chemical bondings such as oxides states of an element and those resulting from different excitation states (i.e. Auger, shake-up lines) are marked by grey boxes. The Bi 4f and Te 3d core level in the Bi_2Te_3 bonding are colored in yellow.
The literature values [174] used to identify the photolines are compiled in table 3.3.2. Figure 3.3.5 summarizes the results of the first measurement for sample A. Three measurement series were recorded: as prepared (pink spectra), after the first cleaning cycle (dark red spectra) and after the second cleaning cycle (red spectra).
The overview spectra in (a) indicate the presence of Bi, Te, O, C, Al and Cu. While Bi, Te, O and C are signatures from the sample, the Al signal is attributed to the Al sample holder. The Al peak is only visible after the second cleaning cycle and is possibly caused by misalignment. The source of the copper

signal could not be determined. No Cl signal resulting from the polymer dissolution in dichloromethane (CH_2Cl_2) is observed. This reveals that the organic solvant neither leaves Cl contamination traces nor forms compounds such as Te_2Cl_3, $TeCl_4$, $BiCl_3$ or BiOCl. Comparing the spectra after each cleaning cycle, the Bi and Te core level as well as the corresponding Auger electron signals increase significantly or become firstly visible. At the same time the C 1s and O 1s signals are reduced and almost vanish into the background after the second cleaning step. This is a first hint that a non-negligible surface contamination accompanies the nanowire synthesis and transfer process. Fortunately, this contamination is successfully removed by standard XPS cleaning methods such as Ar sputtering. The absence of an additional Ar signal after the cleaning cycles points to a suitable method to reduce the contamination without implanting any further Ar atoms.

Table 3.3.2: Summary of literature values [174] for photolines identified for samples A and B.

Element	Core levels	Photoelectron lines (eV)
Bi	$5d_{5/2}$	24
	$5d_{3/2}$	27
	$4f_{7/2}$	157
	$4f_{5/2}$	162
	$4d_{5/2}$	440
	$4d_{3/2}$	464
Te	$4d_{5/2}$	41
	$4d_{3/2}$	42
	$3d_{5/2}$	573
	$3d_{3/2}$	583
	$3p_{3/2}$	820
	$3p_{1/2}$	871
C	1s	285
O	1s	531
Al	$3p_{3/2}$	77
Cu	$3p_{3/2}$	933
	$3p_{1/2}$	953

Figures 3.3.5 (b) and (c) display close-up scans of the C 1s and O 1s signals, respectively, recorded with a higher energy resolution (0.05 eV) compared to the overview spectra (0.5 eV) in figure 3.3.5 (a). Detailed scans are necessary to obtain exact determination of the peak shapes and to extract information about the chemical and compositional changes. The carbon signal of the as prepared sample ((b) pink spectrum) consists of three peaks located at binding energies of about 284.4, 286.0 and 290.8 eV. They are identified as the C-C and C-O chemical states as well as the shake-up lines for the $\pi - \pi^\star$ transition. Shake-up lines occur due to the creation of ions in an excited state instead of the ground state. Their kinetic energy is thus reduced by the energy of the excited state. For carbon, this shake-up line is often observed and corresponds to the $\pi - \pi^\star$ transition and is located at a binding energy about 6 eV higher than that of the ground state [174]. After the first cleaning cycle (dark red spectrum) the C 1s signal is dramatically reduced by about two thirds of its original intensity. Additionally, the shake-up peaks vanished into the background signal. After the second cleaning (red spectrum) only a minor intensity reduction is observed. The Ar treatment removes the natural carbon contamination layer of a few nm already after the first cleaning cycle, but does not reduce the contamination further after the second

cleaning step. It is worth noting that the C 1s signal is always detectable, due to the constant presence of carbon atoms even under UHV conditions. For this reason, the C 1s peak is generally used for the calibration of the measuring system.

The oxygen signal of the as prepared sample ((c) pink spectrum) is broader compared to the C 1s signal and is composed of three photon lines at about 530.0, 532.2 and 533.8 eV. Similar to the carbon appearance, oxygen traces are always present due to contamination, oxidation and exposure to air. Other than for the C 1s signal, the identification of the O 1s peaks is not as straightforward due to the overlapping of different oxides, carbonates and organic contaminations which result in peaks within the range of 529-532 eV[174]. The photoline at high binding energies of about 533.8 eV is attributed to the organic C=O chemical state with more confidence. This organic contamination points to polymer residues, which are possibly still adsorbed on the Bi_2Te_3 nanowire surface. The first cleaning step clearly reduces this signal to almost background values. Overall, the O 1s peaks are reduced by half or more of their intensity indicating a successful removal of surface contamination. Similar to the carbon contamination, this signal is not further decreased by the second cleaning cycle.

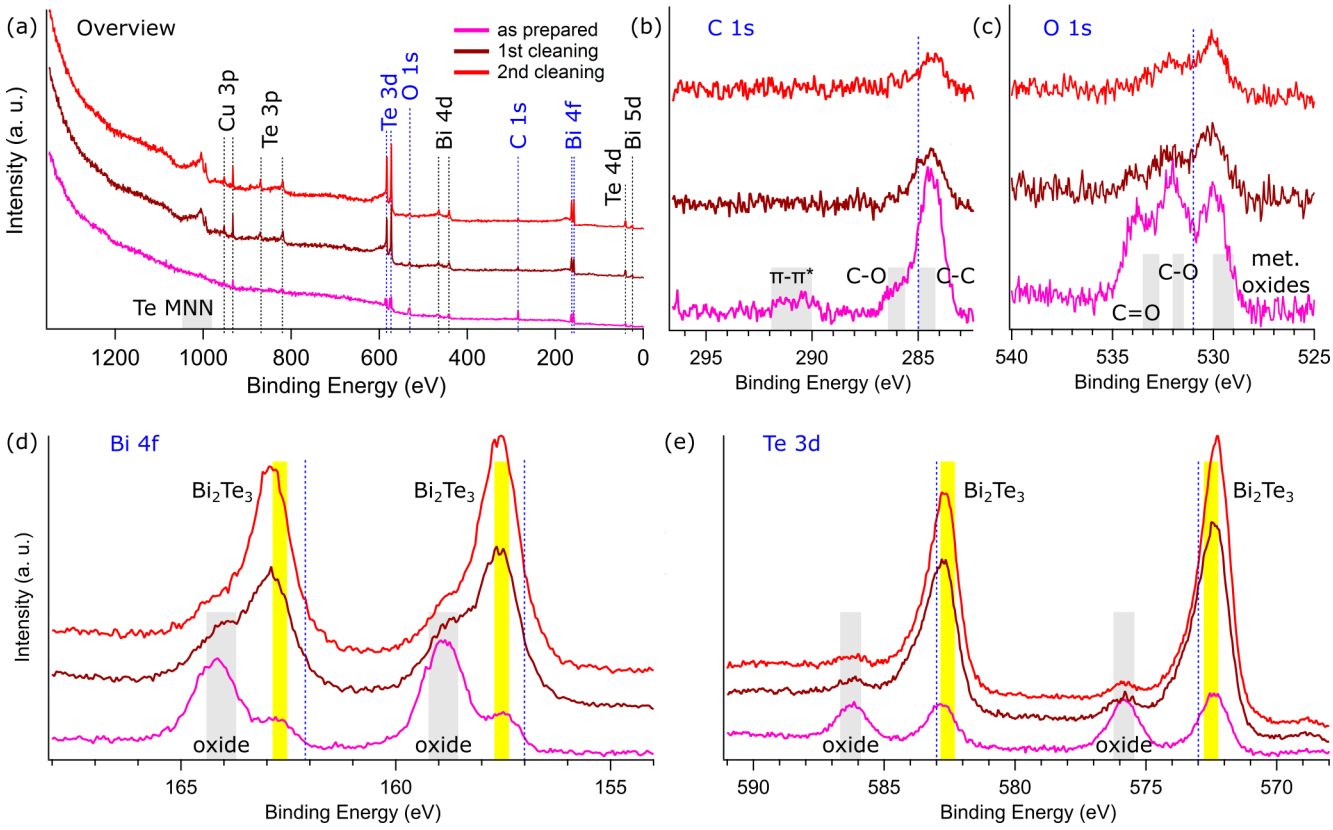

Figure 3.3.5: XPS spectra for sample A after exposure to air for about 1 h. The sample was measured as prepared (pink) and after two times Ar sputtering (500 V, 10 mA for 15 min) (dark red and red): (a) overview spectra and (b) C 1s, (c) O 1s, (d) Bi 4f and (e) Te 3d core levels.

Figures 3.3.5 (d) and (e) present the detailed spectra for the Bi 4f and Te 3d doublets. These core levels were chosen for further analysis, because they exhibit the highest cross section for their final state, resulting in the highest peak intensity [174]. In (d) the bismuth signal is deconvoluted into four peaks at about 157.5, 159.0, 162.9 and 164.2 eV. The Bi 4f core level is spin orbit split into the 7/2 and 5/2 energy explaining the two peaks at about 157.5 and 162.9 eV, respectively. The remaining two peaks

are located at about 1 eV higher binding energies and are attributed to bismuth oxide Bi_2O_3. For the as prepared sample ((d) pink spectrum), the oxide peaks are much more intense than those of the metallic bismuth, indicating a significant surface oxidation. As the sample is Ar sputtered, the oxide intensities are diminished significantly, while at the same time the pure bismuth photoelectron lines gain intensity. After the second cleaning cycle (red spectrum), only a small shoulder indicating remaining oxide is observable. According to literature, the spin orbit splitting results in an intensity ratio of 3:4 for the f level, which the data resembles roughly after the second cleaning step. Similar to the reduction of the C and O contaminants, the oxide peak is mostly removed during the first Ar sputtering cycle. Because of the further oxide removal during the second cleaning step, the pure metallic intensity is increased.
The Te 3d core level measurements displayed in figure 3.3.5 (e) show a similar behavior as for the Bi 4f core level. For the as prepared sample, one doublet at around 572.4 and 582.9 eV binding energies is identified as the spin orbit splitting into Te 3d5/2 and Te 3d3/2 photoelectron lines. The peaks at about 575.9 and 586.3 eV are assigned to oxide peaks forming TeO_2, which are reduced by the first Ar sputtering cycle. After the second cleaning cycle, the oxide signal has almost vanished into the background, while the pure Te signals are clearly distinguishable. As for Bi, the oxide signal is still slightly detectable after the cleaning, probably due to small residues.
Overall, the surface seems to be significantly cleaner after the two rounds of Ar plasma sputtering. The natural carbon and oxygen contamination as well as the bismuth and tellurium oxides are drastically reduced. Due to only slight improvements after the second cleaning, it is expected that many more sputtering cycles are necessary to remove the contaminants completely. On the other hand, one has to keep in mind that sputtering is a destructive method which might change the surface chemistry. An optimal balance between the cleaning and destruction of the surface has still to be found by systematic tests.
Figure 3.3.6 displays the XPS results obtained from the exact same sample (A) after being subsequently exposed to air for one week after the first measurements shown in figure 3.3.5. In this way the nanowires are oxidized simulating the exposure to air occurring in several other applications such as device fabrication by lithography (see section 5.2) or transport to experimental stations.
Figure 3.3.6 (a) presents the three overview spectra recorded after one week in air (purple), an additional month in UHV (black) and after one Ar sputtering cycle (500 V, 10 mA) for 30 min corresponding to the cleaning protocol that was used before (green). The photoelectron lines in the overview spectra refer to the presence of Bi, Te, O, C, Al and Cu as expected taking into account that it is the remeasured sample (A). After one week exposed to air, the C and O peaks are again more pronounced than after the last cleaning in the first measurement (see figure 3.3.5 (a-c)). Under UHV conditions this contamination and oxidation is generally continuing, causing an increase of the corresponding peak intensities. In the present case this increase cannot be verified, because the calibration of the system was readjusted in between the measurements making it impossible to compare peak intensities. After the Ar sputter cleaning, the C and O peaks are not visible in the overview spectrum anymore. Figures 3.3.6 (b) and (c) show a more detailed scan of the C 1s and O 1s level, respectively, confirming the decreasing of the C and O contamination after the Ar sputtering. For the Bi 4f and Te 3d photoelectron lines in figure 3.3.6 (d) and (e), similar results are found. The oxide peak at higher binding energies is dominant and in the case of Bi only a small shoulder indicates the metallic bismuth lines. In both cases, the pure Bi 4f and Te 3d doublet is much better resolved after Ar sputtering. Although the oxide signal is reduced significantly, it

still remains clearly identifiable.

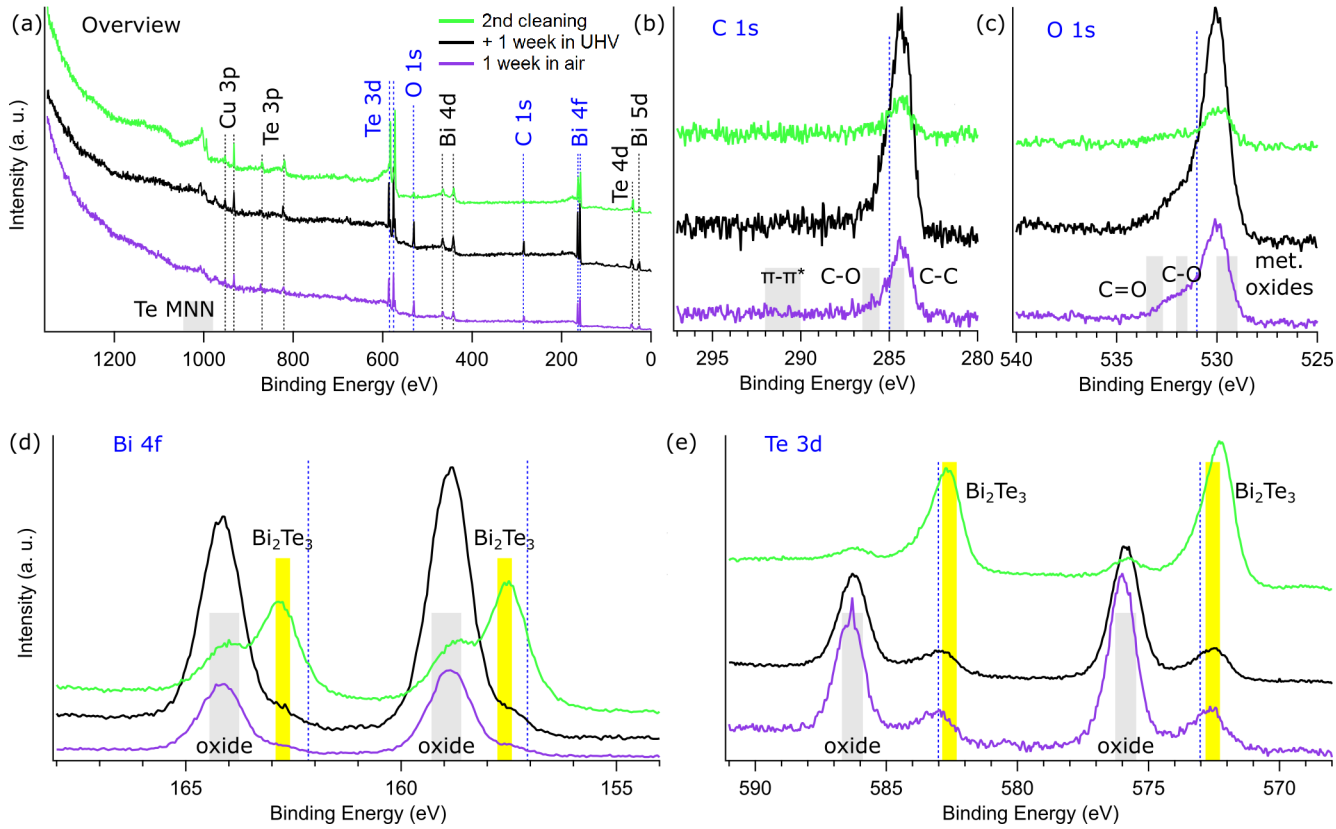

Figure 3.3.6: XPS spectra for sample A after the second measurement. The sample was measured, after one week in air (purple) after one month in UHV (black) and after two times Ar sputtering (500 V, 10 mA for 30 min) (green): (a) overview spectrum and (b) C 1s, (c) O 1s, (d) Bi 4f and (e) Te 3d core levels.

The XPS spectra for sample (B) and the third measurement series are presented in figure 3.3.7. After keeping the sample for one week in dichloromethane, the sample was stored in the UHV chamber for one month together with the previous sample (A). In this part of the experiment possible chemical changes and contaminations due to the storage of the nanowires in dichloromethane were investigated (see section 2.4). XPS spectra were recorded on the as prepared sample (cyan) and after two subsequent cleaning cycles (500 V, 10 mA) for 15 min each (dark blue and blue). As before, Bi, Te, O, C, Al and Cu are identified in the overview spectra (a). After the Ar cleaning the O 1s and C 1s photoelectron lines are visibly reduced.

Figures 3.3.7 (b) and (c) indicate an intensity reduction by about half after the first cleaning cycle followed by almost no further improvement during the second cycle. This was also observed for the previous sample. On the contrary, the difference of the chemical structure of the surface after each cleaning step is more evident for the Bi 4f and Te 3d lines in (d) and (e), respectively. The two doublets and their corresponding oxide peaks are identified. For the as prepared spectra the oxide peaks are dominating for both Bi and Te. After the first cleaning step, the oxide is partly removed resulting in an increase of the metallic photolines, an effect that is more pronounced for Te. After the second sputtering cycle, the oxide peak of Bi is still observable as a peak.

The same behavior is visible for the Te and its oxide which is only slightly further reduced. Compared to

the sample that was not kept in dichloromethane for one week the cleaning rate appears to be lower for sample (B). One explanation could be the additional probability of forming compounds with Cl such as BiOCl and $TeCl_4$ resulting in signals at around 159.9 [174, 175] and 576.9 eV [176] and contributing to the oxide peak.

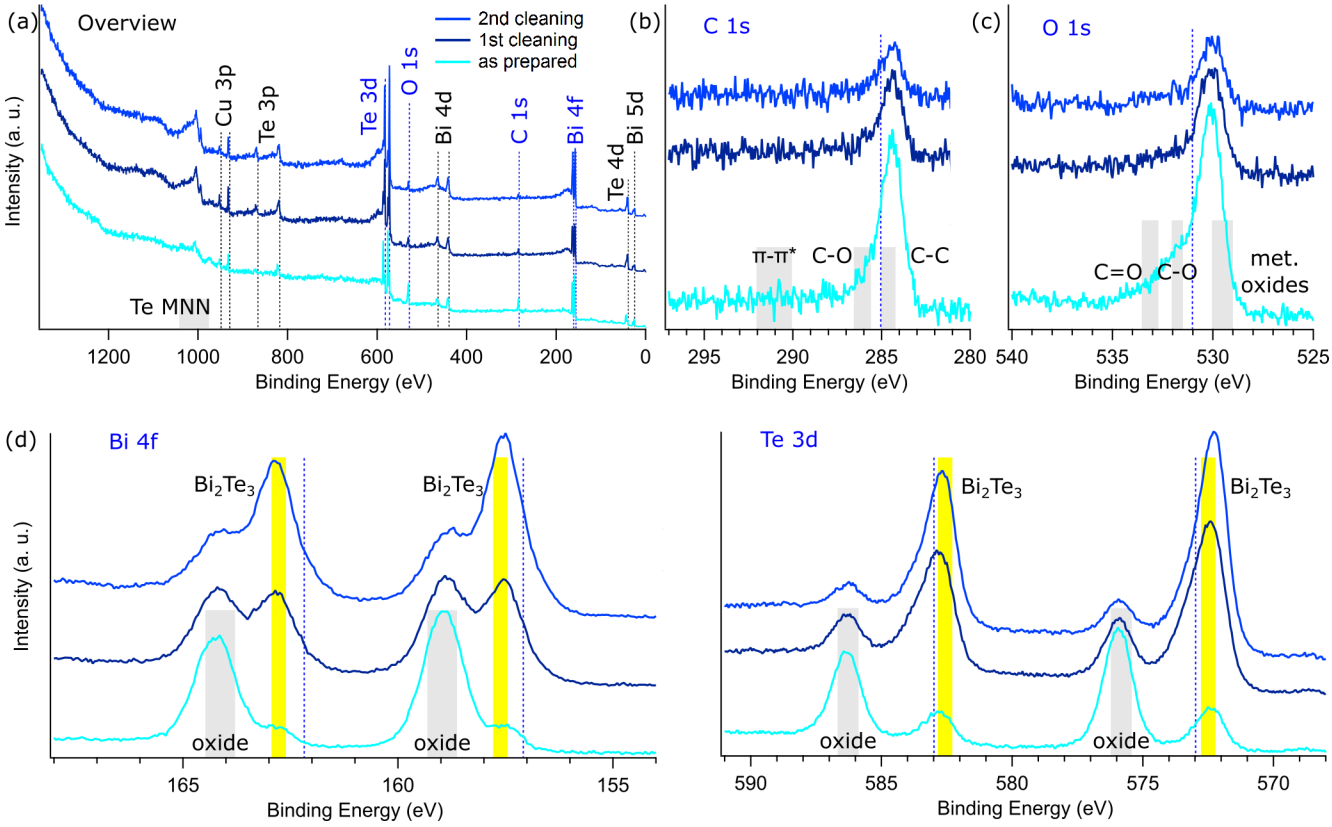

Figure 3.3.7: XPS spectra for sample B after the third measurement. The sample was measured as prepared (cyan) and after two times Ar sputtering (500 V, 10 mA for 15 min) (dark blue and blue): (a) overview spectrum and (b) C 1s, (c) O 1s, (d) Bi 4f and (e) Te 3d core levels.

To get a better understanding of the formation of chlorides, a close-up scan of the Cl 2p peaks was performed as prepared and after the two cleaning cycles. In Figure 3.3.8 the signals at binding energies of 197.7 and 199.4 eV are identified corresponding to the Cl 2p5/2 and Cl 2p3/2 doublet.

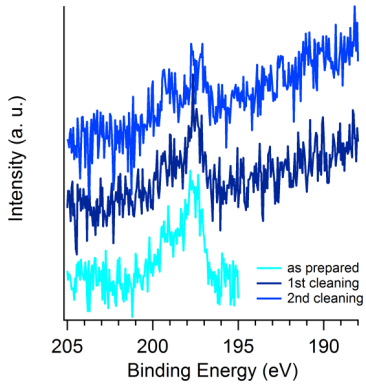

Figure 3.3.8: XPS spectra of the Cl 2p photoline for sample B after the third measurement.

In the same spectra obtained for sample (A) such signals were not detected. As expected from the results shown in figure 3.3.7, the Cl 2p photoelectron lines are clearly reduced after Ar plasma sputtering. Nevertheless, the signal is still visible after the second cleaning step, indicating together with the results from figure 3.3.7 (d) and (e) that further cleaning is needed to remove oxide and chloride contaminants. Figure 3.3.9 summarizes the results for sample (A) before (red) and after being exposed to air for one week (green) as well as for sample (B) (blue). The spectra are the ones measured after a total of 30 min of Ar sputter cleaning at 500 V and 10 mA extracted from figures 3.3.5-3.3.7. The C 1s and O 1s signals are reduced the most for sample (A) compared to its background. On the other hand, the oxygen signal for sample (A) exhibits still different chemical states indicating more carbonates. This could be a hint that the removal of organic polymer membranes is more efficient after storing the sample for one week in dichloromethane. The most important spectra are the ones comparing the three measurements for the Bi 4f and Te 3d doublets. In all three cases the oxide was visibly reduced after the sputtering steps. Nevertheless figures 3.3.9 (d) and (e) show that in direct comparison of the ratios, the freshly prepared sample (A) (red) exhibits the least amount of oxide. Only in this case the oxide peak is suppressed to a slight shoulder. From this follows that to obtain very clean Bi_2Te_3 nanowire surfaces the sample should be prepared freshly and long exposures to air or organic solvants should be avoided. Ar plasma sputtering is an efficient method to remove contaminants such as polymer residues and oxide compounds. On the other hand the destructive cleaning method might influence the surface structure.

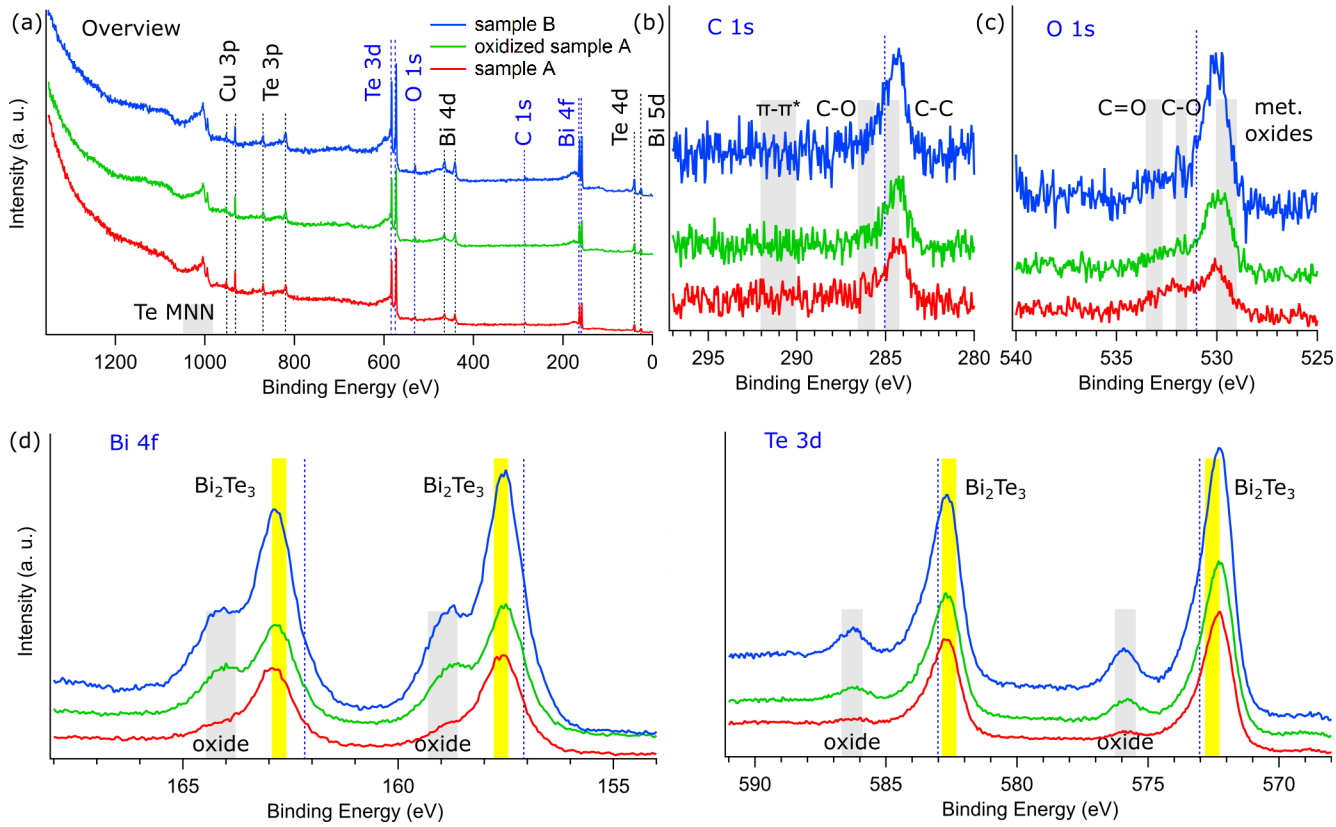

Figure 3.3.9: Summary of XPS spectra for sample A before (red) and after exposure to air for one week (green) as well as for sample B (blue): (a) overview spectrum and (b) C 1s, (c) O 1s, (d) Bi 4f and (e) Te 3d core levels.

3.4 Thermal stability

Annealing experiments were undertaken in order to explore, if the single Bi_2Te_3 nanowires are morphologically and chemically stable at elevated temperatures. This is crucial to know, firstly, for the sample preparation for surface sensitive measuring techniques such as XPS and ARPES usually involving an optimized surface cleaning procedure consisting of sputtering and annealing. Secondly, many nano-engineering processes involve the nanowires to be exposed to high temperatures. For instance, implementing single nanowires into electrical devices by lithography and atomic layer deposition, requires temperatures of around 100°C. Furthermore, nanowires are significantly heated by the Joule effect when an electrical current is applied. Hence, exploring the thermal stability of Bi_2Te_3 nanowires enables an evaluation of their performance within nanoscale electrical devices.
Previous works on annealing of Bi_2Te_3 nanowires were motivated by the optimization of nanostructures for thermoelectric applications. For this reason the concentration, crystal structure as well as the chemical stability were explored for Bi_2Te_3 nanowires electrodeposited in alumina membranes [113, 170–172] and grown by VLS techniques [105]. Annealing temperatures typically range from 150°C to 450°C for several hours up to 100 h. As the annealing temperature is increased, the Bi_2Te_3 composition changes to the Bi_4Te_3 phase due to the high vapor pressure of Te and its favored sublimation [171]. Especially, above 400°C no stable Bi_2Te_3 phase was found due to the melting of Te and subsequent forming of Te-rich sections of the nanowire. The maximum temperature for chemically stable nanowires of 50 nm diameter was found to be 350°C [172]. The reported changes of the crystal structure are not as evident. Annealing non-stoichiometric VLS grown Bi-Te nanowires (e.g. Bi_4Te_5, Bi_6Te_7, BiTe) with few 1000 nm^2 rectangular cross section for 100 h at 250°C in Te atmosphere resulted in single-crystalline Bi_2Te_3 nanowires [105]. For electrodeposited wires with 25 nm diameter annealed for 3 h at 400°C a small change in crystal orientation was observed, while the grain structure was not visibly altered [113].
The aim of this experimental studies was to answer the two following questions.

1. Under which temperature and size conditions do the nanowires become unstable?
2. How do morphological and structural changes occur?

Generally, the melting point for nanostructures of size d smaller than a critical size, drops below that of the corresponding bulk material. Modeling the melting temperature for metals as a function of size[3] resulted in $d < 10$ nm for nanoparticles and $d < 5$ nm for nanostructures (such as wires) [177]. However, the decrease for nanowires turned out to be stronger than for thin films and weaker than for nanoparticles [178]. This melting point depression is explained as a direct consequence of the high surface-to-volume ratio. Atoms binding on the surface exhibit less cohesive energy as the ones binding in the bulk, due to the reduced amount of neighboring atoms. The Lindemann's criterion describes the direct proportionality of the melting temperature to the cohesive energy [179, 180].
Nevertheless, a second effect influencing the thermal stability of nanostructures becomes already important at larger sizes than d and is therefor much more likely to occur for the present wire samples. At diameters above 10 nm, metallic nanowires exhibit Rayleigh instability. This results in the fragmentation of the wires into a chain of nanospheres.

[3] The size refers here to a length scale in one direction and is independent of the dimension.

In order to answer the questions above the nanowires were heated under UHV conditions inside a TEM (EM 912 Omega, Carl Zeiss) at the StEM and observed as the temperature was gradually increased. The wires yielded diameters of 50 and 150 nm and suspended in dichloromethane at GSI (see section 2.4). Four days later, three samples (1-3) were prepared by transferring the Bi_2Te_3 nanowires from the suspension to Si_3N_4 TEM grids. The time between the preparation of the nanowire samples and the actual measurements differed as the following table 3.4.1 indicates:

Table 3.4.1: Schedule of annealing experiments performed on nanowires of different diameters. The wires were transferred to the TEM grids four days after their synthesis.

Sample number	Diameter (nm)	Measurement time after wire transfer (days)
1	50 ± 5	1
2	150 ± 5	8
3	50 ± 5	15

Figure 3.4.1 displays a consecutive series of TEM images of originally 50 nm wide Bi_2Te_3 nanowires of sample 1 heated from 50°C to 360°C within about 105 min. Initially, the sample was heated until 300°C in steps of 20°C within 63 min yielding an average waiting time of about 3 min at each temperature step. Above 300°C this average waiting time per set temperate (20°C steps) was increased to about 15 min. The recording of all images in figure 3.4.1 during this waiting time is added in minutes after the start of the annealing experiments (top left).

Up to 300°C, the annealing did not cause any morphological or geometrical changes of the nanowires. At 300°C, some of the nanowires start to become thinner in certain spots (yellow circles). Further temperature increase results in fragmentation of the continuous wire into smaller sections. At the same time a shell- or tube-like structure becomes visible connecting the nanowire segments. Subsequently, the gap between the fragmented wire enlarges by about 100 to 200 nm. After several minutes of waiting time at a specific temperature this process stops, hinting an equilibrium state. While heating the sample further, the wire morphology is disturbed at a second location undergoing the same process (yellow circle). Interestingly, the fragmentation seems to be erratic and does not exclusively occur at prominent locations such as wire tips or dents. As the temperature is further increased, more and more material disappears leaving discontinuous, fragmented nanowire sections. The tips of the wire fragments are usually sharp and either perpendicular to the nanowire axis or in a defined angle. The tube-like structure remains stable throughout the entire annealing experiment. These observations are confirmed for all nanowires of samples 1 to 3.

For thicker nanowires (sample 2) theses structural changes start to occur at slightly higher temperatures (325°C) and the overall evolution is slower. In this case the nanowires were heated up to 475°C without significant material losses. Before annealing, sample 3 was exposed to ambient conditions for about one week, leading to the formation of a closed oxide layer (see section 3.3.2). The temperature at which structural changes occurred was 350°C and thus also slightly higher than for sample 1. To provide evidence for a correlation between a critical annealing temperature and wire diameter or storage conditions, the following analysis focused on sample 1. The distinct shape of the tips of the wire fragments reminds of the shape of grain boundaries as observed in section 3.2.2 figure 3.2.4. An actual resemblance has to be confirmed, e.g. by HRTEM investigations or imaging the annealing process in the darkfield mode of the TEM.

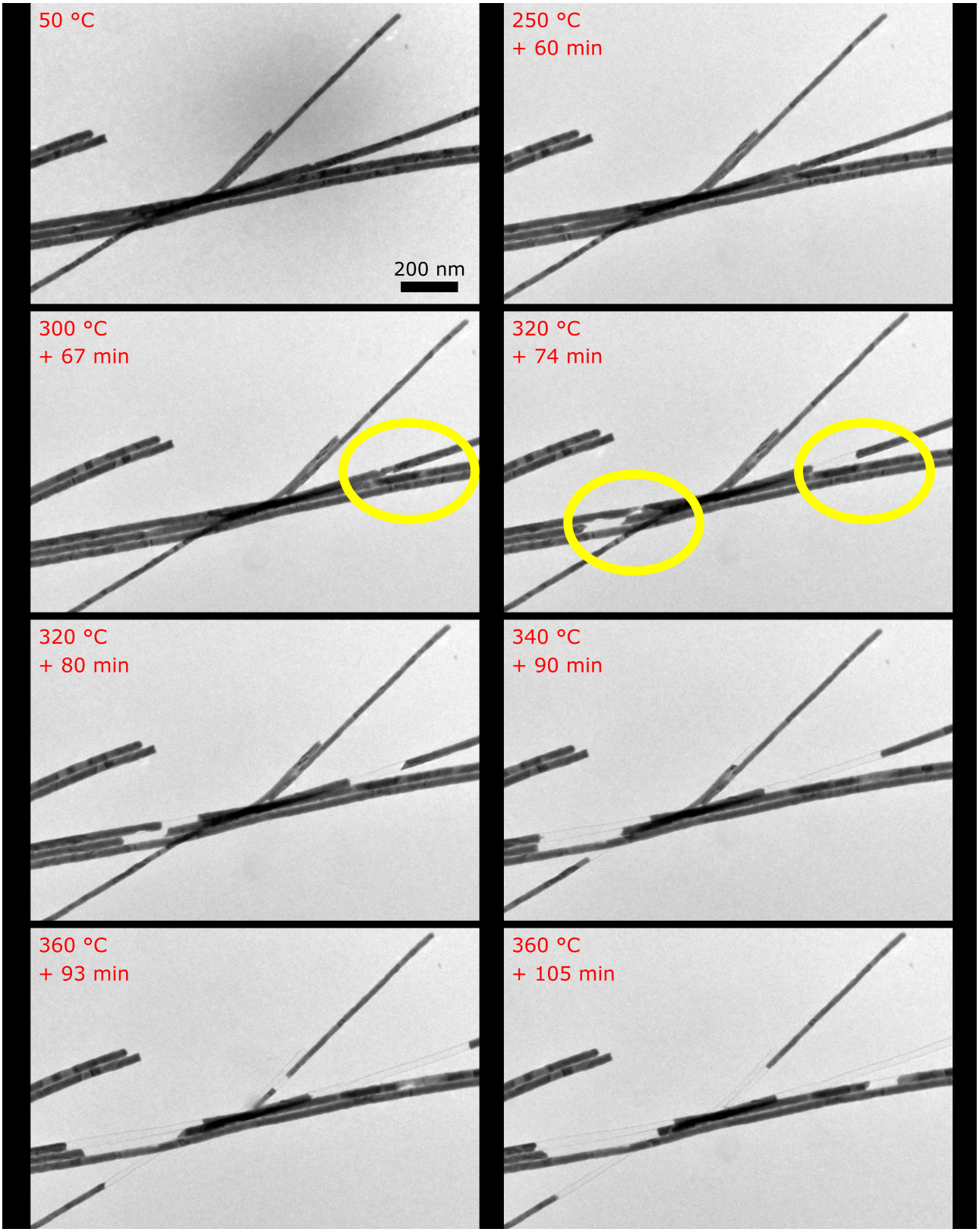

Figure 3.4.1: TEM images of an annealing series of Bi_2Te_3 nanowires with 50 nm diameter on a Si_3N_4 TEM grid (sample 1). The temperature is increased from 50°C (top left) to 360°C (bottom right). The indicated time refers to the elapsed number of minutes after the start of the annealing procedure. The yellow circles mark the beginning of the nanowire fragmentation.

Besides the conversion of the wires from a continuous to a intermittent geometry, the morphology does not exhibit any protuberances, at least not within the resolution of the recorded image as found in [181] for $Bi_{1-x}Sb_x$ nanowires. Annealing experiments performed with 50 nm diameter Bi_2Te_3 nanowires electrodeposited in alumina do not report on any observation of nanowire decomposition or discontinuous geometry until at least 400°C for up to 4 h [113, 170–172]. Instead, it was concordantly reported, that a Te-rich Bi-Te phase coexists with the stoichiometric Bi_2Te_3 phase manifested by the appearance of pure Te crystallites after exposition to temperatures of 300°C for 4 h independent of the atmosphere [170, 171]. Within the limits of the present study, pure Te crystallites were not observed. Nevertheless, locally Te-rich areas close to the surface of the nanowires were found in as prepared nanowires at room temperature. These observations are discussed in section 3.3.1.

The discrepancy with the results presented in literature are probably ascribed to the real time observation within the TEM where during the annealing process the tube-like connection is formed between the wire sections. A similar phenomenon was previously observed for copper nanowires annealed at 600°C (well below the bulk melting temperature of Cu) while performing in-situ TEM during annealing. A carbon coating seems to be created by electron-beam induced graphitization of polymer residues remaining from the synthesis. This carbon tube serves as a stable confinement for the Cu mass transport. At the open ends of the carbon tubes facetted Cu nanoparticles are formed evidencing a diffusion-driven process [182]. The formation of an electron-beam induced carbon coating is also a possible explanation for the observed tube in figure 3.4.1. Such a scenario seems reasonable, because a polymer residue layer was clearly observed in XPS experiments presented in section 3.3.2. On the other hand, no Bi_2Te_3 nanoparticles formed at the open tube ends in the present case suggesting a different mechanism than presented for Cu wires [182].

To shed light on the questions where does the Bi_2Te_3 vanish and what material is the tube made of, figure 3.4.2 presents HRTEM images obtained from two different fragment tips (a, b) and (c, d) in various magnifications.

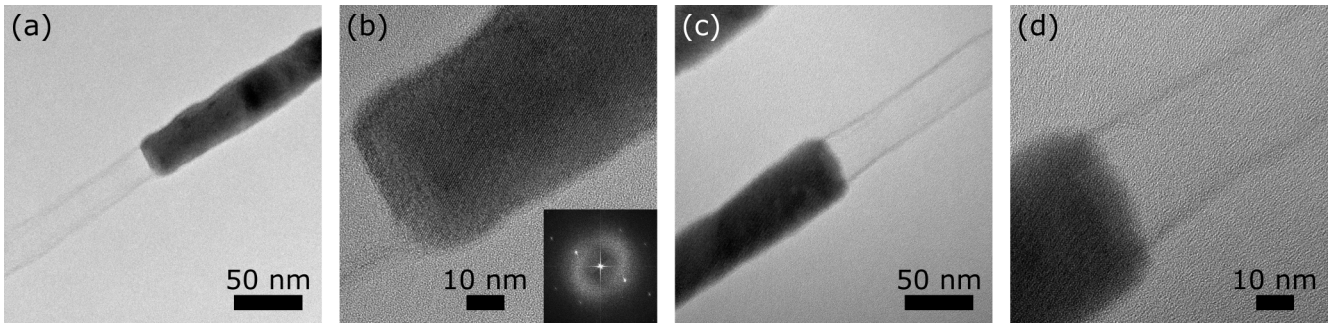

Figure 3.4.2: HRTEM images of two different tips of wire fragments (a,b) and (c,d) after annealing of the 50 nm diameter nanowires to 350°C. The insert in (b) shows the FFT obtained from the visible nanowire section.

The nanowire and the remaining shell are clearly visible. The shell diameter is about 10 nm smaller than that of the Bi_2Te_3 nanowire. The insert in (b) displays the fast Fourier transform of the visible nanowire section exhibiting a regular crystal structure over its complete area. The diameter difference between the wire and the tube can originate either from a swelling of the nanowire section or a shrinking of the tube. Assuming a swelling the diameter increase might be explained by the distribution of the lacking

Bi_2Te_3 material into the adjacent section of the nanowire. In this case, a diameter gradient would be expected along the remaining nanowire, which was not noticed.
Figure 3.4.3 shows TEM images of regions on sample 1 (a-c) and sample 3 (d) at 70°C (a) and around 350°C (b-d) confirming that no nanoparticles are formed at the ends of the original wires. Surprisingly, a difference between the diameters of the tube and the nanowires is not visible in this imaging mode.The green arrows in figure 3.4.3 (a,b) indicate the tip of a particular nanowire. As the temperature is increased, the nanowire is disturbed (see figure 3.4.1 second row, third column) and finally the upper nanowire section vanishes completely. It can be speculated that the material is sublimating. figure 3.4.3 (c) and (d) display two more sections of nanowires that are close to the nanowire end, showing no clear indication that the material is transported in the one or the other direction. For example, if half the volume of the gap in figure 3.4.3 (d) diffuses into the lower segment, its diameter should increase by about 10 nm.

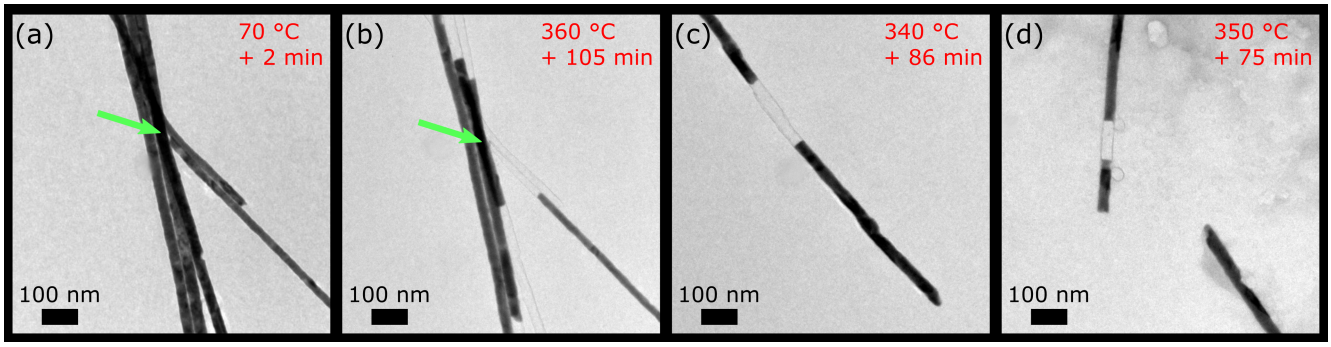

Figure 3.4.3: TEM images of nanowire sections close to the wire tip for sample 1 at 70°C (a), 360°C (b) and 340°C (c) as well as of sample 3 at 350°C.

Finally, EDX linescans were performed in order to clarify the composition of the nanowire sections and the tube close to the separation points. Figure 3.4.4 displays three representative EDX linesscans investigating the atomic percentage of Bi and Te on two different nanowire sections of the sample 1 (a) and (b, c). Each linescan contains 50 points. Following the data treatment described in section 3.3.1, points with less than 100 counts were omitted. The linescans were recorded parallel (a, b) and perpendicular (c) to a separation border. Generally, a deviation from stoichiometric Bi_2Te_3 to a more BiTe composition is detected consistently along the distance of the linescan. In figure 3.4.4 (b), a more stoichiometric composition might be visible at the nanowire edge, analogous to the Te enrichment found for some wires in section 3.3.1.
Furthermore, no trace of Bi or Te was detected outside of the wire or inside the tube as observable in figure 3.4.4 (c). Compared to the nanowires investigated in the previous sections, the change of the chemical composition is in agreement with the observed outgassing of Te [171]. Nevertheless it is worth pointing out, that the nanowires presented in section 3.3.1 and here are synthesized in the same way, but they are not from the same batch. In order to quantify the chemical composition variations during the annealing, the EDX linescans are required to be repeated at different temperatures. In the present case, this measurement could not be performed, because two separate TEM instruments had to be used for annealing and EDX analysis.
The chemical composition of the tube and the nanowire section are compared on figure 3.4.5 presenting EDX mappings of the wire and the tube (a) for Bi, Te, C and O (b-e). Besides these elements small

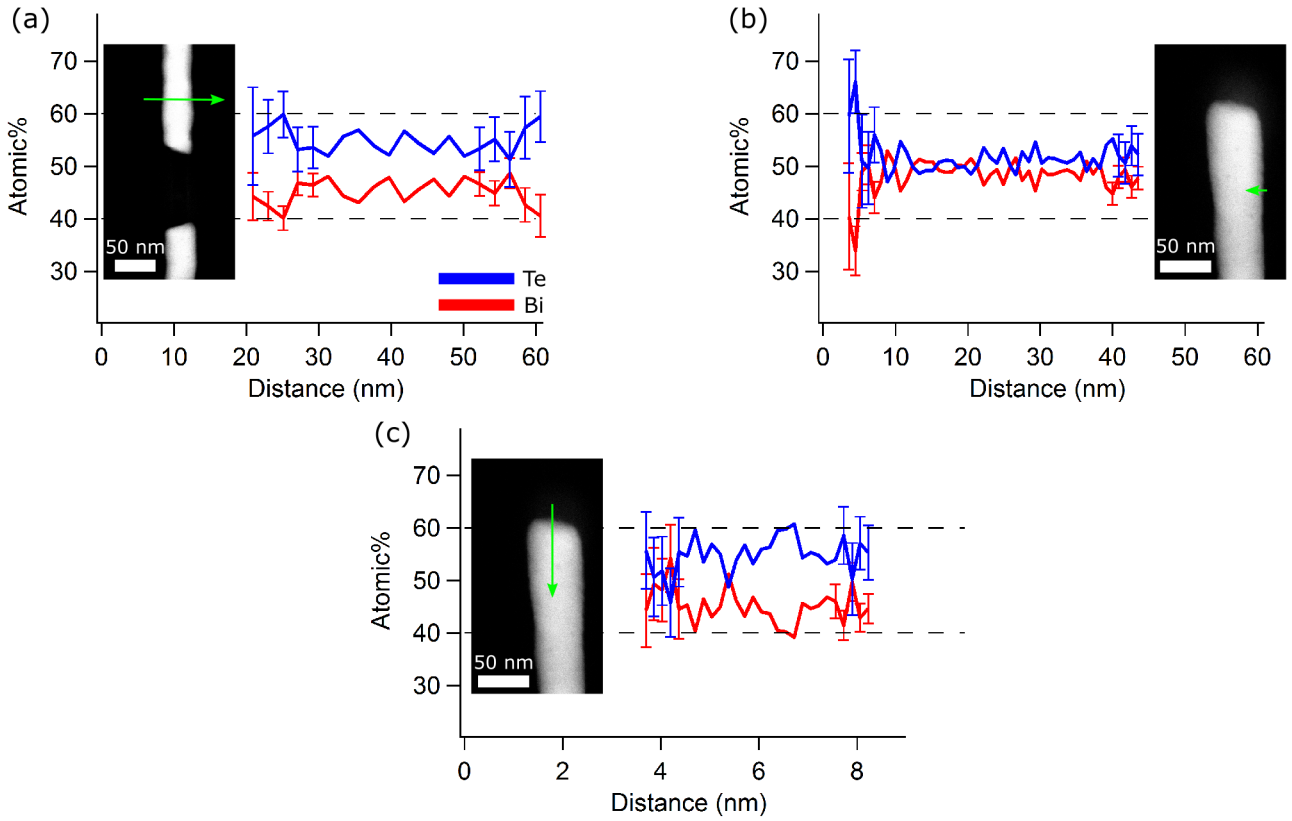

Figure 3.4.4: EDX linescans of three different locations on sample 1 measured perpendicular (a,b) and parallel (c) to the nanowire axis close to a wire fragment tip. The nanowires exhibit a homogeneous chemical composition differing from stoichiometric Bi_2Te_3 to BiTe.

traces of gold and calcium were detected inside the nanowire (Au, Ca) and in the tube (Ca). During the deposition process, traces of Au can possibly originate from diffusion of Au atoms from the working electrode into the wire, although this has not been found using any of the previous characterization methods. The origin of small Ca traces remains unknown and has to be verified. The element mappings give rise to a more complete analysis and confirm the findings of the previous EDX linescans. The Bi (b) and Te (c) content is clearly defined and limited to the area of the nanowire section confirming that the tube does not contain any of the two elements. The O distribution (e) is homogeneous within the wire area as expected from the XPS measurements in section 3.3.2. On the other hand, the oxygen content of the tube is not very well pronounced. The element mapping of the C content (d) shows impressively how conformal and homogeneous the tube entangles the nanowire. Moreover this result indicates that a residual polymer layer which is graphitized by the electron beam, forms homogeneously around the nanowire.

While the second question referring to the content and formation of the tube structure around the nanowire is explained, the exact mechanism of the nanowire separation remains speculative. Certainly, more systematic studies are necessary to clarify the question if the material is lost or where it vanishes to. One possible hypothesis to be tested is that the Te of Te-rich areas is lost due to its high vapor pressure. Considering EDX measurements during the annealing process, this question could answered.

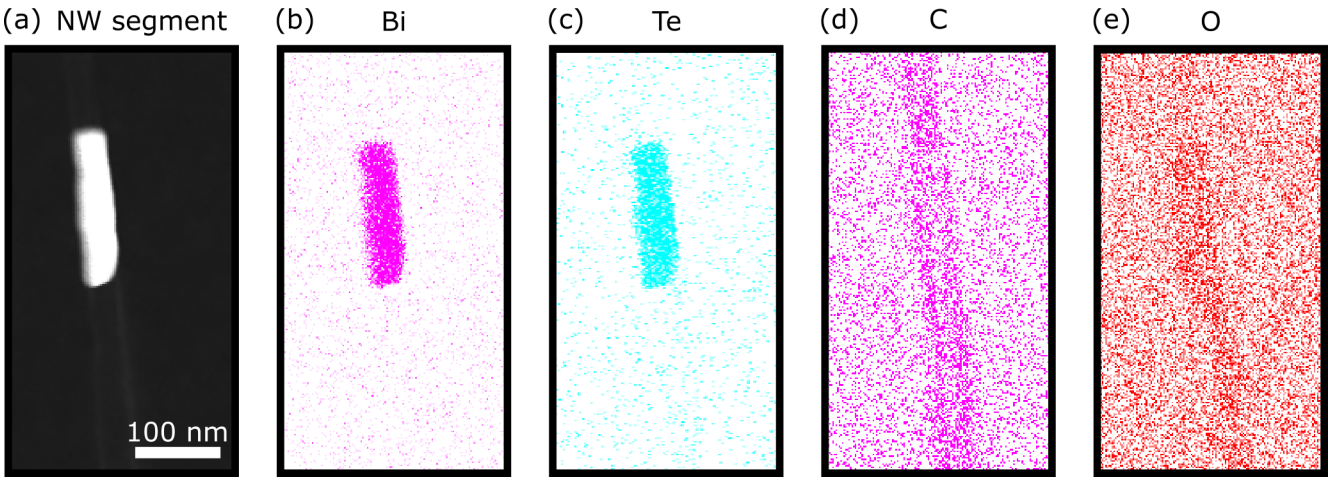

Figure 3.4.5: EDX element mappings of a nanowire section and a tube section (b) for elements Bi (b), Te (c), C (d) and O (e) confirming the carbon content of the tubular structure between the nanowire sections.

3.5 Conclusions of the Bi_2Te_3 nanowire characterization

In this chapter the Bi_2Te_3 nanowires were characterized according to their geometry, morphology, crystallographic structure and chemical composition by means of HRSEM, TEM, XRD, XPS and EDX. Nanowires released from the polymer template exhibit a smooth, round contour and only small surface roughnesses. They consist of single crystalline sections showing a highly textured average crystallographic orientation. For all investigated wire diameters, the preferential texture is the (205) planes perpendicular to the nanowire axis followed by the (101) planes. According to darkfield TEM investigations, single crystalline sections were observed revealing grain sizes up to a few hundred nanometers. The grain boundaries are found to be oriented mostly perpendicular or tilted by 45° with respect to the nanowire axis.
From EDX in TEM linescans a stoichiometric Bi_2Te_3 composition was deduced for individual nanowires. In some cases the surface of the nanowire is slightly enriched by Te. The XPS measurements conducted on nanowires distributed in a spaghetti-like arrangement on a silicon substrate revealed the importance to clean the nanowires by Ar sputtering in order to remove polymer residues and obtain an atomically clean surface. Additionally long exposures to ambient environment should be avoided to prevent oxidation.
The exposure of the nanowires to elevated temperatures by in-situ TEM experiments show thermally stable nanowires of 50 and 100 nm diameter below 300°C. As the temperature increases disturbances of the wire morphology are observed leading to a random fragmentation of some of the nanowires. The gaps between the wire segments increased with temperature. Furthermore a tube, which is confirmed by EDX to consist of carbon, remains to connect the sections. This tube is possibly created by electron beam-induced graphitization of polymer residues covering the as prepared nanowires as found in the XPS investigations. At which temperature the carbon tube is created and thus how it influences the wire fragmentations remains undetermined. The Bi_2Te_3 material from the gaps vanishes, possible by sublimation. Systematic measurements are necessary to reveal the underlying mechanism of the thermal stability under formation of the carbon tube.

In summary, Bi_2Te_3 nanowires with controlled geometry, chemical composition and crystallographic texture are fabricated, enabling investigations of the electronic properties and the topological insulator nature of Bi_2Te_3 as a function of these properties. Moreover, Ar sputter cleaning improves the surface cleanness and removes polymer residues remaining after the dissolution of the nanowire-embedding polycarbonate. Applying this method, very clean nanowire samples are prepared for nano-ARPES measurements and device fabrication. Elevated temperatures of up to 300°C are can be applied to the nanowires without any visible morphological changes or decomposition. Possible variations in the chemical compositions as a function of temperatures are still to be evaluated.

4 Nano-angle-resolved photoemission spectroscopy - nano-ARPES

Angle-**R**esolved **P**hoto**E**mission **S**pectroscopy (ARPES) is a powerful tool to directly visualize the electronic band structure of a given material. In ARPES experiments, the sample is exposed to x-ray radiation resulting in the emission of photoelectrons whose kinetic energy and emission angle are detected. The obtained information directly translates into the binding energy and momentum of the photoelectrons providing the electronic band structure. Moreover, ARPES carried out in spin-resolution mode gives direct information about the distribution of the electron spin orientation on the Fermi surface [183, 184]. In the case of topological insulators, the unique surface states located within the bulk insulating gap are directly observable. Actually, ARPES performed on Bi_2Te_3 and $Bi_{1-x}Sb_x$ thin films were one of the first experiments proofing the existence of topological insulators (see figure 1.1.6 in section 1.1.4) [66, 68–70]. Additionally, stoichiometric single crystalline Bi_2Te_3 thin films grown by molecular beam epitaxy have been investigated by ARPES in terms of their quality, thickness and underlying substrate[185, 186].
ARPES is usually performed on planar samples with a very high surface quality. Furthermore, the results are dependent on the crystallographic orientation of the sample which is crucial to be known. For this reason ARPES studies are usually conducted on single crystalline samples, mostly thin films.
So far, nano-size materials[1] have been unsuitable to be investigated by ARPES, due to the required high spatial resolution coming along with low photon and photoelectron intensities. In recent years, a nano-ARPES facility has been made available at the **A**nalysis **N**ano-spo**T** **A**ngle **R**esolved photo**E**mission **S**pectroscopy (ANTARES) beamline at the **S**ource **O**ptimisée de **L**umière d'**E**nergie **I**ntermédiare de **L**aboratoire d'utilisation du rayonnement électromagnétique (SOLEIL) Synchrotron in Gif-sur-Yvette, France [36]. This setup combines ARPES measurements at sub-micron resolution with imaging techniques recording the core levels with extremely high spatial resolution (several tens of nanometers).
In this work, nano-ARPES measurements were performed on individual Bi_2Te_3 nanowires of about 100 nm diameter prepared on a silicon wafer pursuing the goal to investigate their electronic band structure. These measurements are extremely challenging and a special protocol for the sample preparation had to be developed. Given the small x-ray beamspot of ~ 120 nm, the setup allowed for measurements on small sections along one single nanowire. Additional to the angle-resolved signals, the data was angle-integrated resulting in nano-XPS spectra providing high-resolution information on the chemical structure of the nanowire surface.
The following sections introduce and describe the nano-ARPES measurements conducted at the ANTARES beamline in collaboration with Dr. Maria Carmen Asensio, Dr. José Avila and Dr. Chaoyu Chen. Section 4.1 explains the basic principle of ARPES. While the setup is briefly described in section 4.2, section 4.3 focuses on the sample preparation including nanowire cleaning procedures and the nanowire identification on the silicon substrate by core level imaging. The nano-XPS as well as the final nano-ARPES results are presented in section 4.4. Finally, in section 4.5, first principle electronic band structure calculations for various crystallographic orientations are discussed and compared to the obtained nano-ARPES measurements. These calculations were contributed by Dr. Hongbin Zhang and Zeying

[1] The nano-size refers to more than one dimension, such as it is the case for nanoflakes and nanowires. In contrast, thin films with a macro-sized area and only a nano-size thickness are suitable for ARPES studies.

Zhang from the "Theory of magnetic materials" research group of the Technische Universität Darmstadt.

4.1 Basic principle of ARPES

ARPES is one of the many measuring techniques based on the photoelectric effect which are generally known under the term of **P**hoto**E**lectron **S**pectroscopy or equivalently **P**hoto**E**mission **S**pectroscopy (PES). First observed by H. Hertz [187], the photoelectic effect was fully described by A. Einstein [173] who got awarded the Nobel Prize in Physics (1921) for this work.
Photoemission describes the process of an incident photon transferring its energy to an electron, when hitting a sample. Absorbing the photon energy, the electron escapes the material when acquiring a maximal kinetic energy E_{kin} of

$$E_{kin} = h\nu - \Phi, \tag{4.1}$$

where h is Planck's constant, ν is the incident photon frequency and Φ denotes the work function specific to the material. In ARPES, the binding energy E_B of the electrons as well as the crystal momentum $\mathbf{k}$ and thus the electronic structure of the sample is determined by making use of energy and momentum conservation laws. A schematics of the measurement principle for ARPES is shown in figure 4.1.1 (a) for the exemplary case of measuring a single nanowire.

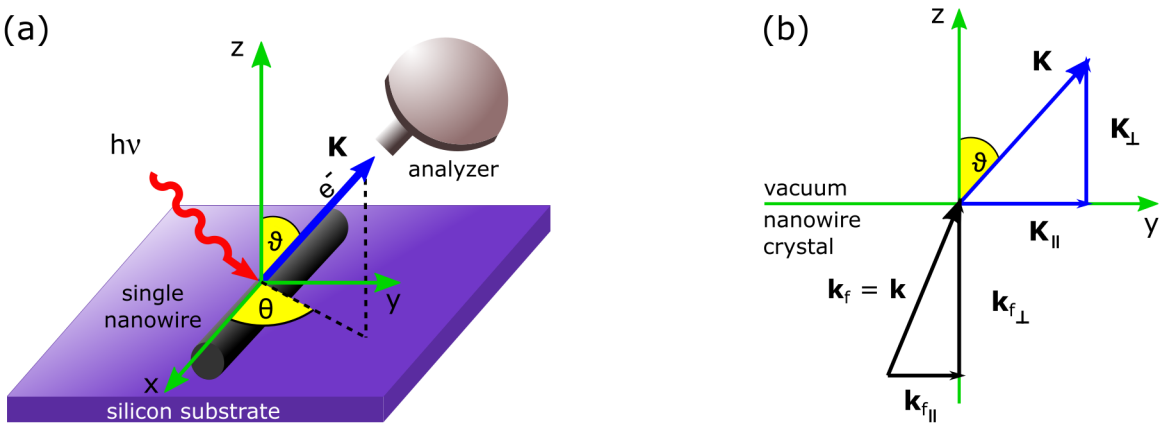

Figure 4.1.1: Basic principle of ARPES: (a) The incident photon $h\nu$ creates the emission of a photoelectron with momentum $\mathbf{K}$ under the angles θ and ϑ. (b) Components of the final crystal momentum $\mathbf{k}_f$ and the photoelectron momentum $\mathbf{K}$ as the electron transverses the (nanowire) crystal-vacuum interface. For photon energies below about 100 eV $\mathbf{k}_f = \mathbf{k}$ holds.

Typical light sources for ARPES are helium discharge lamps and UV-lasers within laboratory equipments or synchrotron radiation with incident photon energies typically around several 100 eV. The ejected photoelectrons are collected in an (multichannel) electron energy analyzer and their kinetic energy E_{kin} and emittance angles θ and ϑ are measured.
By combining these values, the momentum $\mathbf{K} = \mathbf{K}_{\parallel} + \mathbf{K}_{\perp} = \mathbf{p}/\hbar$ of the photoelectrons in vacuum is com-

pletely known. Its absolute value is determined by the kinetic energy of the electron $K = \sqrt{2mE_{kin}}/\hbar$, while its Cartesian components are described as a function of the polar and azimuthal emission angles:

$$K_x = \frac{\sqrt{2m_e E_{kin}}}{\hbar} \cdot \sin\vartheta \cos\theta, \tag{4.2}$$

$$K_y = \frac{\sqrt{2m_e E_{kin}}}{\hbar} \cdot \sin\vartheta \sin\theta, \tag{4.3}$$

$$K_z = \frac{\sqrt{2m_e E_{kin}}}{\hbar} \cdot \cos\vartheta. \tag{4.4}$$

In order to access the electronic band structure of the material, the E_{kin} and $\mathbf{K}$ values for the photoelectrons in vacuum have to be related to their counterparts within the material which are the binding energy E_B and the crystal momentum $\mathbf{k}$. Figure 4.1.1 (b) illustrates the interrelation of the two momenta $\mathbf{k}$ and $\mathbf{K}$ as the photoelectron transverses from the material into the vacuum.
Assuming the electron is not interacting with its environment and making use of the energy conservation law stating $E_i + h\nu = E_f$ with E_i and E_f being the incident and final energetic states of the electron, respectively, the kinetic energy is related to the binding energy of the material as follows.

$$E_{kin} = h\nu - \phi - E_B \tag{4.5}$$

The relation between the occupied energy states within the crystal, including core as well as valence band electronic states and the measured spectrum are sketched in figure 4.1.2. The work function Φ of the material corresponding to the minimal energy necessary to free an electron from the crystal, is equal to the energy barrier resulting from the difference between the Fermi level E_F and the vacuum level E_V (dashed red line). Typically this value amounts to 4-6 eV for a metallic sample. V_0 (dashed blue line) denotes a so called inner potential which will be explained later in this section.
The relation between the different momenta $\mathbf{k}$ and $\mathbf{K}$ is not as straightforward as for the energy relation. In that case it is convenient to consider the so called three step model in which the photoemission process is separately considered for (i) photo-absorption and excitation of the electron into its final electronic state within the sample, (ii) transport to the surface of the material and (iii) transmission of the electron into vacuum. As for step (i) the momentum conservation law is written as $\mathbf{k}_i + \mathbf{k}_{photon} = \mathbf{k}_f$ with $\mathbf{k}_i$ and $\mathbf{k}_f$ being the incident and final electron momenta within the material, respectively. For photon energies below 100 eV their momentum $\mathbf{k}_{photon}$ can be neglected, because it is much smaller then the typical Brillouin zone dimension $2\pi/a$ with a being the atomic distance within the crystal lattice. As a consequence, the momentum conservation law (figure 4.1.1 (b)) simplifies to

$$\mathbf{k}_i = \mathbf{k}_f = \mathbf{k}. \tag{4.6}$$

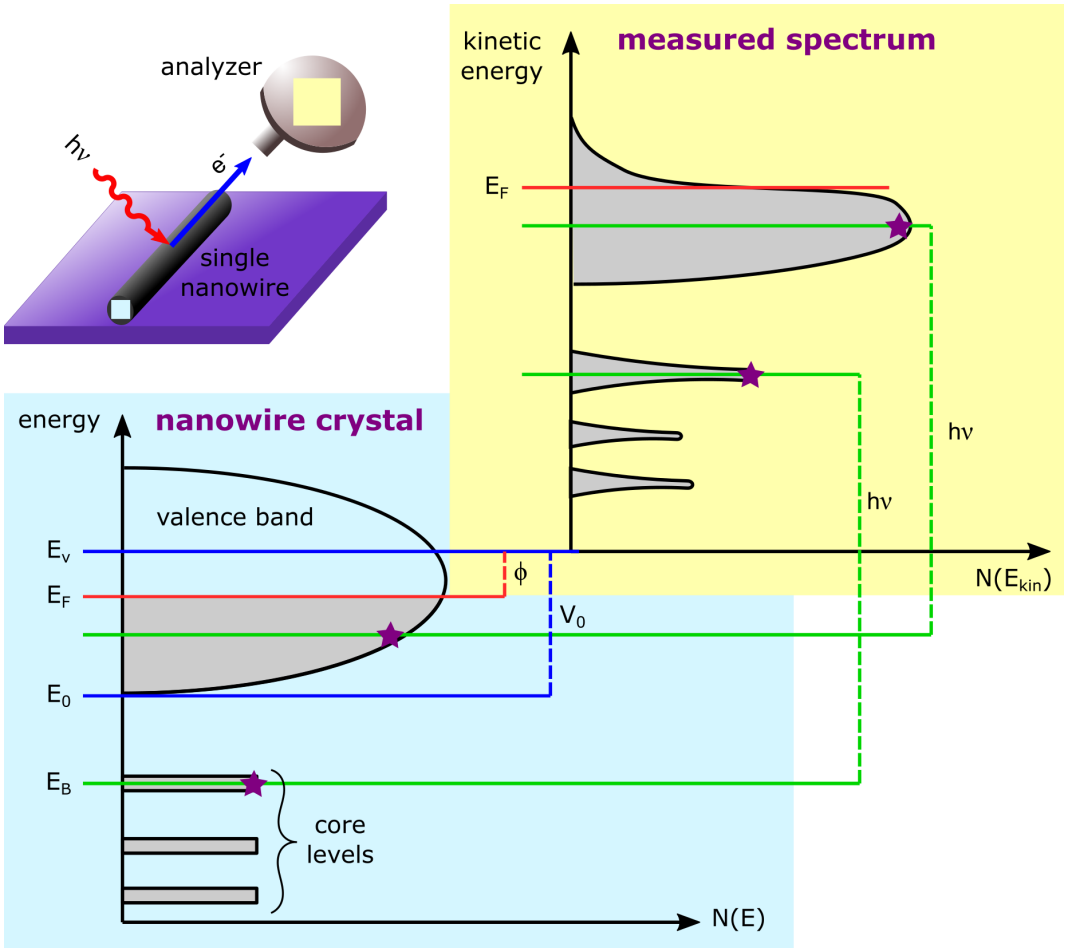

Figure 4.1.2: Schematic representation of the energy states of the nanowire crystal (blue box) and the corresponding photoelectron energy spectrum measured in the analyzer (yellow box). The vacuum level E_V, the bottom of the valence band E_0 (blue) and the Fermi level E_F (red) are identified. The green lines and purple stars indicate the relation between the kinetic energy E_{kin} measured and the binding energy E_B of the photoelectron in the crystal.

The crucial parameter to be considered in the second step (ii) is the inelastic mean free path of the photoelectrons within the sample. Possible trajectories of the electrons inside the sample are schematically depicted in figure 4.1.3 (a). Penetrating the sample, the photons excite photoelectrons as deep as several tens of nanometer (blue). On their way to the surface, the photoelectrons suffer from kinetic energy loss due to inelastic collisions. Electrons undergoing these scattering events are considered as secondary electrons that lost all their initial state information. In the ARPES spectra, they appear as a diffuse background, which increases towards lower kinetic energies (green). For E_{kin} below the energy of the surface barrier Φ the electron is not emitted from the material anymore (purple). For this reason PES is, in general, a very surface sensitive technique in need of an ultra high vacuum ($\approx 10^{-11}$ mbar) and good quality sample surfaces. Interestingly, the relation between the inelastic mean free path and the photon excitation energy seems to be somewhat universal and independent of the sample material especially when referenced to monolayers. A calculation of the "universal" curve as well as experimental data points are provided in figure 4.1.3 (b) [188]. At energies used in the ARPES investigations in the present work (mostly 100 eV), the inelastic mean free path for electrons in Bi amounts to about 0.5 nm [189].

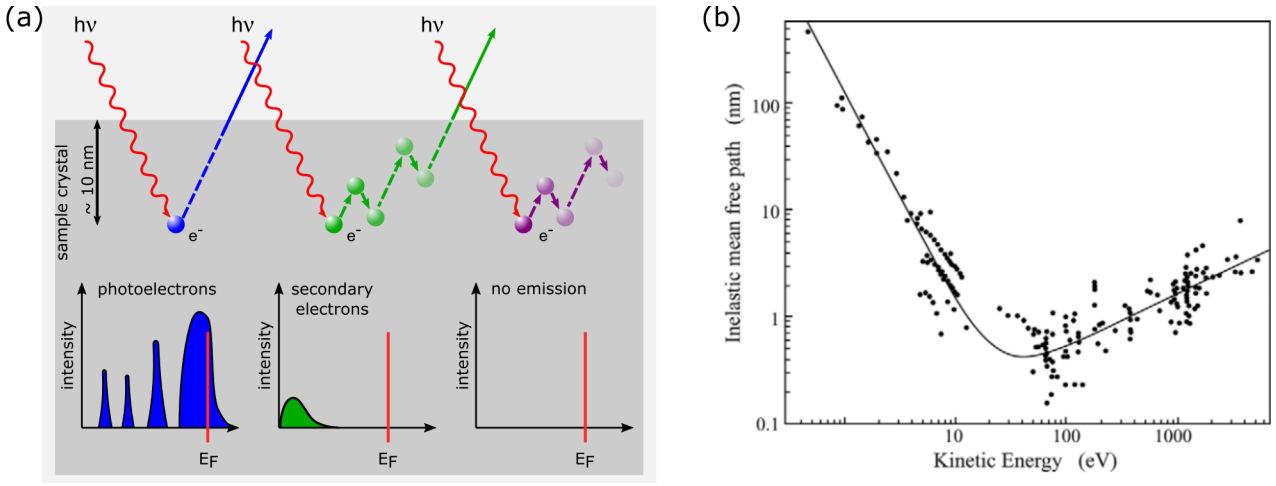

Figure 4.1.3: Transport of photoelectrons to the sample surface: (a) presents three possible trajectories of not scattered photoelectrons (blue), secondary electrons (green) and electrons not overcoming the surface barrier (purple). Additionally, their appearance in the measured spectra is shown. (b) the universal curve of the inelastic mean free path of the photoelectrons as a function of kinetic energy reprinted from [188] with permission from John Wiley & Sons, Inc.. For photon energies of 100 eV an inelastic mean free path of 0.5 nm is expected.

In step (iii) of describing the transmission of the photoelectron through the surface, the influence of the latter has to be carefully taken into account. Due to the translation symmetry in the x-y plane, the parallel component of the electron momentum is conserved and writes as follows

$$K_{\parallel} = k_{\parallel} = \frac{\sqrt{2mE_{kin}}}{\hbar} \cdot \sin\vartheta. \tag{4.7}$$

Because of the refraction at the crystal-vacuum interface due to a potential change, the perpendicular component of the momentum is not conserved ($\mathbf{k}_{\perp} \neq \mathbf{K}_{\perp}$). Besides applying very complex experimental methods, the perpendicular component can be determined by assuming a free-electron model in which the final Bloch states are

$$E_f(\mathbf{k}) = E_{kin} + \phi = \frac{\hbar^2\left(\mathbf{k}_{\parallel}{}^2 + \mathbf{k}_{\perp}{}^2\right)}{2m} - |\,E_0\,|, \tag{4.8}$$

with E_0 referenced to the bottom of the valence band. Substituting equation 4.7 eliminates the $\mathbf{k}_{\parallel}$ component in equation 4.8 resulting in the following expression for the vacuum $\mathbf{k}_{\perp}$:

$$k_{\perp} = \frac{\sqrt{2m}}{\hbar} \cdot \sqrt{E_{kin}\cos^2\vartheta + |\,E_0\,| + \phi} \tag{4.9}$$

with $|\,E_0\,| + \phi = V_0$ defining the inner potential. In order to finalize the three-dimensional electronic band structure the value of the inner potential has to be determined [190]. To do so, various strategies exist that go beyond the scope of this work.

4.2 Nano-ARPES experimental station at the ANTARES beamline

Storing electrons with energies of about 2.5 GeV under extremely stable conditions, the SOLEIL synchrotron delivers brilliant soft x-rays in the range between 10 to 1000 eV to the ANTARES beamline.
The structure of the experimental end-station is schematically and photographically presented in figure 4.2.1. ANTARES consists of four main chambers interconnected and kept under UHV conditions ($\sim 10^{-9}$ mbar). The insertion of the sample takes place at the fast entry chamber which can be vented and evacuated within about 30 min. Adjacently, the preparation chamber offers a variety of methods to improve and characterize the sample quality. Specifically in this work, the availability of an Ar sputter gun and a hot stage for annealing was applied. Multiple samples can be inserted and stored in the carousel within the storage chamber providing places for up to 36 samples. A sample ready for measurements is transfered to the high precision sample stage installed in the main chamber, where it is exposed to the x-ray beam. The beam properties and trajectory are described in more detail elsewhere [34, 36]. Outgoing photoelectrons are detected in the high energy and angular resolved Scienta R 4000 detector connected to the side of the main chamber.

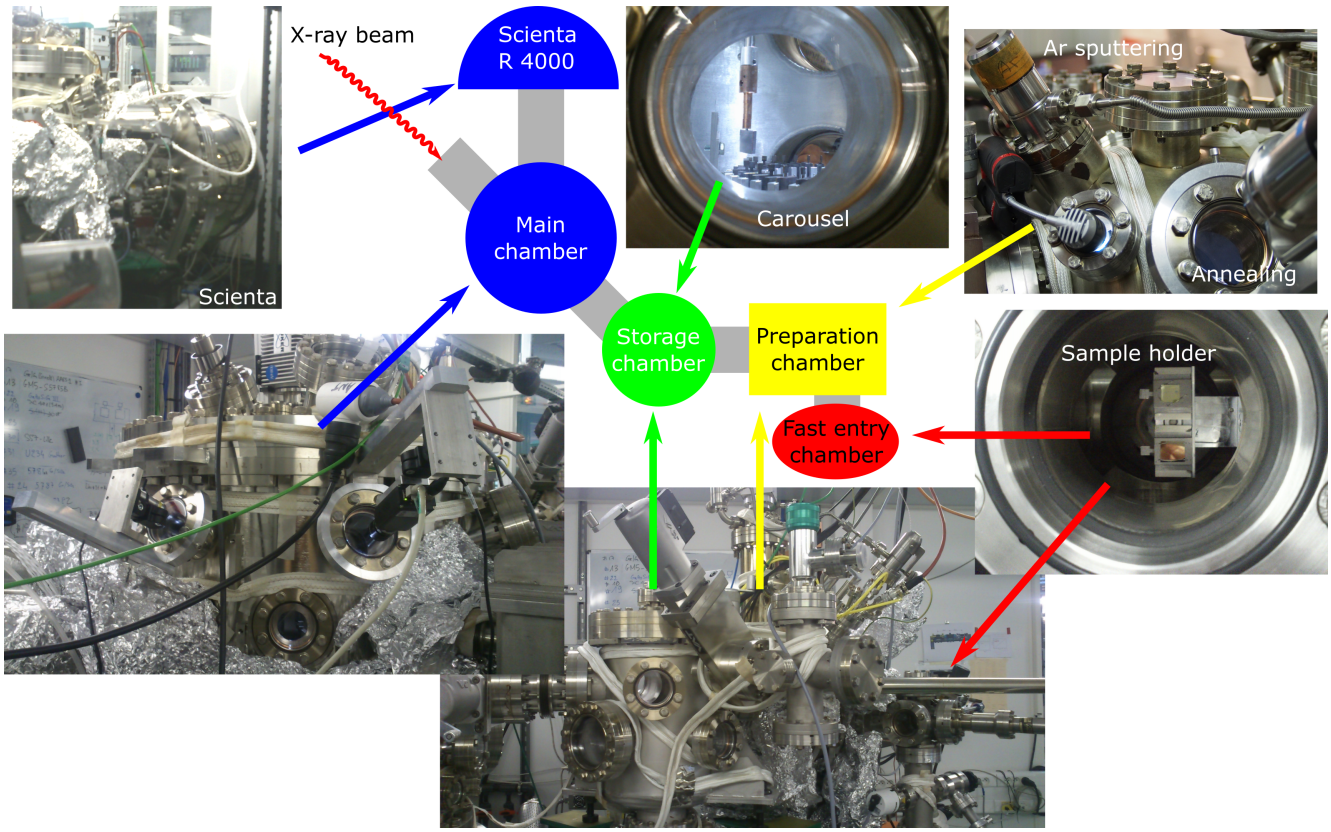

Figure 4.2.1: Layout of the experimental end-station of the ANTARES beamline consisting of four chambers: the fast entry chamber (red) for sample insertion, the preparation chamber (yellow) for sample cleaning, the storage chamber (green) and the main measurement chamber with the adjacent energy and angle analyzer Scienta R 4000 (blue).

Figure 4.2.2 illustrates the microscope layout inside the experimental main chamber in more detail. Different beamspot sized are available depending on the optics used. The macrofocus illuminates an area of several square micrometers obtaining a signal from the nanoobjects under investigation and the

substrate as indicated in (a). In order to obtain illumination or beam spots as small as a few tens of nanometers, high performance optics are required as schematically shown in (b). Within the experimental chamber, the optics arranged in series are a pinhole, a **F**resnel **Z**one **P**late (FZP) and an **O**rder **S**orting **A**perture (OSA) focusing the beam onto a sample stage that is movable with nanometer precision. The FZP focuses the synchrotron radiation to the desired spot size, while the OSA filters higher diffraction orders. The stage holding the sample is mounted exactly at the overlap of the focal points of the optics system and the Scienta detector. The overall spatial resolution of this microscope layout is thus determined by the interplay of the performance of the optics system and the mechanical stability of the nanometer precision stage limited by thermal drift and mechanical vibrations. Employing an interferometric control, these effects can be minimized to thermal vibrations lower than 0.1°C and to mechanical drifts of about 5 nm [35].

The ANTARES beamline offers two operation modes, namely spectroscopy and spectroscopic imaging, both compatible with various spot sizes down to a few tens of nanometers. In this work, spectroscopic imaging was used to identify sections of nanowires to be measured in the spectroscopy mode focusing the photon beam to about 120 nm. Additionally, the spectroscopy mode was employed with larger beam spots in the micrometer range to evaluate the sample quality.

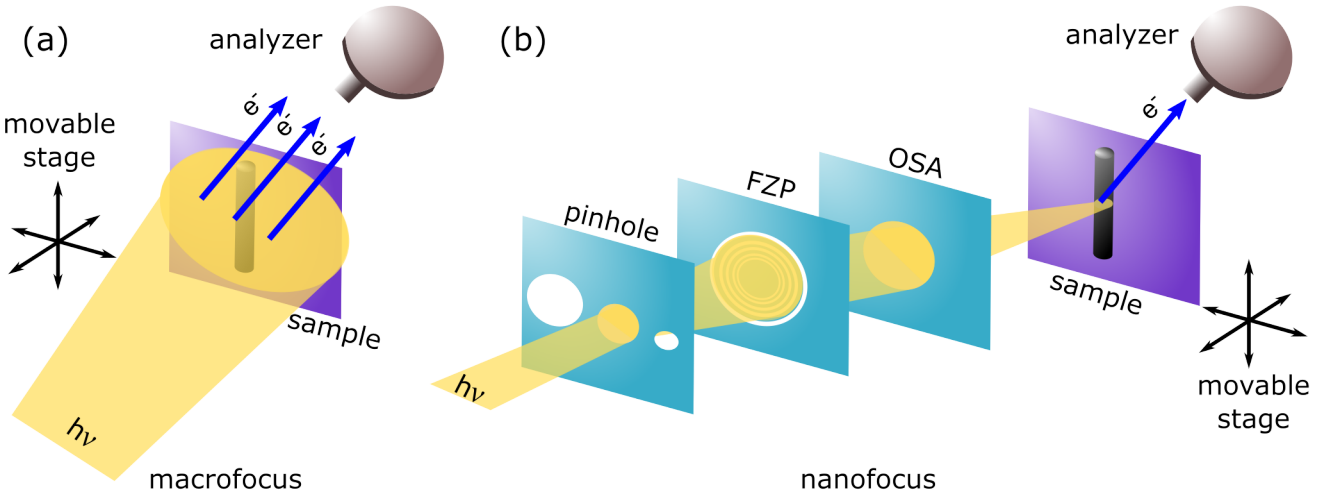

Figure 4.2.2: Schematic setup of the microscope layout inside the main experimental chamber of the ANTARES beamline. In comparison to the macrofocus (a), the nanofocus is obtained by optimally adjusting the pinhole, the Fresnel Zone Plate (FZP) and the Order Sorting Aperture (OSA) focusing the beam onto the high precision sample stage.

4.3 Nanowire sample preparation and characterization

In general, surface-sensitive ARPES measurements necessitate an accurate sample preparation requiring contamination-free and chemically stable surfaces. Inert samples such as gold or graphene are usually prepared under ambient conditions, while the investigated topological insulators are not as inert and demand special treatment. The most common impurities of Bi-based topological insulator materials are oxygen forming oxides and water molecules adsorbed on the surface. To decrease the amount of impurities, a widely used approach is to already grow the sample under UHV conditions e.g. in an adjacent chamber dedicated to chemical vapor deposition or molecular beam epitaxy. Alternatively, samples possible to be exfoliated and synthesized in a different environment, such as large single-crystalline flakes grown perpendicular to the cleaving plane, are cleaved in a special preparation chamber. In both cases, the sample exhibiting a fresh and thus clean surface is transferred directly into the experimental chamber without breaking the UHV [191]. Additionally, a combination of soft argon sputtering and annealing is an established method to improve the surface quality of a given sample [191–194]. The sputtering is supposed to remove contaminants, while the subsequent annealing step heals out possibly induced defects in the crystal structure of the surface.
For investigating individual nanowires a suitable substrate is required. In the case of nano-ARPES measurements, the substrate has to be conductive to avoid charging effects, flat and not made of a material generating photoelectrons of the same or similar kinetic energies as the specimen under investigation. In general, the substrate should create a minimal and unambiguously defined background.
In this work single Bi_2Te_3 nanowires were synthesized under ambient conditions. The transfer process to a suitable substrate was conducted either under ambient conditions or within argon atmosphere. A combination of Ar sputter cleaning and low temperature annealing was employed to clean the samples. Section 4.3.1 describes the test experiments conducted at ANTARES and **DA**rmstädter **I**ntegriertes **SY**stem für **FUN**damentale Untersuchungen (DAISY FUN) resulting in the choice of the substrate and the nanowire cleaning protocol established for Bi_2Te_3 nanowires. Subsequently, the procedure employed to identify the nanowires on their substrate making use of the core level spectroscopic imaging is presented in section 4.3.2.

4.3.1 Choice of substrate

Different silicon-based substrates were prepared for nano-ARPES experiments. Table 4.3.1 gives an overview of the test samples which underwent various Ar sputtering and annealing cycles within an XPS setup that was used to evaluate the cleanness of the substrates. Two setups were employed, namely the ANTARES beamline in angle-integrated or XPS mode and the XPS setup available at the DAISY FUN Laboratory at the Technische Universität Darmstadt (see section 3.3.2).
Chronologically, the test results conducted at ANTARES brought about the decision for the substrate used for the nano-ARPES. The experiments at DAISY FUN were supposed to support and confirm the findings at ANTARES and to prepare for further nano-ARPES measurements explained in more detail in the outlook section 4.6. While the substrates with sample ID A1 and A2 were investigated after the

nanowires were transferred, substrates D3-D6 were analyzed also before adding nanowires.

Table 4.3.1: Different silicon-based substrates available for nano-ARPES measurements undergoing various pre-cleaning strategies.

Sample ID	Substrate	Coating	Pre-cleaning	Test setup
A1	Silicon	native oxide	48% HF	ANTARES
A2	Silicon	Pt/Au	acetone, isopropanol	ANTARES
D3	Silicon	native oxide	acetone, isopropanol	DAISY FUN
D4	Silicon	native oxide	5% HF	DAISY FUN
D5	Silicon	native oxide	5% HF, Piranha	DAISY FUN
D6	Si_3N_4			DAISY FUN

The bare silicon substrate A1 is a commercial boron p-doped wafer (Si-Mat Silicon Materials) only covered by its native oxide layer. Firstly, the silicon oxide layer was removed by dipping in **H**dro**F**luoric acid (HF) (48 %) and rinsing three times in deionized water. In this way, the wafer surface is free of oxygen residues and additionally terminated by hydrogen limiting further oxidation. In a second step, A1 was welded onto a tantalum holder and introduced into a glovebox kept under Ar atmosphere. Inside the glovebox, the nanowires were transferred onto the A1 substrate. In the last step, the sample was transported under Ar atmosphere into the experimental UHV chamber using a sealed transportation chamber.
Substrate A2 consists of the same kind of boron p-doped silicon wafer modified by adding a metallic coating. After a standard cleaning by ultrasonication in aceton (~ 10 min) and isopropanol (~ 10 min), the sample was sputtered with a few nanometer thick platinum layer (Cressington 108auto/SE) followed by a ~300 nm gold layer (Edwards sputter coater S150B). The intermediate Pt layer is necessary to enhance the adhesion of the gold to the silicon substrate. The nanowires were transferred onto the Si/Pt/Au substrate under ambient conditions at GSI and transported to ANTARES. The time of exposure to air was about one week. In both cases the nanowires were transferred using the drop-casting method described in section 2.4 followed by three baths of fresh dichloromethane for 5, 15 and 30 min, respectively.
After insertion through the fast entry chamber, the samples were directly passed to the main measurement chamber. For the evaluation of the cleanness of the substrate and its typical core level signature, a micrometer-size area of samples A1 and A2 was investigated by using ANTARES in angle-integrated, i.e. XPS mode. Without employing the pinhole and the OSA, the incident photon beam was defocused allowing for signals originating from a micrometer-size area of the samples.
Figure 4.3.1 presents XPS spectra recorded with 700 eV (left) and 100 eV (right) photon energy for each of the two samples. In order to also obtain a signal for Bi and Te, a part of the sample covered by a high density of nanowires was chosen. Figures 4.3.1 (a) and (b) were obtained for Bi_2Te_3 nanowires on the Si substrate (A1), while figures 4.3.1 (c) and (d) were recorded for nanowires on the Si/Pt/Au substrate (A2). The four most pronounced peaks measured for the silicon substrate (A1) within a 700 eV range are located at binding energies of about 531, 285, 150 and 99 eV and are identified as O 1s, C 1s, Si 2s and Si 2p photolines, respectively. The smaller peaks at 25-40 eV binding energies higher than the Si 1s and Si 2p core levels are assigned to the characteristic energy loss signal due to electron-electron loss or plasmons [174, 195]. The broad peak at approximately 437 eV coincides with the Bi 4d core level doublet expected at 440 and 464 eV. Possibly the doublet is superposed with its oxide peaks due to the low signal intensity obtained from the nanowire. On the other hand, photoelectron emittance for the Bi 4f core level exhibits the highest cross section and results in signals at 157 and 162 eV which are much more intense than the ones from Bi 4d. These core levels are not observable in the present spectrum meaning the intensity is either too low to be detected at all or hidden in the background dominated by the Si plasmon peaks. Consequently, the broad peak at about 437 eV has a different origin and hides the Bi 4d signal at most.
For tellurium, the 3d core level is expected to possess the highest cross section for photoemission and is located at 573 and 583 eV. Since no signal is detected at these energies for the present spectrum (a), it

can be concluded that the signal from the nanowires is too small to be observable using the micrometer-size beam spot combined with about 5 min recording time. The clear observations of oxygen and carbon also indicates a certain surface contamination covering the sample which might also screen signals from the nanowires. From previous investigations presented in section 3.3.2, it is known that the nanowires are contaminated by polymer residues from the template. In the present case, the surface contamination is a rather surprising finding considering that the silicon substrate representing most of the investigated sample area was pre-cleaned in HF. The oxygen contamination may possibly originate from the welding of the substrate onto the sample holder under ambient conditions. Keeping in mind that carbon contamination is omnipresent, exposure to ambient conditions and to dichloromethane has probably also increased the corresponding signal. In principle, a clean surface for obtaining good nano-ARPES results should exhibit a minimal carbon and oxygen contamination, best decreased to the point of being undetectable.

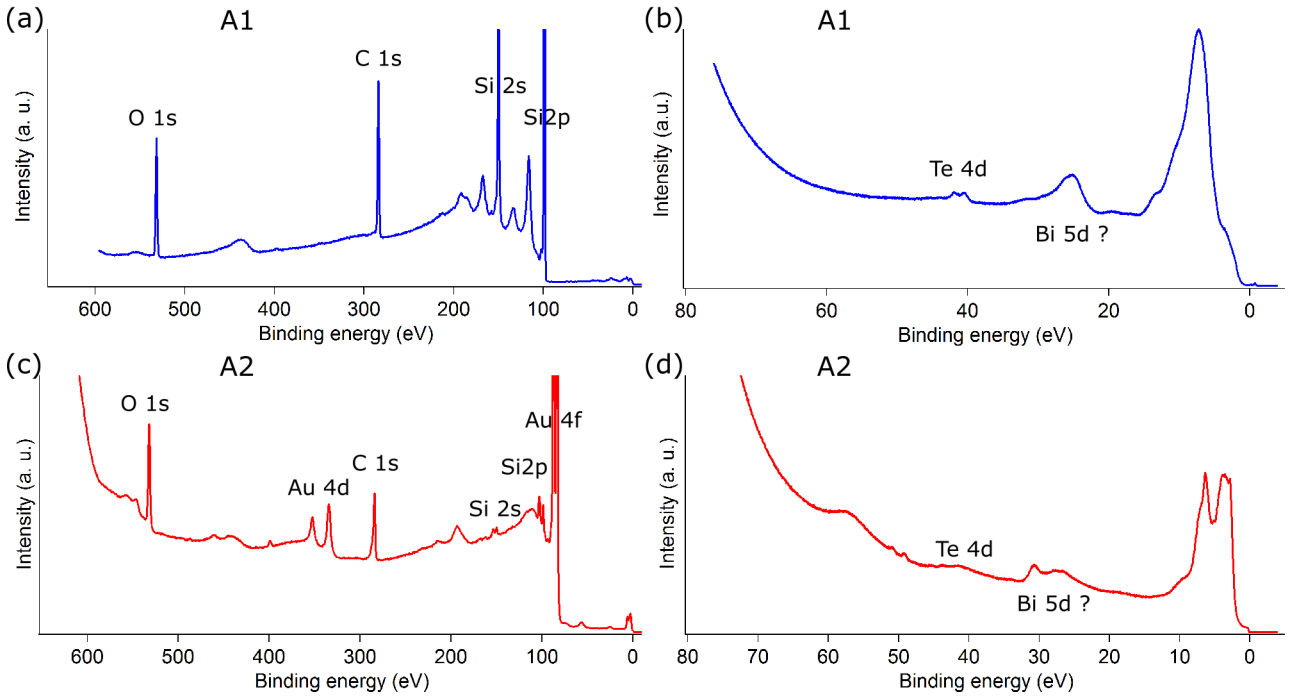

Figure 4.3.1: Core level spectra recorded in the angle-integrated (XPS) mode using a micrometer-size beamspot. (a, b) are 700 and 100 eV spectra recorded from sample A1. (c, d) are 700 and 100 eV spectra measured on A2.

Figure 4.3.1 (b) displays the core level spectra recorded from the same area of the sample adjusting the photon energy to 100 eV. Three features are identified, namely an intense and broad peak at around 7 eV, a less pronounced broad peak at approximately 26 eV and a small doublet at around 40 eV. The doublet can be assigned to the Te 4d core level (41.6 and 39.9 eV), while a Bi 5d signal is expected at 27.7 and 24.7 eV binding energies coinciding with the broad peak found in the spectrum [196–198]. A more detailed analysis on the Bi and Te photolines follows in section 4.4.1. The intense and broad peak at around 7 eV is identified as a background signal caused by valence band signature of the silicon substrate.

Figure 4.3.1 (c) shows the corresponding 700 eV XPS survey for the Pt/Au-coated sample (A2). At about

531 and 284 eV the O 1s and the C 1s signal is detected. Additionally, peaks at approximately 57 and 74 eV (less visible), 84 and 88 eV, 335 and 353 eV as well as 547 eV are identified as the Au 5p, Au 4f, Au 4d doublets and the Au $4p_{3/2}$ core levels, respectively. Although XPS is a surface sensitive technique, the Si 1s and Si 2p at 99 and 150 eV, respectively, as well as their corresponding oxide (SiO_x) at 103 and 154 eV binding energies are observable. This is due to scratches on the substrate surface that removed the sputtered platinum and gold layers. The silicon oxide is pronounced, because the native oxide was not removed prior to the surface modification by HF dipping. Interestingly, no platinum signal was detected hinting that this layer cleaves with the gold layer. As for a possible bismuth signal, there are doublets expected at 157 and 162 eV (Bi 4f), 440 and 464 eV (Bi 4d) as well as 93 and 119 eV (Bi 5p). Close to all these energies, either rather broad signals or only one of the doublet photolines are observed due to an overlap with the substrate signals. Therefore it is no definite indication that the bismuth signal from the nanowires is detected. Looking at the tellurium photolines, doublets are expected at 573 and 583 eV (Te 3d) as well as at 41 and 42 eV (Te 4d). In both cases the signal is not observed. Additional lines are visible at approximately 399 eV which can be assigned to the N 1s photoline resulting from long exposure to ambient conditions. Features at about 194, 215 and 235 eV are not identified. In comparison to substrate A1, the oxygen peak is more intense than the one of carbon which is most probably due to the different pre-cleaning strategies applied.

The spectrum in figure 4.3.1 (d) is obtained from the Bi_2Te_3 nanowires on substrate A2 using 100 eV photons. The most striking signal between 2 and 8 eV is the typical photoemission spectrum from the gold valence band [199]. Furthermore, a broad peak is observed from 25 eV to 29 eV, a binding energy range in which the Bi 5d core level doublet and its corresponding oxide is expected. The peak at about 31 eV cannot be assigned to any elemental photoline that is expected for this sample. Again the signal from Bi and Te are very weak and not clearly resolved as intense narrow photolines. The Te 4d doublet, which is the only core level energy below 100 eV for tellurium, is expected at around 55 eV and not visible in this spectrum.

Overall both substrates show a strong valence band signal. In general, the substrate A1 exhibits a simpler spectrum due to the sole presence of Si, while substrate A2 consists of Au, Pt, Si and SiO_x creating a strong and rather complicated background which might hide weaker signals of the Bi_2Te_3 nanowires. Both substrates show contamination by oxygen and carbon, making it necessary to introduce improved pre-cleaning treatment or additional cleaning procedure.

Additional cleaning by Ar sputtering at ANTARES

For the purpose of improving the surface of the sample, an argon sputter gun available within the preparation chamber of the ANTARES beamline (see figure 4.2.1) was used. The operating conditions recommended by the beamline scientists were 500 V and 38 mA. The distance between the sample and the Ar gun amounts to about 15 cm. Figure 4.3.2 shows the obtained core level spectra of sample A2 recorded in the low focus mode with a micrometer-sized beamspot. The sample was sputter-cleaned for 15 sec (black) and 15 min (blue). After each of the two sputtering cycles the sample was returned to the main chamber and remeasured. Due to mechanical displacements during the use of the sample manipulators inside the UHV setup, it is not guaranteed that the same area of the sample was investigated.

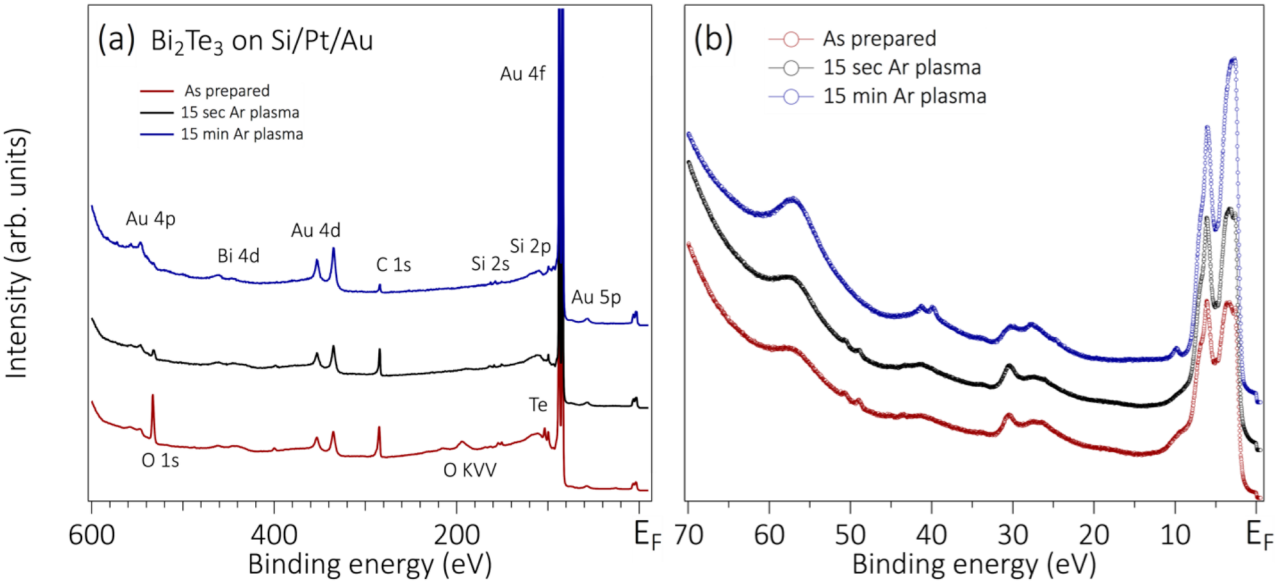

Figure 4.3.2: Core level spectra recorded over 700 eV (a) and 100 eV (b) after the sample was inserted into the UHV chamber (red) as well as after 15 sec (black) and 15 min (blue) of Ar plasma sputtering.

The spectrum of the as-prepared state of the sample is already described in detail in the previous paragraph and figure 4.3.1. The Au and Si signals from the substrate are clearly visible. The oxygen and carbon photolines indicating contamination by oxidation and polymer residues, can be clearly identified at about 530 and 295 eV, respectively. Fifteen seconds of Ar plasma sputter cleaning reduces the oxygen significantly inverting the oxygen to carbon ratio. Only after 15 min the O 1s signal vanishes completely, while at the same time the C 1s photoline is also reduced significantly. Figure 4.3.2 (b) shows that the initially smeared out Te 4d (41.6 and 39.9 eV binding energies) and Bi 5d (27.7 and 24.4 eV binding energies) doublets are resolved after 15 min of plasma cleaning. It is worth pointing out that the Ar sputter treatment is necessary to remove all possible contamination forming due to the oxidation process or remaining polymer residues. On the other hand, sputtering is a destructive method and damages to the surface have to be considered. For the nano-ARPES experiments, all samples were treated with 15 min of Ar sputtering at 500 V and 38 mA.

Another aspect that influences the surface quality of the sample is the fairly long measuring time. Once a sample is suitably clean, nano-ARPES measurements are in principle undertaken over several days. Hence, the surface is tested in terms of aging by recording core level spectra shortly after insertion into the UHV chamber, after 24 h of measuring and after a second cleaning process for samples prepared in the same way as A1. With repeated cleaning the restoring of the surface quality was explored. The results are presented in figure 4.3.3. During these measurements the spectra were recorded using the nano-focused photon beam resulting in higher intensities of the bismuth and tellurium photolines compared to the spectra shown in the previous paragraphs.

After the initial preparation, the superposed or smeared out Bi 5d doublet is observed within the range of 25 to 30 eV, while the Te 4d photolines are visible at around 40 eV binding energy. A small shoulder in each spectrum located at approximately 42 eV indicates some remaining oxide contamination. Keeping the sample inside the main chamber for 24 h under UHV condition, the Te 4d and Bi 5d doublets cannot be identified anymore. This is attributed to the loss of surface quality due to oxidation, which is already indicated by the shoulders of the doublet peaks after the first Ar sputter cleaning step. Introducing a second Ar sputtering step shows that the Te 4d and Bi 5d doublets can be reproduced. To minimize the aging effect the samples were systematically sputter-cleaned every 8-12 h.

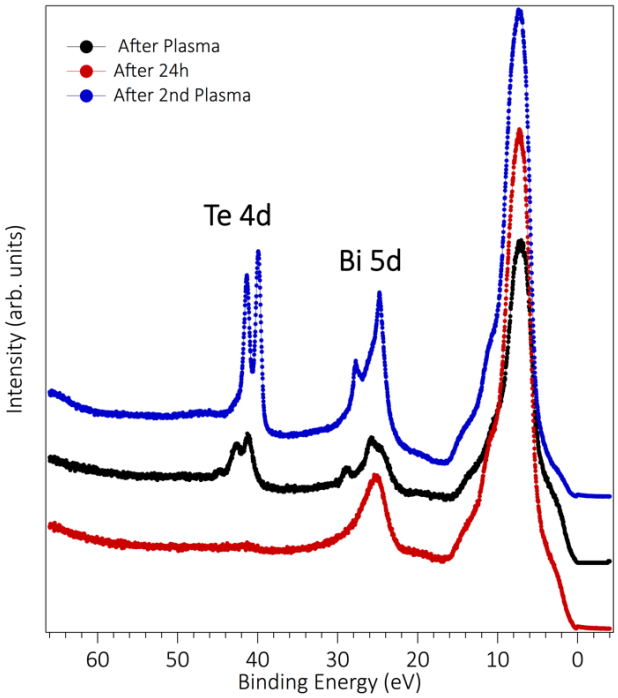

Figure 4.3.3: Core level spectra recorded over 100 eV after the initial preparation (red), after 24h of aging in the UHV (black) and after a second Ar plasma sputtering step (blue). The surface quality decreases significantly with time, but can be recovered by repeatedly Ar sputtering.

Substrates D3, D4 and D5 are boron p-doped silicon wafers (Si-Mat Silicon Materials) without any special coating. Each wafer was cleaned using a different protocol prior to the insertion into the XPS in DAISY FUN (see table 4.3.1). Ultrasonicating D3 in aceton and subsequently in isopropanol for 5 min each is expected to clean the surface roughly without removing the native oxide. D4 was immersed into 5 % HF for 1 min and then thoroughly rinsed in deionized water. Substrate D5 was additionally cleaned using a mixture of 95 % sulfuric acid and 31 % hydrogen peroxide, commonly known as Piranha solution, for 10 min before immersing into the HF bath. Piranha solution is known to remove organic residues as well as elemental carbon. Since it is a strong oxidizing agent forming another oxide layer, that has to be subsequently etched using HF. Substrate D6 is a silicon TEM grid with a suspended silicon nitride (Si_3N_4) membrane serving as carrier for the Bi_2Te_3 nanowires. This substrate was investigated as a pretest for experiments combining TEM investigations of the nanowires with nano-ARPES measurements as described later in section 4.6. Especially the robustness to Ar sputtering was of primary interest.
In order to measure the core level spectra, the samples were irradiated by Al K_α photons providing an excitation energy of 1486.74 eV. The beamspot of the x-ray radiation incident on the target is about 3 mm in diameter. Figure 4.3.4 summarizes the results obtained for substrates D3 (red), D4 (blue), D5 (black) and D5 with transfered nanowires (green) after insertion into the UHV system. For comparison, an overview spectrum (a) was chosen as well as high energy resolution (0.05 eV) scans of the O 1s (b), C 1s (c) and Si 2p (d) photolines.
All four overview spectra exhibit the typical silicon substrate signature between 100 and 200 eV including the Si 2s (151 eV) and Si 2p (99 eV) photolines as well as the energy loss peaks due to plasmonic excitation [174]. For the D5 substrate with additional nanowires neither Bi nor Te signals are traced, indicating that the amount of nanowires spread on the substrate is too low to be detected in this setup. The three peaks around 1000 eV and the sharp photoline at about 531 eV are assigned to the typical Auger lines for oxygen (KLL) and the O 1s core level, respectively. Additionally, the C 1s photoline is clearly identified at approximately 285 eV. Comparing the peak ratios in all four overview spectra, it is obvious that the D3 exhibits the highest amount of oxygen present. This results from the pre-cleaning in aceton and isopropanol which is not suitable to remove any native oxide layer. D4 and D5 show a reduced O 1s and Auger signal, as expected for samples with removed oxide layer. Besides this obvious difference, figure 4.3.4 (b) reveals various O 1s peak shapes for D4, D5 and the D5 samples with nanowires. The O 1s signal recorded from D4 reveals a broad peak centered at about 532 eV with an approximate **F**ull **W**idth at **H**alf **M**aximum (FWHM) of 3 eV. This indicates that organic C-O and C=O bindings expected between 531 and 533 eV are present in the solely HF cleaned sample and identified as a source of contamination. The signal for the two D5 samples, on the other hand, is slightly asymmetric with peak maxima at (531.8±0.5) and (532.4±0.2) eV without and with deposited nanowires, respectively. Adding a cleaning step employing Piranha solution seems to efficiently improve the removal of organic contamination, eliminating C=O bindings.
In terms of the carbon contamination the obtained results in figure 4.3.4 (c) are not as distinct. Besides the elemental C 1s signal at 285 eV, also C-O and C=0 bounds are identified for each substrate at about 2 eV higher binding energies. In this case, the substrate D4 exhibits the most intense C 1s signal while

the additional organic bonds are only present as a slight shoulder in the C 1s peak for D5 (black). This points again towards the ability of the Piranha solution to increase the cleanness of the sample. After transferring the nanowires, the elemental carbon and organic compound contaminations are increased again, which is reasonable, because the nanowires are kept in dichloromethane solution. It is worth mentioning that the carbon signal obtained from D3 cannot be directly compared to those of D4 and D5 because the top surface layer consists of native SiO_x adding to the spectrum.

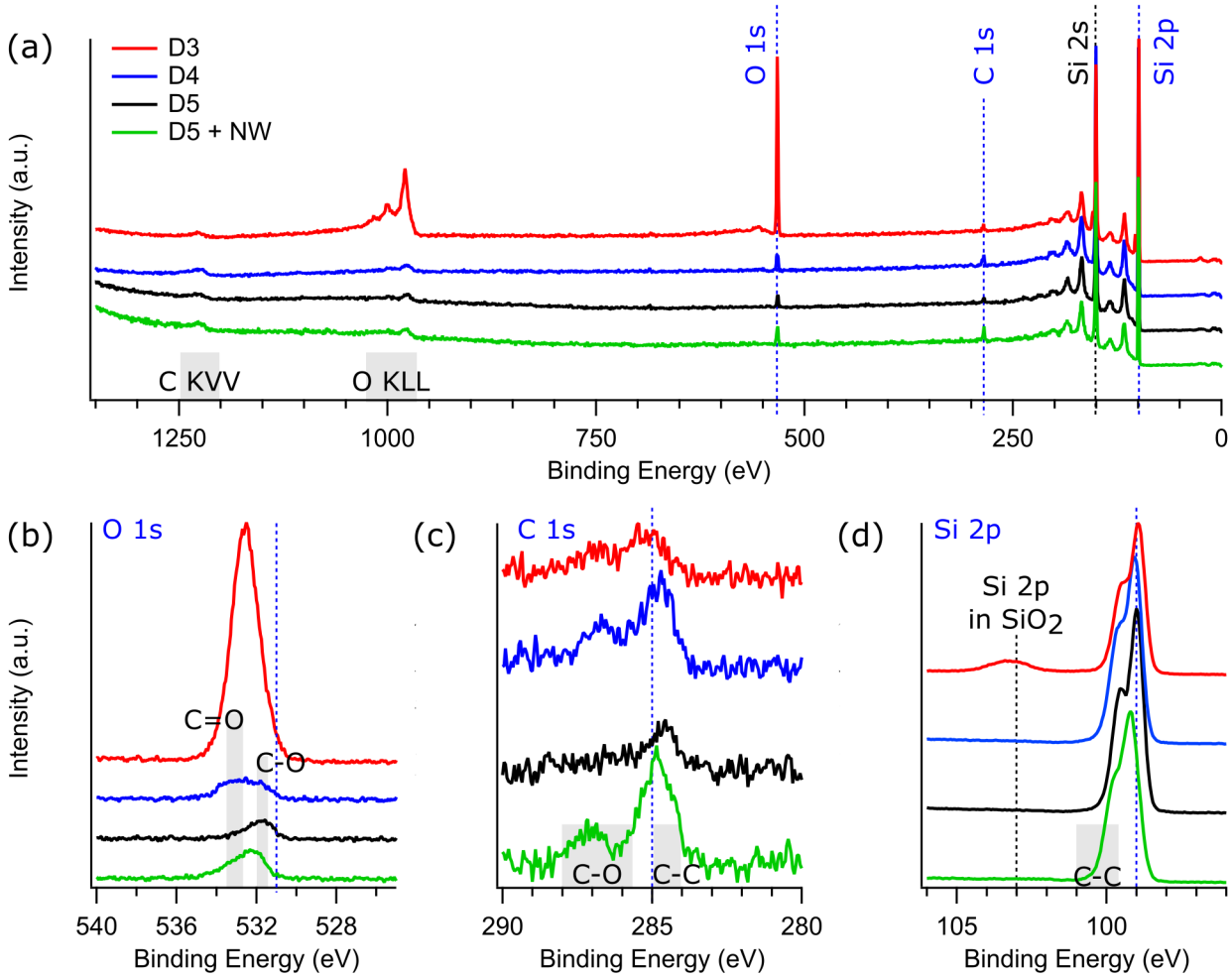

Figure 4.3.4: XPS spectra recorded at DAISY FUN for samples D3-D5 and D5 with additional nanowires (NW). (a) Overview spectra showing the typical background of the silicon wafer at around 150 eV binding energy. (b) O 1s, (c) C 1s and (d) Si 2p photolines indicate the different contamination levels.

A clear indication of the SiO_x presence is displayed in figure 4.3.4 (d). For substrate D3 (red), the SiO_x photoline is found at the expected value of about 103 eV. A silicon oxide signal is absent for substrates D4 and D5 as well as for the sample supporting the nanowires confirming the successful removal of the native oxide.

Overall, the pre-cleaning procedure combining Piranha etch and HF dipping results in clean wafers suitable as substrates for nanowires.

Additional cleaning by Ar sputtering at DAISY FUN

Analogous to the investigations on the effect of Ar sputtering to enhance the surface cleanness performed at ANTARES, the samples D4, D5 and D5 with added nanowires were sputter-cleaned at DAISY FUN. For this reason an argon sputter gun installed inside the measuring chamber about 10 cm from the sample was used at 500 V and 10 mA for 15-30 min. The results of the subsequent XPS measurements are shown in figure 4.3.5 for an overview spectrum (a) and for spectra with high energy resolution of 0.05 eV for O 1s (b), C 1s (c), Si 2p (d) and Ar 2p (e). In addition to the known signature arising from the silicon substrate between 100 and 200 eV binding energy, the O 1s and C 1s photolines are barely visible and significantly reduced for all samples in comparison to the peak ratios in figure 4.3.4 (a). Furthermore, two new photolines appear at about 245 and 320 eV which are assigned to the Ar 2p and Ar 2s core levels. In figure 4.3.5 (b), a shift of the O 1s photoline to about 531 eV binding energy is found for all three samples indicating that all organic contaminations were removed during the Ar sputtering.

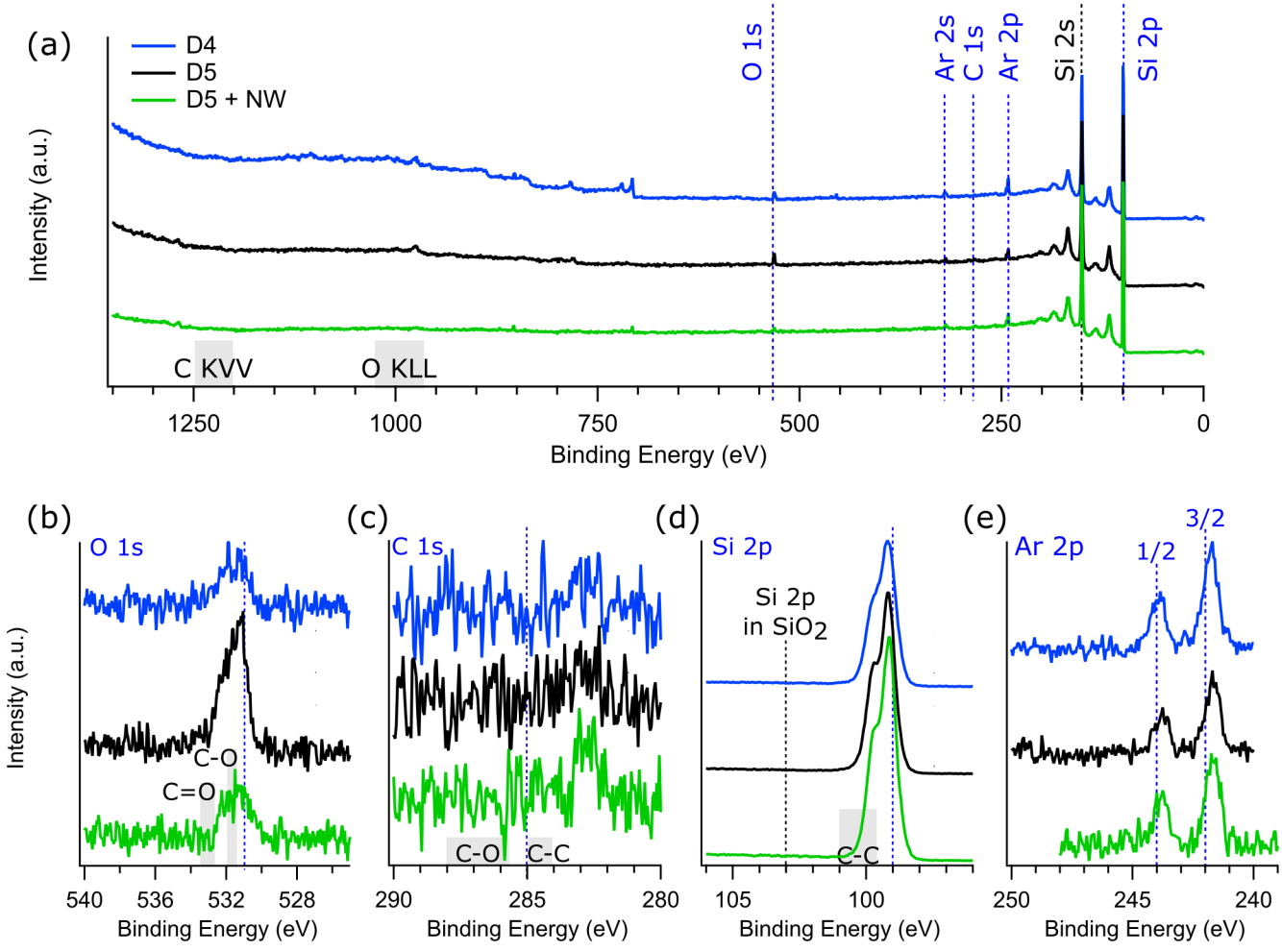

Figure 4.3.5: XPS spectra recorded at DAISY FUN after Ar sputter cleaning for samples D4, D5 and D5 with additional nanowires (NW). (a) Overview spectra showing the typical background of the silicon wafer at around 150 eV binding energy. (b) O 1s, (c) C 1s, (d) Si 2p and (e) Ar 2p photolines indicate the different contamination sources. The appearance of Ar is ascribed to incorporation of Ar atoms into the silicon surface.

The carbon photoline observed previously for the non-sputtered substrate, is not detectable after the sputtering as displayed in figure 4.3.5 (c) indicating the complete removal of the carbon contamination for all three samples. As expected, no significant change is observed for the Si 2p doublet after sputtering keeping the silicon substrate free of oxide. Additionally, a new photoline doublet appears between 240 and 245 eV which is identified as the Ar 2p3/2 at 242 eV and Ar 2p1/2 at 244 eV core levels. The presence of these photolines indicates an incorporation of Ar atoms into the silicon substrate [174].
Overall the sputtering seems to further improve the substrates surface quality. Oxygen-free silicon is only achieved by using Piranha and HF cleaned substrates in combination with Ar sputtering.

4.3.2 Nanowire identification

Aiming at finding single nanowires and investigating specific sections of interest, an imaging method is needed. The usage of typical instruments such as optical and electron microscopy are not realizable within the main measurement chamber, leaving the only possibility of using the ANTARES beamline concept in a microscopy mode. In order to do so, the photon beam is first focused to a spotsize of 100-150 nm employing the pinhole, the FZP and the OSA. Secondly, the Scienta R4000 detector is set to record a certain energy range corresponding to a characteristic photoline emitted from the sample providing spatial contrast. In the present case of Bi_2Te_3 nanowires, the Te 4d or Bi 5d doublet were chosen. To identify the Bi_2Te_3 nanowires on the substrate fixed inside the main chamber, the sample was mapped within a selected area taking advantage of the precise scanning of the sample stage and the focused nano-spot.
Figure 4.3.6 (a) displays a 100 μm x 80 μm mapping recording the Te 4d core level with a step size of 1 μm. The area of the doublet peak is represented by the color code with the lighter red corresponding to the maximum. For comparison, figure 4.3.6 (b) displays a representative HRSEM image of Bi_2Te_3 nanowires lying on the silicon wafer. This image was obtained from another area of the same sample showing nanowires of 100 nm diameter. They are typically between 10-20 μm long due to the breaking off from the back electrode (see section 2.4). The quality of this spectroscopic mapping demonstrates that, similar to the HRSEM image, areas of high nanowire density as well as single wires are well resolved and can be identified. The nano-size focus of the x-ray beam and the precise positioning system ensure the high resolution needed to subsequently locate single nanowires of interest employing a spectroscopic method.
In the present case, the representative area to be investigated is marked by the yellow box in figure 4.3.6 (a) containing a single nanowire. This area of 10 μm x 10 μm was mapped several times recording the Te 4d (c) and the Bi 5d core level (d) with a step size of 400 nm. Both images show a shadow effect separated by a darker line parallel to the nanowire axis. After repeating the mapping on a smaller area and with higher spatial resolution, this effect vanished (see figure 4.4.1). Its origin is unknown.
In general, the Te 4d mapping provides a slightly better resolution and contrast of the nanowire compared to the Bi 5d data. The difference is caused by the superposition of a signal from the silicon substrate at about 25 eV to the Bi 5d photoline. This is demonstrated in Figure 4.3.6 (e) showing two typical core level spectra recorded in highly focused nano-spot nano-ARPES mode over a binding energy range of 65 eV. Focusing the beam to about 100-150 nm, the spectra were recorded from an individual Bi_2Te_3

nanowire (yellow circle in (a)) and from the bare silicon substrate (yellow cross in (a)). Two doublets can be identified at 41.6 and 39.9 eV as well as at 27.7 and 24.7 eV binding energy, originating from the Te 4d and Bi 5d core levels, respectively [196–198]. Both energy ranges of the doublets were set to detected the mappings in figures 4.3.6 (c) and (d). The intense and broad peak at around 7 eV is identified as a background signal caused by the silicon substrate as previously mentioned in section 4.3.1. Additionally, a reference spectrum measured on the pure silicon substrate exhibits a broad peak with a maximum at about 25 eV, adding a background signal to the Bi 5d core level doublet. Both substrate peaks possibly arise from the native oxide on the silicon [200] as well as from the HF treatment of the substrate prior to the nanowire deposition forming silicon mono- and dihydrides [201]. As expected, the intensity of the substrate peaks decreases for spectra obtained on the nanowire. They do not vanish completely due to the beamspot being slightly larger than the wire diameter. Additionally, the beam-to-nanowire position can be misaligned due to the limited stepsize of 100 nm (see top of figure 4.4.1). This background signal is responsible for the reduced resolution of the nanowire in the Bi 5d mapping compared to the one recorded using the Te 4d energy. For this reason, nanowire mappings were always conducted using the Te 4d doublet signal.

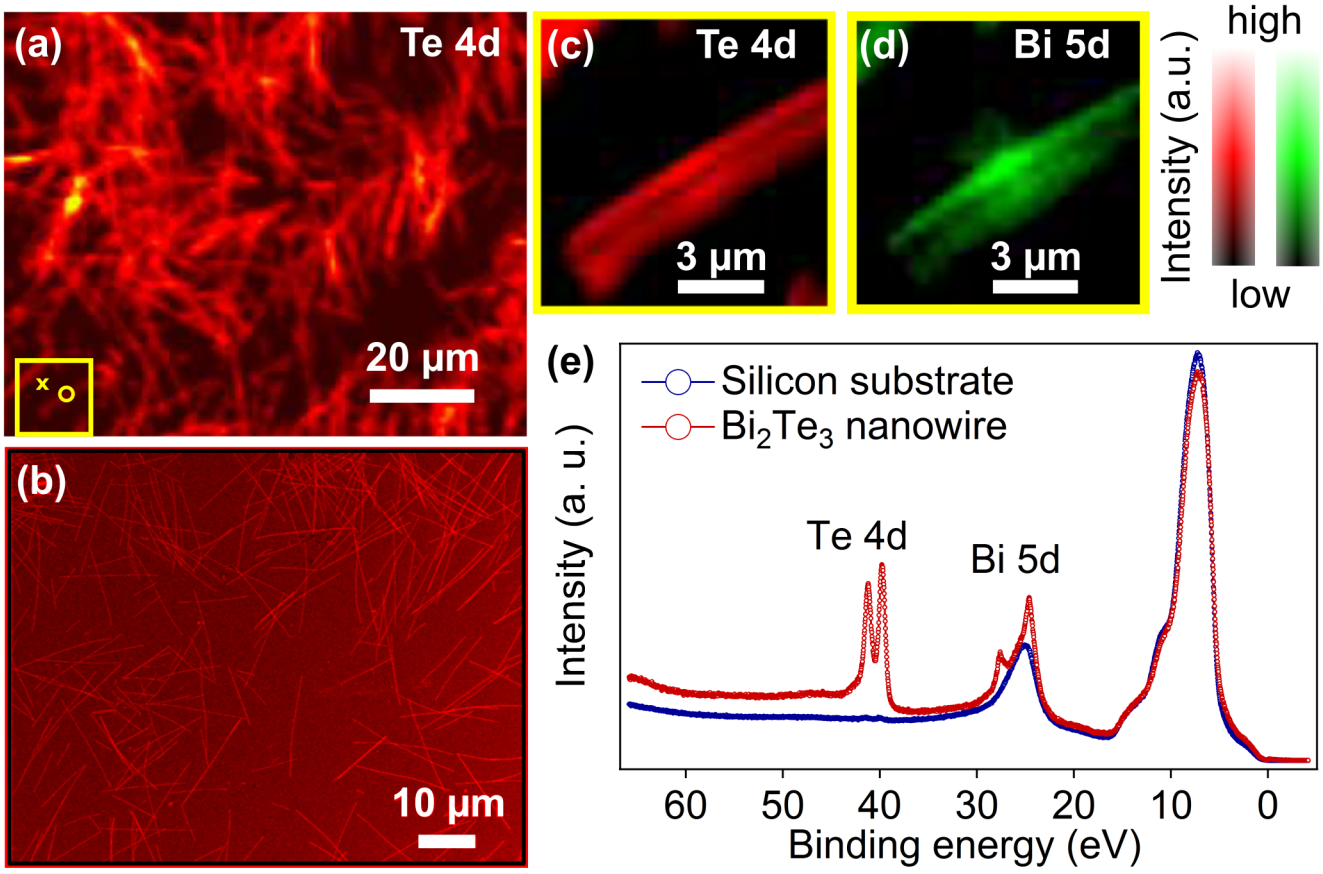

Figure 4.3.6: Identification and selection of Bi_2Te_3 nanowires on the silicon substrate using the Te 4d and Bi 5d doublets. (a) Spectroscopic mapping and (b) HRSEM image showing areas of high nanowire density as well as individual wires. The spectroscopic image of the area indicated in (a) (yellow frame) using the Te 4d (c) and Bi 5d (e) doublet. (e) Core level spectra recorded from the nanowire (yellow circle) and the Si substrate (yellow cross).

4.4 Nano-ARPES and -XPS on single nanowires

Following the careful preparation and cleaning of the samples, sections of Bi_2Te_3 nanowires of 100 nm diameter were chosen on which nano-XPS as well as nano-ARPES measurements were conducted. The nano-XPS studies provide an insight in the chemical homogeneity of the surface along the given nanowire and will be described in detail in section 4.4.1. Nano-ARPES measurements on two segments of nanowires are presented and discussed in terms of the electronic structure difference between different nanowires (section 4.4.2). Following the nano-ARPES discussion, first principles calculations of the Bi_2Te_3 band structures as a function of the crystallographic orientation are introduced in section 4.5 and put in context to the experimental results.

4.4.1 Chemical homogeneity of the nanowire surface

For the evaluation of the chemical structure of the surface along a single nanowire as well as comparing different sections of nanowires, nano-XPS spectra were recorded using an excitation photon energy of 100 eV. As a consequence drawn from chapter 4.3.1, the Bi 5d and Te 4d photolines are clearly observable and are used as a measure for the chemical homogeneity of the nanowire surface. Figure 4.4.1 shows a representative study along one single nanowire. The upper image corresponds to a Te 4d high resolution core level mapping of a section of the nanowire marked by the yellow box in Figures 4.3.6 (a, c, d). It was recorded immediately after the sample had been exposed to Ar plasma (500 V, 38 mA) for 20 min and transferred to the main chamber to obtain the cleanest surface possible as described in section 4.3.1. In this case, the step size of the mapping was reduced to 100 nm in order to image a segment of the nanowire within a 5 μm x 2 μm small area. Consequently, the estimated scanning step size is in the order of the nano-spot focus amounting to about 100-150 nm. Due to the misalignment of the nanowire to the stage positioning, the wire appears significantly larger than its actual diameter. Nevertheless, the image reveals a homogeneous diameter in agreement with the HRSEM and TEM images presented in chapter 3. Furthermore, a continuous and high Te intensity peak contrast along the nanowire axis makes for a brilliant spectroscopic image. The numbers (1) to (4) indicate the four positions on the nanowire from which core level spectra were recorded. They are located between 500 nm and 1 μm apart from each other along the nanowire axis. This distance was chosen to increase the possibility of receiving a signal from differently orientated grains which have an estimated grain size of several hundred nanometers as found in section 3.2.2.

Figure 4.4.1 presents the core level spectra with the Te 4d and Bi 5d doublets for all four positions of the mapping (top). The two peaks of the Te 4d and the Bi 5d doublets, resulting from the spin-orbit coupling, are separated by around 1.5 and 3 eV, respectively, which is consistent with literature values [196–198]. Assuming that the ratios of the nanowire and substrate area recorded on each position were constant, all core level spectra would be normalized to the substrate peak at around 7 eV[2]. For comparison, a core level spectrum obtained from one position on the Si substrate at a distance of approximately 3 μm from the nanowire is added (bottom black curve). Note that this spectrum is not normalized to the ones recorded from the nanowire, because the area of acquisition is solely on the silicon substrate. Similar

[2] For a better representation, this peak was omitted from the range of the spectra shown here.

to Figure 4.3.6 (e), the Bi 5d signal is convoluted by the silicon substrate background resembling the shape of an exponentially smeared out Gaussian as indicated by the dashed black curve at the bottom of Figure 4.4.1.

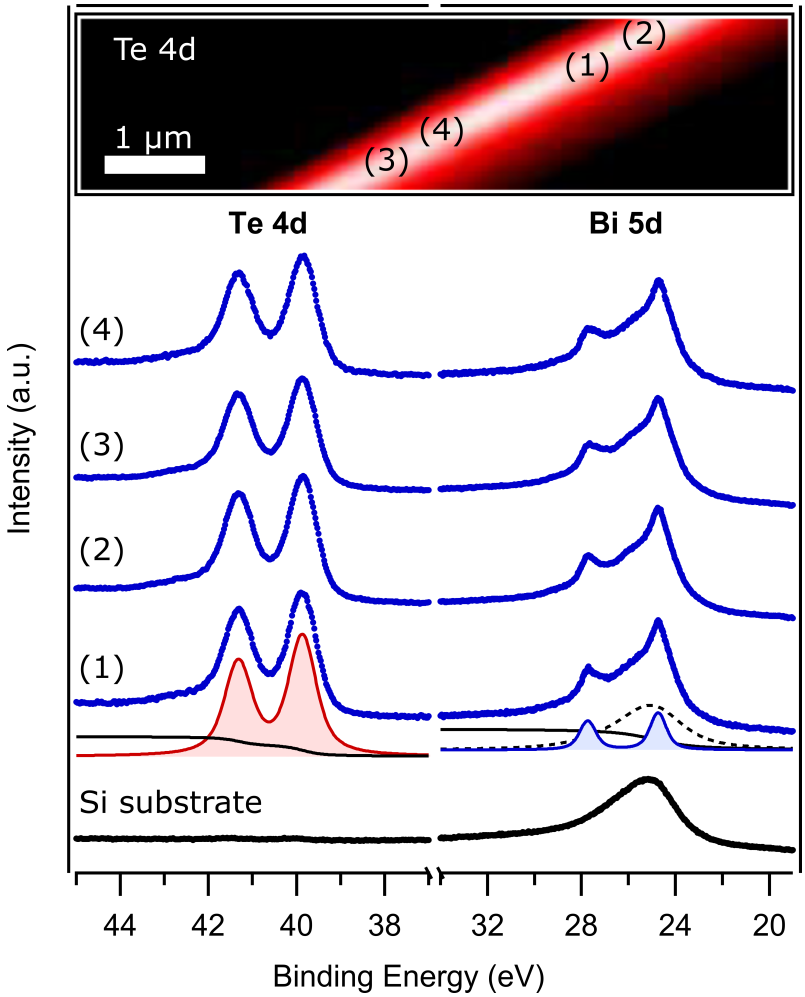

Figure 4.4.1: Study of the chemical composition along an individual Bi_2Te_3 nanowire (top). Core level spectra (blue) were obtained from four different positions up to 1 µm apart from each other. The spectrum recorded from the background as well as a fitted Shirley background are shown (black). Representative peak fits are indicated on position (1) (red and blue shaded curve).

Comparing all four spectra, no peak shift is detected, giving evidence for a constant chemical composition within the chosen wire section. Furthermore a local (oxide) contamination, which would be indicated by additional oxide peaks of the doublets, was not found. After subtracting a standard Shirley background (solid black line) from each of the spectra [199], the peak areas were fitted employing Voigt and Lorentz distributions. This fitting method is indicated representatively on the core level spectrum recorded on position (1) by the solid red and blue shaded curves, respectively. The Bi 5d signal was deconvoluted by keeping the same shape of an exponentially smeared out Gaussian as determined from the fit to the substrate spectrum (dashed black curve). Note that the peak height was not maintained, since the recorded substrate area was not the same. Using a quantitative analysis, it was observed that the peak

areas do not change indicating a constant Bi/Te ratio along the nanowire axis with a spatial resolution better than 150 nm. The precise value could not be reliably determined due to various uncertainties: Firstly, the ratio of signal obtained from the nanowire and the substrate is unknown. Secondly the exact contribution of the substrate peak overlapping the Bi 5d energies is unknown. Nevertheless, assuming similar conditions for the acquisition area for the spectra recorded from the nanowire, these results show that the chemical composition stays homogeneous along the nanowire section. This is in agreement with the findings from the EDX in TEM measurements (see section 3.3.1) obtained from different nanowires synthesized under the same conditions within the same batch. Although the EDX in TEM provides in principle a spatial resolution of 1 nm, the signal comprises not only information from the surface, but also from the bulk of the nanowire. Using the core level spectra obtained at ANTARES, solely the chemical composition of the nanowire surface is probed indicating its homogeneity with a spatial resolution of better than 150 nm.
Similar results were found for core level spectra recorded from nanowire sections on different wires of the same sample.

4.4.2 Electronic structure of nanowires

Angle-resolved photoemission spectra were measured in nano-focus mode using again an incident photon energy of 100 eV and detecting the photoelectrons with a kinetic energy of 91 eV and higher, where 96 eV correspond to the Fermi energy. Consequently, this energy range corresponds to a about 5 eV below the Fermi energy. The raw measurement and the data treatment of the nano-ARPES recordings are shown in Figure 4.4.2.
Using the same data treatment technique for both, the upper row (blue background) shows the nano-ARPES results measured on the silicon substrate, while the lower row (yellow background) displays the data recorded from a nanowire section. The recording positions are indicated schematically by blue and yellow stars in the setup scheme in figure 4.4.2 and on each corresponding nano-ARPES spectrum. In both cases the data is shown in angle-energy space, starting with the raw data in (a). To resolve the energy bands, the data had to be processed, since the signal is too weak meaning the signal-to-noise ratio is very low resulting in no clear observation of any features. Firstly, an appropriate background, displayed in figure 4.4.2 (b), was created for both exemplary cases by fitting a quadratic polynomial to the energy spectrum at each angle. These cuts through the ARPES spectra are also known as energy dispersive curve. Using this technique, the incoherent background signals originating from the substrate or from secondary electrons, which are not uniform along the energy or angle axis, were removed. The nano-ARPES data in figure 4.4.2 (c) shows the subsequently background-subtracted data for both measurements. In the case of the nanowire nano-ARPES data (yellow), the energy bands become already visible in figure 4.4.2 (c), while the signal measured on the substrate (blue) does not show any features. Figure 4.4.2 (d) displays the final result of the nano-ARPES data of the nanowire which is obtained after taking the second derivative of the momentum distribution curve and subsequently applying standard smoothing techniques. For the silicon substrate, no energy bands were resolved after smoothing. This is expected, since the substrate was chemically etched and hydrogen-terminated during the cleaning procedure. Possible arising contamination could also prevent the Si band structure from being resolved.

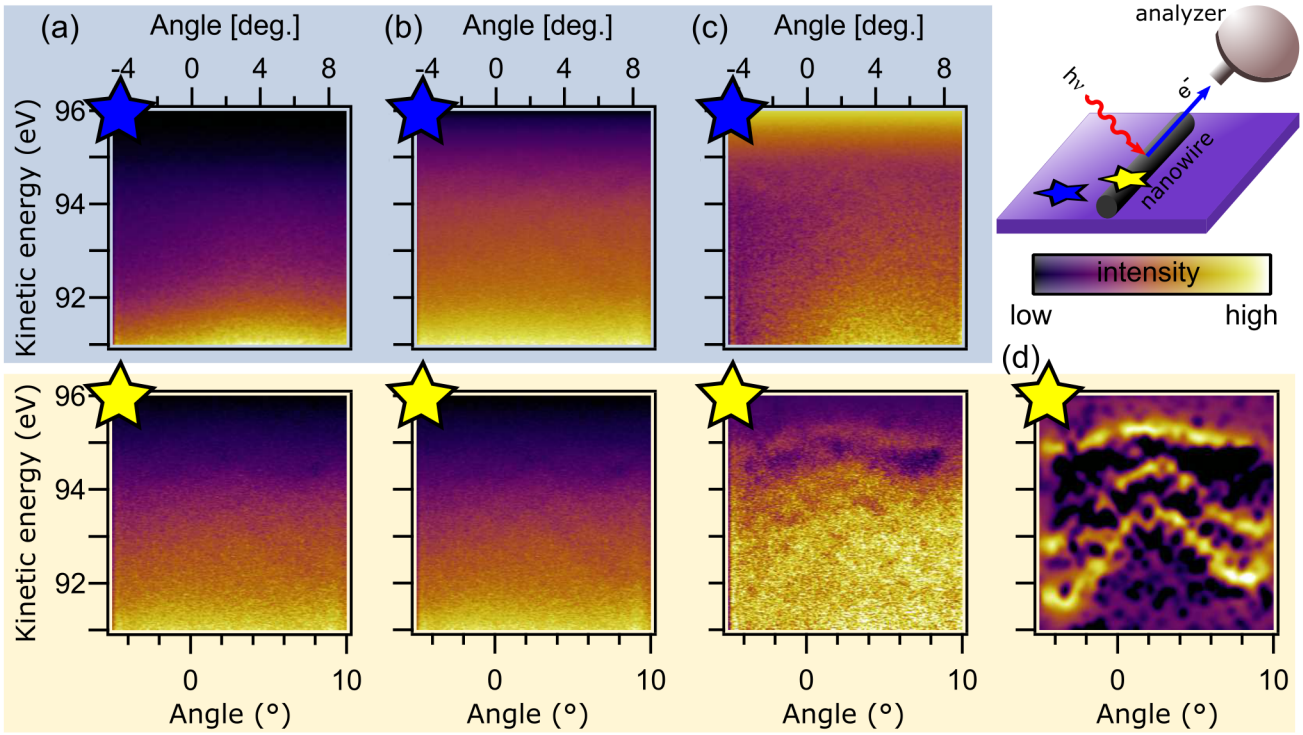

Figure 4.4.2: Nano-ARPES data obtained from the silicon substrate (blue upper row) and from a Bi_2Te_3 nanowire section (yellow lower row) as marked in the setup scheme by blue and yellow stars, respectively. The different steps of data processing the raw data (a) include the construction of a polynomial background (b), the subtraction of this background (c) and a final smoothing of the data (d).

After establishing a strategy to extract the very low nano-ARPES signal, several spectra were recorded from several points on the substrate. The valence band structure of two separate cylindrical nanowire sections was recorded by nano-ARPES as displayed in Figures 4.4.3 (a) and (b).

In this case, the detected angle-kinetic energy data was converted to energy-momentum space employing equations 4.5 and 4.7. This results in nano-ARPES spectra recording the valence band around 5 eV below the Fermi level. The exact acquisition area of the measurements are indicated by the white and the red markers in the Te 4d spectroscopic mappings presented in Figures 4.4.3 (c) and (d), respectively. The nano-ARPES energy-momentum data in (a) was recorded at the position of a single nanowire, while the data in (b) was obtained from a wire belonging to a nanowire bundle. The x-ray beamspot size of 100-150 nm lies within the diameter of the nanowire and is smaller than the large single crystalline grains extending over several hundreds of nanometers as discussed previously. Keeping in mind the absolute surface sensitivity of the technique, the arrangement of the wire within a bundle is only interfering with the measurement to a certain degree: Due to the misalignment of the nanowire and the acquisition area, the signal of two or more nanowires might superimpose. The misalignment is caused by the small, but limited step size of the mapping.

The nano-ARPES data obtained from the single nanowire shows three resolved bands with the maximum of the top band located close to the Fermi level. It is unclear if the Fermi level even lies within the valence band. In that case the nanowire would be p-doped. For clarification a much better energy resolution within this region is required detecting also a smaller energy range below the Fermi level. The

comparison of Figures 4.4.3 (a) and (b) reveals different valence band structures at the two separate positions exhibiting the same chemical composition (see section 4.4.1).

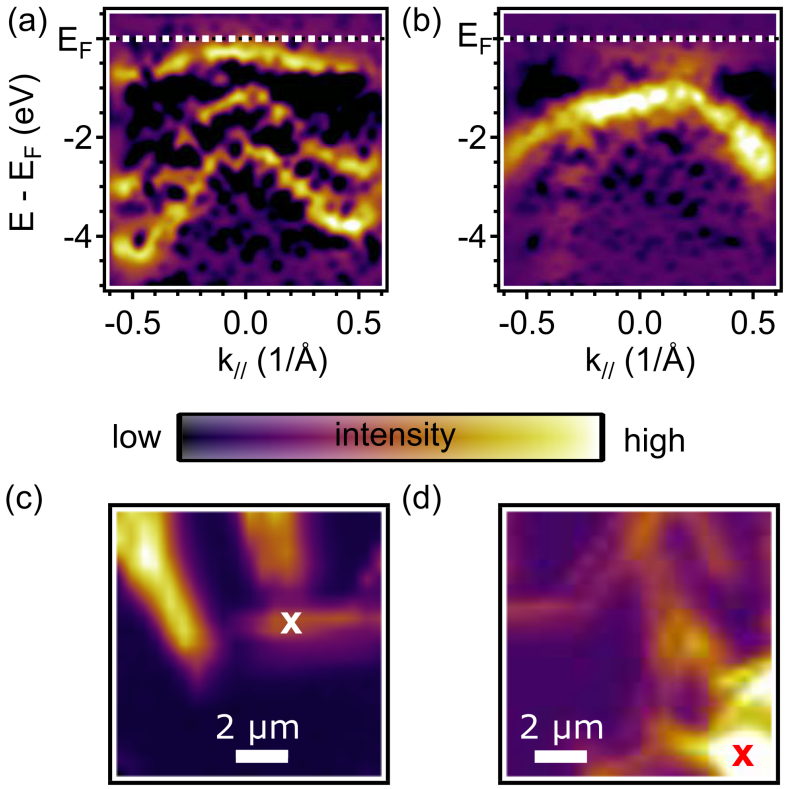

Figure 4.4.3: Nano-ARPES data (a) and (b) from two different sample positions as marked in (c) on an individual wire and in (d) on a bundle of nanowires, respectively.

The energy-momentum data in (b) exhibits different features with the most intense bulk band having its maximum at about 1 eV below the Fermi level. This more complex and less well defined band structure is attributed to a different crystallographic orientation of the nanowire investigated at this position. Another possible reason is that the band structure originates from two consecutive nanowire section surfaces, which belong to different grains and thus different crystallographic orientations. In order to gain a deeper understanding of the influence of the crystal orientation of the grains on the electronic structure of the nanowires, theoretical simulations provide a suitable tool for comparison and will be introduced in the following section.

Despite the different open questions, these experimental measurements are remarkable, because they show that the nano-ARPES technique is a suitable tool to explore the electronic structure of individual nanowires.

4.5 First principles electronic structure calculations for different crystal orientation

For the purpose of assorting the previous nano-ARPES results within the context of the crystallographic orientation of the nanowires, first principles electronic structure calculations were performed in collaboration with Zeying Zhang and Prof. Dr. Hongbin Zhang.

In order to model the experiment, possible crystallographic orientations of the nanowire under investigation have to be known. In the layout of the nano-ARPES experiment the probed surface is parallel to the nanowire axis. Additionally, the cylindrical geometry accounts for a somewhat random distribution of plane orientations, because every possible orientation allowed for Bi_2Te_3 has to be considered. Based on the XRD investigations described in section 3.2.1, boundary conditions for the choice of planes were found and applied. The two dominant plane orientations perpendicular to the nanowire axis are the (205) and the (101) planes. As a consequence, the surface states of the semi-infinite Bi_2Te_3 projected onto such planes are calculated. The orthogonality requirement reduces the number of possible orientations, but due to the cylindrical cross-section of the wires many planes fulfill this requirement.

In the end, three crystallographic orientations were selected in such a way that their normal lies in either the (205) or the (101) plane exhibiting low Miller indices. Figure 4.5.1 (a) shows the hexagonal Bi_2Te_3 unit cell with the (101) and the (205) plane marked in purple in the left and right schematics, respectively. The chosen planes are approximately perpendicular to vectors $[-121]$ and $[-532]$ within the (101) and the (205) plane, respectively. The corresponding planes are highlighted in red and yellow. The plane (green) perpendicular to vector $[010]$ was selected, because it is approximately orthogonal to both plane orientations (101) and the (205). The Miller index notation in (a) denotes the corresponding planes indicated by round brackets.

After finding a strategy to describe the experimental conditions, first principles calculations were performed using the plane-wave pseudo-potential approach. In this picture the electrons are described by a basis set of plane waves that are independent of the atomic positions. The number of plane waves included in the set is chosen by testing the convergence of the total energies with respect to the cutoff energy for the plane waves, given by a value of 550 eV. Moreover, to reach the thermodynamic limit, the convergence with respect to the density of the k-mesh was tested. Under periodic boundary conditions, it is straightforward to imagine the more k-points used, the more unit cells in real space are considered. For the calculations conducted here, a $8\times8\times8$ k-mesh has been applied. Supplementary, the potential for each atom is approximated by a so called pseudo-potential. This potential ignores the core orbitals and only takes the valence states into account resulting in a much simpler form of potential. In the present case the basis for Bi_2Te_3 was chosen to consider the $6s^26p^3$ orbitals for Bi and the $5s^25p^5$ orbitals for Te.

The actual calculation method is based on **D**ensity **F**unctional **T**heory (DFT)[3], a well-established method in computational solid state physics [202, 203]. Generally, the direct solution of the Schrödinger equation for many-body systems is not feasible which led to the development of DFT. The idea is to imagine a system not in terms of the single electron wave function but consider its electron density. The basis for this correlation is the Hohenberg-Kohn theorem which states that the ground state of a system of elec-

[3] A functional is a mapping from a vector space into its (scalar) field. Since the vector space is commonly a function space, one can say that a functional is a function of functions. A famous example of a functional is the Dirac δ-distribution returning the value of any function at the origin.

trons is uniquely determined by its density [204]. In a nutshell, it follows that the ground state energy of the systems can be described by functionals dependent only on the density. These energy functionals consists of several contributions: the kinetic energy of the system, the electrostatic potential between electrons as well as the nuclei, the Hartree potential between electrons and the so called exchange-correlation potential. The latter includes the remaining contributions due to the Coulomb interaction between electrons. In practice, such functionals are evaluated by mapping the realistic charge distribution in crystals onto a homogeneous electronic gas where the energy functionals are parameterized in terms of the charge density. This method is known as the Kohn-Sham construction [205].
Unfortunately, the exchange-correlation contribution is unknown and the topic of ongoing research in DFT. Nevertheless, some established approximations are already available. The most straight forward one is based on describing the systems as a uniform electron gas with a homogeneous electron density and is known as **L**ocal **D**ensity **A**pproximation (LDA). In the present case the exchange-correlation potential was approximated using the **G**eneralized **G**radient **A**pproximation (GGA) interpolated by Perdew, Burke, and Ernzerhof [206]. Compared to the LDA, the GGA approach also takes into account the density gradient at each point of the system.
Finally, the first principles calculations were performed using the plane wave pseudo-potential method as implemented in the VASP code [207, 208]. The output is the Hamiltonian for all k-points in the Brillouin zone of the 3D bulk. In order to obtain the surface electronic structure for nanowires with arbitrary crystallographic orientations, the Wannier interpolation technique is used to parameterize the real space hoppings between the different orbitals of each atom in the system. In addition, the spectra functions for semi-infinite slabs are obtained which serve as a direct comparison to the nano-ARPES measurements. In the present work, the Wannier function orbitals are constructed for the p-orbitals of the Bi and Te atoms using the Wannier90 program [209]. The semi-infinite surface states are obtained using the algorithm proposed in Ref. [210].
The results of the first principles electronic band structure calculations obtained for crystallographic orientations chosen in figure 4.5.1 (a) are shown in figures 4.5.1 (b-d). Obviously, for all three band structures, topological surface states exist at the Fermi energy E_F connecting the valence and conduction bands, due to the nontrivial topological nature of the band gap in Bi_2Te_3. As expected for Bi_2Te_3 the Dirac point is located very close to the valence band [38]. Furthermore, the energy bands displayed in (b) and (c) follow a similar distribution differing mainly at the zone boundaries (close to the M and K points) where the bands of the (-121) plane (red) exhibit an upturn. The energy band structure calculated for the (010) plane (green) shows a different band distribution with the most pronounced spectral weight around 1 and 3 eV below the Fermi energy. Comparing the results to those shown in figure 4.4.3, the calculated band structures along chosen crystallographic orientations are in reasonable agreement with the nano-ARPES measurements. For instance, three parabola-shaped symmetric bands in figure 4.4.3 (a) can be compared to the most intense bands in figure 4.5.1 (b) and (c), where the slight upturn of the bands at the zone boundaries can be attributed to the different crystallographic orientations. Moreover, the nano-ARPES data shown in figure 4.4.3 (b) with intensive weight around 1 eV below the Fermi energy are similar to the surface states obtained for the (010) plane (green) in figure 4.5.1 (d). Thus, based on such calculations, the measured nano-ARPES spectra are certainly arising from different oriented crystal sections of the Bi_2Te_3 nanowire.

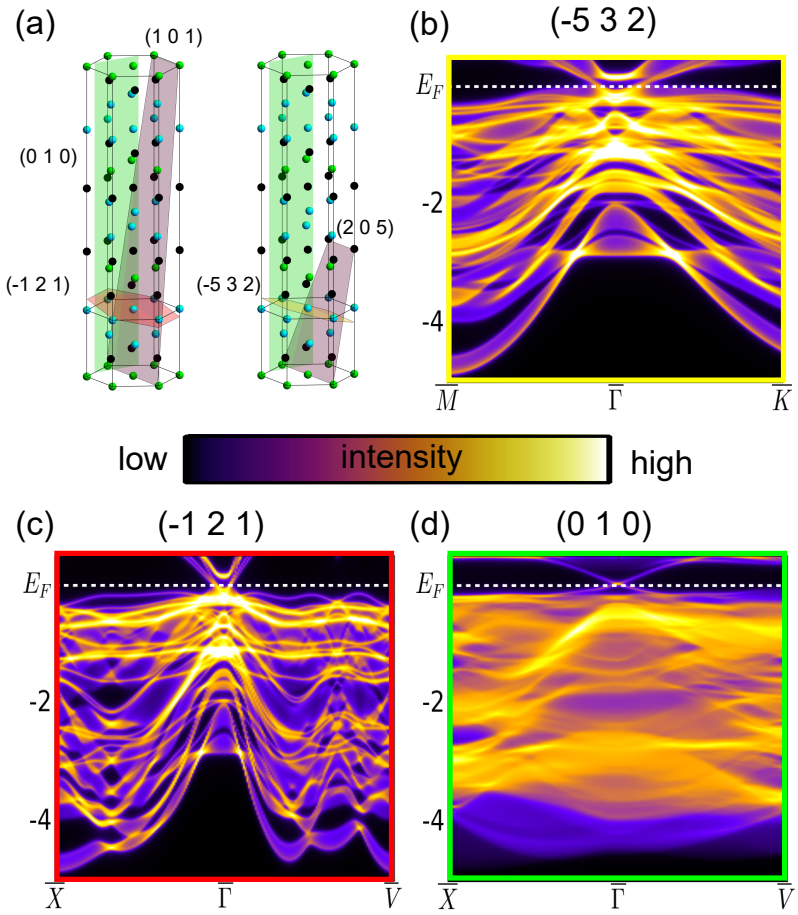

Figure 4.5.1: Electronic structure of Bi_2Te_3 nanowires along different crystallographic orientations. (a) Schematic of plane orientation for planes perpendicular to (101) (purple, left) and (205) (purple, right) planes in the hexagonal lattice. Planes perpendicular to vectors $[-532]$, $[-121]$ and $[010]$ are marked in yellow, red and green, respectively. First principle band structure calculations for (b) (-532) (c) (-121) and (d) (010) planes

4.6 Conclusions from Nano-ARPES measurements and outlook

Nano-ARPES measurements were performed on cylindrical Bi_2Te_3 nanowires with 100 nm diameter randomly distributed on a thoroughly cleaned boron p-doped silicon substrate. Despite the challenges in obtaining an atomically clean surface, the nanowires were successfully identified by spectroscopic core level imaging. Nano-XPS studies conducted on sections of several wires as well as along the nanowires revealed a chemically homogeneous surface structure supporting the EDX in TEM results obtained for the bulk part of the nanowire. After suitable data processing the low-intensity nano-ARPES energy-momentum data was extracted on two sections of nanowires and compared. On a single nanowire, three intense valence bands were observed extending or even crossing the Fermi level. The nano-ARPES data obtained from a nanowire in a cluster showed a more complex electronic band structure with one intense band exhibiting a maximum at about 1 eV below the Fermi energy. The two different band structures can be explained by the varying crystallographic orientation of the nanowires which exhibit a texture

perpendicular to its axis, but due to its cylindrical cross section the texture is constrained parallel to its axis. Additionally, the grain size of several 100 nm exceeds the size of the beamspot, but possible recording of regions with grain boundaries cannot be excluded.
Exemplary, first principles electronic structure calculations for crystal orientations selected based on XRD results were performed, revealing that the valence band structure can indeed vary significantly. The calculations fit to the experimental nano-ARPES data, but for a more accurate relation of the experimental to the calculated data more nano-ARPES measurements are necessary.
These results open a new avenue to characterize the band structure of topological insulators and other nanomaterials. Certainly a detailed analysis of the electronic structure as a function of the crystallographic orientation and size of a given nanostructure should be pursued. Especially in combination with transport measurements, this would help to better understand the behavior of topological surface states at grain boundaries.
The nano-ARPES experiments performed as described here can be conducted to resolve the band gap of the material and possible surface states by enhancing the energy resolution. Furthermore, the influence of the nanowire diameter on the electronic band structure can be explored.
In order to relate the crystal structure of the nanowires, it is proposed to prepare the wires on a suitable TEM grid which is conductive (carbon fiber) instead of a silicon substrate. Prior to nano-ARPES measurements, suitable nanowire sections can be selected in a TEM session. Pre-characterized nanowires can thus be investigated by nano-ARPES and the band structure can be directly related to the crystal orientation. First test experiments have been performed employing a silicon nitrate TEM grid and applying all cleaning procedures described in section 4.3.1. Unfortunately, the substrate is not conductive enough to obtain a clear nano-ARPES signal. Nevertheless, this experiment would provide an important step forward to clarify the relations between, crystal orientation, grain boundaries and the electronic band structure.

5 Magnetotransport measurements

With regards to exploring the topological insulating nature of a certain material, ARPES experiments are the first choice of experimentalists. Providing that the TI is producible as high-quality single crystal or thin film of macroscopic sizes, ARPES gives direct information about the topology of the band structure. By making use of newly developed nano-ARPES facilities even TI nanostructures can be investigated as described in the previous chapter 4 [211].

For TI nanomaterials, the most common way to investigate the surface states is by electrical transport studies. On the one hand, this is because of the limited resolution provided by common non-nano-ARPES setups and on the other hand, this is because of their possible implementation in devices for future electronic applications. Nevertheless, transport measurements on TI nanomaterials are challenging due to the tendency of probing the residual bulk charge carriers despite their reduction by the large surface-to-volume ratio of nanostructures. Additionally, most TI materials such as Bi_2Te_3 and $Bi_{1-x}Sb_x$ do not exhibit their Fermi level within the bulk band gap under ambient conditions [69]. Further doping or electrical gating of these materials is necessary in order to access the surface states. A well-established example for doping is the change from binary to ternary TIs such as $(Bi_{1-x}Sb_x)_2Se_3$ [212], $(Bi_{1-x}Sb_x)_2Te_3$ [213] and Bi_2Te_2Se [214] achieving a surface state contribution of 6% in the latter. A combination of both doping and electrical gating results in the observation of ambipolar surface conduction in $(Bi_xSb_{1-x})_2Te_3$ [19] and Na-doped Bi_2Te_2 nanoplates [215]. Further strategies on the route to surface state investigations and manipulations by transport measurements are capping techniques [216] and the synthesis of TIs into heterostructures [217, 218].

Magneto**R**esistance (MR) measurements are currently one way of providing evidence for surface states in nanostructures via electrical transport [17, 23, 219, 220]. The interplay of many occurring transport phenomena, such as the **S**hubnikov-**d**e **H**aas (SdH), **A**haronov-**B**ohm (AB) oscillations and **W**eak **A**nti**l**ocalization (WAL) effects indicate transport supported by surface states and strong spin-orbit coupling [221]. For diameter- and angle-dependent MR measurements on curved Bi_2Te_3 nanowires, both SdH and AB oscillations as well as weak antilocalization were found hinting nontrivial topological surface states and trivial electronic states. All quantum effects were enhanced with smaller diameters indicating an increasing contribution of the surface states to the transport signal [25, 26]. These findings were complemented by investigations on rectangular shaped Bi_2Te_3 nanowires of different cross section areas pointing to surface state dominated transport [24]. Further magneto-transport experiments elucidate the influence of the fabrication method of Bi_2Te_3 nanowires [222]. Similar evidence of surface states were recently found in other TI nanoobjects, such as Sb_2Te_3 nanowires [223], Bi_2Se_3 nanostructures [17, 224] and Bi_2Se_3/Se coreshell nanowires [21].

The steadily improving sample quality and field-effect device fabrication techniques for TI nanostructures allowed for the combination of gate control and magneto-transport experiments enabling the tuning of the electrical band structure in, i.e. Bi_2Se_3 [225] and $(Bi_{1-x}Sb_x)_2Te_3$ [226]. MR investigations resolving the Dirac cone enable unambiguous evidence of the non-trivial topological nature of the surface states. Recently these measurements have been successfully conducted for Bi_2Te_3 nanowires with rectangular

cross section [27] and nanoribbons [28].
The present work aimed for the contacting of individual Bi_2Te_3 nanowires that are electrodeposited in PC membranes and establishing a good contact, despite of challenges rising from polymer residues and oxide layers. Two different lithography techniques were applied to contact individual Bi_2Te_3 nanowires, which are presented in section 5.2. Investigating the (magneto-)transport characteristics of nanowires of different diameters, finite size and quantum interference effects were studied as a function of wire size. In section 5.3, the two measurement setups to explore the magnetotransport properties of the contacted wires are introduced. Finally, sections 5.4 and 5.5 focus on the results of the magnetotransport investigations in pulsed and static magnetic fields, respectively.

5.1 Introduction to transport phenomena in magnetic fields

Various transport phenomena occur depending on the relation of the system dimensions to certain characteristic length scales describing charge carrier motions. Especially in micro- and nanostructures, these relations are tunable and different transport regimes are defined as schematically indicated in figure 5.1.1. In the following sections charge carriers are considered to be electrons.

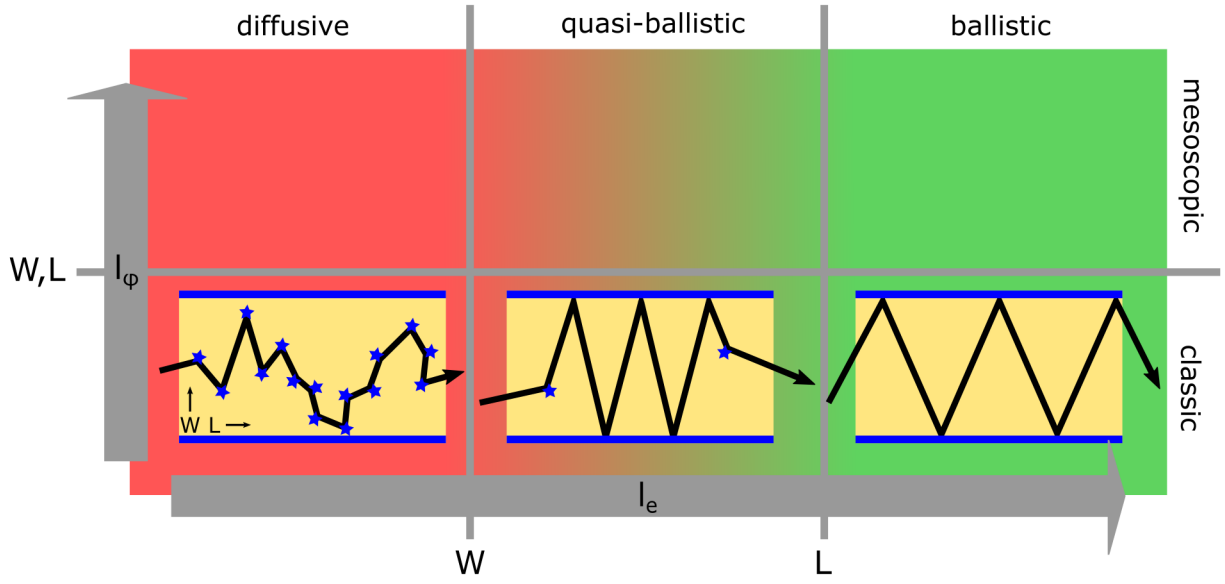

Figure 5.1.1: Schematic representation of the different transport regimes defined by relating the electron mean free path l_e and the phase coherence length l_φ to the sample size including width W and length L

Considering the relation between the electron mean free path l_e, which describes the length a carrier travels between two scattering events, and the system width W and length L three different regimes are distinguished. For $l_e < W, L$ (red), the individual charge carriers undergo many scattering events (blue stars) and follow a random walk motion. This regime is called diffusive regime because the overall charge transport is described by the diffusion of an electron gas as in the Drude model. If $l_e > W, L$ (green), the charge transport is limited by the scattering events with the system boundaries (blue lines). This regime is called ballistic transport. Furthermore, the intermediate state for which $W < l_e < L$

is called quasi-ballistic regime. It is worth mentioning that in systems with anisotropic scattering the carrier mean free path has to be replaced by an effective transport length [81, 227, 228].
Another characteristic length l_φ describes the phase coherence of the charge carrier wave which plays a crucial role for the occurrence of interference phenomena. Above this length, the phase changes and interference effects are averaged out. Thus, this length marks the transition between the quantum and the classical regime. This transport regime is typically realized in microscopic systems at very low temperatures and is referred to as mesoscopic.
When an external magnetic field is applied, the transport characteristics of a system are influenced in the transversal and longitudinal direction resulting in a Hall resistivity ρ_{xy} and magnetoresistance MR, respectively. The MR is commonly defined as

$$\mathrm{MR} = \frac{\rho_{xx}(B) - \rho_{xx}(B=0)}{\rho_{xx}(B=0)}, \tag{5.1}$$

with ρ_{xx} denoting the longitudinal resistivity. In the semiclassical Drude model, ρ_{xx} is predicted to be constant resulting in a zero magnetoresistance, while the Hall resistivity shows a linear dependency with respect to the B-field.[1]. Experimental observations disagree with the Drude model, since at higher magnetic fields and low temperatures oscillations of the longitudinal resistivity and plateaus in the Hall resistivity are found.
Besides oscillations, the magnetoresistance increases with the magnetic field until it either saturates (i), it continues increasing independent of the crystal orientation with respect to the B-field (ii) or it saturates only for certain crystal directions (iii). The reason for a material to belong to one of the three categories lies within its individual electronic structure. Materials with closed Fermi surfaces such as In, Al, Na and Li show MR behavior (i). Materials with equal numbers of different charge carriers (e.g. electrons and holes) like semimetals or semiconductors such as Bi, Sb exhibit the non-saturating behavior (ii). A crystal orientation-dependent MR (iii) is observed for materials with open orbits in their Fermi surface in certain directions such as Cu, Ag, Au, Mg, Zn, Cd, Ga, Tl, Sn, Pb, Pt [229] and doped Bi [230].
In the weak field regime a quadratic increase of the MR is expected according to Kohler's rule

$$\mathrm{MR} \approx (\mu B)^2, \tag{5.2}$$

which takes into account the carrier deflections induced by the Lorentz force [231].
However, for 3D topological insulators the magnetoresistance is experimentally found to be positive and linear [23, 232, 233]. Many different models describing the magnetoresistance behavior for each system exist and their introduction goes beyond the scope of this chapter. A commonly used explanation for the positive linear magnetoresistance was developed by Abrikosov. He assumed a zero-gap system with linear dispersion relation with only the first Landau level occupied in order to explain the linear MR in silver chalcogenides [234]. In that case the system is in the quantum limit and the effect is referred to as quantum magnetoresistance. For 3D topological insulators this explanation is not satisfactory, since the

[1] Employing Hall measurements at low magnetic fields is a common way to measure the charge carrier density n and mobility μ, since $\rho_{xx} = (ne\mu)^{-1}$ and $\rho_{xy} = B/ne$.

linear magnetoresistance is observed to be temperature-independent [232] and thus the system is not in the quantum limit. Wang and Lei considered the linear dispersion relation and a finite positive Zeeman energy splitting to model the temperature-independent MR over a wide range of magnetic field [235]. Besides the positive linear magnetoresistance which might be related to the extraordinary band structure of topological insulators, many other magnetoresistance effects shed light on the electronic transport properties. While the oscillations occurring in the longitudinal resistivity, called Shubnikov-de Haas oscillations, are due to Landau quantization, other phenomena, such as Aharanov-Bohm oscillations, weak anti-localization and universal quantum fluctuations, are attributed to quantum interference effects. The following sections introduce these effects briefly.

5.1.1 Shubnikov-de Haas oscillations

Shubnikov-de Haas (SdH) oscillations were first observed in bismuth rods [236] and arise due to the quantization of the density of states in consequence of the formation of Landau levels. An electron with mass m and charge e exposed to a magnetic field B describes a circular motion with a cyclotron frequency of $\omega_c = eB/m$ as schematically shown in figure 5.1.2 (a). In the case of the electron path consisting of at least one full orbit (upper image), the electronic wave function can interfere with itself. This condition is fulfilled if

$$r_e < l_e, \tag{5.3}$$

with r_e being the radius of the orbit. The lower schematic in (a) displays the case when electrons are not describing a full circle due to their decreased mean free path.

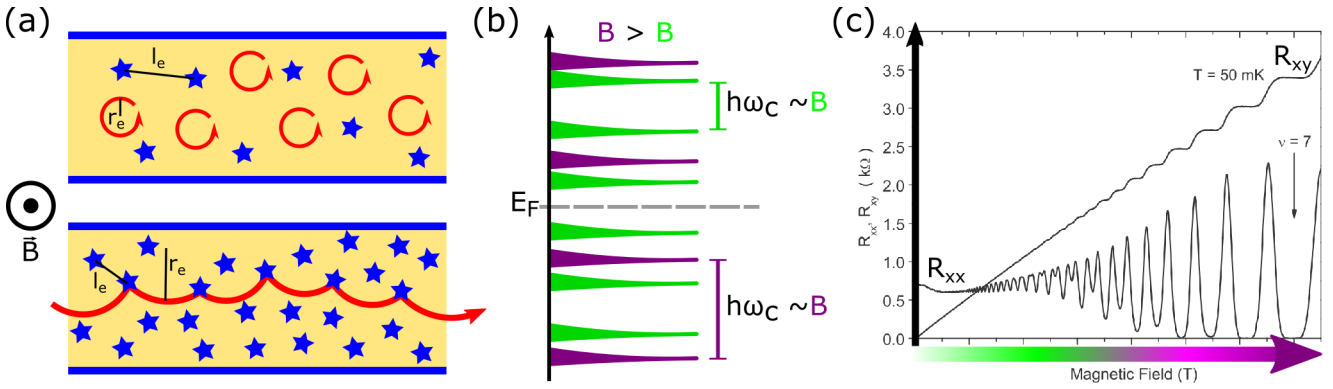

Figure 5.1.2: Shubnikov-de Haas oscillations: (a) shows the electron motion (red) in an external B-field if $r_e < l_e$ (upper schematic) describing full circles and if $r_e > l_e$ (lower schematic). The stars represent scattering events. (b) depicts the Landau level quantization and widening of the energy gap with increasing B-field. (c) presents experimental magnetotransport data of an AlGaN/GaN heterostructure in Hall bar configuration exhibiting Hall plateaus for R_{xy} and SdH oscillations for R_{xx} [237] IOP Publishing. Reproduced with permission. All rights reserved

The interference of the wave functions leads to a quantization of the energy states as depicted in figure 5.1.2 (b). The Hamiltonian resembles the one of the 1D quantum mechanical harmonic oscillator with the energy eigenvalues E_{LL} of

$$E_{LL} = \hbar\omega_c(LL + 1/2), \tag{5.4}$$

with LL denoting the index of the **L**andau **L**evel (LL). The Landau quantization is also the underlying mechanism of the quantum Hall effect resulting in plateaus in ρ_{xy} at high magnetic fields and at low temperatures (chapter 1.1.1). Following, the energy quantization leads to the discretization of the **D**ensity **O**f **S**tates (DOS). The DOS splits into δ-functions located at E_{LL} and separated by an energy gap of $\hbar\omega_c = \hbar eB/m$ being magnetic field dependent. Figure 5.1.2 (b) schematically shows the DOS for two different applied magnetic fields (green and purple). In real systems, perturbations induced by e.g. disorder or charged dopants, yield a broadening of the Landau levels due to the finite lifetime of the charge carriers τ_q. With increasing magnetic field the energy gap between the Landau levels widens. Subsequently, the Landau levels pass through the Fermi energy causing oscillations in the density of states which manifest as an oscillatory magnetoresistivity. Figure 5.1.2 (c) displays typical results when measuring the transverse and longitudinal magnetoresistance, R_{xy} and R_{xx}, of a 2DEG forming in an AlGaN/GaN heterostructure. R_{xy} exhibits Hall plateaus, while the SdH oscillations are observed for R_{xx}. The derivation of an expression for the oscillating longitudinal magnetoresistivity ρ_{xx} is rather complex and the result shall be mentioned here only for the sake of completeness

$$\rho_{xx}(B,T) = \underbrace{\frac{m^\star}{ne^2\tau_0}}_{\text{Drude}} \cdot \left[1 - 2\overbrace{e^{-\pi/(\omega_c\tau_q)}}^{\text{Dingle}} \frac{\lambda(T)}{\sinh(\lambda(T))} \cos\left(2\pi \cdot \frac{\hbar n}{2eB}\right)\right], \tag{5.5}$$

with $\lambda(T) = 2\pi^2 kT/(\hbar\omega_c)$ describing the temperature dependency of the oscillation amplitude [238]. This expression shows that ρ_{xx} oscillates with a $1/B$ periodicity around the classical Drude resistivity. Increasing the temperature leads to a decrease of the oscillation amplitude. The exponential contribution to the amplitude, called Dingle factor takes the finite carrier lifetime τ_q and thus the Landau level broadening into account. This result demonstrates how specific material properties such as carrier density n, lifetime τ_q and effective mass $m^\star$ are deducible from the analysis of the SdH oscillations. For example, minima of the SdH oscillations occur if

$$\frac{\hbar n}{2eB} = i + \gamma, \tag{5.6}$$

with i being an integer denoting the minimum index and γ being a constant. By plotting this index over $1/B$, the density of states can be extracted from the slope of the resulting linear relation which is $\hbar n/(2e)$. The y-axis intercept γ is closely related to the Berry phase and yields 1/2 for conventional metals and zero in topological insulators, i.e. in the Dirac case [25, 239, 240].

5.1.2 Weak (anti-)localization

Localization effects appear in systems with a large phase coherent length, such that $l_\varphi > l_e$, which is typically realized at very low temperatures. In such a case phase-coherent multiple scattering and thus interference effects leading to an enhanced backscattering have to be carefully examined. Simple schematics of both, the weak localization and weak antilocalization effect are displayed in figure 5.1.3. Assuming multiple scattering of an electron in such a way that it returns to its original starting point, two time-reversed paths (red and dark red) are possible.

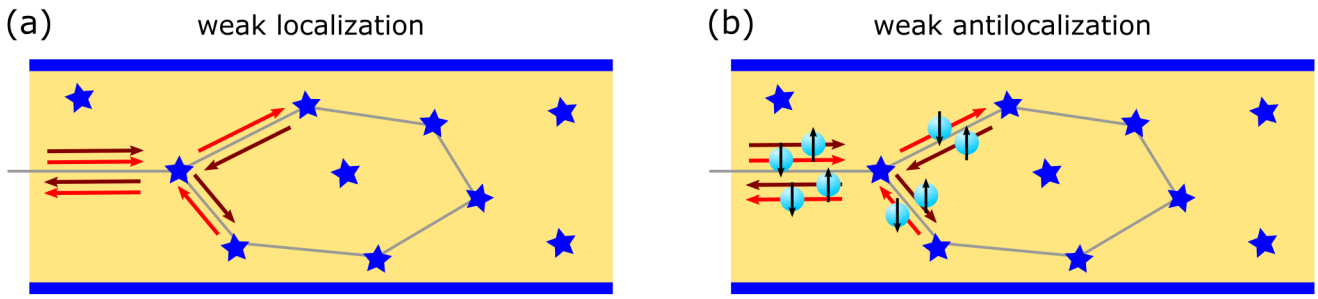

Figure 5.1.3: Schematic representation of weak localization (a) and weak antilocalization (b). The directions of motion along the path (gray) between scattering events (blue stars) are given in red and dark red. The spin directions of the electrons (cyan) are represented by black arrows in (b).

The probability for the electron to return to the starting point is given by

$$|A_1 + A_2|^2 = \underbrace{|A_1|^2 + |A_2|^2}_{\text{classical backscattering}} + \underbrace{A_1 A_2^* + A_1^* A_2}_{\text{interferences}}, \tag{5.7}$$

with A_1 and A_2 being the complex probability amplitudes of the two paths (e.g. clockwise and counter-clockwise). On the right hand side, the first two terms are considered in the classical Drude-Boltzmann theory, while the interference terms are neglected. In the case of time-reversal symmetry, i.e. without magnetic field, the amplitudes for both paths are equal, $A_1 = A_2 \equiv A$. For this reason the classical contributions provide a return probability $\mathscr{P}_{\text{classical}}$ of

$$\mathscr{P}_{\text{classical}} = 2\,|A|^2\,. \tag{5.8}$$

On the other hand, considering the interference terms gives

$$\mathscr{P}_{\text{qm}} = 4\,|A|^2\,, \tag{5.9}$$

which is a two times higher probability for the electron to return, enhancing the backscattering. Consequently, the resistivity of the sample is increased and this effect is called **W**eak **l**ocalization (WL).

In a magnetic field the WL is suppressed, because it directly influences the phase of the path amplitude adding an Aharonov-Bohm phase $\pm\varphi_{AB}$ with the sign depending on the path direction. Hence, the constructive interference due to time-reversal symmetry is lost and the classical value is approached. Furthermore, WL is destroyed at elevated temperatures, because the phase coherence length decreases. Plotting the resistivity versus the magnetic field, the ratio l_φ/l_e determines the shape of the resistivity increase at zero magnetic field due to WL. As the l_φ/l_e decreases the peak becomes broader and eventually vanishes.

In systems with strong **S**pin-**O**rbit **C**oupling (SOC) a related effect called weak anti-localization (WAL) is observed, which exhibits a decrease in resistivity. This effect is explained by the spin-orbit interaction induced spin rotation of the electron during the scattering process. On the time-reversed path the spin rotation is reversed. Introducing the spin-orbit time τ_{SO} defined as the time it takes to completely randomize the spin due to SOC, the WL case is recovered if $\tau_{SO} > \tau_\varphi$.[2] In the opposite case of $\tau_{SO} < \tau_\varphi$, the randomization of the spin orientation leads to a dominating destructive interference [241]. Compared to WL, the backscattering probability in WAL is reduced resulting in a decrease of resistivity.

Topological insulators are expected to exhibit WAL. Due to their spin-momentum locking, the spins on two time-reversed paths always differ by a rotation of π (black arrows). This corresponds to a Berry phase of $\pm\pi/2$ acquired by each path, resulting in a total Berry phase difference of π and thus destructive interference [242]. Analogous to WL, the WAL is destroyed in magnetic fields and at elevated temperatures.

The dependency of the conductivity correction $\Delta\sigma = \Delta\rho^{-1}$ due to localization effects on the magnetic field was described by **H**ikami, **L**arkin and **N**agaoka (HLN) and yields

$$\Delta\sigma = \alpha\frac{e^2}{\hbar}\left[\ln\left(\frac{\hbar}{4eBl_\varphi^2}\right) - \Psi\left(\frac{1}{2}+\frac{\hbar}{4eBl_\varphi^2}\right)\right] \tag{5.10}$$

with α being a constant indicating WL for $\alpha = 1$ and WAL for $\alpha = -1/2$ [243]. From this relation the phase coherence length l_φ can be determined.

5.1.3 Aharonov-Bohm effect

In contrast to Shubnikov-de Haas oscillations, which appear as a consequence of Landau quantization, Aharonov-Bohm (AB) oscillations arise due to quantum interference effects [244].

Aharonov and Bohm considered electrons circulating around a magnetic flux $\Phi = \oint_C \mathbf{A}d\mathbf{s}$, where $\mathbf{A}$ denotes the vector potential, confined to a cylindrical geometry represented by the curve C. Despite the electrons not being exposed to the magnetic field B itself, they acquire a so called Aharonov-Bohm phase of

$$\Delta_{AB} = -\frac{e}{\hbar}\oint_C \mathbf{A}d\mathbf{s} = -2\pi\frac{e}{h}\Phi = -2\pi\frac{\Phi}{\Phi_0}, \tag{5.11}$$

[2] The phase coherence time τ_φ is connected to the phase coherence length via $l_\varphi = v_{Fermi}\tau_\varphi$, with v_{Fermi} being the Fermi velocity.

with $\Phi_0 \equiv h/e$ defined as the magnetic flux quantum[3].
Imagining a metallic ring enclosing a magnetic flux with two contacts at positions (0 and π) as shown in figure 5.1.4 (a), there exist two possible propagating paths for the electron partial wave between the contacts. The wave traveling clockwise $|\psi_1\rangle$ (green) acquires a phase of $\pi\frac{\Phi}{\Phi_0}$, while propagating counterclockwise $|\psi_2\rangle$ (red) exhibits a phase of $-\pi\frac{\Phi}{\Phi_0}$. Hence, the transmission probability $\mathcal{T}$ of the electron between the two contacts is related to the interference of the partial waves as

$$\mathcal{T} = |\langle\psi_1|\psi_2\rangle|^2 \propto \cos\left(2\pi\frac{\Phi}{\Phi_0}\right), \tag{5.12}$$

causing an oscillation with periodicity Φ/Φ_0. Taking into account the measurable quantities magnetic field B and cross section area of the ring S, related to the magnetic flux as $\Phi = B \cdot S$, the periodicity yields

$$\Delta B = \frac{h}{eS} = \frac{\Phi_0}{S}. \tag{5.13}$$

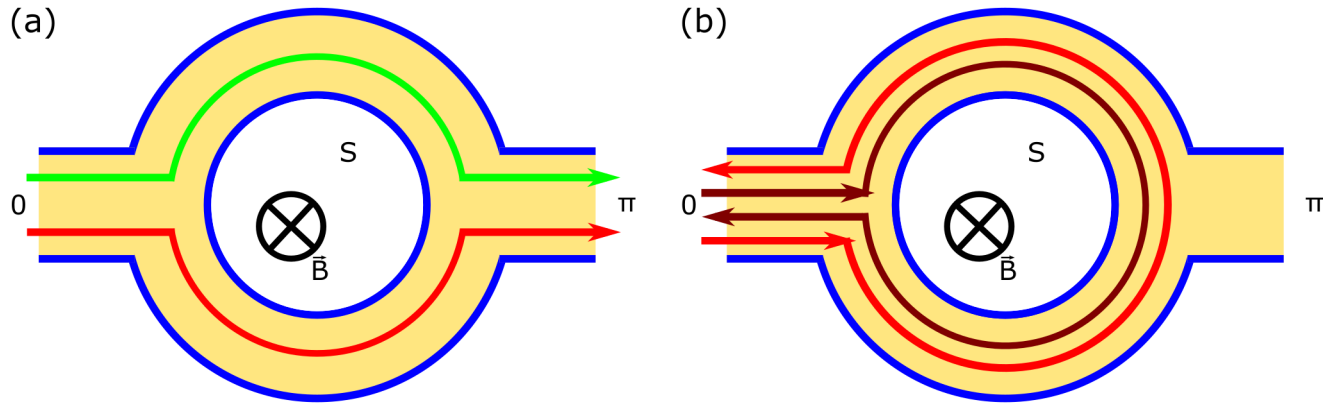

Figure 5.1.4: Schematics of possible propagating paths (green, red and dark red) for electrons inside a metallic ring (yellow) enclosing the area S between contacts 0 and π under an external magnetic field B. The Aharanov-Bohm effect (a) describes interferences after half revolutions, while the Altshuler-Aronov-Spivak effect (b) considers interferences between time-reversal paths.

Besides interference of the partial waves after half revolutions of the ring, interferences of time-reversal paths, i.e. counter-propagating full revolutions of the ring, have to be considered (red and dark red). This situation is displayed in figure 5.1.4 (b). In that case, an enhancement of backscattering is expected similar to weak localization effect explained in more detail in the previous section. Yielding also B-field-dependent oscillations with periodicity of

$$\Delta B = \frac{h}{2eS} = \frac{\Phi_0}{2S}. \tag{5.14}$$

[3] Aharonov and Bohm intended to show that the vector potential A is not only a mathematical construct, but has a physical meaning.

this is called the **A**ltshuler-**A**ronov-**S**pivak (AAS) effect.
Both effects are limited to a transport regime in which the phase coherent length l_ϕ is larger than the diameter of the ring. Consequently, the AB and AAS oscillations are best observed at very low temperatures and vanish with increasing temperature. Furthermore, in experiments the influence of the Lorentz force creating a circular motion of the electrons has to be considered. In the weak field regime enforcing a large cyclotron radius r_c the Lorentz force is negligible.
AB and AAS differ in the sense that the AB oscillations depend on the geometry and dimensions of the observed system, while the AAS oscillations only relate to the time-reversibility of the paths. In other words the AB oscillations are expected to average out in a sample consisting of many rings in series (e.g. a cylinder), while AAS are insensitive to sample-averaging [81, 238].
Applying a magnetic field along a topological insulator nanowire exactly replicates the experiment geometry to probe the AB and AAS oscillations, because the topological surface states form a ring enclosing a magnetic flux. Investigating the longitudinal magnetoresistance, an oscillating period of Φ_0 is expected with the maximum at $\Phi_0/2$ and a minimum at $B = 0$ [245, 246]. The first experimental observation of AB oscillations in TI materials were realized in Bi_3Se_3 nanoribbons (rectangular cross section) synthesized by gold-catalyzed VLS growth [17]. Since then, observing AB and AAS oscillations in the magnetoresistance behavior of TI nanowires and nanoribbons is a common technique to provide direct evidence of topological surface states [24, 223, 247].

5.1.4 Universal conductance fluctuations

In a diffusive regime ($l_e < L, W$) with the phase coherence length exceeding the size of the system ($L, W < l_\varphi$) another type of interference effect appears. In such a sample many different scattering paths forming closed loops (backscattering) are available which lead to interference effects similar to the situation described for WL and WAL in section 5.1.2. Each loop circumferences a different area gaining a phase difference which is specific to the distribution of scattering centers, i.e. defects. In this case, resulting conductance fluctuations of about e^2/h are not averaged out and are only dependent on the configuration of defects instead of the sample geometry (see AB effect). This is why they are called universal conductance fluctuations. If the defect configuration is modified, the interference paths change randomly. Hence, every sample exhibits conductance fluctuations specific to its defect distribution. An external magnetic field adds a randomized relative phase to each interfering path, resulting in the conductance oscillation as the B-field is ramped [238].
As for the phenomena described previously, universal conductance fluctuations vanish with increasing temperature. From the analysis of the magnetoconductance behavior the phase coherence length can be determined, but no direct information about surface states can be drawn.

5.2 Single nanowire contacting

For transport measurements on single nanowires, different approaches to establish an electrical contact are available. One exceptional method is to contact a single nanowire electrodeposited in membranes with a single pore [248]. Making use of the working electrode as one contact, the nanowire cap outgrowing the membrane (see section 2.3) serves as a second contact to establish a two-point configuration.

These contacts offer a very high-quality ohmic contact, because they are immediately created during the fabrication process of the nanowires. Naturally, this method is also applicable for contacting nanowire arrays employing multi-pore membranes.
Since single nanowires embedded in a single-pore membrane constitute a special configuration and only offer two-point contacting, the most commonly used techniques are lithographic methods such as optical, electron beam and laser scanning lithography. The term lithography is a composition of the ancient greek words for "stone" ("lithos") and "to write" ("graphein") and was firstly used as a macroscopic printing technique. Nowadays, a world without lithography is unimaginable, since it is required for micro- and nanoelectronic chip fabrication and thus crucial for the existence of almost every electronic computing device.
Modern-day lithography for micro- and nanostructuring is similar to the developing of a conventional photo and is schematically presented in figure 5.2.1. Analogous to a photographic film, the light-sensitive area in lithography processes is provided by a so-called resist, a polymer, which is typically spin-coated onto the sample of choice (1, 2). When exposing this resist to a suitable light or electron source, it is chemically modified either in a way that the solubility of the exposed area is enhanced or reduced. Taking advantage of this modification, patterns of areas of different solubility are created in the resist (3). By employing a suitable developer the areas of higher solubility are selectively removed (4). Two different kinds of resists are distinguished: The so-called "positive" resist exhibits a higher solubility in the exposed areas (as presented in figure 5.2.1), while the "negative" resist shows higher solubility of the non-exposed areas. After development, the complete structure is coated by the desired contact material using different coating techniques, such as sputtering or evaporation. Since for electrical contact a metal is required, this step is also referred to as metalization (5). In the last step, the remaining resist including the coating layer is removed employing a suitable remover. This step is called liftoff and the remaining coating replicates the developed structure, which corresponds to the exposed area when using a positive resist (6).
Before employing lithographic techniques, a suitable resist type and an appropriate exposure technique have to be chosen. Depending on the required resolution of the structure and the economic demands, the (light-)source is selected. Electron beams expose structures as fine as below 1 nm, while laser-scanning techniques provide in general less resolution. On the other hand, the optical lithography employing a mask is unbeatable in terms of economic efficiency, because **E**lectron **B**eam **L**ithography (EBL) is limited by a time consuming sample alignment process.
Furthermore, the lithography techniques are grouped in maskless (direct-write) and masked lithography. In direct-write techniques the light or electron source is provided in the form of a focused beam that is scanned over the sample and directly exposes the resist in the desired areas. Masked techniques require a pre-fabricated mask replicating the lithography design. By placing the mask between the sample and a diffuse light source, the resist is exposed within the desired areas. Masks can be reused many times and, once fabricated, offer a fast way of producing large amounts of structures. For this reason the masked methods are favored for industrial chip production. In contrast, direct-write methods are slower in exposure, but offer a higher design flexibility.

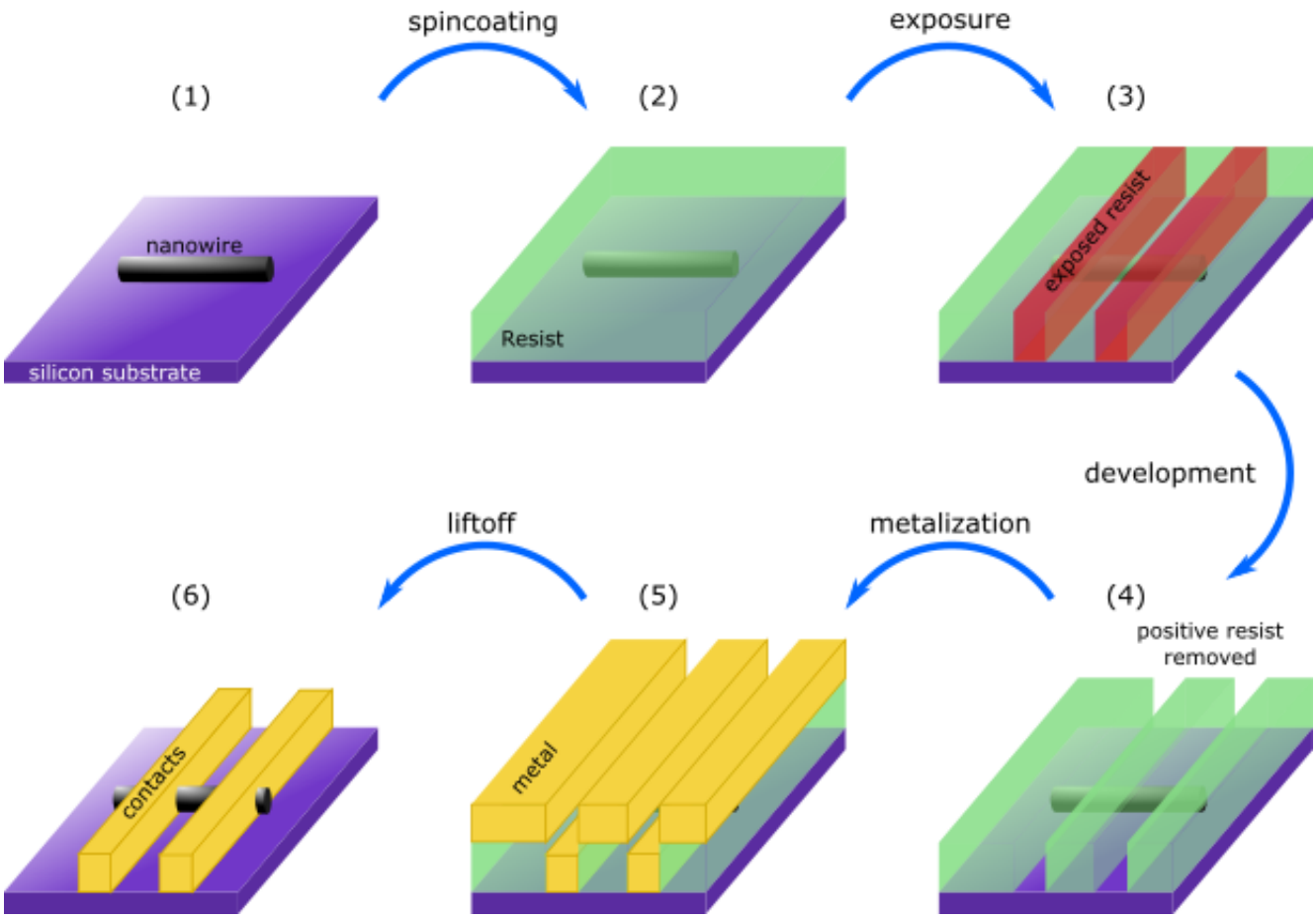

Figure 5.2.1: Schematic presentation of the process steps (1-6) to contact an individual nanowire lying on a silicon substrate by lithographical methods.

In this work, individual nanowires were contacted by optical laser scanning as well as electron beam lithography which are both direct-write methods. The laser scanning lithography was performed at GSI using a Heidelberg Instruments μPG 101 with a Laser with 405 nm wavelength. EBL was performed in various facilities within the involved collaborations for transport measurements employing a Raith150 (Raith) at the **L**aboratoire **N**ational des **C**hamps **M**agnétiques **I**ntenses (LNCMI) in Toulouse and a NVision 40 (Carl Zeiss) at the Leibniz-**I**nstitut für **F**estkörper- und **W**erkstoffforschung (IFW) in Dresden.
Lithography is a multi-step process in which the many parameters defining each fabrication step have to be carefully chosen in order to obtain the best results for each experiment. The following sections describe the process for the single Bi_2Te_3 nanowire contacting performed in this work in more detail.

5.2.1 Laser scanning lithography

The complete laser lithography process at GSI was made available in 2014. Firstly, the parameter in each lithography step had to be optimized for the use of contacting individual nanowires. This work was started by Dr. Loïc Burr for gold nanowires [249] and carried out in collaboration with Fatima Boui [250] and Lisette Haarmann [251] for Bi_2Te_3 nanowires of different thicknesses.
For all lithography processes the Bi_2Te_3 nanowires were transferred onto p-doped silicon substrates with

and without 100 nm thick thermal oxide using the methods described in section 2.4. After the wire transfer and before spincoating the resist, the samples were rinsed in acetone and isopropanol for several seconds and subsequently blow dried using nitrogen.
Two different positive resists of about 0.5 µm (AZ1505) and 1.8 µm (AZ1518) thickness were used and compared. In general, the height variation of the substrate should be much smaller than the resist thickness to guarantee overall coverage. In the present case of up to 150 nm thick nanowires, choosing a thin resist (0.5 µm) is reasonable. Nevertheless, figure 5.2.2 illustrates the motivation behind comparing the two resists for perfectly sharp edges (left) and flanks (right). After the metalization, the lift off process might be hindered by the interconnection of the metalized layer due to resist flanks. The ratio of the thickness of the layer to that of the resist has to be taken into account. In the case of vertical resist edges (a, c), the metallic areas on top of the developed structure and the remaining resist do not get in contact and the resist is easily soluble. If the developed edges exhibit flanks, the metallic layer interconnects and blocks the dissolution of the resist and thus the liftoff process. By employing a thicker resist, this effect can be minimized as schematically shown by comparing figures 5.2.2 (b) and (d).

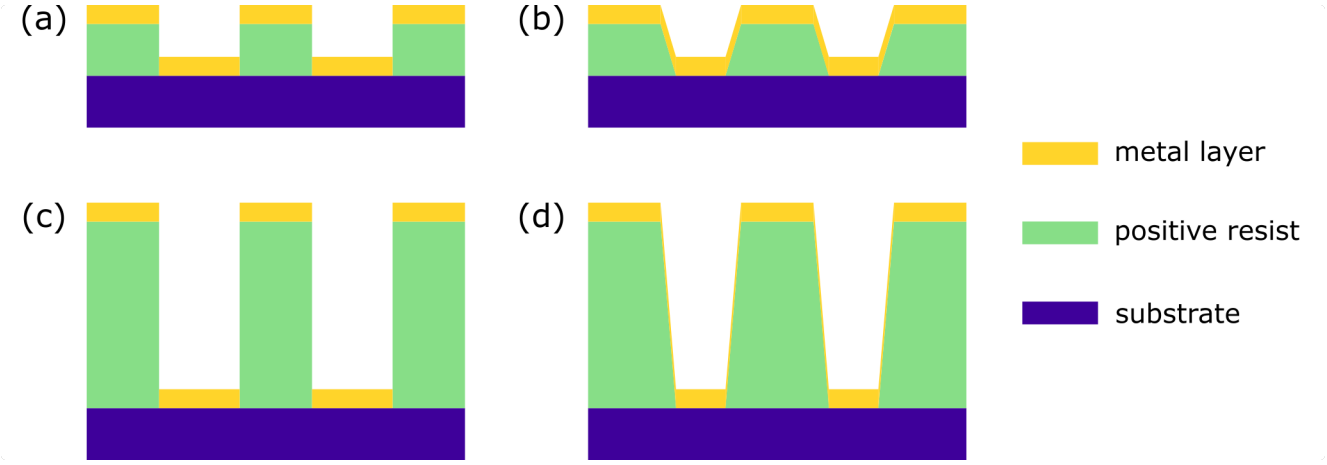

Figure 5.2.2: Schematic presentation of the relation between the photoresist thickness and the liftoff quality for (a,b) thin and (c,d) thick resist.

In order to obtain a uniform resist layer by spincoating, the spinning velocity and the coating time are adjustable. In the present case, both resist types were spincoated at 4000 rpm for 40 sec. To stabilize the resist, the sample was baked on a hot plate at 100°C for 30 to 108 sec. Subsequently, the individual nanowires and the location of exposure were easily identified in the optical microscope of the µPG 101. The exposure of the resist was adjusted using two parameters, the laser output power and the pixel pulse duration, i.e. exposure time per pixel, which were changed between 5-20 mW and 10-90 %, respectively, depending on the kind of resist applied. For both resists, the corresponding developer AZ 351B was used in a recommended 1:4 and a 1:6 dilution with deionized water. The developing time was varied between 30 s and 180 s and the sample was rinsed in a flow of deionized water for about 1 min afterwards. Before sputter coating the metallic contact consisting of a Cr/Au layer, the sample was Ar plasma cleaned (500 V acceleration voltage for several seconds) to remove resist rests and the usually forming oxide layer. In the last step, the liftoff was performed by immersing the samples in an aceton bath at room temperature. Table 5.2.1 summarizes all combinations of parameters tested for both kinds of resists. The parameters

to obtain the best result are highlighted in the red and blue depending on the resist used.

Table 5.2.1: Parameters used in each step of the laser scanning lithography process for two positive resist of different thicknesses: AZ1505 (0.5 µm, red) and AZ1518 (1.8 µm, blue). The exposure and development parameters giving the best results are highlighted in color.

Step	Parameter	AZ1505	AZ1518 A	AZ1518 B
Spin coating	Spinning (rpm)	4000	4000	4000
	Time (sec)	40	40	40
Baking	Temperature (°C)	100	100	100
	Time (sec)	30	108	108
Exposure	Laser output power (mW)	**10**, 15, 20	5, 7, 10, 11, **12**	10, 11, 12, 13
	Pixel pulse duration (%)	60, **70**, 80	10, 35, **70**	50, 70, 90
Development	Dilution	**1:4**	**1:4**	1:6
	Time (sec)	30, 35, **40**	40, 45, **50**	60, 180
Metalization	Ar plasma (sec)	10	60	60
	Cr (nm)/Au (nm)	5/100	10/145	10/145

Criteria for good results are exactly replicated, well-resolved designs with sharp edges as well as minimal flanks after the development and after the liftoff. In order to qualify, the lithography results were compared on the basis of optical microscopy images recorded after both steps. Figure 5.2.3 gives an example of an under-developed (a), an ideal (b) and an over-developed (c) structure. All three times a specially developed test design including structures with distances down to the resolution limit of 1 µm given by Heidelberg Instruments was exposed and developed.

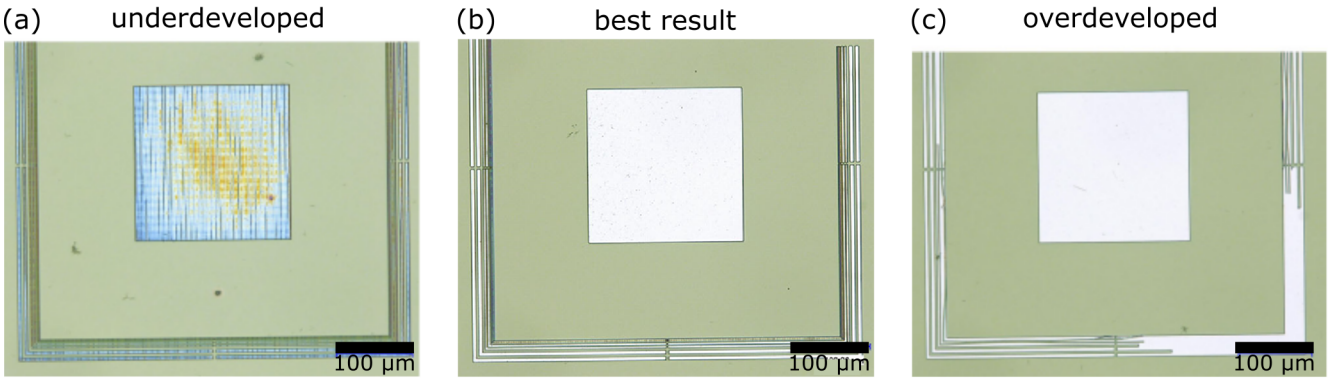

Figure 5.2.3: Optical micrographs after the development of a test design: (a) under-developed result with interference colors indicating resist rests. (b) best result with a defined structure. (c) over-developed structure merging the fine structure lines.

The line structure is arranged as an open frame around a squared marker. Not exposed areas that are still covered by resist of the original thickness, appear green. The optical micrograph in (a) shows an under-developed structure indicated by the interference colors of a remaining resist film inside the square and also the lines. The opposite effect is found in (c) displaying an over-exposed structure: While the middle square is perfectly defined, the lines within the frame are merged into each other and thus not well resolved. Both cases should be avoided to obtain the best parameters for a successful lithography process. For comparison, the ideal development of the structure is displayed in figure 5.2.3 (b).
Figure 5.2.4 displays representative optical micrographs for standard four-point structures (2 µm contact width) after the development (a, c) and after the liftoff (b, d) for both resist types using the best parameter combination investigated. In both cases the structure is well resolved after the development and nicely replicated after the liftoff. The contacted nanowire is clearly visible and covered by at least two contacts. Fibers of metal that are found attached to the contacts still require for an optimization of the liftoff process (d). More details of the lithography optimization process can be found in [250, 251].

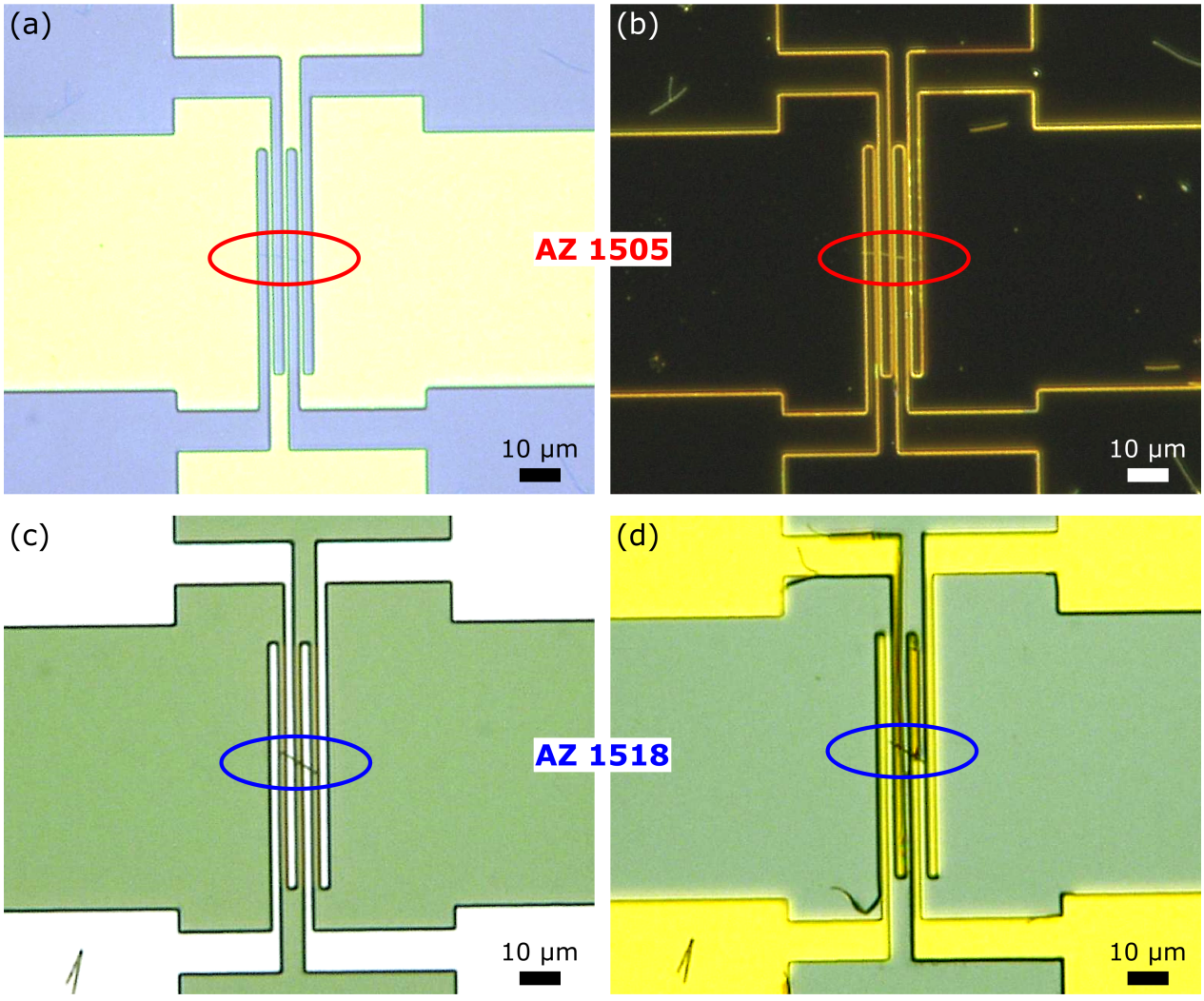

Figure 5.2.4: Representative optical microscopy images of a standard four-point structure using AZ 1505 (a, b) and AZ 1518 (c, d) showing the structures after the development (a, c) and after the liftoff (b, d). Image (b) is recorded with indirect light.

5.2.2 Electron beam lithography

Electron beam lithography (EBL) was carried out to contact individual nanowires for magnetoresistance measurements, because it offers a higher resolution and thus smaller contact distances. Considering that the electrodeposited Bi_2Te_3 nanowires consist of several hundred nanometer long single crystalline grains, the probability of measuring only one grain, is enhanced by patterning smaller contact distances. Two different setups were used, one within a cleanroom environment at the **L**aboratoire d'**A**nalyse et d'**A**rchitecture des **S**ystème (LAAS) in Toulouse, the second one at the Leibniz-**I**nstitut für **F**estkörper- und **W**erkstoffforschung (IFW) in Dresden. For simplicity reasons only the sample preparation carried out in Dresden is presented here. Employing EBL for contacting small nanostructures of bismuth compounds is a well established procedure for both collaborators.

The sample used for EBL is prepared in the same way as for the laser lithography (see section 5.2.1). In some cases the substrate was pre-patterned with metallic markers to align the nanowire to the desired contact design before exposure. This is necessary, because using the electron beam for imaging would immediately expose the area of interest. In contrast to the μPG 101 laser lithography there is no integrated optical microscope available and thus it is not possible to search for the nanowire online. Instead, the nanowires are located and chosen with respect to those markers outside of the EBL using an optical microscope. For the substrates without pre-patterned markers, orientation markers are firstly created close to the nanowires. Following, a contact structure with up to ten contact lines were designed individually for each chosen wire using a suitable software such as Klayout or others. Afterwards, the electron-sensitive positive resist, here polymethyl methacrylate (PMMA), also known as acrylic glass, is spincoated (AR-P 672.05, 4000 rpm for 30 sec) onto the sample and pre-baked (150°C, 10 min). Subsequently, the exposed structures were developed in a suitable developer (MIBK-1P diluted 1:3) for about 1.5 min. All structures were Ar plasma cleaned for 1 min prior to the metalization of 5 nm Cr and 70 nm Au. The liftoff was carried out in acetone at room temperature and lasted several hours up to days.

Figure 5.2.5 shows a representative series of SEM images of a successfully contacted Bi_2Te_3 nanowire of 50 nm diameter. Six contact lines of distances between 240 nm and 1 μm are distributed over about half the length of the nanowire. The images (a-c) display top views of the nanowire employing different magnifications. Four alignment markers in the shape of crosses and a tag "N_c" are visible. Images (d-f) show the nanowire under a 60° tilt to the electron beam. Images (d) and (e) are rotated horizontally by about 90° to (c) giving a side view of the contacts. The complete coverage of the nanowire by the metallic contact and their precise definition are clearly observable in (f). The contacts are about 500 nm wide and exhibit sharp edges.

Concluding from the SEM images an electrical contact should be established for this nanowire. Nevertheless, it is not sufficient to judge the quality of the contacts by microscopy images, since the electrical contact is influenced by the interface between the nanowire and the contact metal. For instance, if an oxide layer forming on the surface of Bi_2Te_3 is not removed thoroughly by Ar plasma cleaning, an insulating or capacitive layer is preventing good ohmic contact.

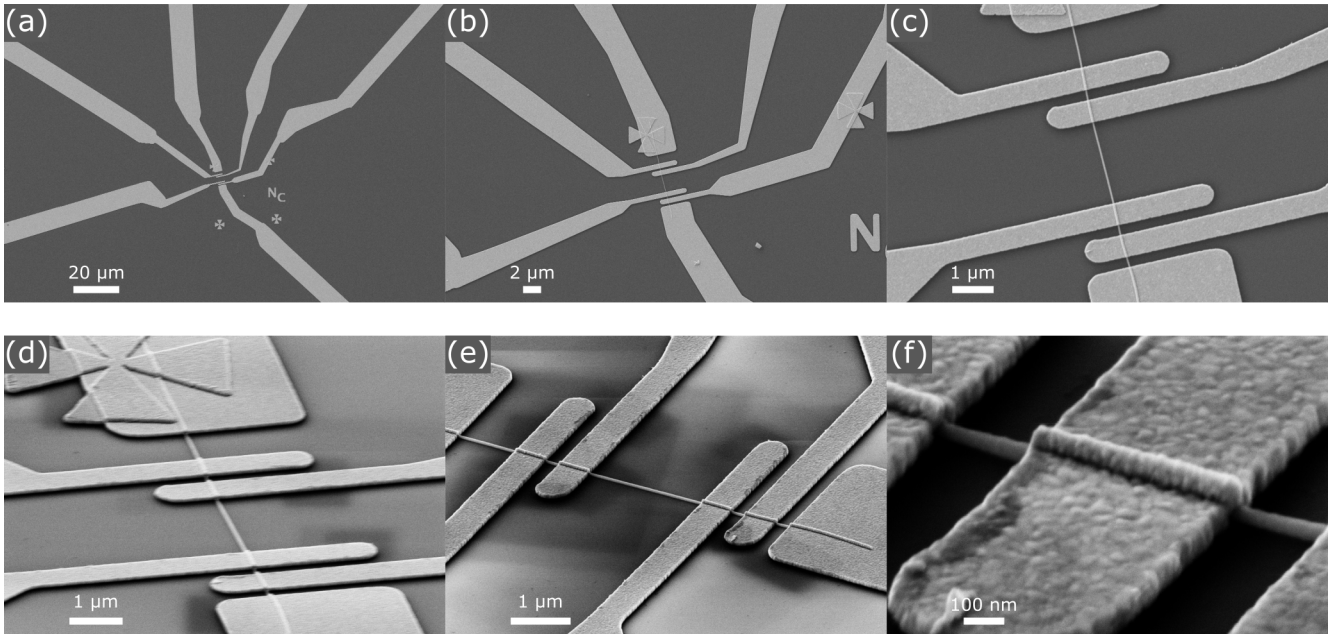

Figure 5.2.5: SEM images of a single Bi_2Te_3 nanowire of 50 nm diameter contacted by electron beam lithography (EBL). (a-c) shows top views of six contacts lines of various distances with different magnifications. (d-f) displays a view under 60° recorded with different magnifications.

5.3 Setup - magnetoresistance measurements at low temperature

Magnetoresistance measurements were performed down to liquid helium temperatures in two setups providing different magnetic fields. At the LNCMI in Toulouse, a pulsed magnetic field of up to 55 T was applied. The IFW in Dresden provides a static 2D magnetic field with 1 T in x-direction and simultaneously up to 12 T in z-direction. Making use of the on-site EBL facilities, about half of the nanowire samples were directly contacted in Toulouse and Dresden following the description in 5.2.2.
Measuring at low temperatures requires mounting the samples on an insert (about 1.5 m long) that was introduced into a cryostat. For electrical transport measurements, the samples were wire bonded to a chip carrier which is mounted on one end of the insert. Figure 5.3.1 (a) shows one sample mounted on the chip carrier socket with 24 pins at the end of the insert (IFW setup). Additionally to the electrical connections for sourcing and measuring, a thermometer is located in the vicinity of the sample for temperature control. After insertion into the cryostat, the corresponding nanowire contacts were connected to perform low noise measurements of small signals using lock-in amplifiers (Stanford Research Systems Model SR830 DSP) and compensation techniques. More details on the low noise electrical measurement setup at IFW and LNCMI are available in [252] and [253], respectively. Figures 5.3.1 (a) and (b) present a picture of the cryostat containing the magnet with installed insert of the setup used at IFW Dresden. The setup at LNCMI in Toulouse follows a similar scheme.

Pulsed magnetic field

The pulsed magnetic field is created by discharging a series of capacitors through an electromagnetic coil following the principle of a conventional electromagnet. The coils are specially developed at

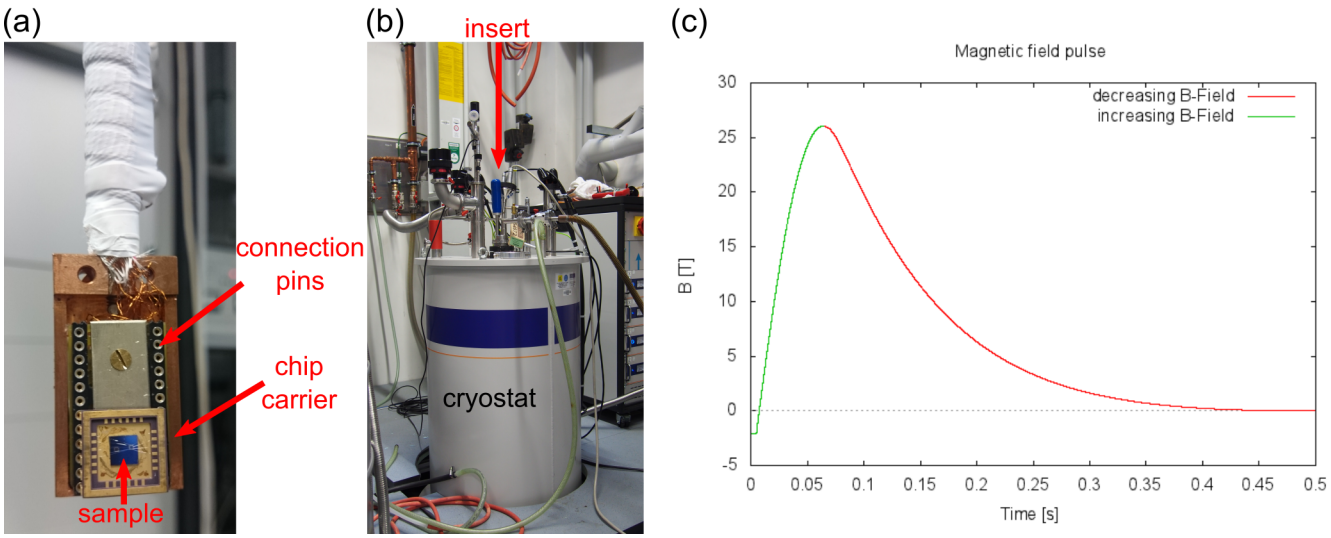

Figure 5.3.1: Photos of the magnetoresistance measurement setup at IFW in Dresden: (a) the sample wire-bonded on a chip carrier and mounted at the end of the insert. (b) the cryostat containing the magnet and the insert. (c) Profile of the magnetic field pulse at LNCMI in Toulouse.

LNCMI [254]. Together with a capacitor bench of 15 MJ, pulsed magnetic fields up to 60 T are generated. The current passes through the coil within about 0.5 sec and is adjustable in order to obtain the desired intensity of the magnetic field. Figure 5.3.1 (c) presents the profile of the magnetic field as a function of time. One notices that the increase and decrease of the magnetic field is not symmetric with its shape depending on the employed coil [255]. After one pulse the coil has to cool down, which takes about 40 min after a 60 T pulse [253].
For the magnetotransport measurements in pulsed magnetic fields performed in this work, a DC current of 10 μA was applied to Bi_2Te_3 nanowires with diameters of 25 and 75 nm contacted in a two-point configuration.

Static magnetic field

In contrast to the short, but high intense pulsed magnetic field, a superconducting magnet provides long term fields that can be swept at different rates from mT/sec to persistent modes. Superconducting magnets are commercially available. At the IFW a magnetic fields of up to 1 T were employed perpendicular and up to 12 T parallel to the nanowire axis. For low magnetic field investigations of the weak antilocalization effect at LNCMI, a superconducting magnet generating field of up to 5 T was used.
In this work, nanowires investigated in a static magnetic field at IFW were of 50 nm and 100 nm diameter. DC currents between 20 and 50 A were applied in two- and four-point configuration. In the static field setup at LNCMI the 85 nm diameter nanowire was investigated by applying 10 μA DC current in a two-point configuration.

5.4 Magnetoresistance - pulsed B-field

Magnetoresistance measurements in pulsed magnetic fields were performed in collaboration with Dr. Walter Escoffier and Dr. Fabrice Iacovella of the "Nano-objects and semiconducting nano-structures"-group at LNCMI in Toulouse.
Bi_2Te_3 nanowires prepared for these measurements as described in chapter 2 exhibited a diameter of 25, 50 and 75 nm. Table 5.4.1 provides an overview of the samples used for magnetotransport measurements and the corresponding dimensions of their transport channel, i.e. the wire section between the probing contacts.

Table 5.4.1: The transport channel dimensions of investigated Bi_2Te_3 nanowires with cylindrical geometry: diameter d, channel length L and measurement configuration. The sample used for magnetoresistance measurements are marked by a $\star$.

Sample ID	d (nm)	L (μm)	Configuration
A$\star$	25 ± 5	3.6 ± 0.5	2-point
B	45 ± 5	1.0 ± 0.5	2-point
C	75 ± 5	2.0 ± 0.5	2-point
D	75 ± 5	10.0 ± 0.5	2-point
E$\star$	75 ± 5	10.0 ± 0.5	2-point

Nanowires of the same diameter (C-E) originate from only one array of electrodeposited nanowires. The thinner nanowires A and B were contacted using EBL at LAAS in Toulouse, while samples C, D, E were processed employing the laser scanning lithography at GSI. The metalization, liftoff and wire bonding was performed at LNCMI for all five samples. Consequently, the time passing between the structure development and metalization ranged from several days up to two weeks. During this time, the wires were transported and stored in air which lead to the magnetoresistance measurements being performed between two and five weeks after the structure development. Samples C and D were prepared on the same silicon substrate and chip carrier providing for simultaneous insertion into the magnetic field, while the other samples had to be measured one after the other.
After each processing step (liftoff, wire bonding) and before mounting the samples into the cryostat, the contacts were tested under ambient conditions. The contact resistance was found to be negligible. Unfortunately, several contacts broke during the extensive testing and measurement preparation which was probably due to electrostatic discharging. Nevertheless, for all five samples a two-point contact remained stable. For the actual MR measurement series at various temperatures, samples marked by a $\star$ in table 5.4.1 were chosen. In all cases the magnetic field was applied perpendicular to the nanowire axis.
Figure 5.4.1 presents SEM images of the corresponding nanowires with diameters of about 25 nm (a) and 75 nm (b-d) contacted in a four-point configuration. All images were recorded after the MR measurements. The colored frames and corresponding close-ups indicate the relevant transport channel for each sample in accordance to the color code in table 5.4.1. In all cases, the liftoff was successful and the contacts are positioned well on top of the nanowire. Image (a) reveals that in sample A two nanowires are contacted in parallel which has to be taken into account for the data treatment later. The nanowire in sample C shown in (b) is severely damaged after the measurements. Between the small contact distances the nanowire is broken, while between the large contact distance it completely vanished. These nanowire

failures are a common problem in electrical transport measurements on single metal nanowires [249]. They are caused by exceeding the maximum current density applicable, which is lower than for their bulk counterpart, and thus electromigration and Joule heating [256, 257] causes the failure. Images (c) and (d) show that the two-point contacts in samples D and E remained intact after the measurements.

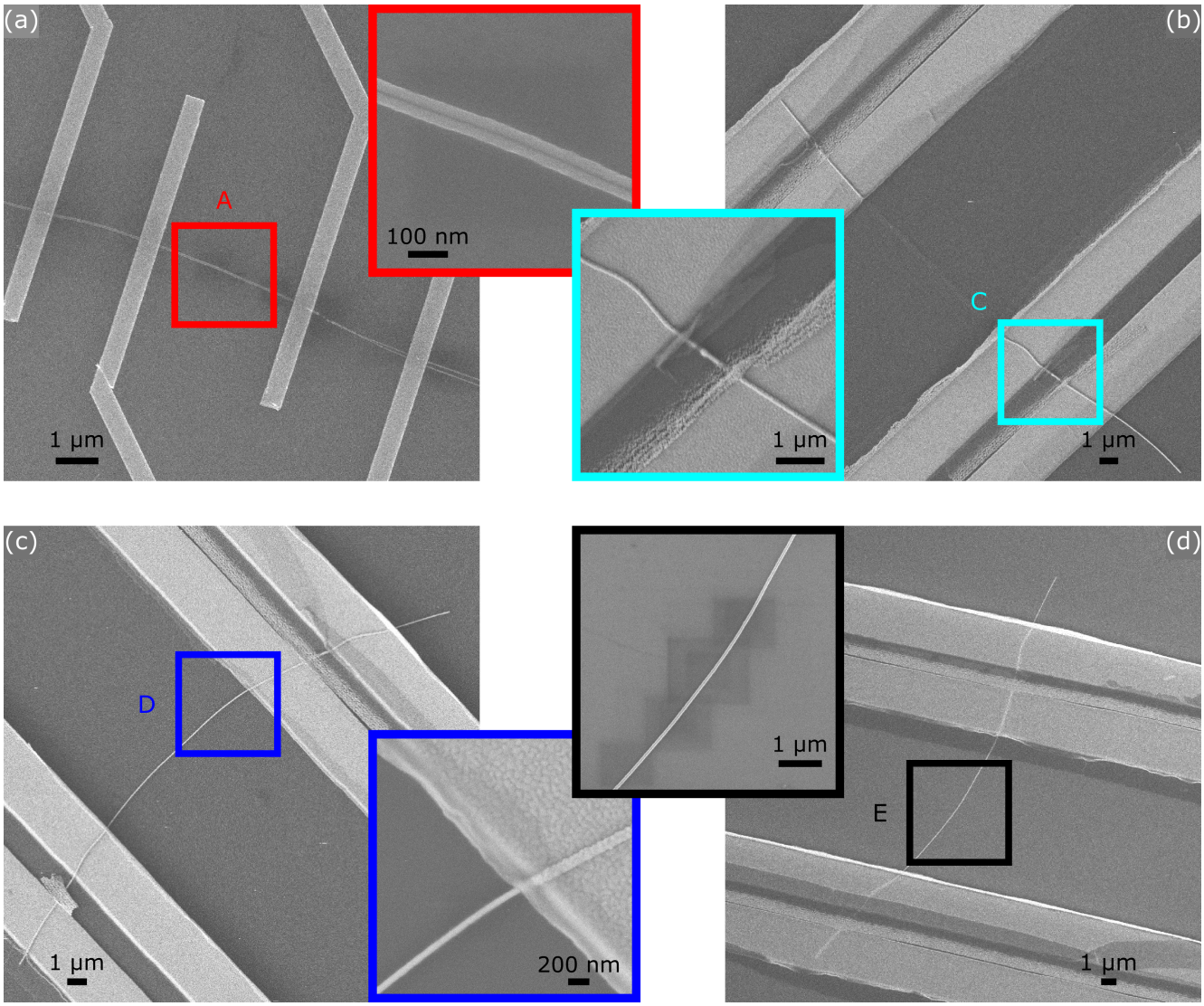

Figure 5.4.1: SEM images of the four nanowires A, C, D and E contacted by EBL (a) and laser lithography (b-d) recorded after the MR measurements. The colored frames and close-ups show the specific nanowire section employed for the two-point transport measurements. The colors correspond to those defined in table 5.4.1.

5.4.1 Electrical characterization

In the first step, all samples were characterized electrically by recording their resistivity ρ as a function of temperature T within a range from room to liquid helium temperatures as displayed in figure 5.4.2. Figure 5.4.2 (a) presents the ρ-T-curve applying a current of 10 µA during the cooling (magenta) and heating (black) of sample E. The overlapping of both curves confirms a stable temperature behavior of

the sample. The missing data is caused by recording gaps during the six hour cooling process.
Figure 5.4.2 (b) compares the recorded resistivity versus temperature behavior for all samples. In all cases, a metallic behavior was found indicated by the decrease of the resistivity with temperature. At close to 300 K, ρ amounted to about 2.5 and 1.0 mΩcm for 25 and 75 nm thick wires, respectively. The residual resistivity ratio (RRR) defined as ρ_{250K}/ρ_{4K} calculated for samples A, B, D, and E ranges from 1.1 to 1.4.
The metallic temperature dependence is typical for heavily doped, small gap semiconductors and has been confirmed for Bi_2Te_3 in the form of nanowires produced by catalytic growth [24], as thin films [242] and as macroscopic single crystalline [258, 259] as well as polycrystalline samples [30]. In the case of, single crystalline Bi_2Te_3 nanowires of diameters between 50 and 320 nm, electrodeposited in anodic aluminum oxide membranes metallic characteristics were found between 25 and 220 K. Above these temperatures a resistivity hump and below a resistivity increase was observed. This unique behavior is attributed to the contribution of surface and bulk transport channels being in competition for the case of a TI material [25, 26]. At room temperature, resistivity values for pulsed electrodeposited thin films amount to about 1 mΩcm [242, 260]. For macroscopic crystals about 1 mΩcm [258], 1.4 mΩcm [30] and 1.6 mΩcm [259] were measured. Compared to the resistivity range shown in figure 5.4.2 (b), these literature values are similar to those found for nanowires with 75 nm diameters.
For VLS grown Bi_2Te_3 nanowires RRR values of 4 were found [24], which is almost four times higher than the values obtained here. In general, the lower the RRR the more dominant is scattering by impurities and defects. Since the samples used in this work are polycrystalline, the lower values compared to VLS grown single crystalline samples seem reasonable.

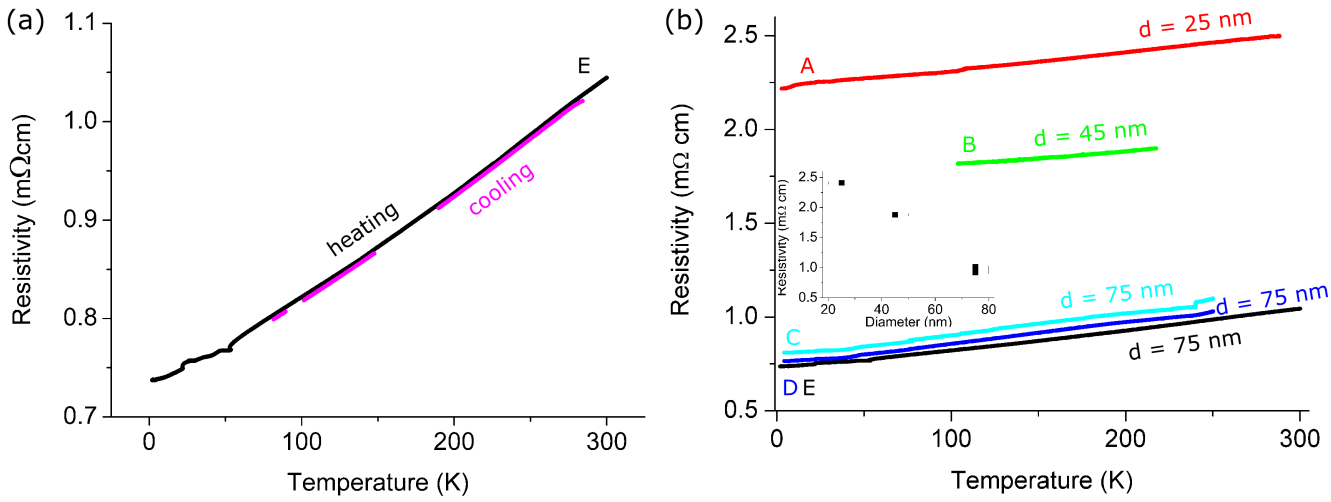

Figure 5.4.2: The temperature dependent resistivity curves for samples A-D according to the color code in table 5.4.1. (a) The reproducibility between heating and cooling cycles representatively shown for sample E. (b) The resistivity increases with decreasing wire diameter.

The resistivity clearly increases with decreasing wire diameter, while the transport channel length, of the order of μm, and thus the aspect ratio does not seem to influence the resistivity characteristics. This becomes especially obvious, since temperature-dependent ρ measured for the 75 nm wires exhibit similar values, although the aspect ratio is different (see table 5.4.1). The inset in figure 5.4.2 (b) displays the

ρ values as a function of diameter at 200 K emphasizing the increase of up to 1.5 mΩcm between 75 and 25 nm diameter. Although it seems like this increase follows a linear relation, more data points are necessary to confirm this behavior.
Size-dependent resistivity values have previously been observed in many nanostructured (semi-)metals, such as bismuth nanowires [261, 262] and copper nanowires [263]. This relation is commonly traced back to the reduction of the sample size in the order of the electron mean free path. Consequently, scattering at the grain boundaries is enhanced leading to a higher resistivity. A model describing these quantum size effects was first developed by Fuchs and Sondheimer [264] and later expanded by Mayadas and Shatzkes also taking into account grain boundary scattering [265]. In both models the increase of resistivity with decreasing diameter is not linear, but follows more a 1/diameter-like behavior.
In electrochemically deposited Bi_2Te_3 nanowires, the electron mean free path was estimated to about 40 nm in wires of 52 nm diameter [89]. Assuming a similar electron mean free path, the size-dependent resistivity observed in the present Bi_2Te_3 nanowires points towards finite size effects.

5.4.2 Magnetoresistance in perpendicular B-field

Magnetoresistance measurements in perpendicular B-field were performed as a function of temperature. Representatively, the results of samples A and E are discussed. For the remaining samples the temperature series could not be completed. In order to obtain the best signal with reduced noise, a DC current of 10 μA was applied using standard lock-in techniques.
Figure 5.4.3 summarizes the magnetoresistance results obtained for sample E for a wire of 75 nm in diameter. For six different temperatures between 2 and 200 K, a pulsed magnetic field up to 53 T was applied. As evident from figure 5.4.2 the resistance increases with temperature and exhibits kΩ order of magnitude as shown in figure 5.4.3 (a). For all temperatures the magnetoresistance also increases with magnetic field and does not show any sign of saturation. This is consistent with previous findings for MR of Bi_2Te_3 thin films up to 60 T [233].
Figure 5.4.3 (b) displays the MR as defined in equation 5.1 versus the magnetic field. The lower the temperature, the more pronounced is the MR increase over the magnetic field range. At 1.7 K the MR rises by about 4.5%, which is comparable to 2-4% (for 16 T) reported in literature for electrodeposited Bi_2Te_3 nanowires of 50 to 320 nm [25, 26]. On the other hand, VLS grown nanowires exhibit MR values of close to 10% within a 2 T range [24, 27]. For Bi_2Te_3 thin films of about 55 nm thickness a MR of 30% was recorded for a field range of up to 60 T [233]. Also giant magnetoresistances of about 400% in 7 T, 600% in 13 T and 450% in 16 T fields were observed in single crystals [266], 20 nm thick nanosheets [23] and 100 nm thick films [267] of Bi_2Te_3, respectively.
At high magnetic fields above 20 T, the MR curves exhibit quadratic, non-saturating behavior for all temperatures. Possible signal oscillations visible especially at higher temperatures were not reproducible and are thus not assigned to originate from any quantum transport phenomena. Applying Kohler's rule (equation 5.2), a quadratic fit to the MR data over the full magnetic field range provides a rough estimation of the charge carrier mobility (dashed gray curves in figure 5.4.3 (b)). Only considering the MR curves recorded at 50 K and higher results in mobilities between 30 and 40 $cm^2V^{-1}s^{-1}$. This is about four times lower than the room temperature mobility found for single crystalline nanowires (≈50 nm diameter) electrodeposited in anodic aluminum oxide membranes [89]. In that case the mobility was

estimated from Seebeck measurements. Furthermore, a very high mobility of about 45000 $cm^2V^{-1}s^{-1}$ was calculated from SdH oscillations observed for one single crystalline Bi_2Te_3 nanowire (44 x 200 nm rectangular cross section) grown by VLS [27]. For comparison, electrochemically deposited films of 300 to 500 nm thickness revealed mobilities between 10 and 20 $cm^2V^{-1}s^{-1}$ [260] obtained from Hall measurements. Similarly, 100 nm thick CVD-grown Bi_2Te_3 films showed that the mobility varies from below 10 to 300 $cm^2V^{-1}s^{-1}$ with increasing granular density, which was attributed to a better interconnectivity [267]. Macroscopic single crystals (n-type) yield mobilities around 200 $cm^2V^{-1}s^{-1}$ [76].

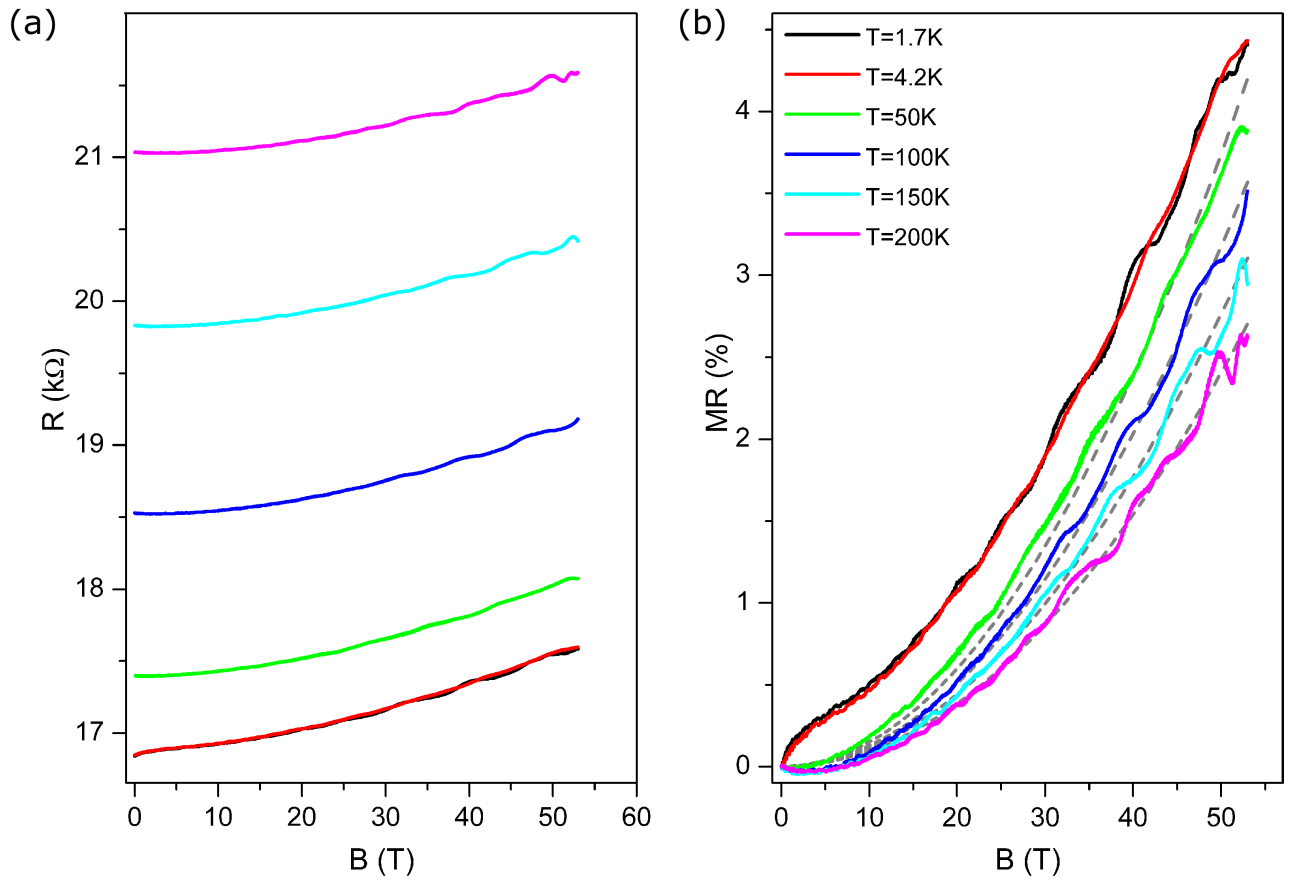

Figure 5.4.3: Magnetotransport of a 75 nm diameter Bi_2Te_3 nanowire as a function of temperature: (a) Resistance and (b) MR $= (R(B) - R(B = 0))/R(B = 0) \cdot 100$ as a function of the magnetic field up to 53 T. The resistance dip as $B \to 0$ at 2K (black curve) and 4K (red curve) manifests the WAL effect. Possible oscillations visible are not reproducible. The dashed gray lines show a quadratic fit to MR data recorded at 50, 100, 150 and 200 K.

In comparison, the value estimated by employing Kohler's rule for the nanowires used in this work is comparable to mobilities measured on several hundred nanometer thin electrodeposited Bi_2Te_3 films. Also, 100 nm thick CVD grown films with low intergranular connectivity experience similar mobility values while single crystalline samples, nanowires or bulk, yield much higher mobilities. Considering the difference in crystal quality, the mobility values in Bi_2Te_3 nanowires investigated here can be explained by their polycrystalline structure consisting of several hundred nanometer long grains. If only one of these grains was contacted, i.e. by smaller contact distances, the mobility would be expected to increase to a value comparable to that in [26].

In contrast to the quadratic MR at high B-fields, the behavior in the low field range of $B < 5$ T signifi-

cantly differs for the low temperature (2 and 4 K) curves. As the magnetic field approaches zero, the MR abruptly decreases. This magnetoresistance cusp is typically a consequence of the weak antilocalization effect which is observed in topological insulator materials [26, 242, 243, 268]. As predicted, the effect is destroyed by higher magnetic fields and vanishes at elevated temperature. This WAL effect was investigated in more detail applying a 1 T static magnetic field created by a superconducting magnet. The results are presented together with the those obtained from the measurements at IFW in section 5.6.
Analogous to the MR investigations for sample E, sample A was measured in the pulsed magnetic field setup. With a diameter of only 25 nm this nanowires is the thinnest Bi_2Te_3 nanowire investigated by MR measurements so far.
The results are presented in figure 5.4.4 diagrammed in resistance (a) and MR (b) versus magnetic field. Due to the observed WAL and the absence of oscillations in sample E, a magnetic field up to about 20 T was applied for each measurement within a temperature range of 2 to 15 K. In this way, by focusing on the WAL behavior, the shortened cooling time of the coil allowed for an efficient use of the granted magnet time. It is important to point out that two nanowires were contacted in parallel in sample A. Most likely, they are attached to each other due to van der Waals forces rather than arising from the wire deposition into two overlapping pores. The separation of the two wires is visible in figure 5.4.1 (a). It should be emphasized that in contrast to the temperature-dependent resistivity curve (figure 5.4.2), the untreated resistance data for the two parallel contacted nanowires is shown in 5.4.4.
In the low field regime ($B < 2$ T) the resistance decreases with temperature as expected from the temperature-dependent resistivity curve. Additionally, the magnetoresistance effect is more pronounced as the temperature decreases. Consequently, the resistance increases as the sample is cooled from 15.5 to 2 K while applying magnetic fields between 2 and 20 T.
The MR behavior is positive over the entire magnetic field range similar to the previous sample E with 75 nm diameter. At 1.7 K, the MR effect is most pronounced and yields 5.5% at 20 T, which is approximately five times larger compared to sample E within the same range. All in all, the MR behavior appears different from that found for 75 nm diameter wires. A resistance dip within the zero field region, is not explicitly visible. Furthermore, the behavior close to 20 T indicates a saturating MR, but should be clarified by MR measurements in higher B-fields.
Additionally, oscillations with a long period ($\approx$ 10T) and low amplitude are reproducibly observed modulating the MR curve between 5 to 20 T as indicated by the gray dashed lines in 5.4.4 (b). These oscillations vanish for the measurements at 12.2 K or higher temperatures. So far, their origin is unclear, because none of the in section 5.1 described quantum transport effects accounts for an explanation of these oscillations. The perpendicular configuration and sample geometry rule out the AB and AAS effect. Also, 1/B periodicity characteristics of SdH oscillations cannot be determined from these measurements given that there is only one full period observable.
A comparison of the MR behavior of two parallel nanowires of 25 nm to the single nanowire of 75 nm is rather difficult. Firstly, the interface between the nanowires is not characterized and it remains unclear if there is a gap or full contact. The electron transport on the surface is most probably disturbed by such an interface. Secondly, the impact of a high field pulse on nanowires that are attached to each other is unknown. Additional vibrations may occur and influence the MR signal.
In order to explore possible changes in the MR as a function of nanowires diameter, more measurements

also up to higher magnetic fields are required. Especially a repetition of the MR experiments with wire diameters of 25 nm would provide further information to interpret the results displayed in 5.4.4. In general, it is expected that possible transport oscillations are more pronounced in thinner wires with a higher surface-to-volume ratio [26].

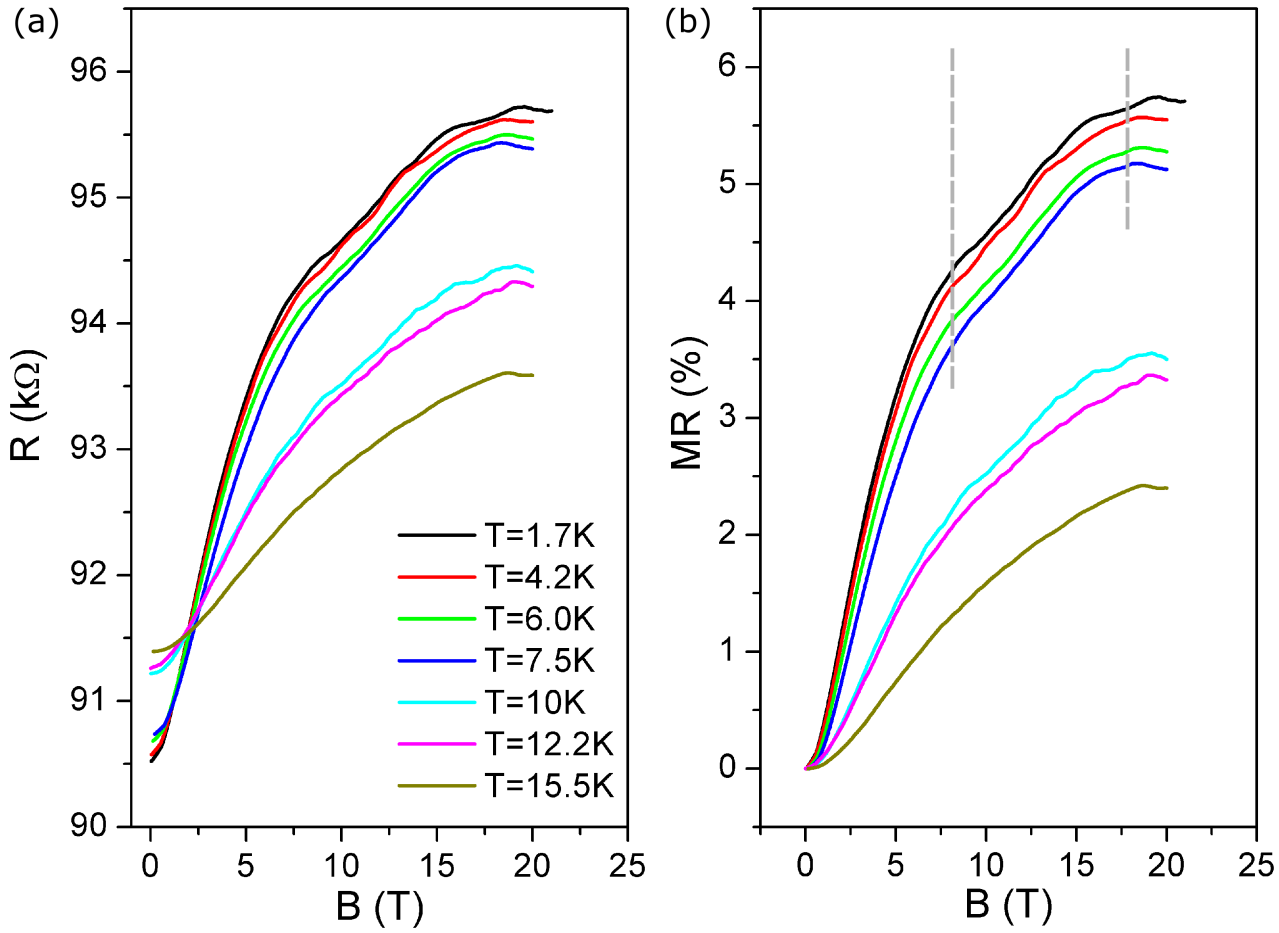

Figure 5.4.4: Magnetotransport of two 25 nm diameter Bi_2Te_3 nanowires attached in parallel recorded at different temperatures: (a) Resistance and (b) MR = (R(B)-R(B=0))/R(B=0)·100 as a function of the magnetic field up to 20 T. The gray dashed line indicate reproducible oscillation maxima.

5.5 Magnetoresistance - static B-field

The magnetoresistance measurements in a 2D static B-field were carried out in collaboration with Dr. Romain Giraud, Dr. Joseph Dufouleur and Hannes Funke of the "Quantum transport"-group (Institute for Solid State Research) at the IFW in Dresden.
The contacting was performed by making use of the on-site electron beam lithography. The time between the nanowire transfer to the silicon sample, the contacting and the final measurement amounted to about eight months. During this time the samples were stored under ambient conditions. Under these conditions, a surface oxide layer of a few nanometers is expected to form [269], which was removed by Ar plasma treatment previous to the metalization of the contacts.
Two contacted Bi_2Te_3 nanowires with 50 and 100 nm diameter were selected for wire bonding onto two chip carriers. Between six and eight Cr/Au contacts with distances between 250 nm and 2 µm were placed on each nanowire enabling different measurement configurations. Table 5.5.1 provides an overview of the measured transport channels, where I, II and III-VI correspond to the 50 and 100 nm diameter nanowire, respectively. Later in this chapter the MR results of sections marked by ⋆ are discussed.

Table 5.5.1: The transport channel diameter d and length L of investigated Bi_2Te_3 nanowire sections of cylindrical geometry. Additionally, the measurement configuration and the contact numbers, through which the current is injected, are given. The samples for which for magnetoresistance measurements are presented in this work are marked by a ⋆.

ID	Measuring contact	d (nm)	L (µm)	Configuration	Injection contact	Current (nA)
I	1-4	50 ± 5	1.1 ± 0.5	2-point	1-4	20
II	2-5	50 ± 5	2.1 ± 0.5	4-point	1-3	100
II⋆	2-5	50 ± 5	2.1 ± 0.5	3-point	2-3	20
III	16-8	100 ± 5	1.4 ± 0.5	3-point	7-8	50
III⋆	16-8	100 ± 5	1.4 ± 0.5	4-point	7-15	50
IV	7-16	100 ± 5	2.0 ± 0.5	2-point	7-16	100
V	7-8	100 ± 5	3.4 ± 0.5	2-point	7-8	50
VI⋆	7-15	100 ± 5	5.4 ± 0.5	2-point	7-15	50

Figure 5.5.1 displays a photo of the insert with the two samples mounted next to each other enabling both nanowires to be investigated simultaneously. The orientation of the nanowires was chosen in a way that a 1 T B-field is applied perpendicular to the wire axis and a 12 T B-field in parallel. The advantage of this layout is that the sample does not have to be removed form the cryostat in order to change the orientation for low field measurements. Furthermore, the fields can be applied at the same time. In order to investigate possible AB oscillations, the higher B-field was oriented in parallel.
SEM images of the contacted wires with 50 and 100 nm diameter recorded before the transport measurements are shown in (b) and (c), respectively. In both cases, the contacts are very well aligned to the straight nanowires. A damaged part of the nanowire in (c) was fixed by placing a bigger rectangular contact patch on the wire. The colored arrows indicate the measured transport channel following the color code in table 5.5.1.
After testing each contact, the nanowire sections I-VI remained intact for measurements. The contacted nanowires displayed stable resistance values in the kΩ-range, which indicates that possible surface oxidation was successfully removed before the metalization. By comparing different configurations (four-

point and two-point) and taking also the available infrastructure (e.g. lock-in amplifiers with and without compensation) into account, the optimal connections for low noise measurements of small signals were found. The final setup for the temperature-dependent resistance recordings yielded one two-point (I, red) and four-point (II, black) measurement as well as one four-point (III, cyan) and two two-point measurements (IV, green and V, blue). The configuration for the MR measurements for these sections was changed to one two-point (I, red) and one three-point (II, black) measurement as well as one four-point (III, cyan) and one two-point measurement (VI, orange). The corresponding current injection contacts are added in table 5.5.1.

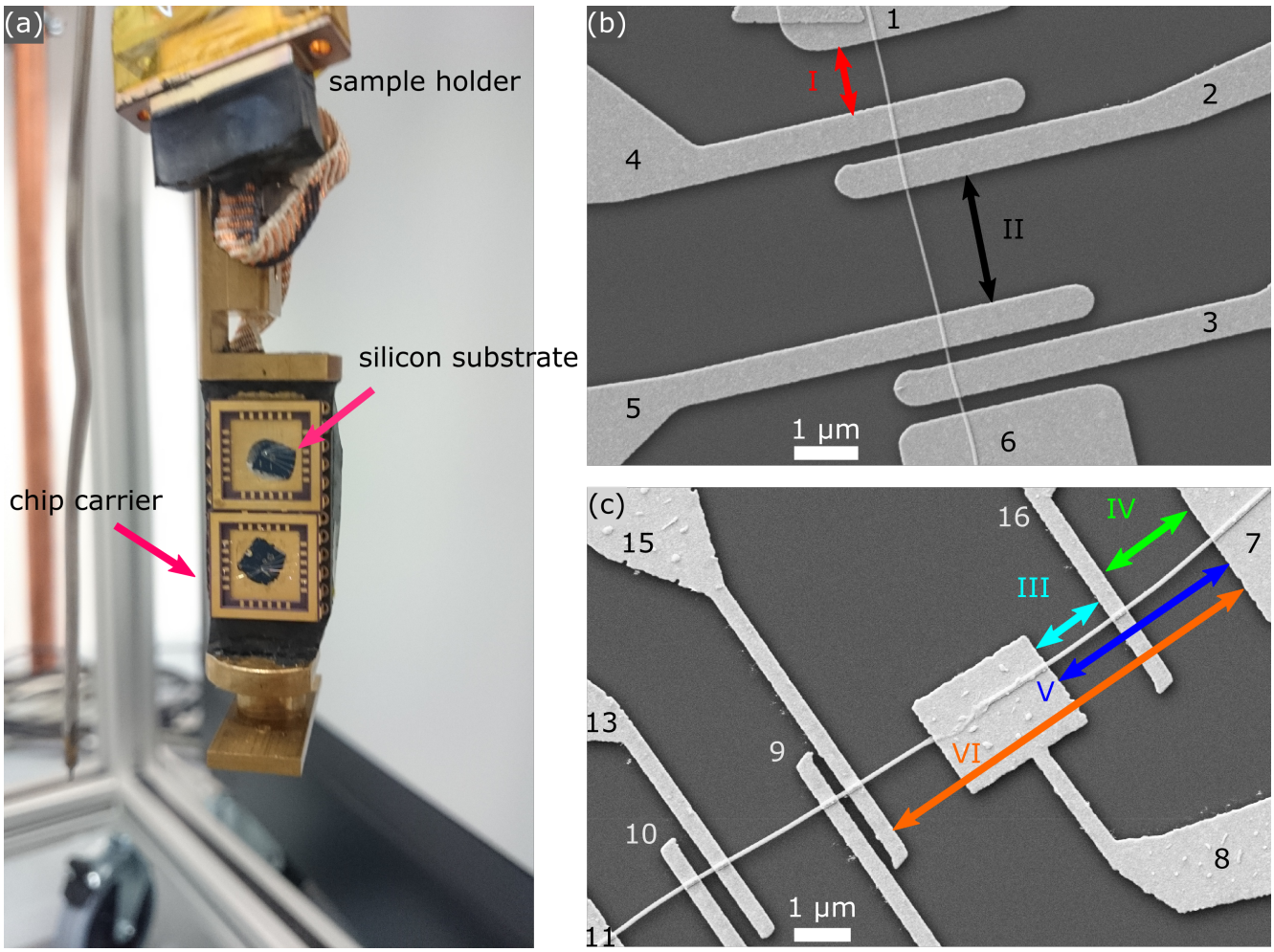

Figure 5.5.1: Nanowire samples ready for transport measurements in static magnetic field: (a) shows a photo of the two contacted samples, each bond to a chip carrier, mounted next to each other on the insert. (b) and (c) display SEM images of the contacted nanowires with 50 nm and 100 nm diameter, respectively. The contacts are numbered. The measured transport channels are marked by arrows following the color code defined in table 5.5.1.

5.5.1 Electrical characterization

First, five transport channels (I-V) were characterized on the basis of their temperature-dependent resistivity as shown in figure 5.5.2 (a) within a range from 15 to 300 K. The black arrows indicate whether the curve was recorded during heating or cooling of the sample. Currents of 20 nA (I), 50 nA (III, V) and

100 nA (II, IV) were injected into the corresponding contacts numbered in table 5.5.1, while the voltage across the transport section was recorded.
The obtained resistance, calculated using Ohm's law, includes not only that of the actual wire sections, but also cable R_{cable} and contact R_c resistances which have to be taken into account. The R_{cable} of each cable, that connects the sample at the tip of the insert inside the cryostat to the measuring instruments under ambient conditions, amounts to about 135 $\Omega \pm 10\%$. Depending on the measurement configuration, R_{cable} was subtracted from the resistance curves: In four-point measurements, there is by definition no R_{cable} contribution. In the case of three-point and two-point measurements, one and two cable resistances have to be subtracted, respectively. The estimation of the contact resistance R_c of the interface between the Bi_2Te_3 nanowire and the Cr/Au patch poses a more complicated task. For this contact geometry, it has been observed that the current tends to flow partially or completely through the contacts due to its lower resistance with respect to the nanowire. Compared to a standard Hall bar geometry, this results in a pseudo-four-point measurement in which the interface resistance, crossed twice (per contact) by the current, matters [219, 252]. Consequently, every contact adds $R_{contact}$ independent of the measurement configuration.
For example, the four-point measurement of section II with the current injected through contacts 1-5 yields eight interface resistances, two for each contact 1-5. Although patch 4 is not actively involved in the measurement, the current might partially flow through it. From the available measurements only a rough estimation of the contact resistance is possible using the values of sections III-V, because

$$R_V \stackrel{!}{=} R_{IV} + R_{III}. \tag{5.15}$$

Inserting the measured resistance values $R_{n,\text{section ID}}$, the contact resistance $R_{c\,n}$ and the cable resistance R_{cable} with n being the contact number, equation 5.15 expands to

$$\begin{aligned} R_{7-8,V} - R_{c7} - R_{c16} - R_{c8} - 2 \cdot R_{cable} &= R_{7-16,IV} - R_{c7} - R_{c16} - 2 \cdot R_{cable} \\ &\quad + R_{16-8,III} - R_{c16} - R_{c8} - R_{c7} - R_{cable} \\ \Leftrightarrow R_{c7} + R_{c16} &= R_{7-16,IV} + R_{16-8,III} - R_{7-8,V} - R_{cable}. \end{aligned}$$

Using the resistance values of III-V obtained at room temperature and $R_{cable} = 135\ \Omega$, a contact resistance for $R_{c7} + R_{c16}$ of about 30 Ω was estimated. Assuming all contacts of the same size yield a similar contact resistance, the low value of a few tens of Ω justifies that only the cable resistance was subtracted before calculating the resistivity values displayed in figure 5.5.2. In order to actually measure R_c, two-terminal transfer length measurements are required, recording the resistance in a two-point configuration as a function of channel length on the same device.
All nanowire sections exhibit metallic behavior indicated by the resistivity decreasing with temperature. Despite a small deviation at higher temperatures, the ρ-T-curves for sections I and II are very similar. This is not surprising considering both sections are part of the same nanowire, but the data underlines the previous finding that the resistivity changes with the wire diameter and not with the channel length (section 5.4.1). The RRR defined as $\rho_{295\,K}/\rho_{15\,K}$ amounts to about 1.2 (I, II). In contrast to that, the

resistivity of sections III, IV and V are shifted to each other by approximately 0.1 mΩcm at 15 K, but exhibit a similar RRR of 1.5 (III), 1.7 (IV) and 1.6 (V). These values are comparable to those found in section 5.4.1 for wires with 27 and 75 nm diameters indicating various scattering effects. Furthermore, the absolute resistivity values also match the trend of increasing with reducing wire diameter, but do not seem to vary with channel length.

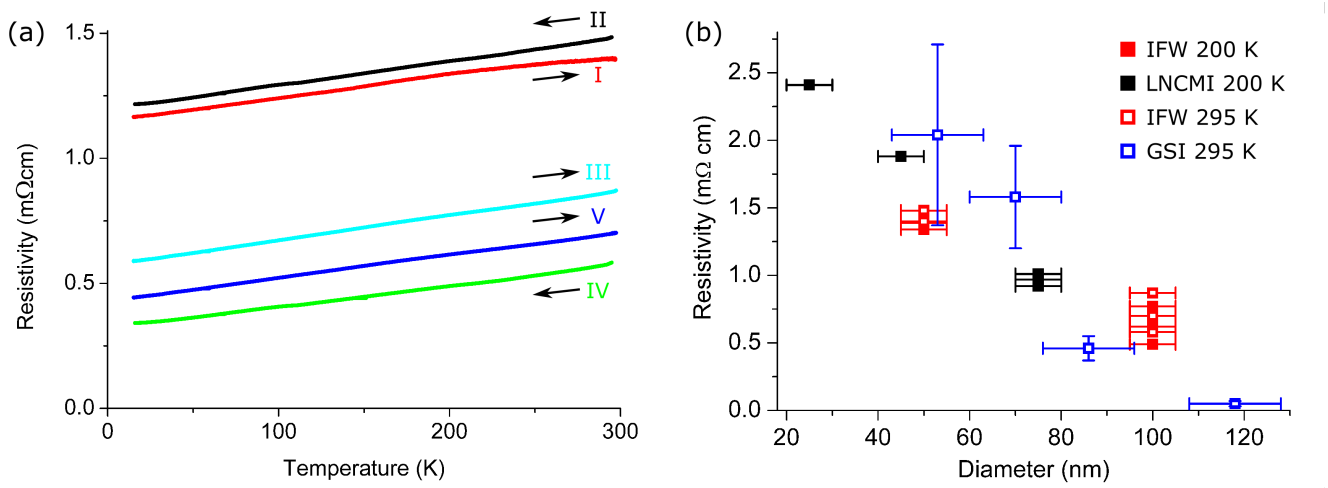

Figure 5.5.2: The temperature (a) and diameter (b) dependence of the resistivity for various samples: (a) I, II (50 nm) and III-V (100 nm) measured at IFW according to the color code in table 5.5.1. (b) compilation of samples measured at IFW (I-V, red), at LNCMI (A-E) and at GSI (blue). The recording temperatures were 200 K (filled squares) and 295 K (open squares).

Figure 5.5.2 (b) compiles the resistivity values for Bi_2Te_3 nanowires of various diameters between 20 and 130 nm at 200 K (full squares) and at 295 K (open squares). The data extracted from figure 5.5.2 (a) is displayed in red. For a diameter of 100 nm, the values deviate up to about 0.5 mΩcm. The recorded ρ values using the setup at LNCMI in Toulouse are shown in black (compare to the inset in figure 5.4.2 (b)). Additionally, resistivity values of electrodeposited Bi_2Te_3 nanowires contacted by laser scanning lithography are displayed. They were measured employing four micromanipulators (Cascade Microtech DPP105) for connection and a Keithley SourceMeter 2636A for sourcing and measuring. The current was swept between -10 and 10 nA and the samples displayed a linear I-V-curve indicating Ohmic behavior. Except the nanowire with a diameter of around 50 nm, all samples were measured in four-point configuration. Compared to the measurements at IFW and LNCMI, the average resistivity values of up to six different nanowires are displayed resulting in a relatively larger uncertainty estimation for thinner nanowires. Further details about these particular samples and the setup can be found in [251]. For all three measurements, the resistivity increases with decreasing wire diameter and the values complement one another hinting finite size effects. The suggested linear increase still has to be confirmed by taking into account the contact resistances, which could not be precisely investigated due to the unavailability of two-terminal transfer length and the low number of four-point measurements. The Fuchs-Sondheimer [264] and the Mayyadas-Shatzkes [265] predict a much steeper increase of resistivity for smaller nanowires due to enhanced surface and grain boundary scattering. In the present case this steep increase was not observed.

For topological insulators, the opposite behavior is expected, namely a conductivity increase with decreasing wire diameter. Assuming separate contributions from the bulk σ_b and surface σ_s conductivity, the influence of σ_s increases with the surface-to-volume $\frac{s}{v}$ ratio as

$$\sigma = \sigma_b + \sigma_s \frac{s}{v}. \tag{5.16}$$

This has been theoretically shown considering single-crystalline Bi_2Te_3, Bi_2Se_3 and Sb_2Te_3 nanostructures with perfect surfaces [97] and experimentally confirmed in cylindrical $Bi_2(Te_xSe_{1-x})$ with diameters between 40 to 200 nm [270]. Together with the metallic temperature-dependence of the conductivity, the increasing conductivity strongly indicates topological surface-state dominated transport.
In the present investigations, the surface state transport is not resolved. This can be possibly explained by additional bulk transport scattering due to grain boundaries overwhelming the surface contribution.

5.5.2 Magnetoresistance in perpendicular B-field

Magnetoresistance measurements in magnetic field B_x of 1 T applied perpendicularly to the nanowire axis were performed at low temperatures between 2 and 15 K. At the same time, no B-field B_z was applied parallel to the wire axis.
Figure 5.5.3 shows the representative results obtained from a 50 nm II (a, b) and a 100 nm VI (c, d) diameter section, both measured in a two-point configuration injecting 20 nA and 50 nA DC current, respectively. For all temperatures, both field directions were swept at 20 mT/min. This leads to symmetric curves mirrored at zero magnetic field for all MR recordings. In the displayed case, the minimum resistance value was shifted to around B = -0.03 T and used for the calculation of MR (equation 5.1) instead of B = 0 T.
Figures 5.5.3 (a, c) and (b, d) display the results for both sections as a function of the magnetic field in terms of absolute resistance and MR, respectively. At zero B-field the resistance decreases with temperature, while at 1 T the magnetoresistance behavior leads to a resistance increase with temperature. As expected, the influence of the B-field is most pronounced at low temperatures of 2 K (black curves).
A prediction about the MR behavior in terms of linearity and saturation cannot be made from these low-field data. On the other hand, the clear cusp around zero B-field provides a strong hint that the weak antilocalization effect is observable for both wire sections. With increasing temperature the WAL diminishes and vanishes at around 15 K (cyan curves) in all samples. This is a consequence of the decreasing l_φ/l_e ratio determining the shape of the WAL cusp.
Comparing the MR behavior of the thinner (figure 5.5.3 (b)) with respect to the thicker (figure 5.5.3 (d)) nanowire, the shapes of the MR curves exhibit two prominent differences: Firstly, the MR of the 50 nm diameter wire section is approximately five times larger than for the 100 nm wire section at all temperatures. At 2 K, the MR amounts to 3% for the thinner and 0.6% for the thicker nanowire section. A more pronounced WAL effect for thinner samples has been observed for electrodeposited Bi_2Te_3 nanowires [26]. Secondly, the WAL cusp for the 100 nm diameter (d) is much sharper than that recorded for the 50 nm wire (b). Consequently, the destruction of the WAL occurs at much lower fields of about 0.3 T. The difference in peak shapes might result from the l_φ and l_e characteristic lengths, which certainly

differ between the two samples due to e.g. grain boundaries. A more detailed analysis of the WAL effect is presented in section 5.6.

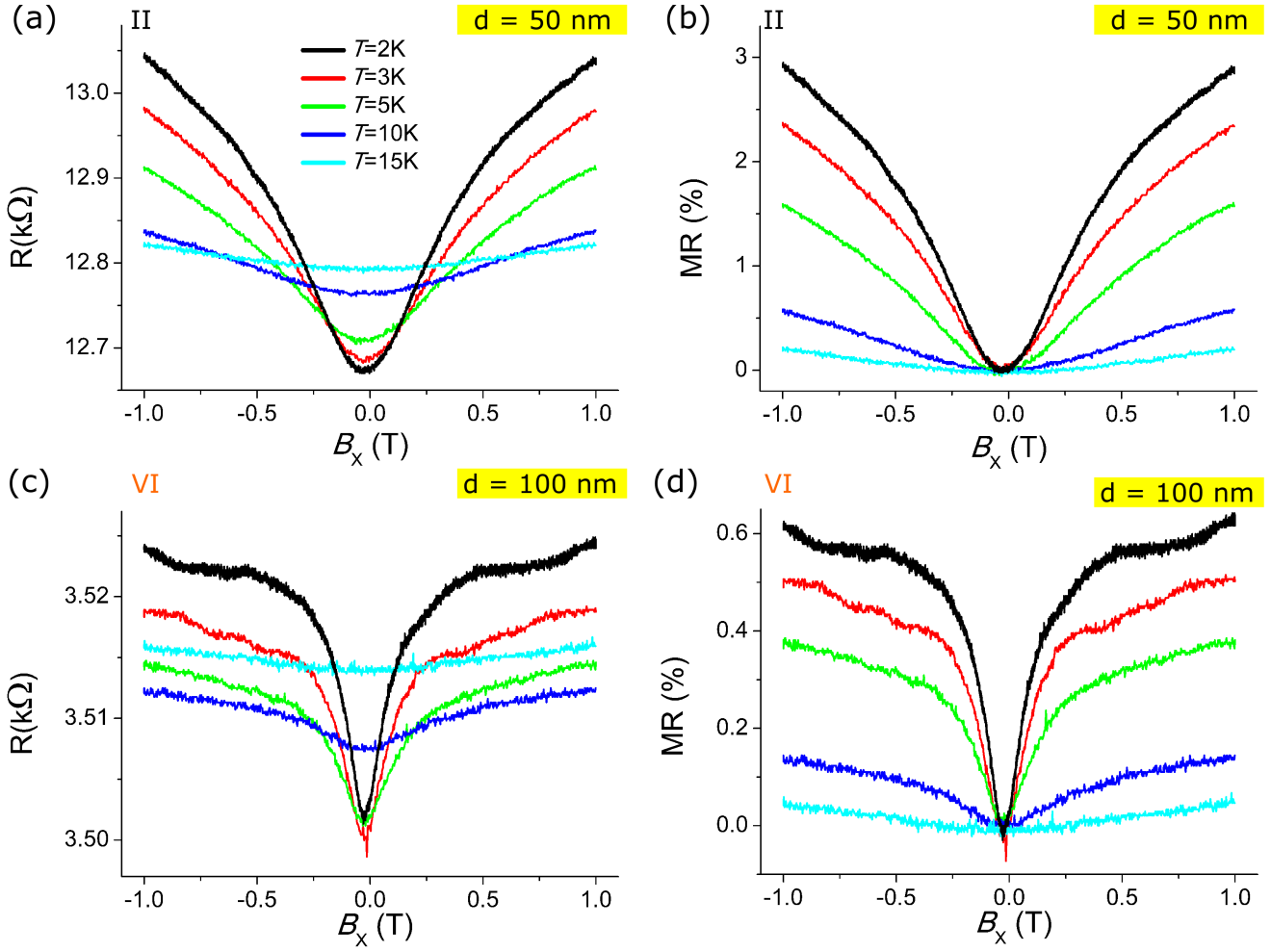

Figure 5.5.3: Magnetotransport measurement of a 50 nm (a, b) and a 100 nm (c, d) Bi_2Te_3 nanowire for various temperatures. (a, c) display the resistance R and (b, d) the MR = (R(B)-R(B=0))/R(B=0)·100 as a function of the magnetic field up to 1 T applied perpendicular to the wire axis.

5.5.3 Magnetoresistance in parallel B-field

A magnetic field of up to 12 T was applied in parallel to the nanowire axis for measurements at temperatures between 2 and 15 K. The ramping rate was 100 mT/min in both field orientations for temperatures of 3 K and higher. For the measurements of 2 K a rate of 15 mT/min was chosen for only the positive field direction. Representative results are presented in figure 5.5.4 for section II (a, b) and III (c, d) displaying the resistance R (a, c) and the MR (b, d) as a function of the magnetic field. Sections II and III were measured in a two- and four-point configuration injecting 20 nA and 50 nA DC current, respectively.
As in the perpendicular B-field setup, the change of the resistance while ramping the magnetic field is more pronounced as the temperature decreases. This is particularly seen for the thin wire section, where

the curves recorded at 2 (black) and 3 K (red) are still clearly distinguishable.
The MR behavior at higher fields above 1 T displays a linear positive magnetoresistance, which yields slopes of approximately 11 Ω/T in (a) and 0.6 Ω/T in (c). This is in accordance to literature and is typically observed in topological insulator materials [23, 232, 233]. Nevertheless, it is worth mentioning that B-fields higher than 12 T provide a more effective evidence, if the MR is indeed linear.

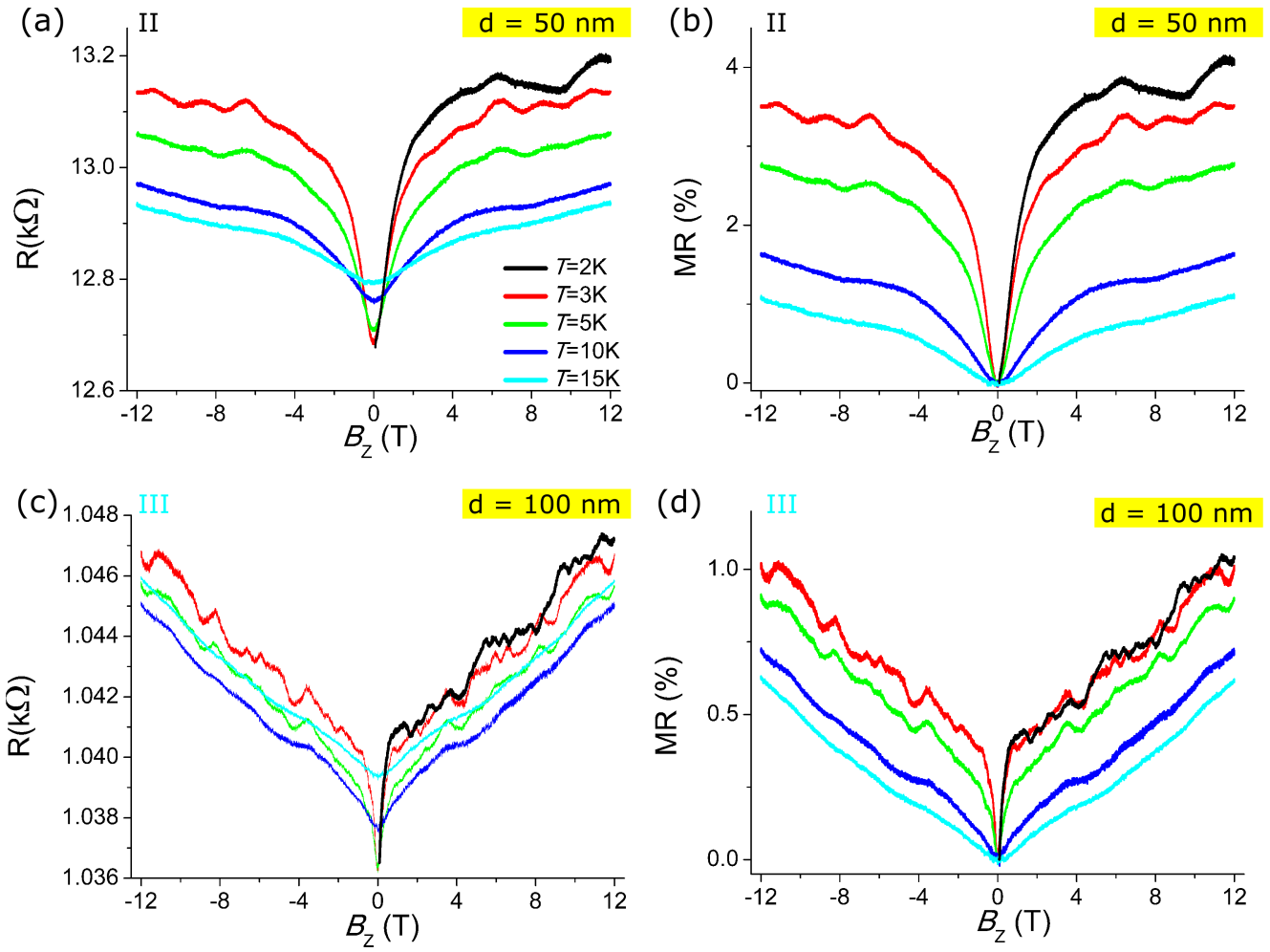

Figure 5.5.4: Magnetotransport measurement of a 50 nm (a, b) and a 100 nm (c, d) Bi_2Te_3 nanowire for various temperatures. (a, c) display the Resistance R and (b, d) the MR = (R(B)-R(B=0))/R(B=0)·100 as a function of the magnetic field up to 12 T applied parallel to the wire axis.

Additionally, reproducible MR oscillations are observable at higher B-fields and low temperatures which might result from AB oscillations. The oscillations vanish for temperatures above 5 K as has previously been reported for electrodeposited Bi_2Te_3 nanowires [25]. As in the case of the perpendicular applied B-field, the WAL dip is clearly visible within the low field region for both sections (-2 to 2 T for d = 50 nm and -1 to 1 T for d = 100 nm) at all temperatures, but almost completely vanishes at 15 K.
Comparing the MR values at 12 T for both sections, the MR for the thinner nanowire (b) is up to four times higher than for the thicker wire (d). This shows once more the trend of an increasing MR effect with reducing wire diameter. As for the MR recording in the perpendicularly applied B-field, the WAL

cusp of the thicker nanowire is much sharper. A more detailed analysis of the WAL effect is presented in the followin section 5.6.

5.6 Weak antilocalization in perpendicular and parallel B-field

LNCMI setup

In order to investigate the WAL effect at low magnetic field, sample E (75 nm diameter) was remeasured in a perpendicular B-field of up to 1 T employing a superconducting magnet and a variable temperature insert. The magnetic field was slowly ramped at about 3 mT/s. Figure 5.6.1 (a) presents the recorded MR at temperatures between 1.7 and 7.5 K. The resistance cusp around zero field is clearly visible and more pronounced as the temperature decreases. At higher temperatures, the cusp broadens and gradually disappears. The exact temperature at which the WAL cusp disappears was not fully determined, but also taking into account figure 5.4.3 it should range between 7.5 and 50 K. This is consistent with previous investigations on electrodeposited Bi_2Te_3 nanowires of 50 to 300 nm diameter by Ning et al. [26]. Figure 5.6.1 (b) displays the magnetoconductance difference $\Delta G = G(B) - G(B = 0)$ as a function of the magnetic field calculated from the MR curve recorded at 2 K (black in (a)).

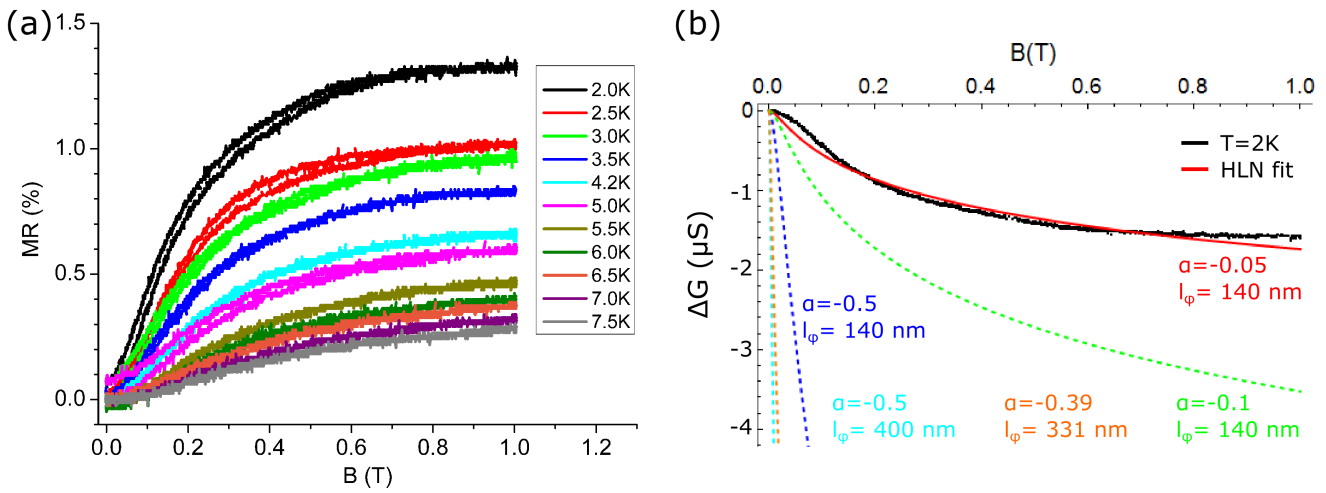

Figure 5.6.1: Magnetotransport of the 75 nm diameter Bi_2Te_3 nanowire measured in figure 5.4.3 up to 1 T (ramping 3mT/s and return): (a) WAL cusp at zero field gradually vanishes as the temperature is increased. (b) The $\Delta G = G(B) - G(B = 0)$ recorded as a function of the magnetic field at 2 K (black) and the corresponding HLN fit (red). The dashed curves are plotted by using different α and l_φ values for the 2D HLN model on equation 5.10.

A well known procedure to quantify the WAL effect in thin films and nanowires is to employ the HLN model for 2D systems and fit equation 5.10 to the data. The best possible fit (red) yields a prefactor of $\alpha \approx -0.05$ and a phase coherence length $l_\varphi \approx 140$ nm, but the quality of the fit is not satisfactory. For comparison, several parameter combinations of α and l_φ are plotted as dashed curves. In order to obtain the blue line, only α was changed to yield -0.5 as predicted for topological insulators with a single surface state [243]. So far, experimental values found for α range between -0.3 and 1 for various thin films of Bi_2Te_3 [242], Bi_2Se_3 [271–273], Sb_2Te_3 [274] and $Bi_2(Se_xTe_{1-x})_3$ [275]. The results obtained

for Bi_2Te_3 are plotted as orange dashed curve [242]. For α values close to -0.5 one surface channel was assumed, while higher values around -1 were related either to a decoupled contribution of two surface states or a mixed contribution of bulk and surface states. For the nanowires presented here, α is much smaller due to the comparably weak MR effect, which is evident from the blue and green dashed HLN curves with $\alpha = -0.5$ and $\alpha = -0.1$ while $l_\varphi = 140$ nm. For this reason the present α value cannot be explained by the common explanations given for TI materials. The calculated phase coherence length value of $l_\varphi \approx 140$ nm is comparably lower than those experimentally observed before in thin films of various TI materials ranging from 175 to 500 nm [242, 271–275].
A possible explanation for the unphysical α and the low l_φ values lies within the contacting of the nanowires as performed here. As mentioned before, the contact resistance has to be carefully taken into account. Partial current flow through the contacts adds interface resistance which requires a renormalization factor to δG. If is R_{NW} and G_{NW} are the pure nanowire resistance and conductance, respectively, then the conductance should yield a renormalization factor of $\delta G = \delta(1/R) \approx \delta R_{NW}/(1 + R_c \cdot G_{NW})^2$. Since it was not possible to evaluate the exact contact resistance from the available measurements, the HLN fit only provides effective parameters.
Furthermore, one can speculate, that the curved surface and thus different conduction channels might play a role.

IFW setup

The WAL effect observed in the MR data displayed in figures 5.5.3 and 5.5.4, were analyzed using a different approach. Similar to the evaluation shown in the previous paragraph, the HLN fit is not feasible without renormalizing ΔG according to the contact resistance.
Fortunately, a rather rough method to extract information about the phase coherence length exists. Taking into account the critical magnetic field value B_c at which the WAL effect is destroyed (represented by the half width half maximum of the WAL cusp), a relation to the sample size can be established [227]. The phase factor of an electron traveling along a closed loop enclosing area A is proportional to the magnetic flux passing through A. Thus, the largest area that can be enclosed by phase coherent electron paths is directly related to B_c. For finite samples, different geometrical situations have to be distinguished: In the case of the magnetic field applied perpendicular to the nanowire, the relation yields

$$B_c \sim \frac{\Phi_0}{l_\varphi \cdot d}, \tag{5.17}$$

with $\Phi_0 = h/e$ being the magnetic flux quantum and d being the measured nanowire diameter. In the second case of the magnetic field oriented parallel to the nanowire, the relation changes to

$$B_c \sim \frac{\Phi_0}{D \cdot D}, \tag{5.18}$$

where D denotes the effective wire diameter. Both relations are only valid, if the phase coherence length exceeds the size of the sample.
Figure 5.6.2 summarizes the MR results for 50 and 100 nm diameter wires in perpendicular (a, c) and

parallel (b, d) B-field configuration. The thinner nanowires show deviating MR values of about 3% (II) and 1.5% (I) over 1 T at 2K (perpendicular case). On the other hand, the MR behavior amounts to similar values at 12 T in the parallel configuration, while the discrepancy was also recorded in the low-field regime. The thick wire sections III and VI, exhibit almost identical MR behavior.

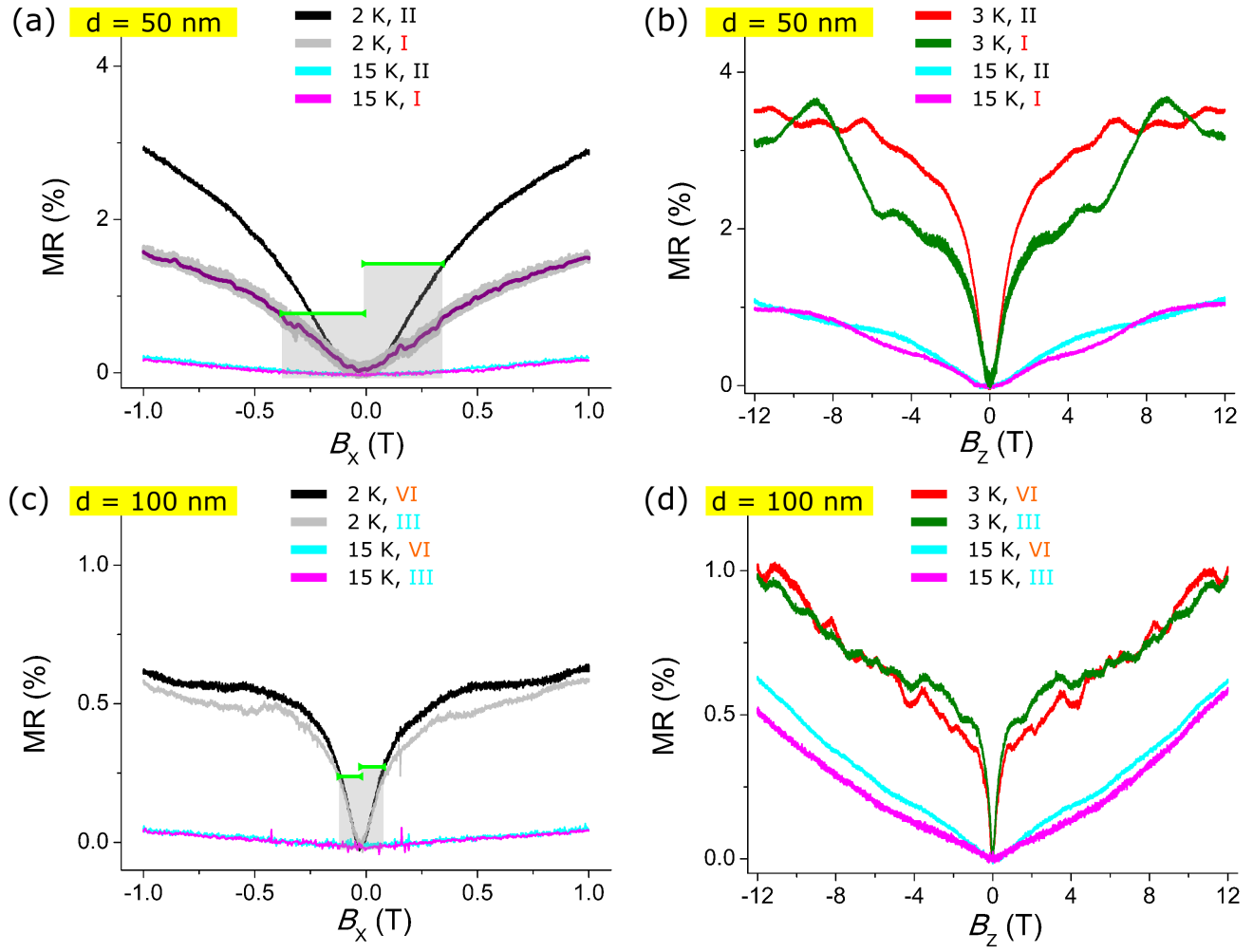

Figure 5.6.2: Magnetotransport measurement of a 50 nm (a, b) and a 100 nm (c, d) Bi_2Te_3 nanowire for various temperatures. (a, c) display the Resistance R and (b,d) the MR = (R(B)-R(B=0))/R(B=0)·100 as a function of the magnetic field up to 12 T applied parallel to the wire axis.

The critical magnetic field B_c at which the WAL effect is destroyed is defined as the half width at half maximum of the cusp as indicated by a green line and gray box for the different wire sections in figures 5.6.2 (a) and (c). Employing equations 5.17 and 5.18, the phase coherence length l_φ and the effective nanowire diameter D were be estimated. The uncertainties were calculated by standard propagation of uncertainties. On the other hand, the MR curve could not be renormalized according to proper contact resistance values, which might result in larger deviations. The results are summarized in table 5.6.1 for sections I-III and VI at temperatures of 2, 3 and 5 K. Additionally, the critical field and l_φ of sample E (see figure 5.6.1) measured in the LNCMI setup was determined. The diameter d was always measured by SEM.

In all cases, l_φ is larger than the nanowire diameter justifying the use of equations 5.17 and 5.18. Ge-

Table 5.6.1: Extracted phase coherence length l_φ and effective diameter D from the WAL effect for samples I, II, III, VI and E at different temperatures employing equations 5.17 and 5.18. The critical fields B_c are determined by the half width half maximum of the WAL cusp.

ID	Temperature (K)	d (nm)	$B_{c,\perp}$ (T)	$B_{c,\parallel}$ (T)	l_φ (nm)	D (nm)
I	3	50 ± 5	0.39 ± 0.01	0.79 ± 0.01	210 ± 22	72 ± 1
	5		0.48 ± 0.01	1.01 ± 0.01	171 ± 17	64 ± 1
II	2	50 ± 5	0.38 ± 0.01	0.71 ± 0.01	217 ± 22	76 ± 1
	3		0.41 ± 0.01	0.74 ± 0.01	203 ± 21	75 ± 1
	5		0.45 ± 0.01	0.85 ± 0.01	183 ± 19	70 ± 1
III	2	100 ± 5	0.10 ± 0.01	-	426 ± 49	-
	3		0.10 ± 0.01	0.23 ± 0.01	416 ± 47	135 ± 3
	5		0.15 ± 0.01	0.28 ± 0.01	273 ± 23	121 ± 2
VI	2	100 ± 5	0.11 ± 0.01	-	377 ± 39	-
	3		0.11 ± 0.01	0.24 ± 0.01	372 ± 38	131 ± 3
	5		0.13 ± 0.01	0.32 ± 0.01	326 ± 30	114 ± 2
E	2	75 ± 5	0.16 ± 0.02	-	343 ± 48	-
	3		0.19 ± 0.02	-	286 ± 35	-
	5		0.23 ± 0.02	-	239 ± 26	-

nerally, the phase coherence length tends to decrease with increasing temperatures, as expected. Within the uncertainties, the values are similar for sections measured from the same nanowire. For both sections of the 50 nm diameter wire (I, II) l_φ amounts to an average of about 207 nm at 3 K with only small deviations. The 100 nm diameter wire sections (III, VI) exhibit an average l_φ value of (394 ± 31) nm at 3 K. For sample E with an intermediate diameter l_φ was lies in between these values. These results are in agreement with observations made in thin films [242, 272, 273, 275]. Furthermore, electrochemically deposited Bi_2Te_3 nanowires were found to yield phase coherence lengths of around 400 nm for diameters of 50, 100 and 300 nm [26]. In the present work, similar values are obtained for the thicker wire sections, whose l_φ is about twice as large as for wires of half the diameter. A possible reason for the diameter-dependency could be finite size effects due to boundary scattering, which interfere with the localization effects [227]. The effective diameter D calculated from equation 5.18, exceeds the one measured by SEM up to about 35 nm. This is not surprising considering that the WAL behavior could not be renormalized taking into account the contact resistance.

5.7 Conclusions of magnetotransport measurements and outlook

Individual Bi_2Te_3 nanowires with diameters between 25 and 100 nm were successfully contacted by laser scanning and electron beam lithography. Especially, the Ar plasma treatments used to clean the nanowire surface before contacting, are of crucial importance to establish good quality contacts. The laser scanning lithography process at GSI was optimized for two positive resists with different thicknesses (AZ1505 and AZ1518). After the liftoff process the desired structure was exactly replicated. In order to obtain the maximal resolution of 1 µm structures technically achievable, further optimization is needed by employing negative or image reversal resists in which an undercut prevents the flanks to be coated and facilitates the liftoff.

Temperature-dependent resistivity measurements were performed down to 4.2 K, revealing metallic behavior for all samples. Furthermore, the resistivity increased from about 0.1 to 2.5 mΩcm with decreasing diameter indicating finite size effects. The expected resistivity decrease for topological insulator nanowires was not observed.

Magnetotransport measurements were successfully conducted and compared in pulsed and static magnetic field, yielding up to 55 and 12 T, respectively. The B-fields were applied in parallel and perpendicular to the contacted nanowire axis. Generally, the MR was found to be positive and non-saturating, increasing either quadratic or linear. Applying Kohler's rule, the mobility was estimated to 30-40 $cm^2V^{-1}s^{-1}$ which is only four times lower than that reported for electrodeposited single crystalline Bi_2Te_3 nanowires [89]. The linear MR behavior is in accordance to literature and is typically observed in topological insulator materials [23, 232, 233]. Except for the sample with two 25 nm wires contacted in parallel, all samples exhibit a resistance cusp in the weak field regime indicating WAL effects. A rough estimation of l_φ was performed relating the critical magnetic field at which the WAL effect is destroyed to the sample size. In accordance to literature, the obtained l_φ values amounted to about 200 and 400 nm for nanowires with 50, 75 and 100 nm diameter, respectively.

Additionally, reproducible MR oscillations were observed for samples measured in a perpendicular static B-field. These oscillations vanish at temperatures higher than 5 K in agreement with previous reports [25]. In this configuration, the oscillations can be due to the AB effect. A full qualitative analysis of these oscillations is being prepared for publication. Further magnetotransport measurements are also proposed to include gating, in order to sweep the Fermi level and investigate the MR according to the electronic band structure.

6 Summary and outlook

Cylindrical Bi_2Te_3 nanowires with diameters between 25 to 100 nm were fabricated by electrochemical deposition in ion track-etched polycarbonate membranes providing independent control of their geometry, morphology, crystallographic structure and chemical composition. The successful realization of nano-ARPES and magnetotransport studies on individual nanowires are demonstrated.

The structural properties were analyzed by HRSEM, XRD, TEM, XPS and EDX. Up to several hundred nm long single crystalline sections are found, while the overall crystallographic orientation is highly textured with the (205) and (101) plane preferably perpendicular to the wire axis. For individual nanowires the chemical composition is stoichiometric, in some cases exhibiting a local Te enrichment at the wire surface. Besides the chemical composition, the quality of the nanowire surface was evaluated by XPS. Polymer residues originating from the dissolution process to release the wires from their template are found and successfully removed by Ar sputtering. This finding is of major importance to provide a clean surface for nano-ARPES investigations and to establish good electrical contacts for transport measurements. Furthermore, the thermal stability, which is crucial for various device fabrication and cleaning methods such as soft baking during lithography, was analyzed by in-situ transmission electron microscopy during thermal annealing. The nanowires remain stable without morphological changes until 300°C.

A protocol for the preparation of individual Bi_2Te_3 nanowires for nano-ARPES measurements was established and successfully applied. The unique nano-ARPES at the SOLEIL synchrotron provided nano-XPS information along a single nanowire as well as nano-ARPES recordings from different wire sections revealing their electronic band structure. The chemically homogeneous composition along the nanowires is confirmed, while the electronic structure changes for different sections. This is attributed to varying crystallographic orientations depending on the rotation of the nanowire with respect to its axis. First-principles calculations performed for crystal orientations, which were selected depending on the texture evaluation by XRD, match the experimental results and demonstrate the orientation dependency.

The second major set of experiments conducted in this dissertation were magnetotransport measurements as a function of nanowire diameter. First, a method for the electrical contacting of single Bi_2Te_3 nanowires had to be established, employing several lithographical processes. Especially, the optimization of the parameters for the laser scanning lithography at GSI, are an important development of this thesis. Second, the nanowires were characterized electrically by conducting temperature-dependent resistivity measurements from room to liquid Helium temperatures. Nanowire samples with diameters of about 25, 50, 75 and 100 nm reveal metallic behavior. The resistivity increase with decreasing diameter hints towards the influence of finite size effects. A decrease in resistivity as expected for topological insulator nanowires due to their high surface-to-volume ratio, is not observed.

The actual magnetotransport measurements were performed in pulsed (up to 55 T) and static (up to 12 T) magnetic field applied perpendicular and parallel to the nanowire axis. For all samples, the MR is positive and non-saturating, increasing either quadratic or linear. A linear increase has been reported for TI materials. In all cases, the characteristic decrease of the MR in the zero-field regime and at very low temperatures is appointed to the WAL effect. At higher magnetic fields and elevated temperatures

this quantum interference phenomenon vanishes, as expected. From the WAL data, the phase coherence length l_φ was roughly estimated making use of the correlation between the critical field at which WAL is destroyed and the sample geometry. The obtained l_φ values exhibit a size dependency ranging from about 200 nm for 50 nm diameter wires to 400 nm for 100 nm diameter wires.

On the basis of the results presented in this dissertation a full electrical characterization of individual Bi_2Te_3 nanowires is possible. Future nano-ARPES measurements require an improvement of the resolution of the band structure. Additionally, nano-ARPES recordings in combination with subsequent TEM investigations would provide the direct experimental link between crystallographic orientation and electrical band structure. Furthermore, magnetotransport studies employing a gated nanowire could complement the information about the band structure. As a function of nanowire diameter, the transition point at which possible surface states provide the dominant electrical signal could be investigated using both methods.

Bibliography

[1] J. Manyika, M. Chui, P. Bisson, J. Woetzel, R. Dobbs, J. Bughin, and D. Aharon. The internet of things: Mapping the value beyond the hype. Technical report, McKinsey Global Institute, Washington, DC, USA, 2015.

[2] K. Ashton. That "internet of things" thing. *RFiD Journal*, 22(7):97–114, 2009.

[3] P. Fraga-Lamas, T. M. Fernández-Caramés, M. Suárez-Albela, L. Castedo, and M. González-López. A review on internet of things for defense and public safety. *Sensors*, 16(10):1644, 2016.

[4] D. Miorandi, S. Sicari, F. De Pellegrini, and I. Chlamtac. Internet of things: Vision, applications and research challenges. *Ad Hoc Networks*, 10(7):1497 – 1516, 2012.

[5] D. Kong and Y. Cui. Opportunities in chemistry and materials science for topological insulators and their nanostructures. *Nat. Chem.*, 3(11):845–849, November 2011.

[6] L. D. Hicks and M. S. Dresselhaus. Thermoelectric figure of merit of a one-dimensional conductor. *Phys. Rev. B*, 47(24):16631–16634, 1993.

[7] D. Pesin and A. H. MacDonald. Spintronics and pseudospintronics in graphene and topological insulators. *Nat. Mater.*, 11(5):409–416, 2012.

[8] S. A. Wolf, D. D. Awschalom, R. A. Buhrman, J. M. Daughton, S. von Molnár, M. L. Roukes, A. Y. Chtchelkanova, and D. M. Treger. Spintronics: A spin-based electronics vision for the future. *Science*, 294(5546):1488–1495, 2001.

[9] M. Z. Hasan and C. L. Kane. Colloquium: Topological insulators. *Rev. Mod. Phys.*, 82(4):3045–3067, 2010.

[10] X.-L. Qi and S.-C. Zhang. Topological insulators and superconductors. *Rev. Mod. Phys.*, 83(4):1057–1110, 2011.

[11] L. Fu and C. L. Kane. Superconducting proximity effect and majorana fermions at the surface of a topological insulator. *Phys. Rev. Lett.*, 100(9):096407, 2008.

[12] L. Fu. Topological crystalline insulators. *Phys. Rev. Lett.*, 106(10):106802, 2011.

[13] S.-Y. Xu, I. Belopolski, D. S. Sanchez, C. Zhang, G. Chang, C. Guo, G. Bian, Z. Yuan, H. Lu, T.-R. Chang, P. P. Shibayev, M. L. Prokopovych, N. Alidoust, H. Zheng, C.-C. Lee, S.-M. Huang, R. Sankar, F. Chou, C.-H. Hsu, H.-T. Jeng, A. Bansil, T. Neupert, V. N. Strocov, H. Lin, S. Jia, and M. Z. Hasan. Experimental discovery of a topological Weyl semimetal state in TaP. *Sci. Adv.*, 1(10):e1501092, 2015.

[14] S.-M. Huang, S.-Y. Xu, I. Belopolski, C.-C. Lee, G. Chang, B. K. Wang, N. Alidoust, G. Bian, M. Neupane, C. Zhang, S. Jia, A. Bansil, H. Lin, and M. Z. Hasan. A Weyl fermion semimetal with surface Fermi arcs in the transition metal monopnictide TaAs class. *Nat. Commun.*, 6(7373), 2015.

[15] T. Zhang, P. Cheng, X. Chen, J.-F. Jia, X. Ma, K. He, L. Wang, H. Zhang, X. Dai, Z. Fang, X. Xie, and Q.-K. Xue. Experimental demonstration of topological surface states protected by time-reversal symmetry. *Phys. Rev. Lett.*, 103(26):266803, 2009.

[16] Z. Alpichshev, J. G. Analytis, J.-H. Chu, I. R. Fisher, Y. L. Chen, Z. X. Shen, A. Fang, and A. Kapitulnik. STM imaging of electronic waves on the surface of Bi_2Te_3: topologically protected surface states and hexagonal warping effects. *Phys. Rev. Lett.*, 104(1):016401, 2010.

[17] H. Peng, K. Lai, D. Kong, S. Meister, Y. Chen, X.-L. Qi, S.-C. Zhang, Z.-X. Shen, and Y. Cui. Aharonov-Bohm interference in topological insulator nanoribbons. *Nat. Mater.*, 9(3):225–229, 2010.

[18] D. Kong, J. C. Randel, H. Peng, J. J. Cha, S. Meister, K. Lai, Y. Chen, Z.-X. Shen, H. C. Manoharan, and Y. Cui. Topological insulator nanowires and nanoribbons. *Nano Lett.*, 10(1):329–333, 2010.

[19] D. Kong, Y. Chen, J. J. Cha, Q. Zhang, J. G. Analytis, K. Lai, Z. I. Liu, S. S. Hong, K. J. Koski, S.-K. Mo, Z. Hussain, I. R. Fisher, Z.-X. Shen, and Y. Cui. Ambipolar field effect in the ternary topological insulator $(Bi_xSb_{1-x})_2Te_3$ by composition tuning. *Nat. Nanotechnol.*, 6(11):705–709, 2011.

[20] H. Zhu, C. A. Richter, E. Zhao, J. E. Bonevich, W. A. Kimes, H.-J. Jang, H. Yuan, H. Li, A. Arab, O. Kirillov, J. E. Maslar, D. E. Ioannou, and Q. Li. Topological insulator Bi_2Se_3 nanowire high performance field-effect transistors. *Sci. Rep.*, 3:1757–, April 2013.

[21] S. S. Hong, Y. Zhang, J. J. Cha, X.-L. Qi, and Y. Cui. One-dimensional helical transport in topological insulator nanowire interferometer. *Nano Lett.*, 14:2815–2821, March 2014.

[22] J. J. Cha, K. J. Koski, and Y. Cui. Topological insulator nanostructures. *Phys. Status Solidi RRL*, 7(1-2):15–25, 2013.

[23] X. Wang, Y. Du, S. Dou, and C. Zhang. Room temperature giant and linear magnetoresistance in topological insulator Bi_2Te_3 nanosheets. *Phys. Rev. Lett.*, 108(26):266806, 2012.

[24] B. Hamdou, J. Gooth, A. Dorn, E. Pippel, and K. Nielsch. Surface state dominated transport in topological insulator Bi_2Te_3 nanowires. *Appl. Phys. Lett.*, 103(19):193107, 2013.

[25] M. Tian, W. Ning, Z. Qu, H. Du, J. Wang, and Y. Zhang. Dual evidence of surface Dirac states in thin cylindrical topological insulator Bi_2Te_3 nanowires. *Sci. Rep.*, 3:1212, 2013.

[26] W. Ning, H. Du, F. Kong, J. Yang, Y. Han, M. Tian, and Y. Zhang. One-dimensional weak antilocalization in single-crystal bi2te3 nanowires. *Sci. Rep.*, 3(1564), March 2013.

[27] J. Gooth, B. Hamdou, A. Dorn, R. Zierold, and K. Nielsch. Resolving the Dirac cone on the surface of Bi_2Te_3 topological insulator nanowires by field-effect measurements. *Appl. Phys. Lett.*, 104(24):243115, 2014.

[28] L. A. Jauregui, M. T. Pettes, L. P. Rokhinson, L. Shi, and Y. P. Chen. Gate tunable relatisvistic mass and Berry's phase in topological insulator nanoribbon field effect devices. *Sci. Rep.*, 5(8452), 2015.

[29] J. P. Fleurial, L. Gailliard, R. Triboulet, H. Scherrer, and S. Scherrer. Thermal properties of high quality single crystals of bismuth telluride-part I: Experimental characterization. *J. Phys. Chem. Solids*, 49(10):1237–1247, 1988.

[30] J. W. G. Bos, H. W. Zandbergen, M.-H. Lee, N. P. Ong, and R. J. Cava. Structures and thermoelectric properties of the infinitely adaptive series $(Bi_2)_m(Bi_2Te_3)_n$. *Phys. Rev. B*, 75(19):195203, 2007.

[31] A. Fülöp, Y. Song, S. Charpentier, P. Shi, M. Ekström, L. Galletti, R. Arpaia, T. Bauch, F. Lombardi, and S. Wang. Phase transition of bismuth telluride thin films grown by MBE. *Appl. Phys. Express*, 7(045503):1–4, 2014.

[32] A. Bostwick, E. Rotenberg, J. Avila, and M. C. Asensio. Zooming in on electroni structure: Nano-ARPES at SOLEIL and ALS. *Synchrotron Radiation News*, 25(5):19–25, 2012.

[33] J. Avila, I. Razado, S. Lorcy, R. Fleurier, E. Pichonat, D. Vignaud, X. Wallart, and M. C. Asensio. Exploring electronic structure of one-atom thick polycrystalline graphene films: A nano angle resolved photoemission study. *Sci. Rep.*, 3(2439):1–8, 2013.

[34] J. Avila, I. Razado-Colambo, S. Lorcy, B. Lagarde, J. L. Giorgetta, F. Polack, and M. C. Asensio. Antares, a scanning photoemission microscopy beamline at soleil. *J. Phys. Conf. Ser.*, 425(19):192023, 2013.

[35] J. Avila, I. Razado-Colambo, S. Lorcy, J. L. Giorgetta, F. Polack, and M. C. Asensio. Interferometer-controlled soft x-ray scanning photoemission microscope at SOLEIL. *J. Phys. Conf. Ser.*, 425(13):132013, 2013.

[36] J. Avila and M. C. Asensio. First nanoARPES user facility available at SOLEIL: an innovative and powerful tool for studying advanced materials. *Synchrotron Radiation News*, 27(2):24–30, 2014.

[37] H. J. Goldsmid and R. W. Douglas. The use of semiconductors in thermoelectric refrigeration. *Br. J. Appl. Phys.*, 5:386–389, 1954.

[38] H. Zhang, C.-X. Liu, X.-L. Qi, X. Dai, Z. Fang, and S.-C. Zhang. Topological insulators in Bi_2Se_3, Bi_2Te_3 and Sb_2Te_3 with a single Dirac cone on the surface. *Nat. Phys.*, 5(6):438–442, 2009.

[39] P. Gehring, H. M. Benia, Y. Weng, R. Dinnebier, C. R. Ast, M. Burghard, and K. Kern. A natural topological insulator. *Nano Lett.*, 13(3):1179–1184, 2013.

[40] Pascal Gehring. *Magnetotransport properties of Topological Insulator thin films*. PhD thesis, École Polytechnique Fédérale de Lausanne, 2014.

[41] T. Ozawa and H. Shimazaki. Pilsenite re-defined and wehrlite discredited. *Proceedings of the Japan Academy, Series B*, 58(10):291–294, 1982.

[42] H. Shimazaki and T. Ozawa. Tsumoite, BiTe, a new mineral from the Tsumo mine, Japan. *American Mineralogist*, 63:I162–1165, 1978.

[43] N. J. Cook, C. L. Ciobanu, T. Wagner, and C. J. Stanley. Minerals of the system Bi–Te–Se–S related to the tetradymite archetype: review of classification and compositional variation. *The Canadian Mineralogist*, 45(4):665–708, 2007.

[44] Sigma Aldrich. Material safety data sheet bismuth(III) telluride, May 2013.

[45] M. H. Francombe. Structure-cell data and expansion coefficients of bismuth telluride. *Br. J. Appl. Phys.*, 9(10):415, 1958.

[46] J. R. Drabble and C. H. L. Goodman. Chemical bonding in bismuth telluride. *J. Phys. Chem. Solids*, 5(1):142–144, 1958.

[47] R. T. Delves, A. E. Bowley, D. W. Hazelden, and H. J. Goldsmid. Anisotropy of the electrical conductivity in bismuth telluride. *Proceedings of the Physical Society*, 78(5):838, 1961.

[48] P. W. Lange. Ein Vergleich zwischen Bi_2Te_3 und Bi_2Te_3S. *Naturwissenschaften*, 27(8):133–134, 1939.

[49] Mikio Nakahara. *Geometry, topology and physics*. CRC Press, 2003.

[50] Klaus Jänich. *Topologie*. Springer-Verlag, 2013.

[51] M. V Berry. Quantal phase factors accompanying adiabatic changes. *Proc. R. Soc. A*, 392(1802):45–57, 1984.

[52] K. v. Klitzing, G. Dorda, and M. Pepper. New method for high-accuracy determination of the fine-structure constant based on quantized Hall resistance. *Phys. Rev. Lett.*, 45(6):494–497, 1980.

[53] D. J. Thouless, M. Kohmoto, M. P. Nightingale, and M. den Nijs. Quantized Hall conductance in a two-dimensional periodic potential. *Phys. Rev. Lett.*, 49(6):405–408, 1982.

[54] F. D. M. Haldane. Model for a quantum Hall effect without Landau levels: condensed-matter realization of the "parity anomaly". *Phys. Rev. Lett.*, 61(18):2015–2018, 1988.

[55] C. L. Kane and E. J. Mele. Quantum spin Hall effect in graphene. *Phys. Rev. Lett.*, 95(22):226801, 2005.

[56] C. L. Kane and E. J. Mele. Z_2 topological order and the quantum spin Hall effect. *Phys. Rev. Lett.*, 95(14):146802, 2005.

[57] J. E. Moore and L. Balents. Topological invariants of time-reversal-invariant band structures. *Phys. Rev. B*, 75(12):121306, 2007.

[58] Charles Kittel. *Introduction to solid state physics*. John Wiley & Sons, 2005.

[59] Franz Schwabl. *Advanced quantum mechanics*. Springer Science & Business Media, 2005.

[60] H. A. Kramers. General theory of paramagnetic rotation in crystals. *Proc. Acad. Sci. Amsterdam*, 33:959, 1930.

[61] L. Fu and C. L. Kane. Topological insulators with inversion symmetry. *Phys. Rev. B*, 76(4):045302, 2007.

[62] L. Fu, C. L. Kane, and E. J. Mele. Topological insulators in three dimensions. *Phys. Rev. Lett.*, 98(10):106803, 2007.

[63] B. A. Bernevig, T. L. Hughes, and S.-C. Zhang. Quantum spin Hall effect and topological phase transition in HgTe quantum wells. *Science*, 314(5806):1757–761, 2006.

[64] M. König, S. Wiedmann, C. Brüne, A. Roth, H. Buhmann, L. W. Molenkamp, X.-L. Qi, and S.-C. Zhang. Quantum spin hall insulator state in HgTe quantum wells. *Science*, 318(5851):766–770, 2007.

[65] B. Lenoir, M. Cassart, J.-P. Michenaud, H. Scherrer, and S. Scherrer. Transport properties of Bi-rich Bi-Sb alloys. *J. Phys. Chem. Solids*, 57(1):89–99, 1996.

[66] D. Hsieh, D. Qian, L. Wray, Y. Xia, Y. S. Hor, R. J. Cava, and M. Z. Hasan. A topological Dirac insulator in a quantum spin Hall phase. *Nature*, 452(7190):970–974, 2008.

[67] Y. Xia, D. Qian, D. Hsieh, L. Wray, A. Pal, H. Lin, A. Bansil, D. Grauer, Y. S. Hor, R. J. Cava, and M. Z. Hasan. Observation of a large-gap topological-insulator class with a single Dirac cone on the surface. *Nature Phys.*, 5(6):398–402, 2009.

[68] D. Hsieh, Y. Xia, D. Qian, L. Wray, F. Meier, J. H. Dil, J. Osterwalder, L. Patthey, A. V. Fedorov, H. Lin, A. Bansil, D. Grauer, Y. S. Hor, R. J. Cava, and M. Z. Hasan. Observation of time-reversal-protected single-dirac-cone topological-insulator states in Bi_2Te_3 and Sb_2Te_3. *Phys. Rev. Lett.*, 103(14):146401, 2009.

[69] Y. L. Chen, J. G. Analytis, J-H Chu, Z. K. Liu, S-K Mo, X. L. Qi, H. J. Zhang, D. H. Lu, X. Dai, Z. Fang, S. C. Zhang, I. R. Fisher, Z. Hussain, and Z-X Shen. Experimental realization of a three-dimensional topological insulator, Bi_2Te_3. *Science*, 325(5937):178–181, 2009.

[70] H.-J. Noh, H. Koh, S.-J. Oh, J.-H. Park, H.-D. Kim, J. D. Rameau, T. Valla, T. E. Kidd, P. D. Johnson, Y. Hu, and Q. Li. Spin-orbit interaction effect in the electronic structure of Bi_2Te_3 observed by angle-resolved photoemission spectroscopy. *Europhys. Lett.*, 81(5):57006, 2008.

[71] Y. Ando. Topological insulator materials. *J. Phys. Soc. Jpn.*, 82(10):102001, 2013.

[72] I. Vobornik, U. Manju, J. Fujii, F. Borgatti, P. Torelli, D. Krizmancic, Y. S. Hor, R. J. Cava, and G. Panaccione. Magnetic proximity effect as a pathway to spintronic applications of topological insulators. *Nano Lett.*, 11(10):4079–4082, 2011.

[73] Y. Tanabe, K. K. Huynh, R. Nouchi, S. Heguri, G. Mu, J. Xu, H. Shimotani, and K. Tanigaki. Electron and hole injection via charge transfer at the topological insulator $Bi_{2-x}Sb_xTe_{3-y}Se_y$-organi molecule interface. *J. Phys. Chem. C*, 118(7):3533–3538, 2014.

[74] J. Tang, L.-T. Chang, X. Kou, K. Murata, E. S. Choi, M. Lang, Y. Fan, Y. Jiang, M. Montazeri, W. Jiang, Y. Wang, L. He, and K. L. Wang. Electrical detection of spin-polarized surface states conduction in $(Bi_{0.53}Sb_{0.47})_2Te_3$ topological insulator. *Nano Lett.*, 14(9):5423–5429, 2014.

[75] Y. Ando, T. Hamasaki, T. Kurokawa, K. Ichiba, F. Yang, M. Novak, S. Sasaki, K. Segawa, Y. Ando, and M. Shiraishi. Electrical detection of the spin polarization due to charge flow in the surface state of the topological insulator $Bi_{1.5}Sb_{0.5}Te_{1.7}Se_{1.3}$. *Nano Lett.*, 14(11):6226–6230, 2014.

[76] David Michael Rowe. *Thermoelectrics handbook: macro to nano*. CRC press, 2006.

[77] S. B. Riffat and X. Ma. Thermoelectrics: a review of present and potential applications. *Applied Thermal Engineering*, 23(8):913–935, 2003.

[78] L. E. Bell. Cooling, heating, generating power, and recovering waste heat with thermoelectric systems. *Science*, 321(5895):1457–1461, 2008.

[79] R. Franz and G. Wiedemann. Über die Wärme-Leitungsfähigkeit der Metalle. *Ann. Phys. (Berlin)*, 165(8):497–531, 1853.

[80] L. D. Hicks and M. S. Dresselhaus. Effect of quantum-well structures on the thermoelectric figure of merit. *Phys. Rev. B*, 47(19):12727–12731, 1993.

[81] C. W. J. Beenakker and H. van Houten. Quantum transport in semiconductor nanostructures. *Solid state physics*, 44:1–228, 1991.

[82] J. P. Heremans. Low-dimensional thermoelectricity. *Acta. Phys. Pol. A*, 108(4):609, 2005.

[83] B. Qiu, L. Sun, and X. Ruan. Lattice thermal conductivity reduction in Bi_2Te_3 quantum wires with smooth and rough surfaces: A molecular dynamics study. *Phys. Rev. B*, 83:035312, Jan 2011.

[84] R. Venkatasubramanian, E. Siivola, T. Colpitts, and B. O'Quinn. Thin-film thermoelectric devices with high room-temperature figures of merit. *Nature*, 413(6856):597–602, 2001.

[85] X. Tang, W. Xie, H. Li, W. Zhao, Q. Zhang, and M. Niino. Preparation and thermoelectric transport properties of high-performance p-type Bi_2Te_3 with layered nanostructure. *Appl. Phys. Lett.*, 90(1):12102, 2007.

[86] L.-D. Zhao, S.-H. Lo, Y. Zhang, H. Sun, G. Tan, C. Uher, C. Wolverton, V. P. Dravid, and M. G. Kanatzidis. Ultralow thermal conductivity and high thermoelectric figure of merit in SnSe crystals. *Nature*, 508(7496):373–377, 2014.

[87] B. Zhong, Y. Zhang, W. Li, Z. Chen, J. Cui, W. Li, Y. Xie, Q. Hao, and Q. He. High superionic conduction arising from aligned large lamellae and large figure of merit in bulk $Cu_{1.94}Al_{0.02}Se$. *Appl. Phys. Lett.*, 105(12), 2014.

[88] M. C. Schmitt, H. Reith, D. Huzel, and F. Völklein. New measuring techniques for the investigation of thermoelectric properties of nanowires. *AIP Conf. Proc.*, 1449(1):385–388, 2012.

[89] A. Mavrokefalos, A. L. Moore, M. T. Pettes, L. Shi, W. Wang, and X. Li. Thermoelectric and structural characterizations of individual electrodeposited bismuth telluride nanowires. *J. Appl. Phys.*, 105(10):104318, 2009.

[90] H. S. Shin, S. G. Jeon, J. Yu, Y.-S. Kim, H. M. Park, and J. Y. Song. Twin-driven thermoelectric figure-of-merit enhancement of Bi_2Te_3 nanowires. *Nanoscale*, 6(11):6158–6165, 2014.

[91] P. Ghaemi, R. S. K. Mong, and J. E. Moore. In-plane transport and enhanced thermoelectric performance in thin films of the topological insulators Bi_2Te_3 and Bi_2Se_3. *Phys. Rev. Lett.*, 105(16):166603, 2010.

[92] R. Takahashi and S. Murakami. Thermoelectric transport in topological insulators. *Semicond. Sci. Technol.*, 27(12):124005, 2012.

[93] L. Muchler, F. Casper, B. Yan, S. Chadov, and C. Felser. Topological insulators and thermoelectric materials. *Phys. Status Solidi*, 7(1-2):91–100, 2 2013.

[94] F. Rittweger, N. F. Hinsche, P. Zahn, and I. Mertig. Signature of the topological surface state in the thermoelectric properties of Bi_2Te_3. *Phys. Rev. B*, 89(3):35439, 2014.

[95] Y. Xu, Z. Gan, and S.-C. Zhang. Enhanced thermoelectric performance and anomalous Seebeck effects in topological insulators. *Phys. Rev. Lett.*, 112(22):226801, 2014.

[96] H. Osterhage, J. Gooth, B. Hamdou, P. Gwozdz, R. Zierold, and K. Nielsch. Thermoelectric properties of topological insulator Bi_2Te_3, Sb_2Te_3, and Bi_2Se_3 thin film quantum wells. *Appl. Phys. Lett.*, 105(12):123117, 2014.

[97] J. Gooth, J. G. Gluschke, R. Zierold, M. Leijnse, H. Linke, and K. Nielsch. Thermoelectric performance of classical topological insulator nanowires. *Semicond. Sci. Technol.*, 30(1):15015, 2015.

[98] Kunihito Komoto and Takao Mori. *Thermoelectric nanomaterials: materials design and applications*, volume 182. Springer series in materials science (ISSN 0933-033X), 2013.

[99] Y. Xia, P. Yang, Y. Sun, Y. Wu, B. Mayers, B. Gates, Y. Yin, F. Kim, and H. Yan. One-dimensional nanostructures: Synthesis, characterization, and applications. *Adv. Mater.*, 15(5):353–389, 2003.

[100] R. S. Wagner and W. C. Ellis. Vapor–liquid–solid mechanism of single crystal growth. *Appl. Phys. Lett.*, 4(5):89–90, 1964.

[101] J. E. Allen, E. R. Hemesath, D. E. Perea, J. L. Lensch-Falk, Z. Y. Li, F. Yin, M. H. Gass, P. Wang, A. L. Bleloch, R. E. Palmer, and L. J. Lauhon. High-resolution detection of Au catalyst atoms in Si nanowires. *Nat. Nanotechnol.*, 3(3):168–173, 2008.

[102] S. Barth, J. J. Boland, and J. D. Holmes. Defect transfer from nanoparticles to nanowires. *Nano Lett.*, 11(4):1550–1555, 2011.

[103] R. G. Hobbs, N. Petkov, and J. D. Holmes. Semiconductor nanowire fabrication by bottom-up and top-down paradigms. *Chem. Mater.*, 24(11):1975–1991, 2012.

[104] Q. Wei, Y. Su, C. J. Yang, Z. G. Lui, H. N. Xu, Y. D. Xia, and J. Yin. The synthesis of Bi_2Te_3 nanobelts by vapour-liquid-solid method and their electrical transport properties. *J. Mater. Sci.*, 46(7):2267–2272, 2011.

[105] B. Hamdou, J. Kimling, A.T. Dorn, E. Pippel, R. Rostek, P. Woias, and K. Nielsch. Thermoelectric characterization of bismuth telluride nanowires, synthesized via catalytic growth and post-annealing. *Adv. Mater.*, 25(2):239–244, 2013.

[106] J. Andzane, G. Kunakova, S. Charpentier, V. Hrkac, L. Kienle, M. Baitimirova, T. Bauch, F. Lombardi, and D. Erts. Catalyst-free vapour-solid technique for deposition of Bi_2Te_3 and Bi_2Se_3 nanowires/nanobelts with topological insulator properties. *Nanoscale*, 7(38):15935–15944, 2015.

[107] G. E. Possin. A method for forming very small diameter wires. *Rev. Sci. Instrum.*, 41(5):772–774, 1970.

[108] T. Sun, X. B. Zhao, T. J. Zhu, and J. P. Tu. Aqueous chemical reduction synthesis of Bi_2Te_3 nanowires with surfactant assistance. *Materials Letters*, 60(20):2534–2537, 2006.

[109] E. J. Menke, M. A. Brown, Q. Li, J. C. Hemminger, and R. M. Penner. Bismuth telluride (Bi_2Te_3) nanowires: synthesis by cyclic electrodeposition/stripping, thinning by electrooxidation, and electrical power generation. *Langmuir*, 22(25):10564–10574, 2006.

[110] S. A. Sapp, B. B. Lakshmi, and C. R. Martin. Template synthesis of bismuth telluride nanowires. *Adv. Mater.*, 11(5):402–406, 1999.

[111] A. L. Prieto, M. S. Sander, M. S. Martín-González, R. Gronsky, T. Sands, and A. M. Stacy. Electrodeposition of ordered Bi_2Te_3 nanowire arrays. *J. Am. Chem. Soc.*, 123(29):7160–7161, 2001.

[112] M. S. Sander, A. L. Prieto, R. Gronsky, T. Sands, and A. M. Stacy. Fabrication of high-density, high aspect ratio, large-area bismuth telluride nanowire arrays by electrodeposition into porous anodic alumina templates. *Adv. Mater.*, 14(9):665–667, 2002.

[113] M. S. Sander, R. Gronsky, T. Sands, and A. M. Stacyă. Structure of bismuth telluride nanowire arrays fabricated by electrodeposition into porous anodic alumina templates. *Chem. Mater.*, 15(1):335–339, 2003.

[114] C. Jin, X. Xiang, C. Jia, W. Liu, W. Cai, L. Yao, and X. Li. Electrochemical fabrication of large-area, ordered Bi_2Te_3 nanowire arrays. *J. Phys. Chem. B*, 108(6):1844–1847, 2004.

[115] C. Frantz, N. Stein, L. Gravier, S. Granville, and C. Boulanger. Electrodeposition and characterization of bismuth telluride nanowires. *J. Electron. Mater.*, 39(9):2043–2048, 2010.

[116] O. Picht, S. Müller, I. Alber, M. Rauber, J. Lensch-Falk, D. L. Medlin, R. Neumann, and M. E. Toimil-Molares. Tuning the geometrical and crystallographic characteristics of Bi_2Te_3 nanowires by electrodeposition in ion-track membranes. *J. Phys. Chem. C*, 116(9):5367–5375, 2012.

[117] C. Frantz, N. Stein, Y. Zhang, E. Bouzy, O. Picht, M. E. Toimil-Molares, and C. Boulanger. Electrodeposition of bismuth telluride nanowires with controlled composition im polycarbonate membranes. *Electrochim. Acta*, 69:30–37, 2012.

[118] N. Peranio, E. Leister, W. Töllner, O. Eibl, and K. Nielsch. Single-crystalline, stoichiometric Bi_2Te_3 nanowires for transport in the basal plane. *J. Electron. Mater.*, 41(6):1509–1512, 2012.

[119] D.-A. Borca-Tasciuc and G. Chen. Anisotropic thermal properties of nanochanneled alumina templates. *J. Appl. Phys.*, 97(8):084303, 2005.

[120] K. G. Biswas, T. D. Sands, B. A. Cola, and X. Xu. Thermal conductivity of bismuth telluride nanowire array-epoxy composite. *Appl. Phys. Lett.*, 94(22):223116, 2009.

[121] J. Vetter and R. Spohr. Application of ion track membranes for preparation of metallic microstructures. *Nucl. Instr. Meth. Phys. Res. Sec. B*, 79(1):691–694, 1993.

[122] M.E. Toimil-Molares, V. Buschmann, D. Dobrev, R. Neumann, R. Scholz, I. U. Schuchert, and J. Vetter. Single-crystalline copper nanowires produced by electrochemical deposition in polymeric ion track membranes. *Adv. Mater*, 13(1):5, 2001.

[123] M. E. Toimil-Molares. Characterization and properties of micro- and nanowires of controlled size, composition, and geometry fabricated by electrodeposition and ion-track technology. *Beilstein J. Nanotechnol.*, 3:860–883, 2012.

[124] M. E. Toimil-Molares, J. Brötz, V. Buschmann, D. Dobrev, R. Neumann, R. Scholz, I. U. Schuchert, C. Trautmann, and J. Vetter. Etched heavy ion tracks in polycarbonate as template for copper nanowires. *Nucl. Instr. Meth. Phys. Res. Sec. B*, 185(1–4):192–197, 2001.

[125] S. Karim, M. E. Toimil-Molares, F. Maurer, G. Miehe, W. Ensinger, J. Liu, T. W. Cornelius, and R. Neumann. Synthesis of gold nanowires with controlled crystallographic characteristics. *Appl. Phys. A*, 84(4):403–407, 2006.

[126] T. W. Cornelius, J. Brötz, N. Chtanko, D. Dobrev, G. Miehe, R. Neumann, and M. E. Toimil-Molares. Controlled fabrication of poly- and single-crystalline bismuth nanowires. *Nanotechnology*, 16(5):246, 2005.

[127] L. Movsesyan, I. Schubert, L. Yeranyan, C. Trautmann, and M. E. Toimil-Molares. Influence of electrodeposition parameters on the structure and morphology of ZnO nanowire arrays and networks synthesized in etched ion-track membranes. *Semiconductor Science and Technology*, 31(1):14006, 2016.

[128] S. Mueller, C. Schoetz, O. Picht, W. Sigle, P. Kopold, M. Rauber, I. Alber, R. Neumann, and M. E. Toimil-Molares. Electrochemical synthesis of $Bi_{1-x}Sb_x$ nanowires with simultaneous control on size, composition, and surface roughness. *Cryst. Growth Des.*, 12(2):615–621, 2012.

[129] M. Cassinelli, S. Müller, Z. Aabdin, N. Peranio, O. Eibl, C. Trautmann, and M. E. Toimil-Molares. Structural and compositional characterization of $Bi_{1-x}Sb_x$ nanowire arrays grown by pulsed deposition to improve growth uniformity. *Nucl. Instr. Meth. Phys. Res. Sec.B*, 365:668–674, 2015.

[130] M. F. P. Wagner, F. Völklein, H. Reith, C. Trautmann, and M. E. Toimil-Molares. Fabrication and thermoelectrical characterization of three-dimensional nanowire networks. *Phys. Status Solidi*, 2016.

[131] O. Picht, J. Krieg, and M. E. Toimil-Molares. Bi_2Te_3 nanowires by electrodeposition in polymeric ion track membranes: Synthesis and characterization. In O. Eibl, K. Nielsch, N. Peranio, and F. Völklein, editors, *Thermoelectric Bi_2Te_3 Nanomaterials*, pages 33–53. Wiley-VCH Verlag GmbH & Co. KGaA, 2015.

[132] I. Schubert, L. Burr, C. Trautmann, and M. E. Toimil-Molares. Growth and morphological analysis of segmented AuAg alloy nanowires created by pulsed electrodeposition in ion-track etched membranes. *Beilstein J. of Nanotechnol.*, 6:1272–1280, 2015.

[133] L. Burr, I. Schubert, W. Sigle, C. Trautmann, and M. E. Toimil-Molares. Surface enrichment in Au–Ag alloy nanowires and investigation of the dealloying process. *J. Phys. Chem. C*, 119(36):20949–20956, 2015.

[134] C. Trautmann. Observation and chemical treatment of heavy-ion tracks in polymers. *Nucl. Instr. Meth. Phys. Res. B*, 105(1-4):81–85, 1995.

[135] Christina Trautmann. Micro- and nanoengineering with ion tracks. In R. Hellborg, H. J. Whitlow, and Y. Zhang, editors, *Ion Beams in Nanoscience and Technology*, Particle Acceleration and Detection, pages 369–387. Springer Berlin Heidelberg, 2010.

[136] F. Xiu, L. He, Y. Wang, L. Cheng, L.-T. Chang, M. Lang, G. Huang, X. Kou, Y. Zhou, X. Jiang, Z. Chen, J. Zou, A. Shailos, and K. L. Wang. Manipulating surface states in topological insulator nanoribbons. *Nat. Nanotechnol.*, 6(4):216–221, 2011.

[137] R. Spohr. *Ion Tracks and Microtechnology: Principles and Applications*. Informatica International, Incorporated, 1990.

[138] R. L. Fleischer, P. B. Price, and R. M. Walker. *Nuclear Tracks in Solids: Principles and Applications*. University of California Press, 1975.

[139] M. Toulemonde, C. Dufour, A. Meftah, and E. Paumier. Transient thermal processes in heavy ion irradiation of crystalline inorganic insulators. *Nucl. Instr. Meth. Phys. Res. Sec. B*, 166:903–912, 2000.

[140] R. L. Fleischer and P. B. Price. Tracks of charged particles in high polymers. *Science*, 140(3572):1221–1222, 1963.

[141] Y. Sun, Z. Zhu, Z. Wang, Y. Jin, J. Liu, M. Hou, and Q. Zhang. Swift heavy ion induced amorphisation and chemical modification in polycarbonate. *Nucl. Instr. Meth. Phys. Res. Sec. B*, 209:188–193, 2003.

[142] F. Dehaye, E. Balanzat, E. Ferain, and R. Legras. Chemical modifications induced in bisphenol A polycarbonate by swift heavy ions. *Nucl. Instr. Meth. Phys. Res. Sec. B*, 209:103–112, 2003.

[143] F. Petersen and W. Enge. Energy loss dependent transversal etching rates of heavy ion tracks in plastic. *Radiation Measurements*, 25(1):43–46, 1995.

[144] C. Trautmann, S. Bouffard, and R. Spohr. Etching threshold for ion tracks in polyimide. *Nucl. Instr. Meth. Phys. Res. Sec. B*, 116(1):429–433, 1996.

[145] P. Apel, A. Schulz, R. Spohr, C. Trautmann, and V. Vutsadakis. Track size and track structure in polymer irradiated by heavy ions. *Nucl. Instr. Meth. Phys. Res. B*, 146(1-4):468–474, 1998.

[146] T. W. Cornelius, P. Y. Apel, B. Schiedt, C. Trautmann, M. E. Toimil-Molares, S. Karim, and R. Neumann. Investigation of nanopore evolution in ion track-etched polycarbonate membranes. *Nucl. Instr. Meth. Phys. Res. B*, 265:553–557, 2007.

[147] A.I. Vilensky, D.L. Zagorski, V.Ya. Kabanov, and B.V. Mchedlishvili. UV- and γ-sensitization of latent tracks in polyethylene terephthalate. *Radiat. Meas.*, 36(1–6):131–135, 2003.

[148] G. Pépy, P. Boesecke, A. Kuklin, E. Manceau, B. Schiedt, Z. Siwy, M. Toulemonde, and C. Trautmann. Cylindrical nanochannels in ion-track polycarbonate membranes studied by small-angle x-ray scattering. *J. Appl. Cryst.*, 40(s1):388 –392, 2007.

[149] W. DeSorbo. Ultraviolet eeffect and aging effect on the etching characteristics of fission tracks in polycarbonate film. *Nuclear Tracks*, 3(1-2):13–32, 1979.

[150] P. Apel. Track etching technique in membrane technology. *Radiat. Meas.*, 34:559 – 566, 2001.

[151] B. Kuttich, M. Engel, C. Trautmann, and B. Stühn. Tailored nanochannels of nearly cylindrical geometry analysed by small angle x-ray scattering. *Appl. Phys. A*, 114(2):387–392, 2014.

[152] Z. Siwy, P. Apel, D. Baur, D. D. Dobrev, Y. E. Korchev, R. Neumann, R. Spohr, and K.-O. Trautmann, C. andVoss. Preparation of synthetic nanopores with transport properties analogous to biological channels. *Surf. Sci.*, 532âĂŞ535:1061 – 1066, 2003. Proceedings of the 7th International Conference on Nanometer-Scale Science and Technology and the 21st European Conference on Surface Science.

[153] P. Y. Apel, I. V. Blonskaya, S. N. Dmitriev, O. L. Orelovich, and B. A. Sartowska. Ion track symmetric and asymmetric nanopores in polyethylene terephthalate foils for versatile applications. *Nucl. Instr. Meth. Phys. Res. Sec. B*, 365:409 – 413, 2015.

[154] Janina Krieg. Fabrication and characterization of arrays of conical metal nanowires. Bachelor thesis, Technische Universität Darmstadt, June 2010.

[155] B. E. Fischer and R. Spohr. Production and use of nuclear tracks: imprinting structure on solids. *Rev. Mod. Phys.*, 55:907–948, 1983.

[156] M. Engel, B. Stühn, J. J. Schneider, T. Cornelius, and M. Naumann. Small-angle x-ray scattering (SAXS) off parallel, cylindrical, well-defined nanopores: from random pore distribution to highly ordered samples. *Appl. Phys. A*, 97(1):99–108, 2009.

[157] T. W. Cornelius, B. Schiedt, D. Severin, G. Pépy, M. Toulemonde, P. Y. Apel, P. Boesecke, and C. Trautmann. Nanopores in track-etched polymer membranes characterized by small-angle x-ray scattering. *Nanotechnology*, 21(15):155702, 2010.

[158] Anne Spende. *Surface modification of etched ion-track polymer membranes by atomic layer deposition*. PhD thesis, Technische Universität Darmstadt, 2016.

[159] G. Guillot and F. Rondelez. Characteristics of submicron pores obtained by chemical etching of nuclear tracks in polycarbonate films. *J. Appl. Phys.*, 52(12):7155–7164, 1981.

[160] Marco Cassinelli. *Thermoelectric Properties of $Bi_{1-x}Sb_x$ Nanowires Electrodeposited in Etched Ion-Track Membranes*. PhD thesis, Technische Universität Darmstadt, 2016.

[161] A. J. Bard, L. R. Faulkner, J. Leddy, and C. G. Zoski. *Electrochemical methods: fundamentals and applications*, volume 2. Wiley New York, 1980.

[162] Cynthia G Zoski. *Handbook of electrochemistry*. Elsevier, 2006.

[163] Milan Paunovic and Mordechay Schlesinger. *Fundamentals of electrochemical deposition*, volume 45. John Wiley & Sons, 2006.

[164] E. Budevski, G. Staikov, and W. J. Lorenz. Electrocrystallization: Nucleation and growth phenomena. *Electrochim. Actas*, 45(15–16):2559–2574, 2000.

[165] P. Magri, C. Boulanger, and J.-M. Lecuire. Synthesis, properties and performances of electrodeposited bismuth telluride films. *J. Mater. Chem.*, 6(5):773, 1996.

[166] Oliver Picht. *Growth and characterization of bismuth telluride nanowires*. PhD thesis, Ruperto-Carola University of Heidelberg, Heidelberg, Germany, 2010.

[167] B. Y. Yavorsky, N. F. Hinsche, I. Mertig, and P. Zahn. Electronic structure and transport anisotropy of Bi_2Te_3 and Sb_2Te_3. *Phys. Rev. B*, 84(16):165208, 2011.

[168] K. Yamana, K. Kihara, and T. Matsumoto. Bismuth tellurides: BiTe and Bi_4Te_3. *Acta Crystallogr. Sect. B*, 35(1):147–149, Jan 1979.

[169] G. Cliff and G. W. Lorimer. The quantitative analysis of thin specimens. *J. Microsc.*, 103(2):203–207, 1975.

[170] W. Wang, X. Lu, T. Zhang, G. Zhang, W. Jiang, and X. Li. Bi_2Te_3/Te multiple heterostructure nanowire arrays formed by confined precipitation. *J. Am. Chem. Soc.*, 129(21):6702–6703, 2007.

[171] J. Lee, A. Berger, L. Cagnon, U. Gösele, K. Nielsch, and J. Lee. Disproportionation of thermoelectric bismuth telluride nanowires as a result of the annealing process. *Phys. Chem. Chem. Phys.*, 12(46):15247–15250, 2010.

[172] J. Lee, J. Kim, W. Moon, A. Berger, and J. Lee. Enhanced Seebeck coefficients of thermoelectric Bi_2Te_3 nanowires as a result of an optimized annealing process. *J. Phys. Chem. C*, 116(36):19512–19516, 2012.

[173] A. Einstein. Über einen die Erzeugung und Verwandlung des Lichtes betreffenden heuristischen Gesichtspunkt. *Ann. Phys. (Berlin)*, 322(6):132–148, 1905.

[174] John F. Moulder. *Handbook of X-ray Photoelectron Spectroscopy: A Reference Book of Standard Spectra for Identification and Interpretation of XPS Data*. Physical Electronics Division, Perkin-Elmer Corporation, 1992.

[175] W. E. Morgan, W. J. Stec, and J. R. Van Wazer. Inner-orbital binding-energy shifts of antimony and bismuth compounds. *Inorganic Chemistry*, 12(4):953–955, 1973.

[176] M. K. Bahl, R. L. Watson, and K. J. Irgolic. X-ray photoemission studies of tellurium and some of its compounds. *J. Chem. Phys*, 66(12):5526–5535, 1977.

[177] Y. F. Zhu, J. S. Lian, and Q. Jiang. Modeling of the melting point, Debye temperature, thermal expansion coefficient, and the specific heat of nanostructured materials. *J. Phys. Chem. C*, 113(39):16896–16900, 2009.

[178] M. Li and T.-S. Zhu. Modeling the melting temperature of nanoscaled bimetallic alloys. *Phys. Chem. Chem. Phys.*, 18(25):16958–16963, 2016.

[179] K. K. Nanda, S. N. Sahu, and S. N. Behera. Liquid-drop model for the size-dependent melting of low-dimensional systems. *Phys. Rev. A*, 66(1):013208, 2002.

[180] Gerhard Wilde. *Nanostructured Materials*. Frontiers of Nanoscience. Elsevier Science, 2009.

[181] M. Cassinelli, A. Romanenko, H. Reith, F. Völklein, W. Sigle, C. Trautmann, and M. E. Toimil-Molares. Low temperature annealing effects on the stability of Bi nanowires. *Phys. Status Solidi*, 2015.

[182] M. E. Toimil-Molares, L. Röntzsch, W. Sigle, K.-H. Heinig, C. Trautmann, and R. Neumann. Pipetting nanowires: In situ visualization of solid-state nanowire-to-nanoparticle transformation driven by surface diffusion-mediated capillarity. *Adv. Funct. Mater.*, 22(4):695–701, 2012.

[183] D. Hsieh, Y. Xia, L. Wray, D. Qian, A. Pal, J. H. Dil, J. Osterwalder, F. Meier, G. Bihlmayer, C. L. Kane, Y. S. Hor, R. J. Cava, and M. Z. Hasan. Observation of unconventional quantum spin textures in topological insulators. *Science*, 323(5916):919–922, 2009.

[184] D. Hsieh, Y. Xia, D. Qian, L. Wray, J. H. Dil, F. Meier, J. Osterwalder, L. Patthey, J. G. Checkelsky, N. P. Ong, A. V. Fedorov, H. Lin, A. Bansil, D. Grauer, Y. S. Hor, R. J. Cava, and M. Z. Hasan. A tunable topological insulator in the spin helical Dirac transport regime. *Nature*, 460(7259):1101–1105, 2009.

[185] Y.-Y. Li, G. Wang, X.-G. Zhu, M.-H. Liu, C. Ye, X. Chen, Y.-Y. Wang, K. He, L.-L. Wang, X.-C. Ma, H.-J. Zhang, X. Dai, Z. Fang, X.-C. Xie, Y. Liu, X.-L. Qi, J.-F. Jia, S.-C. Zhang, and Q.-K. Xue. Intrinsic topological insulator Bi_2Te_3 thin films on Si and their thickness limit. *Adv. Mater.*, 22(36):4002–4007, 2010.

[186] G. Wang, X.-G. Zhu, Y.-Y. Sun, Y.-Y. Li, T. Zhang, J. Wen, X. Chen, K. He, L.-L. Wang, X.-C. Ma, J.-F. Jia, S. B. Zhang, and Q.-K. Xue. Topological insulator thin films of Bi_2Te_3 with controlled electronic structure. *Adv. Mater.*, 23(26):2929–2932, 2011.

[187] H. Hertz. Über einen Einfluss des ultravioletten Lichtes auf die elektrische Entladung. *Ann. Phys. (Berlin)*, 267(8):983–1000, 1887.

[188] M. P. Seah and W. A. Dench. Quantitative electron spectroscopy of surfaces: A standard data base for electron inelastic mean free paths in solids. *Surface and Interface Analysis*, 1(1):2–11, 1979.

[189] S. Tanuma, C. J. Powell, and D. R. Penn. Calculations of electron inelastic mean free paths. II. data for 27 elements over the 50-2000 eV range. *Surf. Interface Anal.*, 17(13):911–926, 1991.

[190] A. Damascelli. Probing the electronic structure of complex systems by ARPES. *Phys. Scripta*, 2004(T109):61, 2004.

[191] Frank Ortmann, Stephan Roche, and Sergio O. Valenzuela. *Topological Insulators: Fundamentals and Perspectives*. John Wiley & Sons, 2015.

[192] J. Krumrain, G. Mussler, S. Borisova, T. Stoica, L. Plucinski, C. M. Schneider, and D. Grützmacher. MBE growth optimization of topological insulator Bi_2Te_3 films. *J. Cryst. Growth*, 324(1):115 – 118, 2011.

[193] Y. Guo, M. Aisijiang, K. Zhang, W. Jiang, Y. Chen, W. Zheng, Z. Song, J. Cao, Z. Liu, and H. Peng. Selective-area van der Waals epitaxy of topological insulator grid nanostructures for broadband transparent flexible electrodes. *Adv. Mater.*, 25(41):5959–5964, 2013.

[194] P. M. Coelho, G. A. S. Ribeiro, A. Malachias, V. L. Pimentel, W. S. Silva, D. D. Reis, M. S. C. Mazzoni, and R. Magalhaes-Paniago. Temperature-induced coexistence of a conducting bilayer and the bulk-terminated surface of the topological insulator Bi_2Te_3. *Nano Lett.*, 13(9):4517–4521, 2013.

[195] L. Ley, S. Kowalczyk, R. Pollak, and D. A. Shirley. X-ray photoemission spectra of crystalline and amorphous Si and Ge valence bands. *Phys. Rev. Lett.*, 29(16):1088–1092, 1972.

[196] R. A. Pollak, S. Kowalczyk, L. Ley, and D. A. Shirley. Evolution of core states from energy bands in the 4d5s5p region from Pd to Xe. *Phys. Rev. Lett.*, 29(5):274, 1972.

[197] M. Scrocco. X-ray and electron-energy-loss spectra of Bi, Sb, Te and Bi_2Te_3, Sb_2Te_3 chalcogenides. *J. Electron Spectrosc. Relat. Phenom.*, 50:171–184, 1990.

[198] T. P. Debies and J. W. Rabalais. X-ray photoelectron spectra and electronic structure of Bi_2X_3 (X=O, S, Se, Te). *Chem. Phys.*, 20(2):277–283, 1977.

[199] D. A. Shirley. High-resolution x-ray photoemission spectrum of the valence bands of gold. *Phys. Rev. B*, 5(12):4709–4714, 1972.

[200] M. Delfino, S. Salimian, D. Hodul, A. Ellingboe, and W. Tsai. Plasma cleaned Si analyzed in situ by x-ray photoelectron spectroscopy, secondary ion mass spectrometry, and actinometry. *J. Appl. Phys.*, 71(2):1001–1009, 1992.

[201] T. Takahagi, I. Nagai, A. Ishitani, and H. Kuroda. The formation of hydrogen passivated silicon single-crystal surface using ultraviolet cleaning and HF etching. *J. Appl. Phys.*, 64(6):3516–3521, 1988.

[202] W. Kohn. Nobel lecture: Electronic structure of matter-wave functions and density functionals. *Rev. Mod. Phys.*, 71(5):1253–1266, 1999.

[203] K. Capelle. A bird's-eye view of density-functional theory. *Braz. J. Phys*, 36(4A):1318–1343, 2006.

[204] P. Hohenberg and W. Kohn. Inhomogeneous electron gas. *Phys. Rev.*, 136(3B):B864–B871, 1964.

[205] W. Kohn and L. J. Sham. Self-consistent equations including exchange and correlation effects. *Phys. Rev.*, 140(4A):A1133–A1138, 1965.

[206] J. P. Perdew, K. Burke, and M. Ernzerhof. Gerneralized gradient approximation made simple. *Phys. Rev. Lett.*, 77(18):3865, 1996.

[207] G. Kresse and J. Hafner. *Ab initio* molecular dynamics for liquid metals. *Phys. Rev. B*, 47:558–561, Jan 1993.

[208] G. Kresse and J. Furthmüller. Efficiency of ab-initio total energy calculations for metals and semiconductors using a plane-wave basis set. *Computational Materials Science*, 6(1):15 – 50, 1996.

[209] A. A. Mostofi, J. R. Yates, G. Pizzi, Y. S. Lee, I. Souza, D. Vanderbilt, and N. Marzari. An updated version of wannier90: A tool for obtaining maximally localised wannier functions. *Comp. Phys. Comm.*, 185(8):2309–2310, 2014.

[210] M. P. Lopez Sancho, J. M. Lopez Sancho, and J. Rubio. Highly convergent schemes for the calculation of bulk and surface Green functions. *J. Phys. F: Met. Phys.*, 15(4):851, 1985.

[211] J. Krieg, C. Chen, J. Avila, Z. Zhang, W. Sigle, H. Zhang, C. Trautmann, M. C. Asensio, and M. E. Toimil-Molares. Exploring the electronic structure and chemical homogeneity of individual Bi_2Te_3 nanowires by nano-angle-resolved photoemission spectroscopy. *Nano Lett.*, 16(7):4001–4007, 2016.

[212] J. G. Analytis, R. D. McDonald, S. C. Riggs, J.-H. Chu, G. S. Boebinger, and I. R. Fisher. Two-dimensional surface state in the quantum limit of a topological insulator. *Nature Phys.*, 6(12):960–964, 2010.

[213] J. Zhang, C.-Z. Chang, Z. Zhang, J. Wen, X. Feng, K. Li, M. Liu, K. He, L. Wang, X. Chen, Q.-K. Xue, X. Ma, and Y. Wang. Band structure engineering in $(Bi_{1-x}Sb_x)_2Te_3$ ternary topological insulators. *Nat. Commun.*, 2(574), 2011.

[214] Z. Ren, A. A. Taskin, S. Sasaki, K. Segawa, and Y. Ando. Large bulk resistivity and surface quantum oscillations in the topological insulator Bi_2Te_2Se. *Phys. Rev. B*, 82(24):241306, 2010.

[215] Y. Wang, F. Xiu, L. Cheng, L. He, M. Lang, J. Tang, X. Kou, X. Yu, X. Jiang, Z. Chen, J. Zou, and K. L. Wang. Gate-controlled surface conduction in Na-doped Bi_2Te_3 topological insulator nanoplates. *Nano Lett.*, 12(3):1170–1175, 2012.

[216] K. Hoefer, C. Becker, S. Wirth, and L. Hao Tjeng. Protective capping of topological surface states of intrinsically insulating Bi_2Te_3. *AIP Adv.*, 5(9):097139, 2015.

[217] T. V. Menshchikova, M. M. Otrokov, S. S. Tsirkin, D. A. Samorokov, V. V. Bebneva, A. Ernst, V. M. Kuznetsov, and E. V. Chulkov. Band structure engineering in topological insulator based heterostructures. *Nano Lett.*, 13(12):6064–6069, 2013.

[218] Z. Zhang, X. Feng, M. Guo, Y. Ou, J. Zhang, K. Li, L. Wang, X. Chen, Q. Xue, X. Ma, K. He, and Y. Wang. Transport properties of Sb_2Te_3/Bi_2Te_3 topological insulator heterostructures. *Phys. Status Solidi RRL*, 7(1-2):142–144, 2013.

[219] J. Dufouleur, L. Veyrat, A. Teichgräber, S. Neuhaus, C. Nowka, S. Hampel, J. Cayssol, J. Schumann, B. Eichler, O. G. Schmidt, B. Büchner, and R. Giraud. Quasiballistic transport of Dirac fermions in a Bi_2Se_3 nanowire. *Phys. Rev. Lett.*, 110(18):186806, 2013.

[220] J. Dufouleur, V. Veyrat, E. Xypakis, J. H. Bardarson, C. Nowka, S. Hampel, B. Eichler, O. G. Schmidt, B. Büchner, and R. Giraud. Pseudo-ballistic transport in 3D topological insulator quantum wires. *arXiv:1504.08030v1 [cond-mat.mes-hall]*, 2015.

[221] L. Fang and W.-K. Kwok. Quantum phenomena in transport measurements of topological insulator nanostructures (review article). *Low Temp. Phys.*, 40(4):280–285, 2014.

[222] H.-S. Kim, H. S. Shin, J. S. Lee, C. W. Ahn, J. Y. Song, and Y.-J. Doh. Quantum electrical transport properties of topological insulator Bi_2Te_3 nanowires. *Current Applied Physics*, 16(1):51–56, 2016.

[223] B. Hamdou, J. Gooth, A. Dorn, E. Pippel, and K. Nielsch. Aharonov-Bohm oscillations and weak antilocalization in topological insulator Sb_2Te_3 nanowires. *Appl. Phys. Lett.*, 102(22):223110, 2013.

[224] Y. Yan, Z.-M. Liao, Y.-B. Zhou, H.-C. Wu, Y.-Q. Bie, J.-J. Chen, J. Meng, X.-S. Wu, and D.-P. Yu. Synthesis and quantum transport properties of Bi_2Se_3 topological insulator nanostructures. *Sci. Rep.*, 3:1264, 2013.

[225] B. F. Gao, P. Gehring, M. Burghard, and K. Kern. Gate-controlled linear magnetoresistance in thin Bi_2Se_3 sheets. *Appl. Phys. Lett.*, 100(21):212402, 2012.

[226] J. Tian, C. Chang, H. Cao, K. He, X. Ma, Q. Xue, and Y. P. Chen. Quantum and classical magnetoresistance in ambipolar topological insulator transistors with gate-tunable bulk and surface conduction. *Sci. Rep.*, 4:4859, 2014.

[227] Supriyo Datta. *Electronic transport in mesoscopic systems*. Cambridge University Press, 1997.

[228] Harald Ibach and Hans Lüth. *Solid-State Physics*. Springer-Verlag Berlin Heidelberg, 4 edition, 2009.

[229] Charles Kittel. *Quantum Theory of Solids*. John Wiley & Sons, New York, 1987.

[230] K. Hong, F. Y. Yang, K. Liu, D. H. Reich, P. C. Searson, C. L. Chien, F. F. Balakirev, and G. S. Boebinger. Giant positive magnetoresistance of Bi nanowire arrays in high magnetic fields. *J. Appl. Phys.*, 85(8):6184–6186, 1999.

[231] M. Kohler. Zur magnetischen Widerstandsänderung reiner Metalle. *Ann. Phys. (Berlin)*, 424(1-2):211–218, 1938.

[232] H. Tang, D. Liang, R. L. J. Qiu, and X. P. A. Gao. Two-dimensional transport-induced linear magneto-resistance in topological insulator Bi_2Se_3 nanoribbons. *ACS Nano*, 5(9):7510–7516, 2011.

[233] S. X. Zhang, R. D. McDonald, A. Shekhter, Z. X. Bi, Y. Li, Q. X. Jia, and S. T. Picraux. Magneto-resistance up to 60 tesla in topological insulator Bi_2Te_3 thin films. *Appl. Phys. Lett.*, 101(20):202403, 2012.

[234] A. A. Abrikosov. Quantum magnetoresistance. *Phys. Rev. B*, 58(5):2788–2794, 1998.

[235] C. M. Wang and X. L. Lei. Linear magnetoresistance on the topological surface. *Phys. Rev. B*, 86(3):035442, 2012.

[236] L. Schubnikow and W. J. de Haas. A new phenomenon in the change of resistance in a magnetic field of single crystals of bismuth. *Nature*, 126:500, 1930.

[237] W. Knap, V. I. Falko, E. Frayssinet, P. Lorenzini, N. Grandjean, D. Maude, G. Karczewski, B. L. Brandt, J. Lusakowski, I Grzegory, M. Leszczynski, P. Prystawko, C. Skierbiszewski, S. Porowski, X. Hu, G. Simin, M. Asif Khan, and M. S. Shur. Spin and interaction effects in Shubnikov-de Haas oscillations and the quantum Hall effect in GaN/AlGaN heterostructures. *J. Phys. Condens. Matter*, 16(20):3421, 2004.

[238] Thomas Ihn. *Semiconductor Nanostructures: Quantum states and electronic transport*. Oxford University Press, 2010.

[239] G. P. Mikitik and Y. V. Sharlai. Manifestation of Berry's phase in metal physics. *Phys. Rev. Lett.*, 82(10):2147–2150, 1999.

[240] Y. Zhang, Y.-W. Tan, H. L. Stormer, and P. Kim. Experimental observation of the quantum Hall effect and Berry's phase in graphene. *Nature*, 438(7065):201–204, 2005.

[241] G. Bergmann. Weak anti-localization - an experimental proof for the destructive interference of rotated spin 1/2. *Solid State Commun.*, 42(11):815–817, 1982.

[242] H.-T. He, G. Wang, T. Zhang, I.-K. Sou, G. K. L. Wong, J.-N. Wang, H.-Z. Lu, S.-Q. Shen, and F.-C. Zhang. Impurity effect on weak antilocalization in the topological insulator Bi_2Te_3. *Phys. Rev. Lett.*, 106(16):166805, 2011.

[243] S. Hikami, A. I. Larkin, and Y. Nagaoka. Spin-orbit interaction and magnetoresistance in the two dimensional random system. *Prog. Theor. Phys.*, 63(2):707–710, 1980.

[244] Y. Aharonov and D. Bohm. Significance of electromagnetic potentials in the quantum theory. *Phys. Rev.*, 115(3):485–491, 1959.

[245] J. H. Bardarson, P. W. Brouwer, and J. E. Moore. Aharonov-bohm oscillations in disordered topological insulator nanowires. *Phys. Rev. Lett.*, 105(15):156803, 2010.

[246] T. Ihn. Topological insulators: Oscillations in the ribbons. *Nat. Mater.*, 9(3):187–188, 2010.

[247] S. Cho, B. Dellabetta, R. Zhong, J. Schneeloch, T. Liu, G. Gu, M. J. Gilbert, and N. Mason. Aharonov-Bohm oscillations in a quasi-ballistic three-dimensional topological insulator nanowire. *Nat. Commun.*, 6:7634, 2015.

[248] M. E. Toimil-Molares, N. Chtanko, T. W. Cornelius, D. Dobrev, I. Enculescu, R. H. Blick, and R. Neumann. Fabrication and contacting of single Bi nanowires. *Nanotechnology*, 15(4):201, 2004.

[249] Loïc Burr. *Ion-track technology based synthesis and characterization of gold and gold alloys nanowires and nanocones*. PhD thesis, Technische Universität Darmstadt, June 2016.

[250] Fatima Boui. Synthese, Characterisierung und Kontaktierung von Bismuttellurid-Nanodrähten. Bachelor thesis, Hochschule RheinMain, Wiesbaden Rüsselsheim, November 2014.

[251] Lisette Haarmann. Electric and thermoelectric properties of single Bi_2Te_3 nanowires and nanowire arrays. Bachelor thesis, Technische Universität Darmstadt, October 2016.

[252] Louis Veyrat. *Quantum Transport Study in 3D Topological Insulators Nanostructures*. PhD thesis, Technische Universität Dresden, 2016.

[253] Fabrice Iacovella. *Transport électronique sous champ magnétique intense dans des gaz d'électrons bidimensionnels*. PhD thesis, L'université Toulouse 3 Paul Sabatier, March 2015.

[254] J. Béard, J. Billette, P. Frings, M. Suleiman, and F. Lecouturier. Special coils development at the national high magnetic field laboratory in Toulouse. *J. Low Temp. Phys.*, 170(5):442–446, 2013.

[255] J. Béard and F. Debray. The french high magnetic field facility. *J. Low Temp. Phys.*, 170(5):541–552, 2013.

[256] D. Aherne, A. Satti, and D. Fitzmaurice. Diameter-dependent evolution of failure current density of highly conducting dna-templated gold nanowires. *Nanotechnology*, 18(12):125205, 2007.

[257] S. Karim, W. Ensinger, S. A. Mujahid, K. Maaz, and E. U. Khan. Effect of etching conditions on pore shape in etched ion-track polycarbonate membranes. *Radiation Measurements*, 44(9-10):779–782, 2009.

[258] D.-X. Qu, Y. S. Hor, J. Xiong, R. J. Cava, and N. P. Ong. Quantum oscillations and Hall anomaly of surface states in the topological insulator Bi_2Te_3. *Science*, 329(5993):821–824, 2010.

[259] Y. S. Hor, D. Qu, N. P. Ong, and R. J. Cava. Low temperature magnetothermoelectric effect and magnetoresistance in Te vapor annealed Bi_2Te_3. *J. Phys. Condens. Matter*, 22(37):375801, 2010.

[260] Y. Ma, E. Ahlberg, Y. Sun, B. B. Iversen, and A. E.C. Palmqvist. Thermoelectric properties of thin films of bismuth telluride electrochemically deposited on stainless steel substrates. *Electrochim. Acta*, 56(11):4216–4223, 2011.

[261] P. Chiu and I. Shih. A study of the size effect on the temperature-dependent resistivity of bismuth nanowires with rectangular cross-sections. *Nanotechnology*, 15(11):1489, 2004.

[262] T. W. Cornelius, M. E. Toimil-Molares, R. Neumann, and S. Karim. Finite-size effects in the electrical transport properties of single bismuth nanowires. *J. Appl. Phys.*, 100(11):114307, 2006.

[263] W. Steinhögl, G. Schindler, G. Steinlesberger, and M. Engelhardt. Size-dependent resistivity of metallic wires in the mesoscopic range. *Phys. Rev. B*, 66(7):075414, 2002.

[264] E Hi Sondheimer. The mean free path of electrons in metals. *Adv. Phys.*, 1(1):1–42, 1952.

[265] A. F. Mayadas and M. Shatzkes. Electrical-resistivity model for polycrystalline films: the case of arbitrary reflection at external surfaces. *Phys. Rev. B*, 1(4):1382–1389, 1970.

[266] N. H. Jo, K. Lee, J. Kim, J. Jang, J. Kim, and M.-H. Jung. Crossover between two-dimensional surface state and three-dimensional bulk phase in Fe-doped Bi_2Te_3. *Appl. Phys. Lett.*, 104(25):252413, 2014.

[267] Z. H. Wang, L. Yang, X. J. Li, X. T. Zhao, H. L. Wang, Z. D. Zhang, and X. P. A. Gao. Granularity controlled nonsaturating linear magnetoresistance in topological insulator Bi_2Te_3 films. *Nano Lett.*, 14(11):6510–6514, 2014.

[268] J. Chen, H. J. Qin, F. Yang, J. Liu, T. Guan, F. M. Qu, G. H. Zhang, J. R. Shi, X. C. Xie, C. L. Yang, K. H. Wu, Y. Q. Li, and L. Lu. Gate-voltage control of chemical potential and weak antilocalization in Bi_2Se_3. *Phys. Rev. Lett.*, 105(17):176602, 2010.

[269] L. V. Yashina, J. Sánchez-Barriga, M. R. Scholz, A. A. Volykhov, A. P. Sirotina, V. S. Neudachina, M. E. Tamm, A. Varykhalov, D. Marchenko, G. Springholz, G. Bauer, A. Knop-Gericke, and O. Rader. Negligible surface reactivity of topological insulators Bi_2Se_3 and Bi_2Te_3 towards oxygen and water. *ACS Nano*, 7(6):5181–5191, 2013.

[270] S. Bässler, B. Hamdou, P. Sergelius, A.-K. Michel, R. Zierold, H. Reith, J. Gooth, and K. Nielsch. One-dimensional edge transport on the surface of cylindrical $Bi_xTe_{3-y}Se_y$ nanowires in transverse magnetic fields. *Applied Physics Letters*, 107(18):181602, 2015.

[271] J. Chen, X. Y. He, K. H. Wu, Z. Q. Ji, L. Lu, J. R. Shi, J. H. Smet, and Y. Q. Li. Tunable surface conductivity in Bi_2Se_3 revealed in diffusive electron transport. *Phys. Rev. B*, 83(24):241304, 2011.

[272] H. Steinberg, J.-B. Laloë, V. Fatemi, J. S. Moodera, and P. Jarillo-Herrero. Electrically tunable surface-to-bulk coherent coupling in topological insulator thin films. *Phys. Rev. B*, 84(23):233101, 2011.

[273] S. Matsuo, T. Koyama, K. Shimamura, T. Arakawa, Y. Nishihara, D. Chiba, K. Kobayashi, T. Ono, C.-Z. Chang, K. He, X.-C. Ma, and Q.-K. Xue. Weak antilocalization and conductance fluctuation in a submicrometer-sized wire of epitaxial Bi_2Se_3. *Phys. Rev. B*, 85(7):075440, 2012.

[274] Y. Takagaki, A. Giussani, K. Perumal, R. Calarco, and K.-J. Friedland. Robust topological surface states in sb_2te_3 layers as seen from the weak antilocalization effect. *Phys. Rev. B*, 86(12):125137, 2012.

[275] J. J. Cha, D. Kong, S.-S. Hong, J. G. Analytis, K. Lai, and Y. Cui. Weak antilocalization in $Bi_2(Se_xTe_{1-x})_3$ nanoribbons and nanoplates. *Nano Lett.*, 12(2):1107–1111, 2012.

List of Abbreviations

AAS	**A**ltshuler-**A**ronov-**S**pivak
AB	**A**haronov-**B**ohm
ANTARES	**A**nalysis **N**ano-spo**T** **A**ngle **R**esolved photo**E**mission **S**pectroscopy
ARPES	**A**ngle-**R**esolved **P**hoto**E**mission **S**pectroscopy
BHZ	**B**ernevig, **H**ughes and **Z**hang
BZ	**B**rillouin **Z**one
DAISY FUN	**DA**rmstädter **I**ntegriertes **SY**stem für **FUN**damentale Untersuchungen
DFT	**D**ensity **F**unctional **T**heory
DOS	**D**ensity **O**f **S**tates
EBL	**E**lectron **B**eam **L**ithography
EDX	**E**nergy **D**ispersive **X**-ray spectroscopy
FWHM	**F**ull **W**idth at **H**alf **M**aximum
FZP	**F**resnel **Z**one **P**late
GGA	**G**eneralized **G**radient **A**pproximation
HAADF	**H**igh-**A**ngle **A**nnular **D**ark-**F**ield imaging
HF	**H**dro**F**luoric acid
HLN	**H**ikami, **L**arkin and **N**agaoka
HRSEM	**H**igh **R**esolution **S**canning **E**lectron **M**icroscopy
HRTEM	**H**igh **R**esolution **T**ransmission **E**lectron **M**icroscopy
IFW	Leibniz-**I**nstitut für **F**estkörper- und **W**erkstoffforschung
LAAS	**L**aboratoire d'**A**nalyse et d'**A**rchitecture des **S**ystème
LDA	**L**ocal **D**ensity **A**pproximation
LL	**L**andau **L**evel
LNCMI	**L**aboratoire **N**ational des **C**hamps **M**agnétiques **I**ntenses
MR	**M**agneto**R**esistance

OSA	**O**rder **S**orting **A**perture
PC	**P**oly**C**arbonate
PES	**P**hoto**E**mission **S**pectroscopy
PET	**P**oly**E**thylene **T**erephthalate
QHS	**Q**uantum **H**all **S**tate
QSHS	**Q**uantum **S**pin **H**all **S**tate
SAXS	**S**mall-**A**ngle **X**-ray **S**cattering
SEM	**S**canning **E**lectron **M**icroscopy
SdH	**S**hubnikov-**d**e **H**aas
SOC	**S**pin-**O**rbit **C**oupling
SOLEIL	**S**ource **O**ptimisée de **L**umière d'**E**nergie **I**ntermédiare de **L**aboratoire d'utilisation du rayonnement électromagnétique
StEM	**St**uttgart institute for **E**lectron **M**icroscopy
TC	**T**exture **C**oefficient
TE	**T**hermo**E**lectric
TEM	**T**ransmission **E**lectron **M**icroscopy
TI	**T**opological **I**nsulator
TKNN	**T**houless **K**ohmoto **N**ightingale and den **N**ijs
TRIM	**T**ime-**R**eversal Invariant **M**omenta
2DEG	**Two**-**D**imensional **E**lectron **G**as
UHV	**U**ltrahigh **V**acuum
UNILAC	**Uni**versal **L**inear **Ac**celerator
VLS	**V**apor-**L**iquid-**S**olid
WAL	**W**eak **A**nti**l**ocalization
WL	**W**eak **l**ocalization
XPS	**X**-ray **P**hotomission **S**pectroscopy
XRD	**X**-**R**ay **D**iffraction

List of Figures

List of Tables

Acknowledgements

This work would not have been possible without the contribution and tremendous effort of many people. I would like to express my deepest gratitude for all the support and help.

Firstly, I am grateful to my PhD supervisor Prof. Dr. Christina Trautmann for giving me the opportunity to be part of the materials research group at GSI. I highly appreciate her inspirational guidance scientifically and personally. I value her encouraging me to take part and even organize conferences and workshops. Thank you a lot for making all my ideas possible.

I am very thankful to my mentor, Dr. Maria Eugenia Toimil-Molares for initiating my PhD project and supporting every idea I had. I am also honored to have been given the opportunity to present my work on many international conferences and especially in front of the DFG, providing me an interesting insight into science politics. Thank you for keeping my back and your effort in proofreading.

I would like to thank Prof. Dr. Ralph Krupke, Prof. Dr. Wolfgang Ensinger and Prof. Dr. Friedemann Völklein for accepting to be part of my examination board. A special thank you goes to Prof. Dr. Ralph Krupke for actively participating in my HGS-HIRe for FAIR PhD committee meeting, for his help with EBL and for co-referring this work.

This project was financially supported by the Deutsche Forschungsgesellschaft (DFG) within the SPP 1666 program. Additional financial and educational support was provided by HGS-HIRe for FAIR.

During this thesis many scientific collaborations have been established and I am honored to have met and worked with enthusiastic scientists all over Europe:

- I thank Dr. Maria Carmen Asensio, Dr. José Avila, Dr. Chaoyu Chen and Stephane Lorcy for their introduction to nano-ARPES experiments at ANTARES and for their support during the beamtimes. Moreover, I acknowledge their contribution to our joint publication.
- An additional value to the interpretation of the nano-ARPES data was provided by Prof. Dr. Hongbin Zhang and Zeying Zhang of the TU Darmstadt. I am extremely thankful for their fast agreement to run the calculations and for their never-ending patience in explaining the basics of DFT to me.
- It was a great pleasure to work with Dr. Walter Escoffier and Fabrice Iacovella from the LNCMI in Toulouse, who introduced me to the field of MR measurements in high B-fields and the sample preparation by EBL. I acknowledge the organization of the financial support by the NEXT scholarship. The friendly atmosphere and the many spare time activities made me feel very welcome.
- I very much enjoyed the magnetotransport measurements with Dr. Romain Giraud, Dr. Joseph Dufouleur and Hannes Funke at the IFW in Dresden. I am especially thankful for teaching me

about the measurement challenges faced in the nanoworld, your help with the data analysis and patience to answer my numerous questions even under time pressure towards the end of my thesis.

- Many open questions were clarified with the help of Dr. Wilfried Sigle at the MPI for Festkörperforschung in Stuttgart, who conducted all TEM and EDX in TEM measurements. Thank you for introducing me to these fascinating instruments, for your interest in my work and the impressively fast corrections of the manuscript of our joint publication.
- Another big contribution to the nanowire characterization was added by Dr. Florent Yang from the TU Darmstadt who spent a lot of effort conducting the XPS measurements at DAISY-FUN. Thank you for all the fruitful discussions we had on this topic.

I am deeply grateful to Fatima Boui and Lisette Haarmann, "my" Bachelor students, who did not only extend my knowledge by their excellent scientific work, but also by their unstoppable curiosity and creative ideas. Stay as you are and keep up the good work!

I would also like to thank Robert Visinka for the metalization of the laser lithography samples.
A special thank you goes to Dr. Markus Bender for showing so much enthusiasm for my ideas on setups for electrical and thermal measurements. Your help and support is very much appreciated.

Joining the same crazy PhD ride were my great colleagues, who became close friends: Dr. Loïc Burr, Dr. Marco Cassinelli, Dr. Christian Hubert, Peter Katrík, Dr. Dimitri Khaghani, Dr. Katharina Kupka, Dr. Liana Movsesyan, Alexey Prosvetov, Dr. Anton Romanenko, Dr. Anne Spende and Michael Wagner. Without you and your motivation the past four years would not have been that much fun.
I would like to especially thank: Anne, Liana and Loïc for proofreading my thesis; Marco and Michael for brain-twisting discussions about TEs and TIs; Liana for her support, motivation, her point of view and being the best officemate I could have wished for; Peter for being up for any activity and for walking alongside me especially during the writing process.
Big thanks also go to Dr. Mercedes Carrillo Solano, Dr. Wouter Maijenburg, Dr. Ina Schubert and Dr. Daniel Severin for sharing their experience about science and life with me in many (friday) fun discussions.

Motivation is essential during the final months of writing and I thank all my friends outside of GSI for showing interest, keeping me focused and providing necessary breaks. This is by far nothing one can take for granted and I am very moved by your affection.

Finally, I owe my deepest gratitude to my family, Martina, Peter and Constantin Krieg. They support me unconditionally, joined in proofreading and closely took part in the ride between deepest desperation and highest overestimation of my capabilities. I have no words fitting to express my love and gratitude.

Thank you! Hakuna Matata!

About the author

04/2013–07/2017	**PhD Student** *Technische Universität Darmstadt, Darmstadt, Germany* *GSI Helmholtz Center for Heavy Ion Research GmbH, Darmstadt, Germany* Department: Material- und Geowissenschaften Thesis: Characterization of individual Bi_2Te_3 nanowires electrodeposited in etched ion-track membranes for nano-ARPES and electrical transport studies
10/2010–03/2013	**Master of Science in Physics** *Stuttgart University, Stuttgart Germany* *Max Planck Institute for Solid State Research, Stuttgart, Germany* Specialization: experimental solid state physics Thesis: Graphene nanoribbon devices for the study of biomolecular interactions
10/2006–09/2010	**Bachelor of Science in Physics** *Technische Universität Darmstadt, Darmstadt, Germany* Thesis: Fabrication and Characterization of arrays of conical metal nanowires